Study of Magnetoelectric and Piezotronic Microstructures and Materials for Biomagnetic Sensing utilizing X-ray Techniques

Dissertation

zur Erlangung des Doktorgrades
der Mathematisch-Naturwissenschaftlichen Fakultät
der Christian-Albrechts-Universität zu Kiel
vorgelegt von

Philipp Jordt

Kiel 2021

Erste/r Gutachter/in:	PD Dr. Bridget M. Murphy
Zweite/r Gutachter/in:	Prof. Dr. Kai Roßnagel
Tag der mündlichen Prüfung:	05.11.2021

ABSTRACT

Detecting electric potential differences from the human physiology is an established technique in medical diagnosis, e.g., as electrocardiogram. It arises from a changing electrical polarization of living cells. Simultaneously, biomagnetism is induced and can be utilized for medical examinations, as well. Benefits in using magnetic signals are, no need for direct skin contact and an increased spatial resolution, e.g., for mapping brain activity, especially in combination with electrical examinations. But biomagnetic signals are very weak and, thus, highly sensitive devices are necessary. The development of small and easy to use biomagnetic sensors, with a sufficient sensitivity, is the goal of the Collaborative Research Centre 1261 - Magnetoelectric Sensors: From Composite Materials to Biomagnetic Diagnostics. This thesis was written as part of this collaboration, with the main focus on the investigation of crystalline structures and structure related properties of piezotronic and magnetostrictive materials by utilizing a selection of X-ray techniques, i.e., X-ray diffraction (XRD), X-ray reflectivity (XRR) and coherent X-ray diffraction imaging (CXDI). Piezotronics, realized by combining piezoelectricity and Schottky contacts in one structure, provides a promising path to enhance sensor sensitivity. A first study investigated the crystalline structure of three piezotronic ZnO rods, spatially resolved by scanning nano XRD and combined with electrical examinations of their Schottky contact properties. It is found that the crystalline quality has a clear impact on the electrical properties of the related Schottky contact, probably due to crystalline defects. A complementary transmission electron microscopy (TEM) and XRD study performed on hybride vapor phase epitaxy (HVPE) grown GaN showed a slight, photoelectrochemical etching related relaxion of strain originating from crystal growth. In a separate study, CXDI was utilized for three-dimensional visualization of strain in a gold coated ZnO rod, with spatial resolution below 30 nm. A distinct strain distribution was found inside the rod, denoted to depletion and screening effects occurring in bent piezotronic structures, and a high strain at the interface may be related to Schottky contact formation. This interface strain agrees with results obtained from TEM. A succeeding CXDI study was conducted on a ZnO rod coated with magnetostrictive FeCoSiB and the possibility for the investigation of the Schottky contacts electrical properties. It was found that FeCoSiB sputtered on ZnO results in an ohmic contact and that an external magnetic field causes a change of the electrical properties, probably due to a strain change, visualized by CXDI. In a fifth study, magnetostrictive FeCo/TiN multilayer structures were investigated by a combined TEM and XRD/XRR approach, showing a relaxation of the structure due to an annealing process and a cube-on-cube structure of the FeCo and TiN layers.

KURZFASSUNG

Das Messen von elektrischen Potentialen des menschlichen Körpers ist eine verbreitete medizinische Technik. Diese entstehen durch eine sich verändernde elektrische Polarisation in lebendigen Zellen. Gleichzeitig entsteht dabei Biomagnetismus, der ebenfalls für medizinische Messungen Verwendung finden kann. Hierbei ist kein direkter Hautkontakt nötig und eine verbesserte räumliche Auflösung ist möglich, insbesondere in Verbindung mit elektrischen Messungen. Jedoch sind hoch sensible Sensoren nötig, um diese schwachen biomagnetischen Signale zu detektieren. Die Entwicklung von kleinen und benutzerfreundlichen biomagnetischen Sensoren ist Aufgabe des Sonderforschungsbereichs 1261 - Magnetoelectric Sensors: From Composite Materials to Biomagnetic Diagnostics. Im Rahmen dieses Projektes wurde diese Arbeit verfasst. Der Fokus lag dabei auf der Untersuchung der kristallinen Struktur und der Eigenschaften von piezotronischen und magnetostriktiven Materialien. Dazu wurden Röntgenbeugung (XRD), Röntgenreflektivität (XRR) und Bildgebung mittels kohärenter Röntgenbeugung (CXDI) verwendet. Der piezotronische Effekt ist eine mögliche Option zur Verbesserung der Sensorsensibilität und entsteht indem der piezoelektrische Effekt Schottky Kontakte beeinflusst. In einer ersten Studie wurde die kristalline Struktur von drei ZnO Nadeln durch nanofokussierte XRD räumlich aufgelöst und mit elektrischen Messungen der Schottky Kontakte kombiniert. Dabei zeigte sich, dass die kristalline Struktur einen Einfluss auf die elektrischen Eigenschaften hat. In einer weiteren Studie wurde durch sich ergänzende Untersuchungen mittels Transmissionselektronenmikroskopie (TEM) und XRD gezeigt, dass mittels HVPE gewachsenes GaN durch photoelektrochemisches Ätzen eine Entspannung der Kristallverformung erfährt. Des Weiteren wurde CXDI verwendet, um die Kristallstruktur in einer mit Gold beschichteten ZnO Nadel in drei Dimensionen und mit einer räumlichen Auflösung von unter 30 nm zu vermessen. Innerhalb der Nadel wurden Veränderungen der Kristallstruktur gemessen und piezotronisch induzierter Elektronenverarmung bzw. Abschirmungseffekten zugeschrieben. Weiter wurde eine Oberflächenverformung mittels TEM und CXDI gefunden und dem Schottky Kontakt zugeschrieben. In einer anschließenden Studie wurden CXDI und elektrische Messungen kombiniert, um eine mit magnetostriktivem FeCoSiB beschichtete ZnO Nadel zu untersuchen. Es zeigte sich, dass auf ZnO abgeschiedenes FeCoSiB zu einem ohmschen Kontakt führt und ein externes Magnetfeld eine Änderung der elektrischen Eigenschaften hervorruft, wahrscheinlich aufgrund einer Dehnungsänderung. In einer fünften Studie wurden magnetostriktive FeCo/TiN Mehrschichtstrukturen mittels TEM und XRD/XRR untersucht und eine Relaxation der Struktur aufgrund eines Glühprozesses gefunden.

CONTENTS

1. INTRODUCTION

This dissertation “Study of magnetoelectric and piezotronic microstructures and materials for biomagnetic sensing utilizing X-ray techniques” was imbedded in the Collaborative Research Centre (CRC) 1261 “Magnetoelectric Sensors: From Composite Materials to Biomagnetic Diagnostics” funded by the Deutsche Forschungsgemeinschaft (DFG). The goal of this CRC is to develop of small, cost effective and easy to use sensors, capable of detecting extremely weak bio magnetic fields arising from the human physiology.[1] These sensors could enable or enhance diagnosis for medical applications, ranging from movement diagnosis, to magnetocardiography (MCG) and magnetoencephalography (MEG) measurements of the hearth and brain and, further, to the positioning of electrodes for deep brain stimulation[2]. To accomplish this goal, the CRC has two project areas.

A) Investigation of materials and effects, suitable for usage in sensors and sensor development

B) Testing of sensors and implementation of developed sensors for medical applications

This thesis was conducted in project area A and as part of project A6 “Microstructure and Structual Change of Magnetoelectric and Piezotronic Sensors”. Project A6 combines high resolution synchrotron-based X-ray scattering techniques and advanced transmission electron microscopy methods to provide a unique view of the structural behavior of materials and model structures, *in situ* as well as operando. Here, the focus is on investigations with X-ray techniques.

Biomagnetic fields have very low amplitudes. For example the hearth produces a typical signal strength of 1-100 pT[3], while the brain exhibits even lower signals of 0.1-10 pT[3]. These effects are more than five magnitudes weaker than the strength of the earth’s surface magnetic field (~30 µT)[4]. This leads to the need for a highly sensitive sensor with a high dynamic range, so it can be used outside of a shielded chamber, e.g., in a doctor’s office or emergency care location.

This level of magnetic field sensitivity was first meet by superconducting quantum interference devices (SQUID) sensors,[3,5,6] enabling the first biomagnetism measurements in the early 1970’s.[7,8] SQUID technology relies on two effects of superconductors, quantization of the magnetic flux causing a compensation current in the device and the Josephson effect enabling the measurement of this current.[6] Modern SQUIDs have a typical sensitivity of 1-10 fT $Hz^{-1/2}$ and are currently the best choice available when measuring weak biomagnetic signals.[3] SQUIDs are often arranged in arrays of typically 300 sensors to measure MEG signals from the brain and map the source location in 3D.

A relatively newly developed sensor type is the optical pumped atomic magnetometer (OPM).[9,10] The most sensitive OPMs are used in a spin-exchange relaxation-free (SERF) mode and reach sensitivities of <1 fT $Hz^{-1/2}$,[9] which is comparable to the SQUIDs performance. In SERF OPMs, a vapor cell containing a gas as resonant medium (e.g., potassium) is pumped with a laser, while a second laser is probing the medium. The basic principle is that the pump laser polarizes the vapor atoms, these undergo a change in magnetic fields due to the Larmor precession and this is monitored by measuring the intensity or polarization change with the probe laser.[9]

Both, SQUID and OPM sensors have limitations that restricts their applications. First, for the SQUID, it is necessary to cool these sensors with liquid helium to keep them at an operational temperature and, additionally, it is necessary to operate the devices in a magnetic field shielded room.[3] In contrast, for the OPM it is necessary to heat the sensor vapor cell up to 180° C as in the case of potassium.[9] This can be dangerous in the vicinity of human tissue. They also require a shielded environment, providing a near-zero magnetic field, as they are easily saturated. For both sensors types these restrictions make their operation quite expensive and inflexible.

To achieve the CRC's goal of developing a small, cost effective and easy to use sensor (usable outside of shielded chambers and without the need for additional cooling) while providing a sufficient sensitivity, a broad range of effects, materials and designs is under investigation to realize a magnetoelectric (ME) sensor. In the CRC, ME sensors are typically realized by combining magnetostrictive and piezoelectric materials in one device[11] to achieve a conversion from a magnetic field to an electrical output, e.g. potential change from piezoelectric effect[12].

Multiple sensor concepts, driven by mechanically soft composites, micro- or multilayer structures for example, based on different effects, e.g., electrically modulation, surface acoustic waves or piezotronic effects, are under investigation within the CRC to enhance the sensor performance and lower the limit of detection.

Our approach to increase the sensitivity is to measure the sensor's current response due to the piezotronic effect[13]. The piezotronic effect, described first in 2006 by Wang and Song,[14] denotes an effect occurring in piezoelectric semiconductors with additional Schottky contacts[15], while exposed to a mechanical stress. The stress induces a piezoelectric potential in the material, that in turn modifies the Schottky contact barrier height and, hence, the electrical properties of the device. This can be utilized, e.g., to generate current[16] or as readout for sensing[17] and may enable an increased limit of detection for senor applications. Over the last one and a half decades, the number of publications has grown for piezotronic applications

ranging from, artificial skin[18], energy harvesting[19], synthetic synapsis[20], to magnetic field sensors[21] as in CRC 1261. Many of these studies focus on finding innovative and new concepts to bring the piezotronic effect into use. Most of the fundamental knowledge on the effect is deduced from mechanical bending and stressing experiments on piezotronic material, while recording current/voltage curves and, thus, investigate the Schottky barrier change as a function of the external stress.[16,22,23] Little is known about the structural changes occurring in piezotronic driven devices and the main goal of this dissertation is to study the crystalline structure and related changes in piezotronic and other materials by the means of X-ray techniques.

More than a century ago, in 1912 Max von Laue and his assistants showed that X-ray radiation can determine crystalline structures on the atomic scale.[24] Two years later he was awarded the Nobel prize for this development. Since then, X-ray diffraction (XRD) has shown its potential as a powerful tool to investigate the crystalline structure of many different kinds of materials.

In this thesis, the focus is on atomic resolution XRD investigations to visualize structural changes in potential sensor materials such as ZnO microstructures coated with magnetostrictive or metallic coatings, in etched GaN and in multilayer stacks, consisting of very thin, alternating TiN and magnetostrictive FeCo layers. The goal of these studies was to obtain a better understanding of the underlying effects and the properties of the chosen materials and thus exploit the piezotronic effect to improve the performance of the CRC's sensors. To investigate the structure and strain response of the samples to electrical and magnetic stimulation *in situ* a number of X-ray techniques were used.

X-ray reflectometry (XRR)[25] enables the investigation of the electron density, the roughness at a surface or interface and the thickness of layers, regardless of whether they are crystalline or amorphous. XRD and the related scanning nanofocus XRD (nXRD),[26,27] enable the investigation of crystalline structure and, thus, strain if present. Depending on the experimental setup, the strain resolution may reach $\sim 10^{-5}$. In the case of scanning nXRD, this can be combined with a spatial resolution of 100 nm or lower, limited by the minimum size of the nanofocused X-ray beam. nXRD requires the intensity and low beam divergence provided at modern synchrotron sources of the third generation.

In the case of coherent X-ray diffraction imaging (CXDI)[27,28] the structure and thus the strain distribution is reconstructed from the measured coherent X-ray scattering data by an algorithm based approach to solve the inverse problem. CXDI has the mayor advantage over nXRD, that it is possible to reconstruct the complex electron density with a spatial resolution below 10 nm and in three dimensions. Here, the coherent fraction of the beam is the limiting factor.

Five manuscripts, four of which have been published, are presented in Chapter 5. The first study investigated the impact of crystal quality in ZnO rods on the Schottky barrier and hence on the piezotronic performance, by a combined approach of nXRD and current/voltage curves. In the second publication, XRD and transmission electron microscopy (TEM) were combined to investigate the structural changes in HVPE grown GaN samples due to etching. The third publication highlights the impact of gold coating on the crystal structure of ZnO in a combined CXDI/TEM approach. For the fourth experiment, a thin ZnO rod was coated partly with magnetostrictive FeCoSiB and current/voltage investigations were performed. CXDI visualized the strain distribution inside the rod while exposed to an external magnetic field. In the fifth paper, an as deposited and an annealed multilayer stack, of thin TiN and FeCo layers, were investigated by XRD, XRR and TEM to visualize the structural change due to annealing.
In the conclusion, a summary of the findings, an outlook and a perspective for future experiments are given.

2. FUNDAMENTALS

2.1 PIEZOELECTRICITY

Piezoelectricity may be separated into the (direct) piezoelectric effect[29], in which a piezoelectric material reacts to an mechanical stress by electric polarization, and the related, inverse/converse piezoelectric effect[30], which induces a strain in the material as a reaction to an external electric field. The piezoelectric effect was discovered by Jacques and Piere Currie while experimenting with Tourmaline in 1880.[31] Since then, it was utilized in many applications, including force sensors,[32] actuators,[33] and ultrasound.[31] In the broader public, the piezoelectric effect may not be as well known, but its applications in electric lighters or diagnostic sonography are present in everyday life .

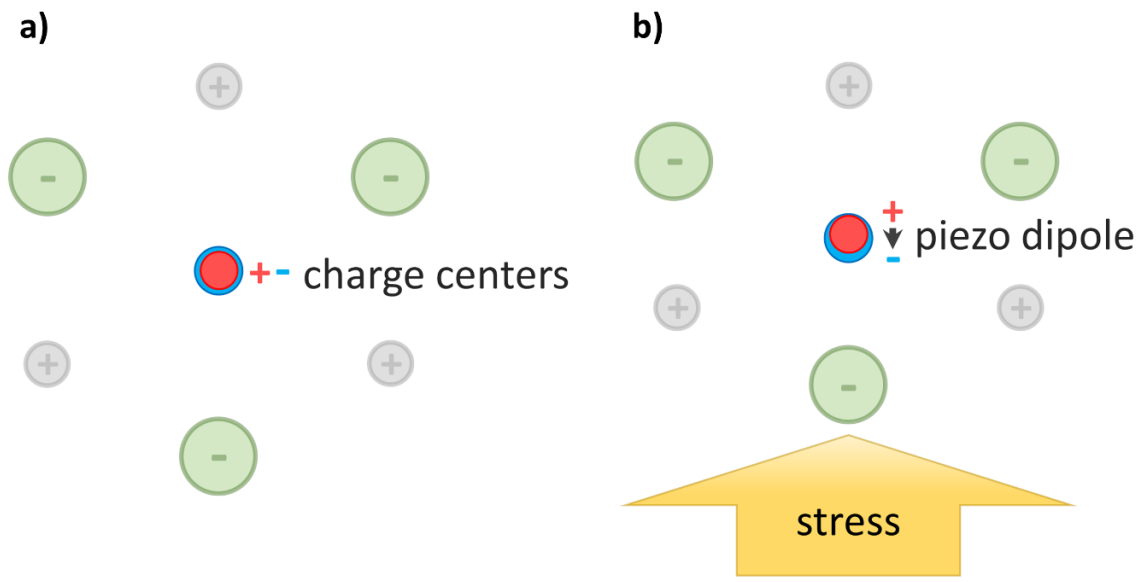

Figure 2.1: Schematic of the piezoelectric effect. a) View on a generic hexagonal crystal structure consisting of two species of atoms with positive or negative charges. Both species have a respective charge center in the middle, overlapping in the unstressed case. b) Application of mechanical stress causes a deformation of the crystal structure and a separation of the charge centers. This separation causes a piezo(electric) dipole moment and, thus, a polarization of the macroscopic crystal, measurable as the piezoelectric potential.

Figure 2.1 shows a two dimensional schematic of the direct piezoelectric effect occurring in a simplified, generic crystal lattice, consisting of two different atom species, grey and green circles. Each of the species has a specific charge, here, positive for grey and negative for green atoms, and to each of the species a charge center can be attributed, red and green circles in Figure 2.1, respectively. In case of an unstressed crystal these two charge centers are overlapping, as seen in Figure 2.1 a). The presence of an additional, external stress causes a

separation of these two charge centers and thus an electric dipole moment is induced, as shown in Figure 2.1 b). The multiple electric dipole moments inside a crystal cause an electric polarization and related piezo charges to accumulate at the surface. This is measurable as a piezo potential between two edges of the crystal. For example in ZnO and other tetrahedrally bonded semiconductors like GaN or AlN,[34] the effect arises from the missing inversion symmetry, causing a polarity.[35] In the related inverse piezoelectric effect, an externally applied electric field causes a polarization of the crystal, inducing a separation of the charge centers and results in a strained crystal.

Polarization P_i in a piezoelectric material is linked to a strain ϵ_{ij} by the piezoelectric strain coefficients e_{ijk}.[36]

$$P_i = e_{ijk}\epsilon_{ij} \tag{2.1}$$

For the inverse piezoelectric effect a strain ϵ_{ij} is occurring for a present electric field E_k and they are connected by the piezoelectric stress coefficients d_{ijk}.[36]

$$\epsilon_{ij} = d_{ijk}E_k \tag{2.2}$$

Furthermore, if free carriers are present in a stressed piezoelectric material, e.g., electrons from donor atoms, these experience a force due to the electric field and move towards the edge of inverse polarity compared to their own. Causing a partial or complete screening of the piezo charges, depending on the carrier concentration.[37]

2.2 Metal-Semiconductor contact

Two contrary behaviors are observable from electrical measurements on metal-semiconductor contacts.[38–40] First, the contact exhibits a rectifying, diode like behavior, with a distinct forward (current flows across the contact) and reverse direction (current is blocked at the contact), the so called Schottky contact, named after Walter Schottky. And second, a non-rectifying, ohmic resistance like behavior, called ohmic contact.

The rectifying Schottky contact is explained by the formation of a potential barrier (Schottky barrier), ideally resulting from difference in work function of the metal and the semiconductors electron affinity. The qualitative mechanism for the formation of the Schottky barrier is shown in Figure 2.2. There in, the idealized formation in absence of surface states or other modifications is described.[39] It is exemplary given for a n-type semiconductor to metal contact, as this is the typical intrinsic doping for ZnO,[41–43] the mainly utilized semiconductor in this thesis.

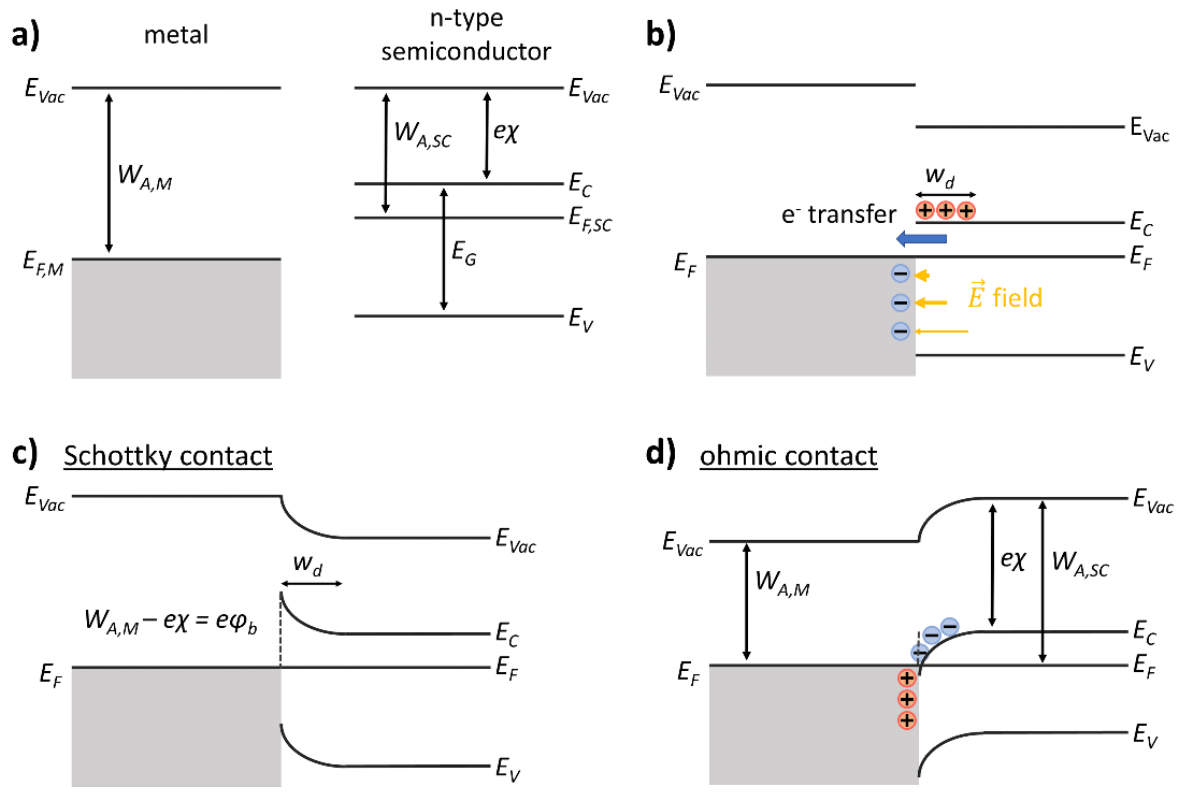

Figure 2.2: Energy band diagrams of a) spatially separated metal and n-type semiconductor materials b) brought into contact, leading to an alignment of the two Fermi levels by electron transfer and causing an electric field. c) Band bending occurring at the Schottky contact with barrier height $e\varphi_b$. d) Band bending in the opposite direction at an ohmic contact. Please note the abbreviations, vacuum energy E_{Vac}, Fermi level E_F, conduction band E_C and valence band E_V of the semiconductor, work function W_A, electron affinity $e\chi$, semiconductor band gap E_G, depletion width w_d. Further, the subscripts $_M$ and $_{SC}$ refer to metal and semiconductor, respectively.

In Figure 2.2 a) spatially separated metal and semiconductor materials are shown. Both materials exhibit a work function W_A, which is the minimum energy necessary to move an electron from the Fermi level E_F to the vacuum level E_{Vac}. The semiconductor exhibits further notable properties, the energy gap E_G which is the difference between conduction band E_C and the valence band E_V, and the electron affinity $e\chi$ with elementary charge e, which in similarity to the work function, is the energy necessary to move an electron from the conduction band to the vacuum. Bringing the materials into contact, as seen in Figure 2.2 b), causes a potential difference between the two Fermi levels and a charge transfer occurs, until the two Fermi levels are balanced in thermal equilibrium.[39] For this, electrons move from the semiconductor into the metal, leaving ionized donor atoms near the interface in a depletion region of width w_d.[39] In the first approximation, a constant space charge density of $\rho(x) = en_d$ with elementary charge e and carrier concentration n_d is present in the semiconductor's depletion region and is

zero outside of it.[39] This causes an electric field $\vec{E}(x)$ at spatial position x in the depletion region with increasing strength towards the interface.[39] The first Maxwell equation can be used to calculate this field.

$$\frac{\partial \vec{E}(x)}{\partial x} = \frac{\rho(x)}{\epsilon_r \epsilon_0} \;\rightarrow\; \vec{E}(x) = \frac{en_d}{\epsilon_r \epsilon_0} \int_{w_d}^{x} dx = \frac{en_d}{\epsilon_r \epsilon_0}(x - w_d) \tag{2.3}$$

With the relative ϵ_r and vacuum permittivity ϵ_0. This electric field causes an additional potential $V(x)$ in the depletion region and thus modifies the band structure.[39]

$$\frac{\partial V(x)}{\partial x} = -\vec{E}(x) \;\rightarrow\; V(x) = -\frac{en_d}{2\epsilon_r \epsilon_0}(x - w_d)^2 \tag{2.4}$$

The resulting energy band diagram of a Schottky contact with potential induced bending of the energy levels in the depletion region is shown in Figure 2.2 c), together with the Schottky barrier height $e\varphi_b$ and depletion width w_d. In the ideal case, the Schottky barrier height may be described in an electrostatic approach by the Schottky Mott rule as $e\varphi_b = W_{A,M} - e\chi$.[39]
Furthermore, the current across a Schottky contact as a function of an applied voltage is typically approximated by the thermionic emission model,[44] assuming that only electrons with an energy greater than the barrier height are able to surpass the barrier. The total current density can be described as a superposition of current flowing from the semiconductor into the metal J_{SM} and from the metal into the semiconductor J_{MS}.[39] While J_{SM} changes with the applied voltage, J_{MS} is independent of the same, due to the fact that the quasi fermi level (imref) is changing inside the semiconductor and thus leads to a barrier height change solely for the electrons approaching from the semiconductor side.

$$J(V) = \overbrace{A^* T^2 \exp\left(-\frac{e\varphi_b}{kT}\right) \exp\left(\frac{eV}{kT}\right)}^{J_{SM}} - \overbrace{A^* T^2 \exp\left(-\frac{e\varphi_b}{kT}\right)}^{J_{MS}} = J_0 \left(\exp\left(\frac{eV}{kT}\right) - 1\right) \tag{2.5}$$

with saturation current density

$$J_0 = A^* T^2 \exp\left(-\frac{e\varphi_b}{kT}\right) \tag{2.6}$$

Including the temperature T, Boltzmann constant k and effective Richardson constant A^*. For the formation of an ohmic contact the work function of the metal has to be comparable or smaller than the electron affinity of the semiconductor.[45] This causes a band bending towards the Fermi level and an overlap of the conduction band with the fermi level, as shown in Figure 2.2 d). Furthermore, a heavily doped semiconductor, e.g., for ZnO $n_d > 10^{18}$ cm^{-3},[45,46] or interdiffusion at the contact region, e.g., of Al and oxygen atoms at

Al/ZnO contacts,[47] lead to an ohmic behavior, due to a thin enough Schottky barrier, enabling electron tunneling through the barrier (field emission).[39,44,45]

The above drawn idealized picture of the Schottky contact formation is not complete and does not necessarily fit experimentally observed results.[40,45,48] Multiple, additional effects may occur, manipulating the metal-semiconductor contact. Some of which are image force lowering due to image charges accumulating in the metal, fermi level pinning, serial resistance and high voltage injection of holes.[39] Furthermore, it is reported that local inhomogeneities of the Schottky barrier have an immense impact on the overall properties of those, especially in combination with high doping concentrations.[40] This multitude of effects leads to vast deviations from the ideal Schottky-Mott rule. Thus, their implications are crucial for the understanding and application of such metal-semiconductor contacts.

2.3 Piezotronic Effect

The piezotronic effect changes the Schottky contacts electric properties of a mechanically stressed, piezoelectric semiconductor.[22,49] It is explained by a modification of the Schottky barrier height and depletion width, due to the strain induced piezoelectric potential and accumulation of piezo charges near the Schottky contact.[50,51] ZnO is a prominent material chosen for investigations of the piezotronic effect.[16,23,52,53]

Figure 2.3 a) depicts a qualitative sketch of the piezotronic effect. A piezoelectric semiconductor with a Schottky contact is exposed to an external mechanical stress, causing a strain in the semiconductor. Due to piezoelectricity a polarization across the semiconductor occurs, causing piezo charges to accumulate at the surfaces and a piezo potential to arise.[22] The Schottky contacts current/voltage (*I-V*) characteristic is changed by the piezo charges/potential, thus the external mechanical stress may be used to tailor the electrical properties of the device and, vice versa, the induced change of the electrical properties may be utilized to measure strain. While a positive piezo potential causes an increase of the measured current, an opposing negative potential causes a decrease in current. This is due to the piezo charges and potential modifying the Schottky barrier height and the width of the depletion region, as shown in Figure 2.3 b). Furthermore, the piezoelectric effect depends on the crystal orientation and can be inverted by changing the sign of the strain, i.e., by applying compressive instead of tensile stress.[22]

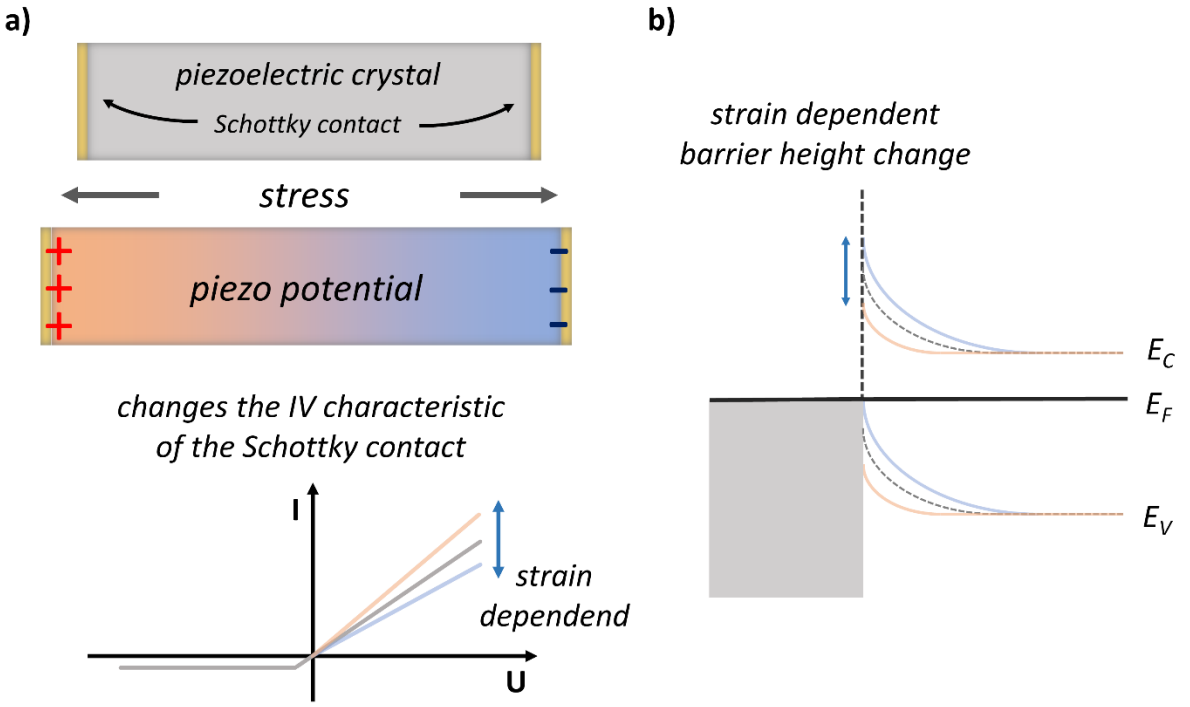

Figure 2.3: a) The piezotronic effect occurs in piezoelectric semiconductors under mechanical stress with additional Schottky contacts. The stress causes a piezo potential and piezo charges (plus and minus signs) in the crystal and a strain dependent change of the *I-V* curve is observable. b) The change of the *I-V* curve is caused by a modification of the Schottky barrier induced bending of the conduction and valence energy bands E_C and E_V, respectively, due to induced piezo potential and piezo charges near the surface. Negative piezo charges accumulating near a Schottky contact result in an increase of the Schottky barrier height and depletion width and a decrease for positive piezo charges. The Fermi level E_F does not change.

Figure 2.4 depicts qualitatively the Schottky barrier modification of a piezoelectric n-type semiconductor, caused by the piezotronic effect.[50] Exemplarily, the case of positive piezo charges, i.e., electron holes, accumulating near a Schottky interface is discussed.[22] Figure 2.4 a) shows the carrier density near the Schottky contact with additional piezo charges, induced by the piezoelectric effect. This may be interpreted as a thin layer of implanted n-dopants at the interface.[39,54] Similar to an increased doping concentration of the whole n-type semiconductor, this causes a decrease of the depletion width w_d. The increased carrier concentration causes an increase of the maximum electric field present in the Schottky contact depletion region, compared to a case without additional piezo charges, see Figure 2.4 b).[54] The Energy band diagram deduced from the electric field, refer to section 2.2, is shown in Figure 2.4 c). The energy bands in the presence of piezo charges exhibit a stronger band bending towards the interface and a thinner overall Schottky barrier thickness. Note that the height of the Schottky barrier should be similar in the ideal and the piezotronic modified case.[39] But an increased

image force lowering, due to the thinner barrier, leads to a height decrease and field emission (tunneling) causes a further reduction of the effective barrier height.[39]

Related arguments may be used to explain an increase of the Schottky barrier height and depletion width in the case of additional negative piezo charges accumulating near the Schottky contact.

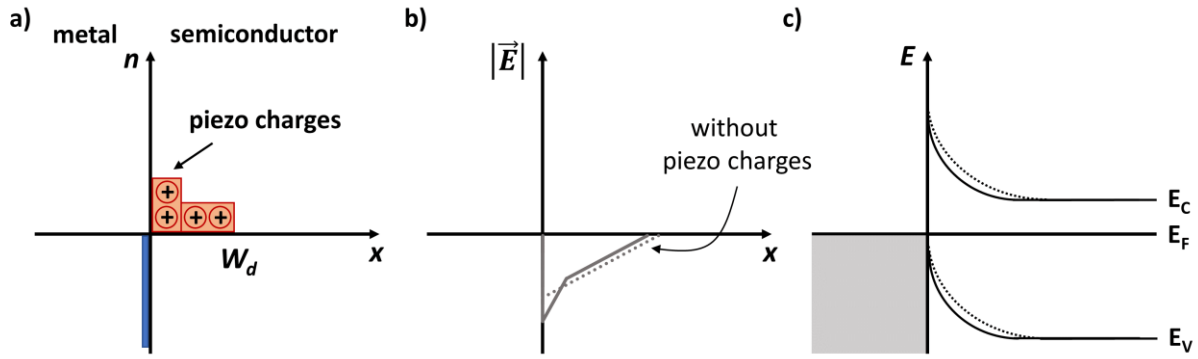

Figure 2.4: Qualitative mechanism of Schottky barrier modification, due to induced positive piezo charges in a piezoelectric semiconductor. a) Charge carrier density n for a Schottky contact region with a depletion width w_d and additional piezo charges. x-axis is the spatial position across the contact. b) Electric field distribution E in presence of piezo charges (solid line) and in absence (dotted line). c) Simplified energy band diagram of a Schottky contact with (solid line) and without (dotted line) piezo charges. Including conduction band E_C, valence band E_V and Fermi level E_F. Accumulation of positive piezo charges at the interface causes a shrinking of the depletion width.

In the discussion above it was assumed that the Fermi level is flat, and, hence, no potential gradient is present inside the crystal. This is an first order approximation, since most of the potential drop is occurring in the Schottky barrier depletion region.[39] But it may be that the piezo potential or a fraction of it are present inside the crystal and causes an additional change of the Schottky barrier, due to the modified Fermi level. And if furthermore free carriers are present, e.g., dopant electrons in n-type semiconductors, this would lead to a charge transport and result in a fully or partly screening of the positive piezo potential, depending on the dopant concentration.[37,55]

2.4 Magnetostriction

Magnetostriction is a material property, describing the deformation of a material while exposed to an external magnetic field H.[56,57] The relative length change Δl is quantified by the magnetostrictive parameter $\lambda(H) = \Delta l/l$. This value saturates for increasing field strengths and, typically, the magnetostriction is described by its saturation magnetostriction λ_s. The magnetostrictive effect is explained by the spin orbit coupling and the related magnetic

anisotropy.[57] Magnetostrictive materials that are volume conserving while exposed to an external magnetic field are exhibiting Joule magnetostriction. But there is volume changing non-Joulian magnetostriction, as well.[58] Some well-known magnetostrictive materials are Fe[56], Ni[56], $CoFe_2O_4$[59] and metallics alloys[60], e.g., $(Fe_{90}Co_{10})_{78}Si_{12}B_{10}$.

2.5 X-RAY SCATTERING

X-ray scattering is nowadays utilized in a variety of techniques to investigate the structure of matter, including X-ray diffraction to resolve crystal structures[61] and measure crystalline lattice changes, i.e., strain,[62], small angle X-ray scattering to resolve structures on huger length scales[63] and powder diffraction[64] from, e.g., powder, glassy or amorphous samples. Further, scattering is used for imaging techniques as in the case of holography[65] and coherent diffraction imaging[66]. Modern synchrotron sources elevate these techniques to a new level by enabling *in situ* and operando experiments. Due to a high photon flux, small beam diameter and small divergence provided by synchrotron sources of the third generation, a huge beam brilliance of $\sim 10^{20}$ is available.[67] Currently, these sources are being replaced by synchrotrons of the fourth generation, providing a brilliance of $\sim 10^{22}$ and a (transverse) coherence fraction of 15 % to 40 % at a photon energy of 12keV, particular important for coherent scattering experiments, e.g., CXDI.[68,69] Further, the synchrotrons are being complemented by X-ray free electron lasers (XFEL)[70,71], providing a peak brilliance of $\sim 10^{33}$ and a (transverse) coherence fraction up to 95% at 12keV photon energy.[70]

2.5.1 KINEMATICAL X-RAY SCATTERING

One of the first descriptions of X-ray scattering from crystalline structures was proposed by father and son, W.H. and L. Bragg in 1913.[72] They found that a constructive interference of scattered photons and, thus, a measurable signal of Bragg reflections is observable, if the beam path length difference of photons scattered from two neighboring crystal lattice planes is a multiple of the photons wavelength λ.[67]

$$m\lambda = 2dsin(\theta_b) \tag{2.7}$$

Integer m is the diffraction order and θ_b the scattering angle of the observed Bragg reflection, related to the crystal lattice distance d.

The short description below is based on the introduction to X-ray scattering from the textbook *Elements of Modern X-ray Physics* by J. Als-Nielsen and D. McMorrow.[67]

In the following it is assumed that the interaction between matter and photons is weak and hence, the involved photons are only scattered once, this is called the kinematical approximation. Furthermore, elastic scattering is assumed, meaning that the photon energy is conserved during the scattering process.

An easy and common way to describe an electromagnetic wave with a wavelength λ is the wavevector $\vec{k}$. It points in direction of wave propagation and has an absolute value of:

$$|\vec{k}| = \frac{2\pi}{\lambda} \tag{2.8}$$

In the classical consideration when an X-ray photon crosses paths with a free electron, a dipole interaction occurs. The alternating electric field of the photon is driving the electron into an oscillating motion, thus radiating an electromagnetic wave, with a phase shift of 180° due to Thompson scattering.

For a free electron the Thomson scattering length $r_0 = 2.82 \cdot 10^{-5}$ Å is found. Referred to as the classical radius of an electron and a basic measure for the ability of an electron to scatter photons.

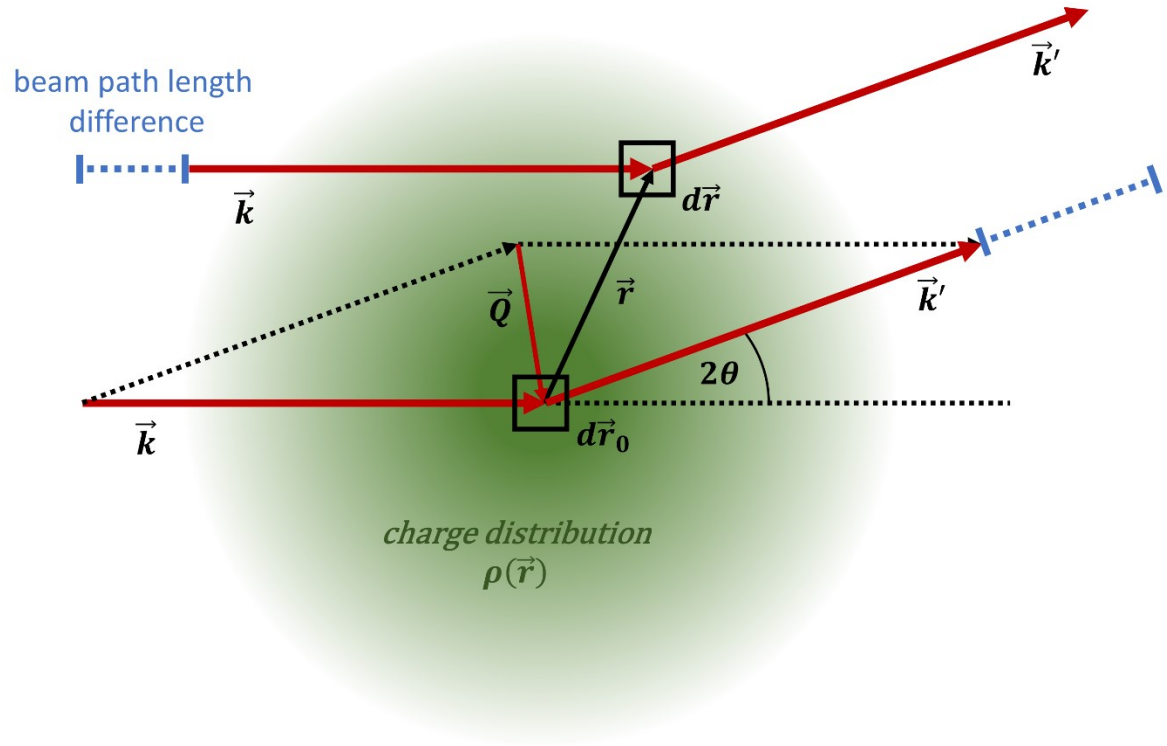

Figure 2.5: Simplified model of the electron charge distribution $\rho(\vec{r})$ of an atom. The incident $\vec{k}$ and scattered $\vec{k}'$ wavevectors define the scattering vector $\vec{Q}$ and the scattering angle θ. From an origin, surrounded by volume fraction $d\vec{r}_0$, a vector $\vec{r}$ is pointing towards a volume fraction $d\vec{r}$. The scattering signal from each volume fraction of the charge distribution must be combined to calculate the total scattering signal of the atom. Due to different beam path lengths for the individual volume fractions a phase shift $\Delta\phi(\vec{r}) = \vec{Q} \cdot \vec{r}$ is included to the calculation of the scattering signal.

To distinguish photon scattering from an atom one must consider the charge distribution $\rho(\vec{r})$ of the atom's electrons, see Figure 2.5. Vector $\vec{r}$ is pointing from an origin to a volume fraction $d\vec{r}$ of the charge distribution. Each volume fraction contributes to the scattering signal and a superposition of the whole volume must be calculated. Due to the spatial separation of the different volume fractions, the scattered waves from each volume fraction exhibits a different beam path length, resulting in a phase shift $\Delta\phi(\vec{r})$.

$$\Delta\phi(\vec{r}) = \left(\vec{k} - \vec{k}'\right) \cdot \vec{r} = \vec{Q} \cdot \vec{r} \tag{2.9}$$

Defining the scattering vector as $\vec{Q} = \vec{k} - \vec{k}'$, with the incident and scattered wavevectors $\vec{k}$ and $\vec{k}'$, respectively. In the elastic scattering case, no energy is lost ($\left|\vec{k}\right| = \left|\vec{k}'\right|$) and therefore the absolute value of the scattering vector is given by.

$$\left|\vec{Q}\right| = \frac{4\pi}{\lambda}\sin(\theta) \tag{2.10}$$

Including the scattering angle θ, defined as half the angle between $\vec{k}$ and $\vec{k}'$.

Scattering from a single atom may be described by the atomic structure factor $F_{atom}(\vec{Q})$ or the proportional atomic form factor $f\left(\vec{Q}\right)$. A small volume fraction $d\vec{r}$ of the charge distribution is contributing $-r_0\rho(\vec{r})d\vec{r}$ to the scattering signal with an additional phase factor $e^{i\vec{Q}\cdot\vec{r}}$, accounting for scattering from spatially separated volumes. This integral can as well be identified as the Fourier transform of the charge distribution in real space into the reciprocal $\vec{Q}$ space.

$$F_{atom}\left(\vec{Q}\right) = -r_o f\left(\vec{Q}\right) = -r_0 \int \rho(\vec{r}) e^{i\vec{Q}\cdot\vec{r}}\, d\vec{r} \tag{2.11}$$

Moving from a single atom to scattering from a molecule is achieved by summation over the atomic form factors f_i of the individual atoms at positions $\vec{r}_i$ in the molecule and by adding a phase factor $e^{i\vec{Q}\cdot\vec{r}_i}$, to account for a phase shift between the different atoms of the molecule. The result is the molecular structure factor $F_{mol}(\vec{Q})$.

$$F_{mol}\left(\vec{Q}\right) = -r_0 \sum_i f_i\left(\vec{Q}\right) e^{i\vec{Q}\cdot\vec{r}_i} \tag{2.12}$$

Instead of the atom's position $\vec{r}_i$ in a single molecule, the atom's position $\vec{r}$ in a crystalline lattice may be described by its position $\vec{r}_j$ inside a unit cell, combined with a lattice position $\vec{R}_n$ of this cell in the crystal lattice, $\vec{r} = \vec{r}_j + \vec{R}_n$. A unit cell describes a repeating atom distribution inside a crystal. Position $\vec{r}_i$ in equation 2.12 is substituted by $\vec{r}$ and the structure factor $F_{cryst}(\vec{Q})$ of the crystal can be written as a combination of two sums, where the first is

the unit cell structure factor also known as basis, describing the electron density inside the unit cell and the second is a sum over all lattice sites.

$$F_{cryst}(\vec{Q}) = -r_0 \sum_j f_j(\vec{Q}) e^{i\vec{Q}\cdot\vec{r}_j} \sum_n e^{i\vec{Q}\cdot\vec{R}_n} \tag{2.13}$$

In general, the scattered intensity is given by the modulus square of the scattering amplitude: $I = \left|A(\vec{Q})\right|^2$ and the scattering amplitude is proportional to the structure factor. Due to the modulus square the phase of the scattering amplitude is lost for the measurable intensity and, hence, the electron density cannot easily be determined by inversely Fourier transform the scattered signal, the well-known phase problem of X-ray scattering.

Studying the exponential of the second sum shows that scattering for large n, hence, huge crystals, is solely observable if the exponent is equal to 0 or a multiple of $i2\pi$.

$$\vec{Q} \cdot \vec{R}_n = multiple\ of\ 2\pi \tag{2.14}$$

The lattice vector $\vec{R}_n$, defining the unit cell position inside a crystal, can be written as the sum of three independent basis vectors of the lattice, $\vec{a}_m; m \in (1,2,3)$, multiplied with integers n.

$$\vec{R}_n = n_1\vec{a}_1 + n_2\vec{a}_2 + n_3\vec{a}_3 \tag{2.15}$$

A respective definition may be introduced for the reciprocal space. The reciprocal lattice describes the positions of Bragg reflections in the space of the scattering vector. Reciprocal lattice vector $\vec{G}$ is the sum of the reciprocal lattice basis vectors $\vec{b}_m; m \in (1,2,3)$ multiplied with integers, called miller indices h, k, l.

$$\vec{b}_1 = 2\pi \frac{a_2 \times a_3}{a_1 \cdot (a_2 \times a_3)}, \qquad \vec{b}_2 = 2\pi \frac{a_3 \times a_1}{a_1 \cdot (a_2 \times a_3)}, \qquad \vec{b}_3 = 2\pi \frac{a_1 \times a_2}{a_1 \cdot (a_2 \times a_3)} \tag{2.16}$$

$$\vec{G} = h\vec{b}_1 + k\vec{b}_2 + l\vec{b}_3 \tag{2.17}$$

Multiplying the lattice vector $\vec{R}_n$ and reciprocal lattice vector $\vec{G}$ results in a multiple of 2π and hence the scattering vector $\vec{Q}$ must be equal to the reciprocal lattice vector $\vec{G}$ to satisfy equation 2.14.

$$\vec{Q} = \vec{G} \tag{2.18}$$

This is the Laue condition, stating that a scattered signal from a crystal is measurable if the scattering vector is equal to a reciprocal lattice vector of the crystal structure, due to a constructive interference of the scattering signals from multiple unit cells.

From the experimentally distinguished reciprocal lattice vector, the lattice spacing d_{hkl} of the investigated crystal lattice can be derived by:

$$d_{hkl} = \frac{2\pi}{|\vec{G}|} \tag{2.19}$$

Combining equations 2.10 and 2.19 shows that the Laue condition (equation 2.18) and Bragg's law (equation 2.7) are equivalent descriptions of coherent scattering processes from crystals.

2.6 X-RAY REFLECTIVITY

X-ray reflectometry/reflectivity (XRR) is a well-known X-ray technique, allowing for surface and near surface investigations in high resolution.[67] Almost a century ago, in the early 1930's Heinz Kiessig described total external reflection and interference observed in X-ray reflectometry experiments.[73,74] Further on, in 1954 Lyman G. Parratt extended the technique and introduced a theoretical framework for modeling reflectivity measurements.[75] Over the past decades the technique was utilized to investigate solid[76], as well as, liquid samples[77,78]. Reflection and refraction at interfaces separating different media are expected for X-rays, due to their electromagnetic wave nature.[67] Refraction and scattering are two equal representations of the same phenomena.[67] For the description of refraction it is common to introduce the refraction index n, it is typically increasing with the photon energy and depicts the resonant behavior of electromagnetic waves at electronic transitions, which depend on the electron configuration of the atoms and molecules.[67] But at each resonance the refraction index drops and in the X-ray regime the refraction index is slightly below one, due to the high photon energy above most, if not all, resonance frequencies of the electron transitions.[67]

$$n = 1 - \delta + i\beta \tag{2.20}$$

The refraction index is modified by the two coefficients $\delta = r_0\lambda^2\rho/2\pi$ and $\beta = \lambda\mu/4\pi$,[79] accounting for scattering and absorption, respectively. With the electron density ρ and the absorption coefficient μ. δ is typically around 10^{-5} and β is even magnitudes smaller.[67] Thus, the index of refraction is just slightly smaller than unity, causing total external reflection to occur at very small angles. From Snell's law and a Taylor series of the cosine function the critical angle θ_c for total external reflection may be calculated as follows.[79]

$$\theta_c \approx \sqrt{2\delta} \tag{2.21}$$

Hence, the critical angle of a material is directly related to its electron density. Below this critical angle, an evanescent wave is still penetrating the probed material to a depth of a few nm and, thus, holds surface sensitive information's.[67]

For recording a reflectivity of a specimen, the wave vector transfer is changed in very fine steps by rotating the sample and, simultaneously, moving the detector. Starting below the critical

angle and up to 2.5 Å^{-1} [78], but this range is depending on the experimental setup, sample and source. The measured, specular reflectivity is defined as the reflected intensity at a given angle divided by the incident intensity; $R(q) = I(q)/I_0$.[79] In case of an ideal, flat sample the idealized Fresnel reflectivity R_F may be calculated by the following equation.[67,79]

$$R_F(q_z) = \left| \frac{q_z - \sqrt{q_z^2 - q_c^2 - \frac{32i\pi^2\beta}{\lambda}}}{q_z + \sqrt{q_z^2 - q_c^2 - \frac{32i\pi^2\beta}{\lambda}}} \right|^2 \qquad (2.22)$$

With the wave vector transfer of the critical angle q_c and a function of the wave vector transfer parallel to the surface normal q_z, thus, related to the specular reflected intensity. In case of non-ideal surface properties the Fresnel reflectivity can be modified by a Debye-Waller like factor; $e^{-q_z^2\sigma^2}$.[67,79] Where σ^2 is a measure for the root mean square of surface roughness, or in case of a graded interface σ may be seen as half width of an error function, describing a non-abrupt electron density decrease towards the surface.

Until now the described sample consisted of a single medium, but if a layer of another medium with a different index of refraction is present on top of the first, the observed reflectivity exhibits oscillations.[67] These oscillations arise from interference of multiple reflections, due to transmission and reflection occurring at the two interfaces and the length of the oscillations Δq is linked to the layer thickness d by $\Delta q = 2\pi/d$.

Further, the electron density profile $\rho(z)$ is directly encoded in the reflectivity, but, due to the phase problem, there is no unique solution to $\rho(z)$ by inversion of the measured reflectivity.[80] A solution to the inversion problem is the creation of a model electron density profile (and absorption profile) from prior knowledge on the sample parameters and refinement of this model, by calculation of an model reflectivity and comparison to the measured dataset.[80] This may be done by an algorithm introduced by Parratt.[67,75] There in, the electron density model is divided into fine layers and the model reflectivity is calculated by taking into account all reflections from the multiple layer interfaces. The algorithm begins with the interface between the lowest layer and the as infinite supposed substrate, further, the reflectivity is found by successively adding the reflected contributions from all layers until the upper most interface, i.e. the sample surface, is reached.

2.7 COHERENCE

The coherence properties of a beam may be described by the concept of coherence lengths.[67,81,82] These define a length scale over which a propagating wavefield preserves a certain degree of coherence.

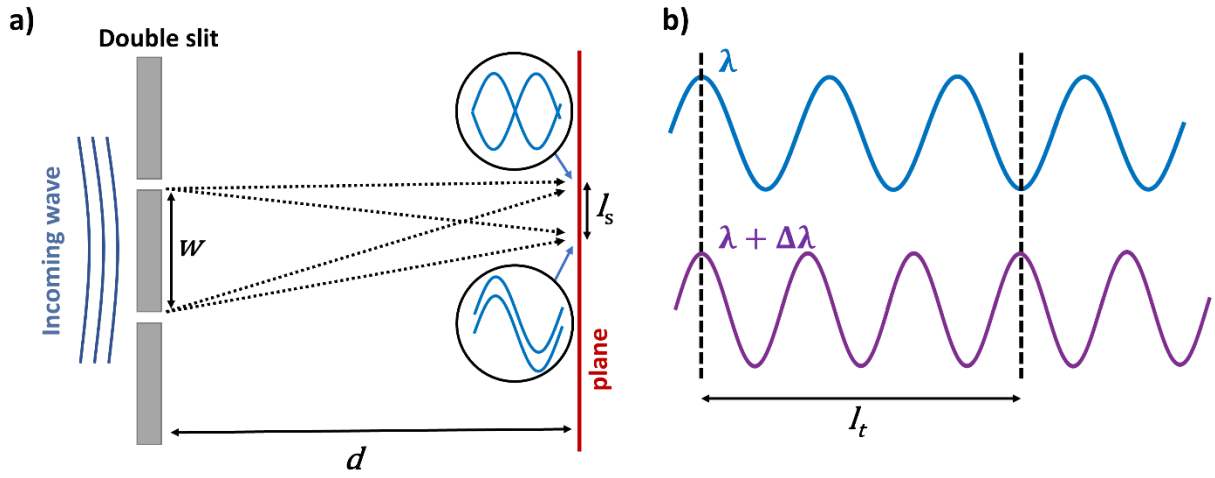

Figure 2.6: a) A double slit is hit by an income wave and from each slit a spherical wave is emitted, separated by distance w. Both waves propagate towards a detector plane at distance d and approach the plane from slightly different directions. The spatial coherence length l_s may be defined as the length difference between the two nearest points of constructive and destructive interference. b) The coherence property in direction of the wave propagation is described by the temporal coherence length l_t. It derives from the different wavelengths of two waves, with wavelength λ and slightly off wavelength $\lambda + \Delta\lambda$.

Spatial or transverse coherence length l_s describes the coherence property of a beam transversely to its propagation direction, given by the spatial size of the source and the experimental geometry.[81] It may be derived from the idea of Young's double slit experiment, see Figure 2.6 a). Simultaneously emitted waves from two slits are detected at a plane, parallel to the two slits and at distance d. Both waves arrive from slightly different directions at a specific point on the plane. Assuming the maximums of the two waves are well aligned in this point and interfere constructively, the spatial coherence length is defined as the distance to a nearest position along the plane, in which the maximum of one wave is overlapped by the minimum of the other and hence destructive interference occurs.[67] The spatial coherence length l_s is defined by the size of the source w and the source to sample distance d.[67,81]

$$l_s = \frac{\lambda d}{2w} \tag{2.23}$$

A vertical and a horizontal length may be introduced to describe the coherence properties of a non-point like source. At synchrotrons of the third generation with a source to sample distance

of 30 m and at an energy of 9 keV, vertical and horizontal spatial coherence lengths of around 20-120 µm and 3-12 µm are achieved, respectively.[82]

Further, the coherence properties of a beam in its propagation direction, i.e., the monochromaticity of the beam, is described by the temporal or longitudinal coherence length l_t.[67,81]

$$l_t = \frac{1}{2}\frac{\lambda^2}{\Delta\lambda} \tag{2.24}$$

This equation defines a length over which two waves, with wavelengths λ and slightly off wavelength $\lambda + \Delta\lambda$ are almost in phase, see Figure 2.6 b). For a (111) reflex of a Si monochromator at 9 keV and a bandwidth of $\frac{\Delta\lambda}{\lambda} = 1.3 \times 10^{-4}$, the temporal coherence length derives to ~0.5 µm and sets an upper, spatial limit to interference effects accessible at modern synchrotrons.[82] It must be noted that these two equations above are true for a chaotic sources of spontaneous emission, but for unimodal laser sources with stimulated emissions the fixed phase relation of the emitted photons and their monochromaticity causing a complete coherence with virtually infinite coherence lengths.[81]

2.7.1 Coherent X-ray Scattering

Coherence is a fundamental property of the photon wavefield and elementary to coherent X-ray scattering experiments.[67,81,82] The recorded signal, i.e., the measured intensity, from a scattering process is directly related to the coherence properties of the probing beam.[67,81] In case of a coherent beam, the coherence length is bigger than the size of the specimen and the resulting intensity is given by the modulus square of the sum of the scattering amplitudes from all individual scattering events; $I(\vec{q}) = |\sum A(\vec{q})|^2$. The individual amplitudes from the multiple scattered waves interfere statically and a superposition of the waves is detected. Causing the detected intensity to be proportional to the number of scatterers, squared, and a coherent speckle with fringes to be detected.[81] The detection of fringes is an indication for coherent scattering. In the opposite case of an incoherent beam the measured intensity is given by the sum of the modulus squares of the individual scattered waves; $I(\vec{q}) = \sum|A(\vec{q})|^2$. The amplitudes have no fixed phase relation and, thus, no static interference is occurring.[81] In this case, the detected intensity is proportional to the number of scatterers.

2.8 Bragg Coherent X-ray Diffraction Imaging

An advanced X-ray technique is Coherent X-ray Diffraction Imaging (CXDI).[83–86] It enables lensless, high resolution imaging (~10 nm) of relatively large crystalline structures (~1 µm). This development was made possible by synchrotron sources of the third generation and their available coherent flux of around 1-40 %[87]. A variant of this technique is Bragg CXDI (BCXDI), a Bragg reflection is utilized to measure the scattered intensity of a crystalline structure and, further, the strain distribution may be retrieved for the specimen.[88–91] The basic idea is to combine the measured coherent diffraction of a specimen with a reconstruction process performed by computer algorithms to overcome the phase problem of usual X-ray diffraction.[86,92,93] Problematic is the loss of the phase information of the complex scattering amplitude, due to the detector solely measuring the intensity. With a high enough coherent beam and over sampling it is possible to retrieve the complex scattering amplitude from the diffraction pattern.[94] Over sampling a specimen means, to perform a fine enough measurement to resolve the structure of the coherent diffraction pattern (speckle) at least at double the Nyquist frequency, proportional to the inverse of the specimens spatial size.[94,95] Miao et al. explained the effect of the over sampling on the measurement as follows: it causes the recorded no-density region of the complex electron density to become bigger than the electron density region of the specimen and, thus, enough information's are obtained to retrieve the complex scattering amplitude.[96] The retrieved amplitude can be Fourier transformed (FT) into the electron density distribution of the specimen, by inverse Fourier transform (iFT).

If a three-dimensional reconstruction of the specimen is desired, the reciprocal space must be mapped in three dimensions.[66,88] This is done by performing a fine rocking scan of the Bragg reflection, the specimen is stepwise rotated perpendicular to the scattering plane and the respective detector images are recorded. A rocking scan causes the scattering vector to rotate around the ideal Bragg condition, given by the reciprocal lattice vector of the specimen. This enables a measurement of the Bragg reflection around its center and, thus, a mapping of its distribution in reciprocal space, as seen from the multiple red lines in Figure 2.7. Figure 2.7 shows a slice (x/y plane) from simulated reciprocal space around a $\{10\bar{1}0\}$ Bragg reflection from a hexagonal structure with a diameter of 1 µm. The red arrow pointing towards the center indicates the direction of the scattering vector in the Bragg condition and the red lines representing multiple detector cuts obtained by a rocking scan. To achieve a sufficient over sampling the rocking scan must be performed with a fine resolution,[94] i.e., in the range of micro degrees, but depends on the sample size. Furthermore, the detector must be positioned at a reasonable distance to the sample to achieve a high enough resolution, typically between 1 m

and 5 m. For the simulation shown in Figure 2.7, the detector to sample distance was set to 2.5 m and a rocking scan with a resolution of 0.002° and a total of 121 steps was chosen. Every 10th step is shown for easier visibility in Figure 2.7.

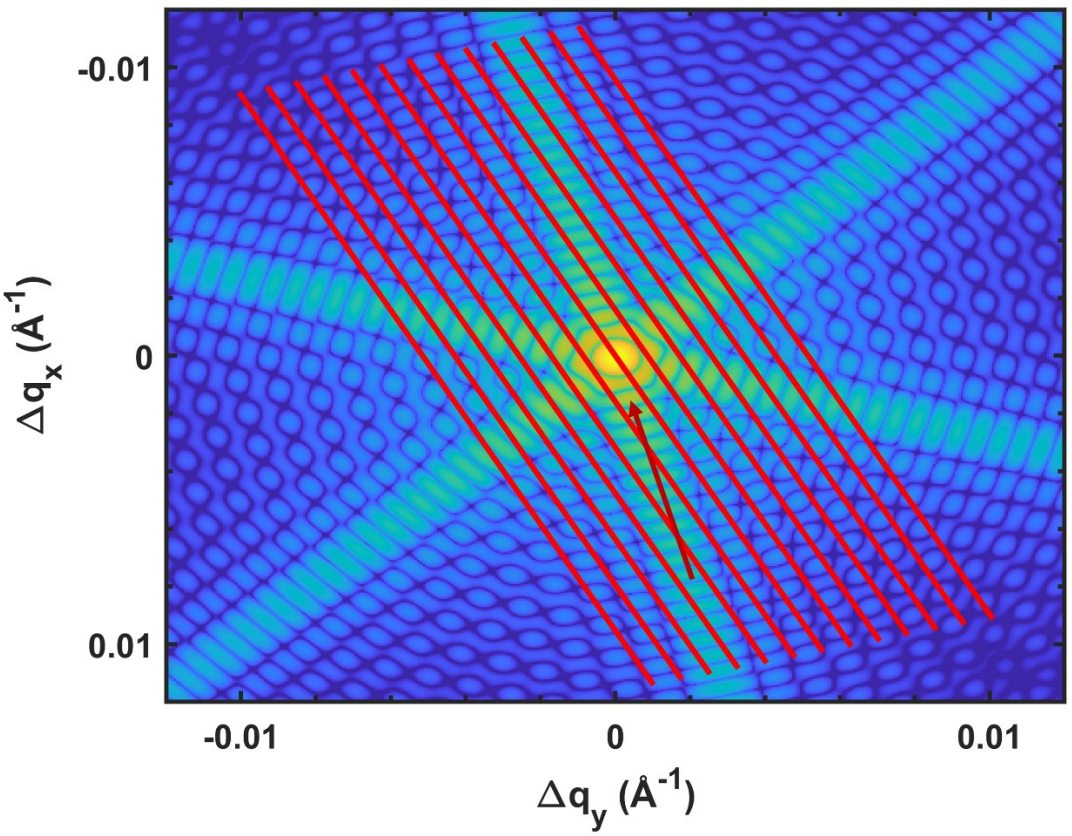

Figure 2.7: Slice (x/y plane) through the simulated reciprocal space around a coherently scattered Bragg reflection of a hexagonal rod. Red arrow indicates the direction of the scattering vector and red lines depicts multiple detector cuts obtained while rocking/rotating the specimen.

Periodically oscillating fringes are visible in Figure 2.7, most prominently along the six main stripes. The oscillation length $\Delta q = 2\pi/D$ is depending on the sample size D in the respective direction.[97] These fringes arise from coherent scattering and a related constructive interference of the scattering amplitude, comparable to a laser illuminated lattice, causing an oscillation of the observed intensity distribution.[82]

The observable intensity $I(\vec{q})$ is related to the complex scattering amplitude $A(\vec{q})$.[67]

$$I(\vec{q}) = |A(\vec{q})|^2 \tag{2.25}$$

If the sample is scattering totally coherently, the intensity is given by the amplitude of the whole sample, but if partly coherent scattering is occurring, e.g., for X-ray beams with smaller coherence length than the sample size, the resulting total intensity is given by a sum of the intensities of each coherently scattering volume faction of the sample, separately.[67]

The complex scattering amplitude consists of its absolute value $|A(\vec{q})|$ and phase $\varphi(\vec{q})$.[82]

$$A(\vec{q}) = |A(\vec{q})|e^{i\varphi(\vec{q})} = FT(\rho(\vec{r})) \tag{2.26}$$

It is further the FT of the complex electron density $\rho(\vec{r})$.

$$\rho(\vec{r}) = \rho_{amp}(\vec{r})e^{i\rho_{ph}(\vec{r})} = iFT\big(A(\vec{q})\big) \tag{2.27}$$

With an amplitude $\rho_{amp}(\vec{r})$ and phase $\rho_{ph}(\vec{r})$ of the electron density. The amplitude is related to the morphology of the specimen and the recovered phase of the complex electron density is related to the displacement field $\vec{u}(\vec{r})$ of the sample, describing the spatial shift of atoms from their ideal lattice positions.[28,82]

$$\rho_{ph}(\vec{r}) = \vec{q} \cdot \vec{u}(\vec{r}) \tag{2.28}$$

The strain $\epsilon_{ij}(\vec{r})$ is given by the derivative of the displacement field with spatial coordinates $x_i \,;\, i \in (1,2,3)$ of $\vec{r}$.[82]

$$\epsilon_{ij}(\vec{r}) = \frac{1}{2}\left(\frac{\partial u_i}{\partial x_j} + \frac{\partial u_j}{\partial x_i}\right) \tag{2.29}$$

In the case of normal strain ($i = j$) this equation simplifies to:

$$\epsilon_{ii} = \frac{\partial u_i}{\partial x_i} \tag{2.30}$$

It should be noted that the strain sensitivity for BCXDI is restricted to the direction of the scattering vector, but the whole strain tensor may be obtained by measuring multiple, independent Bragg reflections.[89]

Figure 2.8 shows the impact of the complex electron densities phase on simulated diffraction patterns for a hexagonal specimen. Figure 2.8 a) highlights the position shift of a Bragg reflection along $\Delta q_{||}$, parallel to the scattering vector, due to a linear phase ρ_{ph}. A non-linear phase of the complex electron density may alter the diffraction pattern in a more complicated way, shown in Figure 2.8 b).

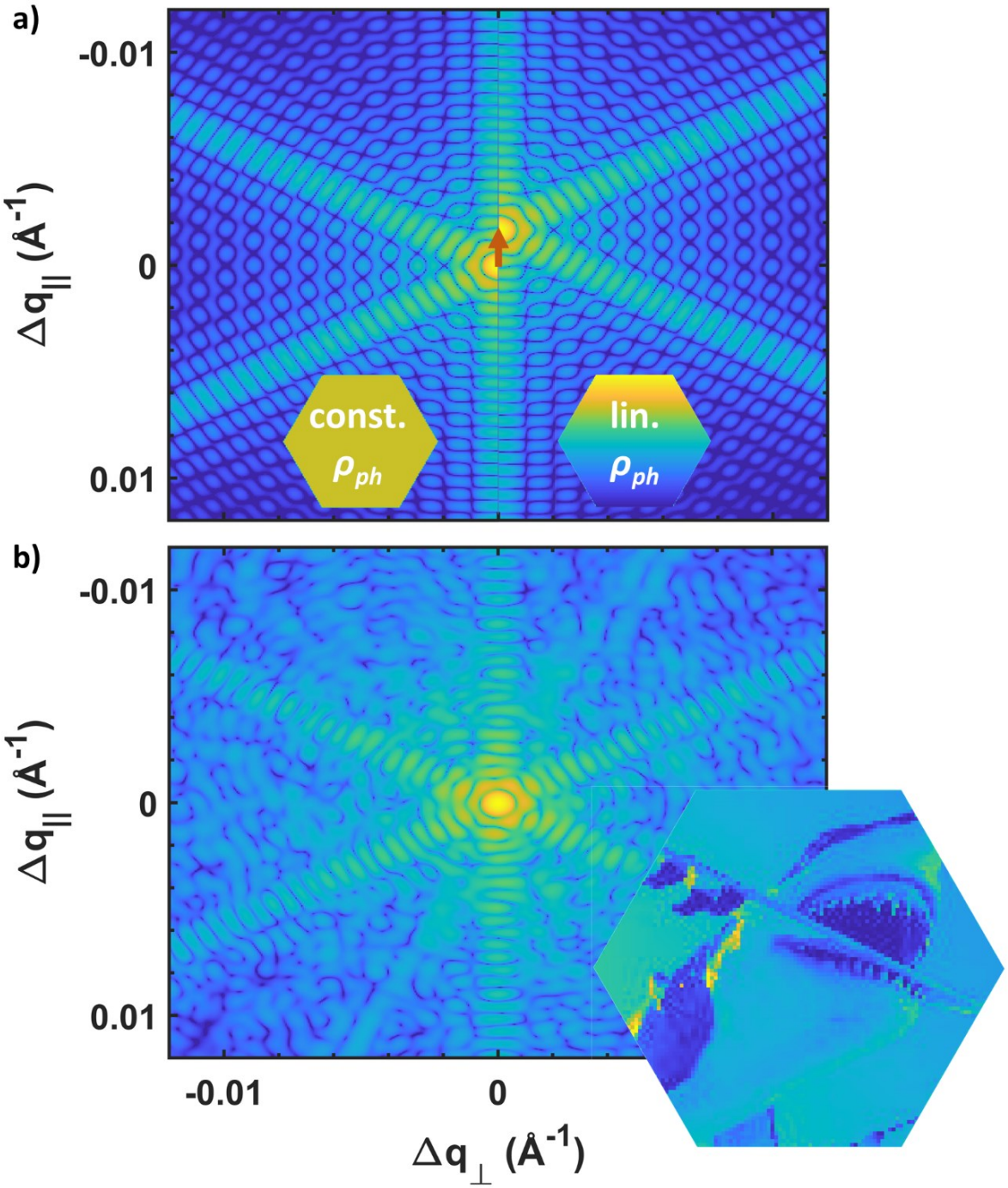

Figure 2.8: a) Simulated 2D cut of the diffraction pattern from a coherently scattering hexagonal specimen with constant (left) and linear (right) phase gradient of the complex electron density, see insets. b) Diffraction pattern simulated for a hexagonal specimen with a non-linear phase of the electron density, see inset. $\Delta q_{||}$ and $\Delta q_{\perp}$ are directions parallel and perpendicular to the scattering vector.

2.8.1 Coherent Data Reconstruction

Reconstruction of the complex scattering amplitude from a measured intensity obtained by CXDI experiments, and thus revealing the electron density of an investigated specimen, became possible by algorithms, implemented over the last decades.[98] Some of whom are the error reduction (ER)[99], hybrid input output (HIO)[82,99], relaxed averaged alternating reflection (RAAR)[100], hybrid projection reflection (HPR)[101] and Difference maps (DM)[102] algorithm. The ER algorithm is an iterative process of conducting Fourier transforms between the real space of the electron density and the reciprocal space of the scattering amplitude and applying constraints to the respective spaces.[82,99] A schematic process flow of the ER algorithm is shown in Figure 2.9. The first iteration of the reconstruction process is initiated with the square root of the measured intensity $|A(\vec{q})| = \sqrt{I(\vec{q})}$ and a random phase φ_0, $A'(\vec{q}) = |A(\vec{q})|e^{i\varphi_0(\vec{q})}$. The next step is Fourier transform it to the electron density $\rho'(\vec{r}) = iFT(A'(\vec{q}))$. Then, the electron density $\rho(\vec{r})$ is generated by applying a real space constraint on $\rho'(\vec{r})$. This is done by the support $S(\vec{r})$, which is basically existing knowledge on the shape of the investigated specimen, together with a function describing the expected electron density behavior inside and outside of the specimen. For the i-th iteration the function is as follows:[82,99]

$$\rho_i(\vec{r}) = \begin{cases} \rho'_i(\vec{r}), & \vec{r} \in S(\vec{r}) \\ 0, & \vec{r} \notin S(\vec{r}) \end{cases} \tag{2.31}$$

For the ER algorithm, the electron density inside the support volume is kept while it is strictly forced to zero, outside of it. The support may be known from prior investigations of the specimen shape, e.g., optical or SEM images.[83,103] Next, the complex scattering amplitude is gained by Fourier transform the electron density, $A(\vec{q}) = FT(\rho(\vec{r}))$. Consecutively, the reciprocal constraint is applied by replacing the absolute value of the amplitude with the square root of the measured intensity from the experiment and amplitude $A'(\vec{q})$ is gained. Thus, one cycle of the reconstruction algorithm is completed. This back and forth propagation, between real and reciprocal space, is conducted until a convergence of the reconstruction is reached, which is typically the case after a few hundreds to thousands of iterations.[98]

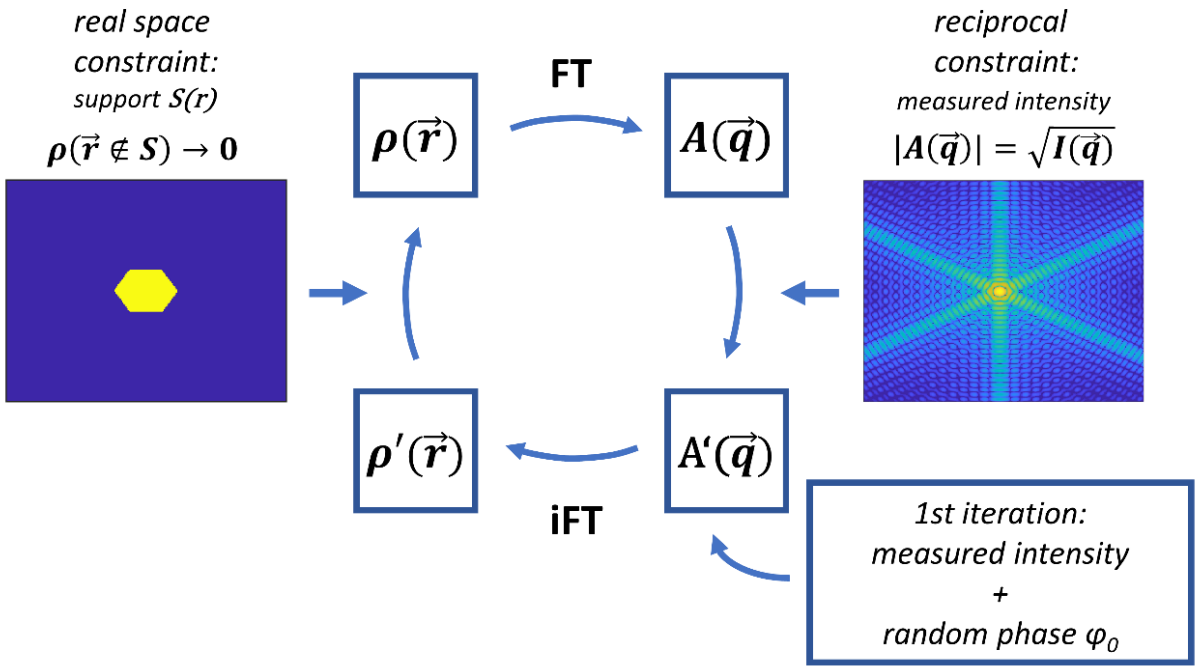

Figure 2.9: Error reduction (ER) algorithm[99] scheme for reconstruction of the complex scattering amplitude $A(\vec{q})$, electron density $\rho(\vec{r})$ and support $S(\vec{r})$ form the measured intensity $I(\vec{q})$. Examples for the real space and reciprocal constraints are given.

The ER algorithm is excellent in finding a minimum but suffers from stagnation at local minima.[82] HIO, a generalized approach of ER, is a possible solution to this problem. Instead of forcing the electron density strictly to zero outside of the support, as done by ER, for HIO the new electron density is attenuated by a factor β, typically in the range of 0.6 to 0.9.[82,99]

$$\rho_i(\vec{r}) = \begin{cases} \rho'_i(\vec{r}), & \vec{r} \in S(\vec{r}) \\ \rho_{i-1}(\vec{r}) - \beta\rho'_i(\vec{r}), & \vec{r} \notin S(\vec{r}) \end{cases} \qquad (2.32)$$

An alternating combination of both, ER and HIO algorithms, has proven to be an effective path to achieve fast convergence of the reconstruction and avoid stagnation.[82,98] It was shown that the reconstructed phase of the complex electron density is most likely a unique solution,[96] but multiple reconstructions are usually performed, in the order of tens to hundreds,[97,104,105] to gain a confident solution.

Prior, it was assumed that the support is already known from supplementary techniques. But this is not possible for every measurement, neither is it necessary to have prior knowledge of the specimen shape, as it was shown that the support can be found simultaneously to the reconstruction process, by the shrink wrap algorithm.[92] For this method the first estimate of the support function if obtained as the Fourier transform of the measured intensity. Further into the reconstruction process, the support will be updated as the Fourier transform of the

reconstructed scattering amplitude convolved with a Gaussian mask.[92] The width of the Gaussian mask shrinks with increasing iteration numbers, realizing a low to high resolution reconstruction, e.g., an update every 20 iterations.

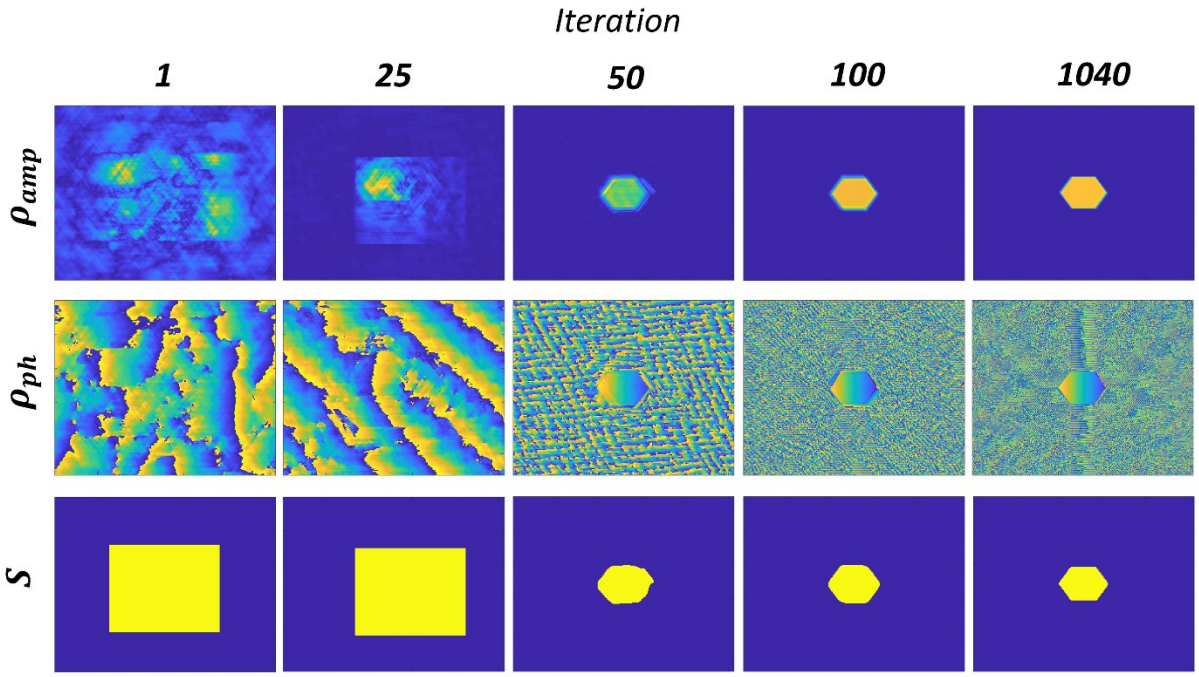

Figure 2.10: Amplitude ρ_{amp} and phase ρ_{ph} of the reconstructed density, as well as the support S, at five iteration steps during the reconstruction process, including the first and last one. These were obtained from a simulated dataset of a hexagonal specimen with a linear phase gradient.

Figure 2.10 shows the reconstructed results from a simulated dataset of a hexagonal specimen with a linear phase gradient. Shown are the amplitude ρ_{amp}, phase ρ_{ph} of the electron density and the support function S for five different iteration steps (1, 25, 50, 100, 1040) during the reconstruction process. A qualitatively reasonable result is reached within 100 iterations, but especially the outermost areas are taking many more iterations, as seen best in the further development of the support. The support was kept fix for the first 40 iterations, thereafter the shrink wrap algorithm updated the shape.

Furthermore, it may be beneficial or necessary for a reconstruction process to take partial coherence of the scattered amplitude into account.[106] To perform a partial coherence correction, the reciprocal constraint (Figure 2.9) is not determined from the measured intensity alone, as it would be sufficient for a fully coherent beam, instead the measured intensity is seen as a convolution of the coherent intensity and a mutual coherence function, describing the coherence properties of the wavefield.[106]

3. MATERIALS

3.1 ZINC OXIDE

Zinc oxide (ZnO)[35] is a heavily investigated semiconductor,[107–110] and a promising candidate, among others, e.g., AlN, GaN, to complement or replace the typically silicon-based semiconductor technology used in recent applications.[34,35,111] Furthermore, ZnO has the potential to enable technologies in the future, such as piezotronic transistors or antimicrobial tissue adhesives with nano particles.[112,113]

ZnO crystallizes either in Rocksalt (high pressure), Zincblende (grown on cubic substrates) or, most commonly, in hexagonal wurtzite structure of space group $P6_3mc$.[34,35] In the following the wurtzite structure form of ZnO is described in detail, as this is the observed structure throughout this work. In Figure 3.1 the hexagonal crystal structure is illustrated with a view on the a) {10-10} and b) {0001} plane, with one side being Zinc terminated and the other being Oxygen terminated.[35] The wurtzite lattice parameters are $a = b = 3.25$ Å and $c = 5.207$ Å.[35] Furthermore, ZnO is showing a size dependent Young's modulus in bulk materials, micro- and nano wires of 111.2 GPa[114], 73.5 GPa[115] and 29 GPa[116].

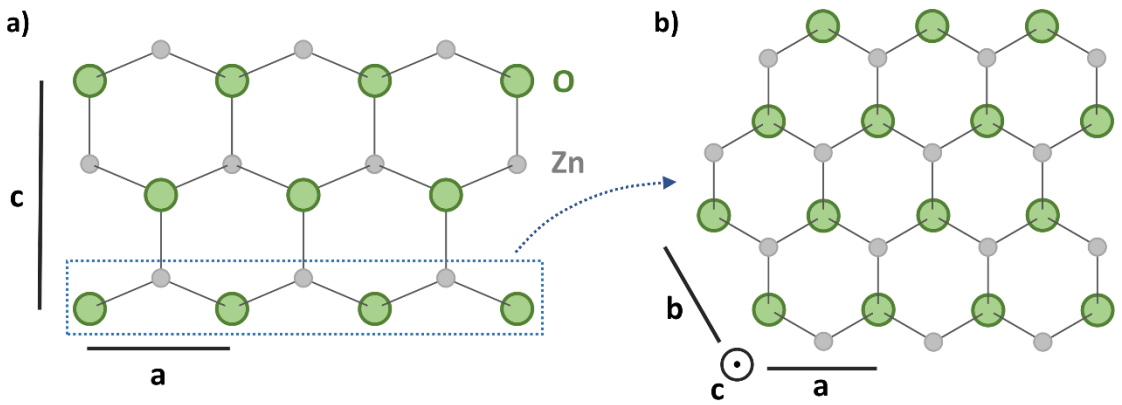

Figure 3.1: a) View on the {10-10} and b) {0001} plane of the ZnO wurtzite structure. Crystal axes a, b and c are included. In a), the upper side is Zinc terminated and the lower side Oxygen terminated.

ZnO is a II-VI semiconductor compound with a direct band gap of ~3.3 eV,[34] exhibiting increased piezoelectric properties,[35] compared to other semiconductor, e.g., GaN and AlN,[117] with piezoelectric strain coefficients e and piezoelectric stress coefficients d (Wurtzite ZnO: $e_{31} = -0.57$ C/m^2, $e_{33} = 1.32$ C/m^2, $d_{31} = -5.43$ pm/V, $d_{33} = 11.7$ pm/V)[35]. In previous studies it was shown that the electrical properties of ZnO are influenced by defects (e.g., oxygen

vacancies)[48,118] and that these defects can be manipulated by ion beam milling or the chosen design and size,[119] leading to altered electrical properties.

The micro- and nanorods utilized in this work were provided by the group of Prof. Adelung (Technical faculty, Kiel University) and their novel flame transport synthesis (FTS) approach to produce tailor made ZnO structures.[120] Diameter ranging from below 1 µm to few hundred µm with typical lengths of tens to hundreds of µm are achievable. A typical batch of ZnO structures grown from FTS technique is shown in Figure 3.2 a) and an optical microscope image of a single, hexagonal ZnO rod with a diameter of ~148.5 µm produced by FTS is shown in Figure 3.2 b). Rods used in the experiments presented in this thesis were similar to the one shown in Figure 3.2. These had to be carefully handpicked from the provided batches of ZnO structures, to enable an optimal accordance of the rods specifications with the experimental objectives.

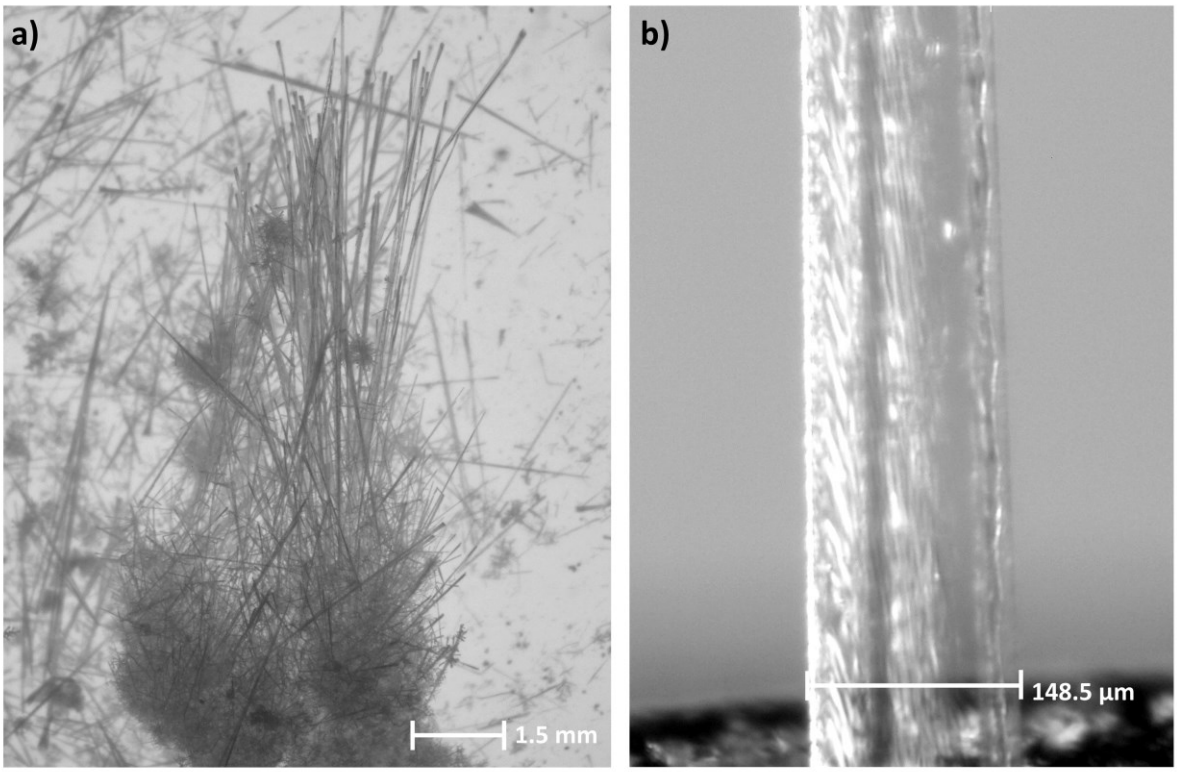

Figure 3.2: a) Optical image of a batch of ZnO structures grown by the flame transport synthesis[120]. b) Optical image of a single, hexagonal grown ZnO rod.

3.2 Gallium Nitride

Gallium nitride (GaN) is a III-V semiconductor compound with a ~3.4 eV wide direct bandgap at room temperature.[121] At room temperature and ambient pressure, it crystallizes in the hexagonal wurtzite structure of space group $P6_3mc$ with lattice parameters $a = b = 3.19$ Å and

c = 5.19 Å,[122,123] but forms a rocksalt structure with lattice parameter a = 4.01 Å for pressure above 37 GPa.[123] Further, it shows piezoelectric properties with a piezoelectric stress coefficients d_{33} = 3.1 pm/V.[117] GaN is under investigation for a wide range of applications, e.g., gas sensing[124], spintronics[125] and piezotronic applications[126].

3.3 FeCoSiB

$(Fe_{90}Co_{10})_{78}Si_{12}B_{10}$, is an amorphous, magnetostrictive metallic alloy[127,128]. These alloys show great potential for sensing applications due to a combination of relatively large magnetostriction ($\lambda_S \approx 10^{-5}$) and soft magnetic behavior.[60,129] FeCoSiB was already used as magnetostrictive coating in different experiments.[62,129,130]

3.4 FeCo/TiN Multilayer Structures

Iron cobalt (FeCo) in its α' phase, at room temperature and around a 50-50 composition, crystallizes in the cubic CsCl crystal structure in space group *Pm3m* with lattice parameter a = 2.85 Å.[131,132] Due to its high intrinsic magnetization and magnetostrictive coefficient $\lambda_S \approx 8 \times 10^{-5}$,[133] FeCo is used in magnetic alloys and composites.[134]

Titan nitride (TiN) is well known for its extreme hardness (8-9 on the Mohs scale)[135] and, thus, is utilized in many applications, including coatings in the mechanical industry, as buffer layer and as diffusion barrier for stabilization of multilayer stacks, i.e., undergoing thermal annealing.[134,135] TiN was observed to crystallize in the cubic NaCl structure (space group *Fm3m*) with lattice parameter a = 4.24 Å.[135]

Multilayers are frequently used to combine properties of different materials in one structure and thus enhance or even enable its application.[134,136] Such a multilayer consists of at least two materials deposited in an alternating process on top of a substrate, see Figure 3.3 a).

It was shown that as-deposited FeCo exhibits hard magnetic properties and a annealing process is necessary to achieve soft magnetic properties,[133] which are beneficial for sensing applications. Furthermore, FeCo loses its soft magnetic properties for high film thickness.[137] Thus, combining both FeCo and TiN in a thin FeCo/TiN multilayer structure is beneficial for the soft magnetic properties, because the FeCo layers are kept thin and the TiN stabilized the structure. Two views of a multilayer with alternating FeCo (0.6 nm) and TiN (1.7 nm) layers obtained by TEM, are shown in Figure 3.3 b). The changing contrast from left to right in the TiN layers may be explained by diffraction contrast, due to crystal orientation.

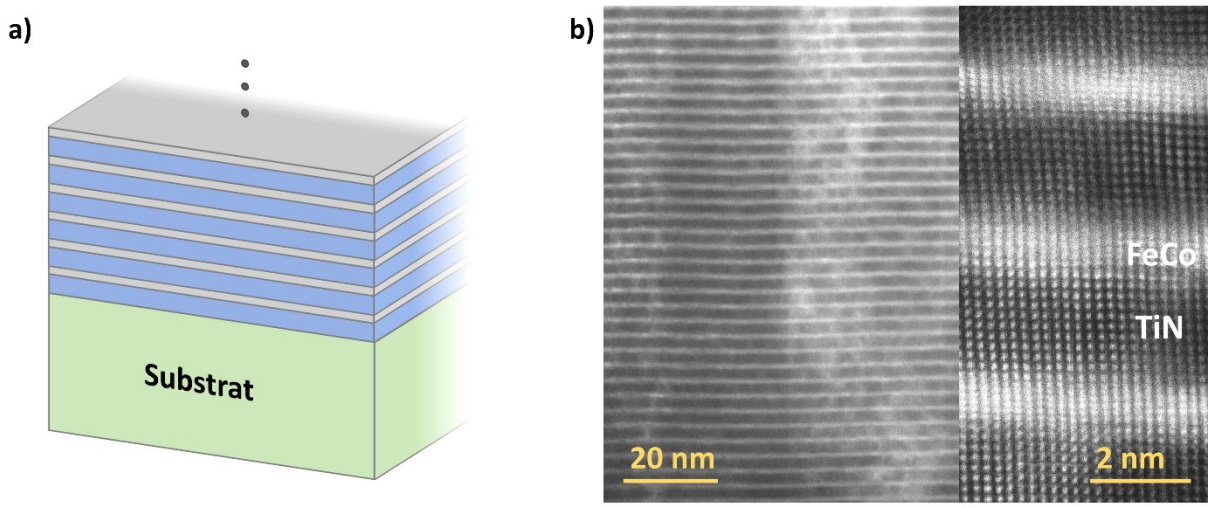

Figure 3.3: a) Sketch of a generic multilayer stack consisting of two different materials (grey and blue, e.g., FeCo and TiN) deposited on top of a substrate. b) TEM image of a FeCo/TiN multilayer at two magnifications.[138]

4. EXPERIMENTAL

4.1 ZNO ROD SAMPLE PREPARATION

Batches of ZnO rods produced by the flame transport synthesis, see section 3.1, had to be screened by optical microscopy for the right quality and size. A new optical microscope (Zeiss Primostar) with a higher magnification, i.e., up to 100 and a theoretical resolution of 800 nm, was acquired, enabling a better characterization of the rods. Rods with the desired characteristics were picked by hand using a glass pipette and placed on to a sample holder, see Figure 4.1, then fixed by a small amount of epoxy, just enough to hold them in place, but as little as possible to not cover the rod all around. Over the years multiple improvements to the sample holder, mounting procedure and coating process have been established. Figure 4.1 a) shows the first version of a 3D printed push-to-pull sample holder provided by Dr. Jorit Gröttrup (AG Adelung, Technical Faculty, Kiel University). First step, the whole sample holder was coated with gold (Au) to achieve a conducting surface, besides small parts covered in Kapton foil to prevent an electrical shortcut between the two contacts, important for electrical examinations. Next, the desired ZnO rod is placed on the sample holder, red circle indicates rough position, and one end of the rod is fixed to the sample holder by silver glue, lower end in this image. Next step was the implementation of an ohmic contact on the other half of the rod by deposition of aluminum (Al) and shading the rest with a piece of Al foil. This end was then fixed by silver glue, as well. Finally, two electrical conducting wires were attached by silver glue, ass seen in Figure 4.1 a). These enabled an electrical examination of the rod and its electrical properties by a sourcemeter.

Two problems arise from this design:

(1) Silver glue tends to deform while drying, causing high mechanical stress
(2) Shading for the Al was very unprecise causing many not usable samples

Figure 4.1 b) shows an optimized version of sample holder design, to specifically tackle these problems. An (almost) volume invariant epoxy (UHU Plus Endfest 300) was chosen to simultaneously fix the two rod tips, causing much less mechanical stress. A sputter holder, see Figure 4.1 c), was built to implement a precise deposition of Au (Schottky contact) and Al (ohmic contact) on the ZnO rod. Comparing the difference in distance between the deposited Au and Al at the left and right side in Figure 4.1 d) gives a precision of ~100 µm for the sputter mask. The main body of the sputter holder is Polytetrafluoroethylene (PTFE, brand name Teflon) of octagonal shape to enable the deposition from multiple directions. The

sputtering mask is a construction of two metal plates, above and below the sample holder, with a 1 × 20 mm² wide slit on both sides. Furthermore, the loose wires from the first version of the sample holder were replaced by a connector to enable an easier and safer connection to the sourcemeter.

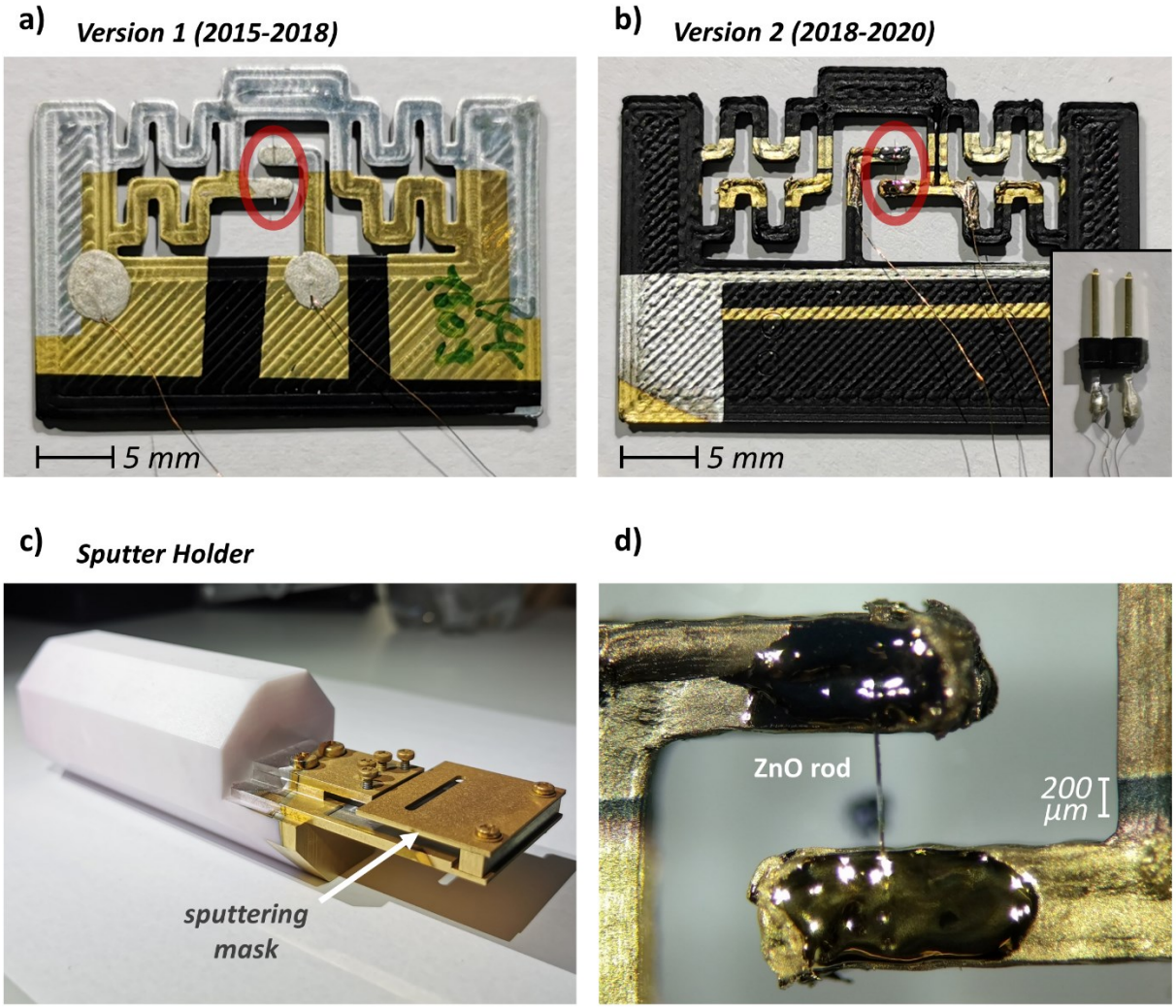

Figure 4.1: a) Example of 3D printed push-to-pull sample holder for a single ZnO rod (red circle) with loose wire connections to the sourcemeter, used in the years 2015-2018. b) Improved sample holder design from the years 2018-2020, with a connector for easier connection to the sourcemeter, see inset, and a more precise deposition of Au and Al realized by a sputter holder. c) Sputter holder designed in 2018, with an included mask (slits at the top and bottom) to enable precise sputtering from one of eight directions, see octagonally shaped main body (PTFE). d) Al (top) and Au (bottom) deposited on a sample holder in the sputter holder.

Another type of sample holder was specifically designed to enable the investigation of ZnO rods with only one end of the rod fixed, thus enabling a further reduction of stress due to the mounting process. The single-end fixed rod (SEFiR) sample holder. Its development started with a fairly simple first approach by mounting a ZnO rod to the tip of a thinned glass pipette and coating it, as seen in Figure 4.2 a). This enabled an investigation of the rod by X-ray

scattering, but no electrical examination of the rod was possible. The next design step was the implementation of connections for electrical measurements of the rod and its metal contacts. The advanced SEFiR sample holder is shown in Figure 4.2 b). It enables a parallel investigation of the structural and electrical properties by X-ray and sourcemeter, respectively. This specific sample holder was coated with FeCoSiB from the top, purchased from Evochem Advanced Materials GmbH.

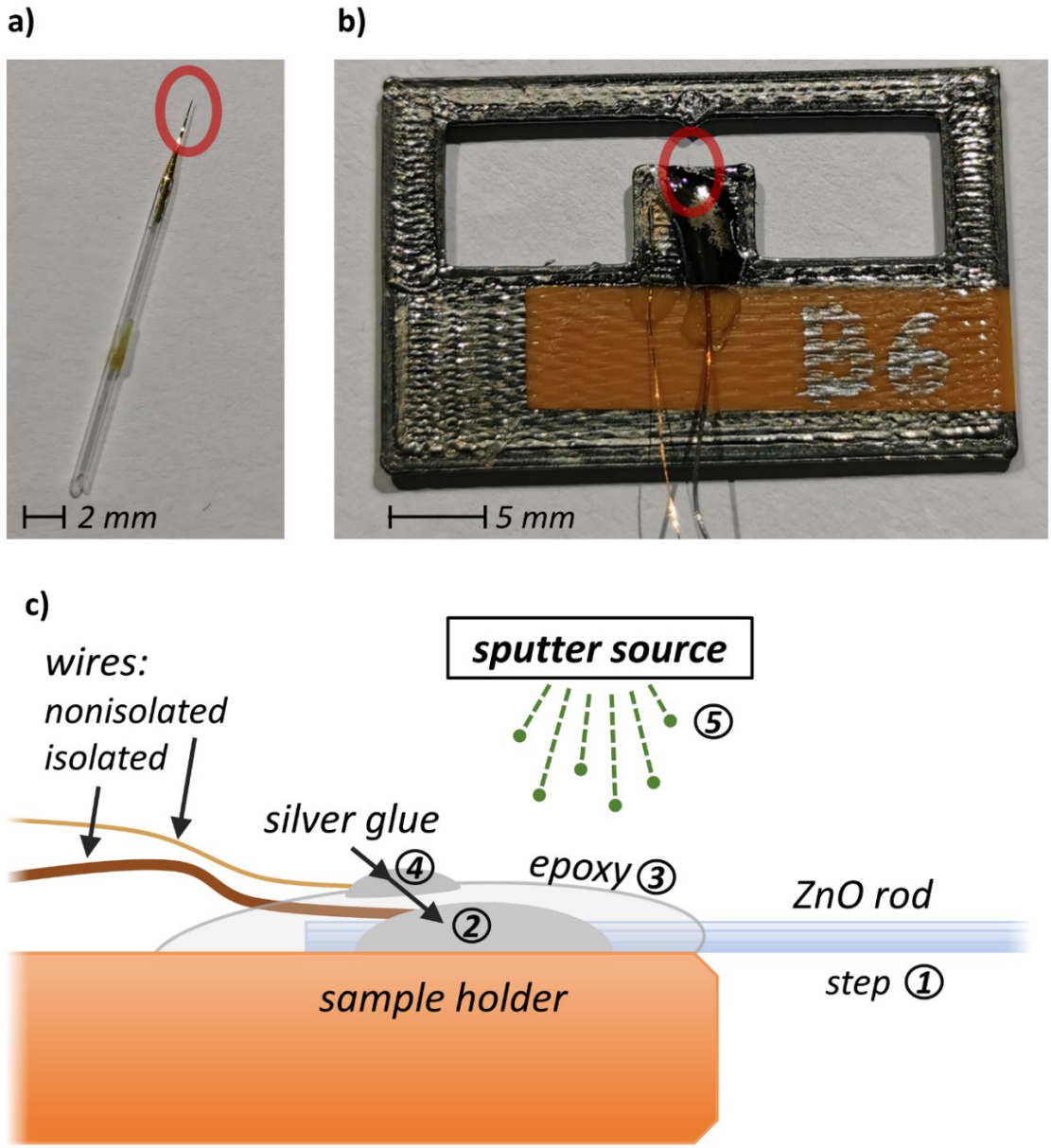

Figure 4.2: a) Single ZnO rod (red circle) with one end fixed to a glass pipette and coated with Au. b) Advanced design of the single-end fixed rod (SEFiR) sample holder with the ability for electrical examinations, here, ZnO rod coated with FeCoSiB. c) Building scheme for the SEFiR design in five steps, starting by fixing the rod on the sample holder.

Figure 4.2 c) depicts a sketch of the construction steps for the advanced SEFiR design.

(1) Fixing the tip of a ZnO rod on top of a 3D printed sample holder with a small amount of adhesive (UHU Sekundenkleber flüssig), parts of the rod tip must be kept free from adhesive to enable conduction later.
(2) An electrically isolated Cu wire is connected to the rod tip by silver glue. Inside the silver glue the isolation must be removed. If an ohmic contact is desired at this rod tip, it must be coated before the silver glue is applied, e.g., with Al.
(3) The silver glue, the (possible) Al coating and a part of the ZnO rod are encapsulated in epoxy (UHU Plus Endfest 300).
(4) An Cu wire is fixed to the sample holder by silver glue.
(5) The whole sample holder is coated with the desired material, e.g., Au, FeCoSiB or Al.

Afterwards, both wires are fixed by adhesive (UHU Sekundenkleber gel) and silver glue to a connector (inset, Figure 4.1 b) to enable electrical investigations. The isolated wire from point (2) and the epoxy encapsulation in (3) prevent an electric shortcut and enable an investigation of the rod's electrical properties.

4.1.1 Deposition techniques

Two different deposition techniques were used in the assembling process of the sample holders; thermal evaporation[139] for the deposition of Au and Al films, and magnetron sputtering[140] for FeCoSiB deposition. Thermal evaporation is a common physical vapor deposition (PVD) process utilized to deposit thin films on substrates.[141,142] Here, the desired material was placed in a tungsten evaporation boat, heated by electrical resistance of the boat above the materials evaporation temperature and deposited on to a substrate placed above the boat. A quartz micro balance was used to monitor the deposition rate and keep it at around 0.5 Å/s. The whole process was performed under vacuum of ~ 10^{-4} mbar, limiting interactions of the evaporated material with contaminants, e.g., air molecules, enabling a ballistic trajectory towards the substrate In the deposition process, performed for this thesis, two sputter masks, see Figure 4.1 c), were used in parallel to deposit two specimen in one run. A Univex 300 vacuum chamber from Leybold vacuum was utilized. But thermal evaporation has its restrictions, e.g., it can't be utilized to deposit alloys, e.g. FeCoSiB, because the different evaporation temperatures of the included materials would cause an altered composition of the resulting film.[143] To deposit such alloys magnetron sputtering[140] may be used. A target of the desired deposition material is mounted on a magnetron sputtering head inside a vacuum chamber and an electric field is applied between the target and the substrate, together with an additional magnetic field. A

plasma, e.g., argon, ignites above the target. The electric field causes an acceleration of the argon ions towards the target and a removal of target material due to impacts. The additional magnetic field increases the ionization rate due to electron trapping and, thus, increases the sputter rate of the process. In this thesis, a radio frequency (RF) magnetron[140] (Mantis Deposition Ltd.) was used. The specimen was placed at a distance of ~15 cm from the target and sputtering power was set to 60 W, limiting the thermal damage of the process and prohibiting thermal deformation of the sample holder. The vacuum chamber was initially pumped to a pressure of $\sim 10^{-8}$ mbar by a combination of rotary vane and turbomolecular pumps, followed by an introduction of argon gas up to $\sim 10^{-2}$ mbar, until the plasma ignites. After ignition, the pressure was reduced to $\sim 6 \cdot 10^{-3}$ mbar. This resulted in a sputtering rate of ~ 0.25 Å/s for FeCoSiB.

4.1.2 Sample Environment

The sample environments, shown in Figure 4.3, are components dedicated to combine the above introduced sample holders, with a connection to a sourcemeter and a piezo actuator to apply a mechanical stress to the sample holder and, thus, to the ZnO rod. Further, the sample environments have an open space below the sample holder to allow X-rays passing through and a goniometer adapter, enabling diffraction experiments on the ZnO structures. Over the years, the sample environment design was improved several times as shown in Figure 4.3. Figure 4.3 a) shows version 1 from year 2015. It is a 3D printed device, housing a piezo actuator, the sample holder, two cables as connection to the sourcemeter and a goniometer adapter. Version 2 from 2017, shown in Figure 4.3 b), is milled from aluminum, providing an easier connection to the sourcemeter via a connector, improving the sample holder clamping by three booms and the piezo actuator is movable on a sliding system, enabling a more precise alignment and less broken rods. Further, Kapton shielding was attached to the back and front of the environment, preventing sample movement due to air flow through the window. Version 3 from 2019 is shown in Figure 4.3 c). There, the piezo actuator is replaced by neodymium (NdFeB) magnets, enabling usage of the magnetostrictive materials. An adjustable magnetic field strength is realized by changing the sample to magnet distance with the sliding system.

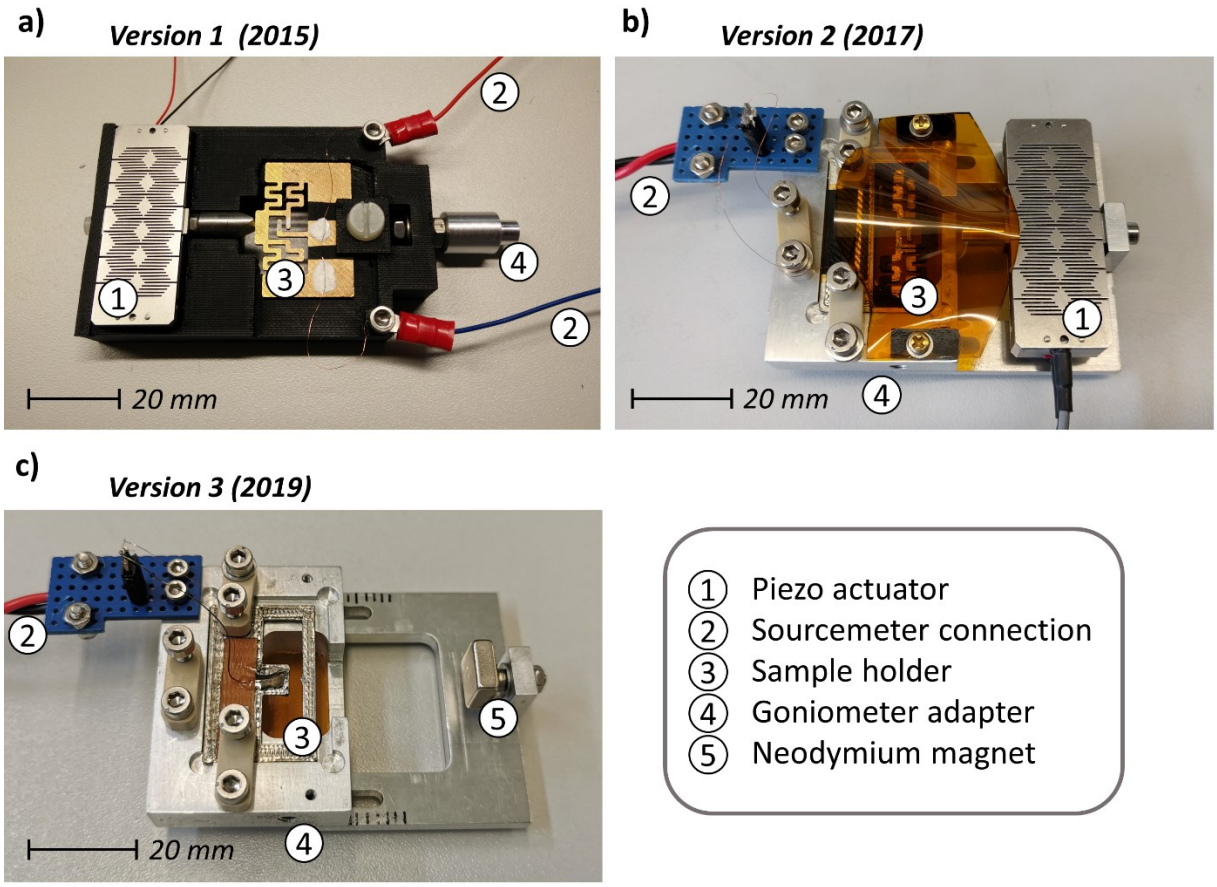

Figure 4.3: Three versions of sample environments. a) 3D printed sample environment constructed in the year 2015. b) Next design iteration built from aluminum, enabling an enhanced sample alignment. Both include a piezo actuator, for application of mechanical stress, a sample holder, compare with Figure 4.1, a cable connection to a sourcemeter and the possibility for X-ray diffraction experiments, see goniometer adapter. c) Third design with the piezo actuator being replaced by a neodymium magnet.

4.2 Current/Voltage Measurement

Current/Voltage (*I-V*) characterization, often referred to as *I-V* curve, is a common and widespread technique to investigate and characterize properties of all sorts of electrical devices and components, e.g., solar cells[144], LEDs[145] and transistors[146]. The measurement principle is quite easy to adapt, a voltage is applied to a device and stepwise changed, while the respective current is recorded. Thus, the current behavior over a given voltage range is examined.

Here, *I-V* curves are introduced to characterize properties of Metal-Semiconductor contacts, see section 2.2. A common and important value to characterize of a Schottky contact is the barrier height $e\varphi_b$. This value may be extracted from a semilogarithmic plot of the current density ($ln\ J$ vs V), fitting its forward direction with a linear function and determining the intersection $ln\ J_o$ of this fit with the $ln\ J$ axis.[39,147]

$$\varphi_b = \frac{kT}{e} ln\left(\frac{A^* T^2}{J_o}\right) \tag{4.1}$$

With Boltzmann constant k, temperature T, effective Richardson constant A^* and elementary charge e. For higher voltages, *I-V* curves usually deviate from the ideal behavior[147] for a solely thermionic emission driven current given by equation 2.5, this may happen due to recombination with holes in the depletion region, high injection of minority carrier, Schottky barrier inhomogeneities and further effects,[39,40] thus the value is typically extracted for a small voltage range and at low voltages (~ 0.1 V - 0.5 V).

A further useful parameter to describe a Schottky contact, extracted from an *I-V* curve, is the ideally factor n.[39,147]

$$n = \frac{e}{kT} \frac{dV}{d(ln\ J)} \tag{4.2}$$

$\frac{dV}{d(ln\ J)}$ is the inverse slope of the semilogarithmic current density plot and it is extracted from the same fit as the barrier height. The ideality factor describes the deviation between a measured and the theoretical current of a Schottky contact obtained from equation 2.5. To quantify how 'ideal' the measured contact behaves. A factor $n = 1$ is the ideal case, while a higher value is a sign for effects, modifying the Schottky barrier, e.g., recombination processes, tunneling or Schottky barrier inhomogeneities.[39,40,45]

4.3 X-RAY INSTRUMENTATION

Three X-ray sources have been utilized throughout this thesis and a comprehensive overview of the specific sources, their specifications and characteristics are given here.

- Laboratory source ***FRED***: Located at Magnussen group laboratory in the institute of experimental and applied physics at Kiel University, is a four-circle diffractometer with a rotating copper anode X-ray source operating at 8.04 keV, a beamsize down to 0.1 mm × 0.1 mm is achievable.[148] Multiple setups are available ranging from a high flux (~2×10^8 ct/s) to a high resolution (~2×10^{-4} Å^{-1}) mode.[148] It is used for X-ray diffraction and reflectometry experiments.
- Beamline ***P03*** (MiNaXS): Undulator beamline at the Deutsches Elektronen Synchrotron (DESY) in Hamburg with two, separate end stations, optimized for micro and nano focused beams.[149,150] The accessible photon energy ranges from 9 keV to 23 keV and a Kirkpatrick-Baez (KB) mirror[151] is used to focus the beam down to 250 nm × 350 nm. For the sample translation a hexapod with an attached piezo stage is available at the nano focus end station. The beamline is used for small and wide-angle X-ray scattering experiments.[152–154] Enabling Bragg diffraction experiments.
- Beamline ***ID-34-c***: Located at the Argonne National Laboratory (ANL), this undulator beamline with a six-circle diffractometer is part of the Advanced Photon Source (APS).[155] Accessible photon energy ranges from 5 keV to 15 keV, with a beam focused by a KB mirror down to roughly 0.6 µm × 0.6 µm with a coherent volume of ~ 0.2 µm^3, but it may be slightly widened by utilizing diffraction from a slit system, enabling the investigation of bigger samples (~ 1 µm).[155] It is dedicated to coherent X-ray scattering experiments.[156,157]

4.4 X-RAY REFLECTOMETRY

For reflectometry measurements, introduced in section 2.6, the laboratory X-ray source FRED was used, see section 4.3. The diffractometer and its reflectometry geometry are shown in Figure 4.4. X-rays are generated by a rotating Cu anode and collimated by a multilayer X-ray mirror. After exiting the anode, the X-ray beam is spatially defined by a motorized slit system followed by an absorber wheel to attenuate the beam intensity to the desired level, i.e. mostly given by saturation of the detector. The specimen sits in the center of a four-circle Eulerian cradle and is fixed on a partly motorized sample stage. After reflecting from the sample, the beam is passing through an evacuated flight tube and is measured by a detector. The utilized

detector was a Mythen 1D strip detector from Dectris. For reflectivity measurements the sample is aligned perpendicular to the beam while shading half of it. Further, the reflected signal is detected for angles from below the critical angle ~ 0.33 °, see section 2.6, up to 5 ° with an angular resolution down to 0.005 °.

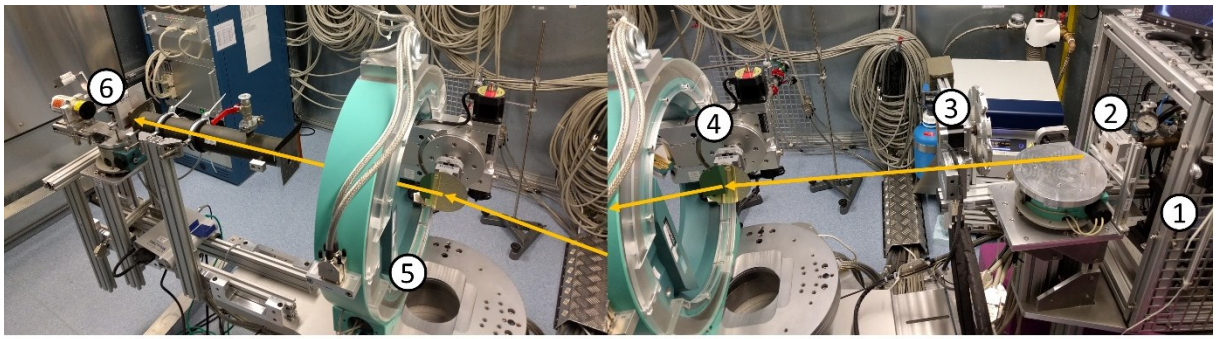

1) X-ray Anode	2) Slit System	3) Absorber Wheel
4) Sample Stage	5) Four Circle Eulerian Cradle	6) Point & 1D Detectors

Figure 4.4: Laboratory source FRED used for X-ray reflectometry investigations. The X-rays are generated by a rotating X-ray anode, passing through a slit system and absorber wheel, the sample is fixed on a motorized sample stage mounted to a four circle Eulerian cradle. The intensity is measured by a detector.

4.5 Scanning Nano X-ray Diffraction

Scanning nanofocus XRD (nXRD) is an X-ray scattering technique, introduced in section 2.5, using a small beam to access spatially resolved information's on the crystalline structure and properties. A small beam diameter, down to 100 nm, is combined with a scanning approach, moving the specimen step wise through a X-ray beam.[26,27,152,158]

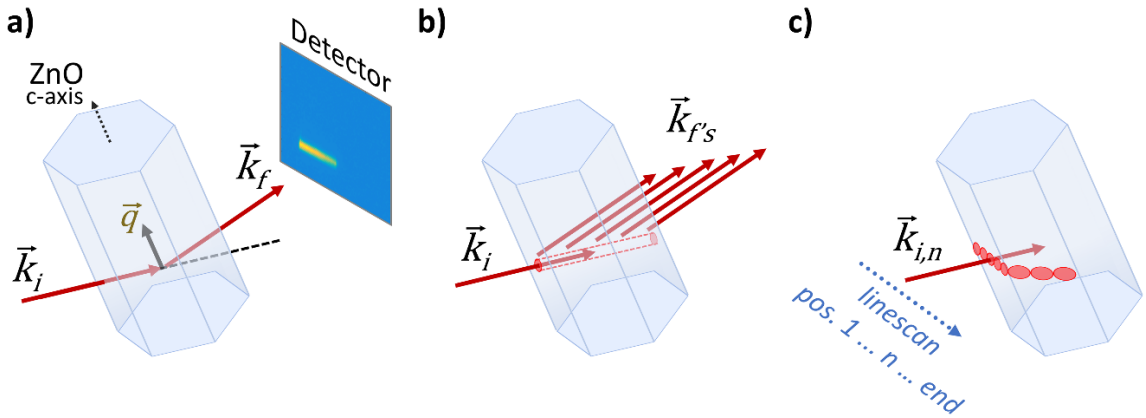

Figure 4.5: a) Scattering geometry for investigation of a {000l} ZnO Bragg reflection, scattering vector $\vec{q}$ is pointing along the c-axis of the rod and is defined by the incoming and final wave vectors $\vec{k}_i$ and $\vec{k}_f$, respectively. b) For nXRD the beamsize is typically much smaller than the specimen size, thus holds informations on a confined crystal volume. The incoming beam is passing through the whole specimen and its scattered signal is a superposition from multiple

coherently scattering regions along this path, indicated by $\vec{k}_{f,s}$. c) A linescan across the rod holds spatial resolved informations.

In Figure 4.5 a) a sketch of the utilized scanning nXRD scattering geometry is shown. An incoming beam is scattered by the crystal structure of a ZnO rod and a Bragg reflection is measurable in the final direction of the beam, with the two respective wave vectors $\vec{k}_i$ and $\vec{k}_f$ being linked to the scattering vector $\vec{q}$. For a measurement of one of the {000l} Bragg reflections, the scattering vector is pointing along the c-axis of the ZnO, here, parallel to the rod axis. Nowadays, the Bragg reflection is typically recorded by a two-dimensional detector and gives access to the lattice parameter of the crystalline structure, size of the coherently scattering crystal volume and the present strain. The incoming beam, with its small diameter, is passing through the whole specimen volume, as seen in Figure 4.5 b). Due to the huge specimen size compared to the coherence length of the beam it is sensible to assume that the scattering does not occur fully coherent and, hence, the scattered intensity recorded by the detector is a superposition of signals from incoherently scattering volumes along the probed volume, indicated by multiple wavevectors $\vec{k}_{f,s}$. Thus, the spatial resolution of this technique is limited to the two dimensions perpendicular to the beam direction. Further, to achieve a spatially resolved measurement the specimen must be moved step wise through the beam, with the scattering signal recorded at each position, as shown in Figure 4.5 c). Typical step size is around the size of the beam diameter and, thus, the spatial resolution is of a similar size. Here, a one-dimensional linescan across a rod is depicted. But two-dimensional scans are possible, as well, by scanning the specimen along the second, perpendicular direction to the beam.

4.6 Coherent X-ray Diffraction Imaging Geometry

Figure 4.6 shows a sketch of the scattering geometry for BCXDI, introduced in section 2.8, investigating a Bragg reflection in the basal plane of a ZnO rod. The incoming beam $\vec{k}_i$ is scattered by the crystal structure in the direction of the final beam $\vec{k}_f$, defining the scattering vector $\vec{q}$ and constructing the scattering plane, which is in the plane of the two scattering vectors. A two-dimensional area detector collects the scattered intensity from the sample and a cut through a simulated reciprocal space around a Bragg reflection of a hexagonal structure is shown as the obtained detector image. Further, a rocking scan of the ZnO rod is performed by rotation around the c-axis of the rod, as depicted in Figure 4.6.

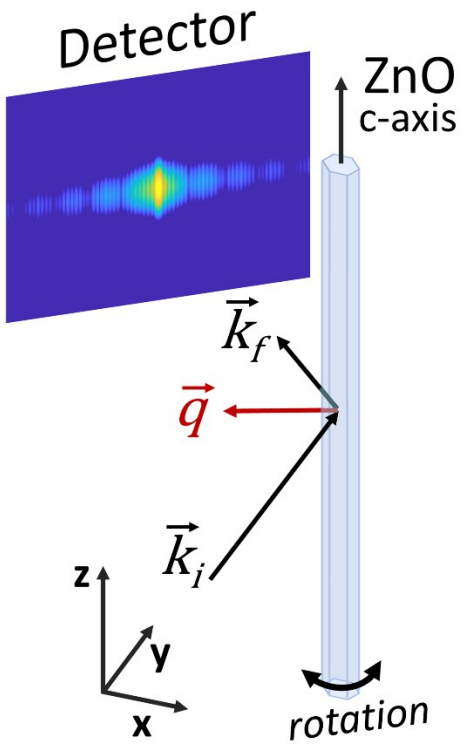

Figure 4.6: X-ray scattering geometry for the investigation of Bragg reflections in the basal plane of a ZnO rod. Scattering vector $\vec{q}$ is defined by the incoming and final wave vector $\vec{k}_i$ and $\vec{k}_f$, respectively. A simulated diffraction pattern is shown as detector image.

The CXDI results presented in this thesis were reconstructed with a combined approach of the ER and HIO ($\beta = 0.9$) algorithms in an alternating usage, and an additional partial coherence correction. The shape was defined by a shrink wrap algorithm with a low to high resolution approach. For every measurement 200 reconstructions with random starts (phase) were performed to achieve a statistically reasonable result. An error metric calculated from the deviation of measured and reconstructed amplitude was used to evaluate and pick the best reconstructions. These were then correlated, to correct for a center symmetric shift of the electron density,[105] and one final reconstruction was calculated.

5. RESULTS

This chapter is consisting of five manuscripts resulting from studies conducted over the course of this doctorate, of which four are published in peer-review journals and one is prepared for submission. The layout of the respective manuscripts is adapted to the thesis and the references are included in the bibliography at the end of the dissertation.

5.1 LOCAL STRAIN DISTRIBUTION IN ZNO MICROSTRUCTURES VISUALIZED WITH SCANNING NANO X-RAY DIFFRACTION AND IMPACT ON ELECTRICAL PROPERTIES

5.1.1 PUBLICATION 1 OVERVIEW

The electrical and structural properties of ZnO microstructures were investigated by means of current/voltage measurements and X-ray investigations, with the goal of correlating the measured electrical characteristics of the microstructures with their crystalline structure and quality. ZnO rods, described in section 3.1, were mounted on dedicated, 3D printed sample holders, see section 4.1. For this, the rods were screened optically to choose those with a good hexagonal appearance, handpick and mount them on sample holders, in total, around 40 to 50 samples were prepared. Roughly the same number of samples broke during the delicate mounting process. For the conduction of, both, electrical and structural investigation on the same rod, two sample environments were constructed, see section 4.1.2, and utilized for two synchrotron beamtimes at the nano focus end station of beamline P03, Petra III located at the DESY in Hamburg. There, the spatially resolved measurements of the ZnO crystal structure were conducted by scanning the ZnO rods through the beam and collecting the Bragg reflections, introduced in section 4.5.
This section is a manuscript published in Advanced Engineering Materials, highlighting the impact of the crystalline structure of three ZnO micro rods on their electric properties, i.e. of the Schottky contact.[159] (https://doi.org/10.1002/adem.202100201)

Local Strain Distribution in ZnO Microstructures Visualized with Scanning Nano X-ray Diffraction and Impact on Electrical Properties

Philipp Jordt, Stjepan B. Hrkac, Jorit Gröttrup, Anton Davydok, Christina Krywka, Niklas Wolff, Lorenz Kienle, Rainer Adelung, Olaf M. Magnussen, Bridget M. Murphy

P. Jordt, Dr. S. B. Hrkac, Prof. Dr. O. M. Magnussen, Dr. B. M. Murphy
Institute of Experimental and Applied Physics, Kiel University, Leibnizstr. 19, 24118 Kiel, Germany
Dr. C. Krywka, Dr. B. M. Murphy
Ruprecht-Haensel Laboratory, Kiel University, 24118 Kiel, Germany
Dr. J. Gröttrup, Dr. N. Wolff, Prof. Dr. L. Kienle, Prof. Dr. R. Adelung
Institute of Material Sciences, Kiel University, Kaiserstr. 2, 24143 Kiel, Germany
Dr. A. Davydok, Dr. C. Krywka
Helmholtz-Zentrum Hereon, Institute of Materials Physics, Geesthacht, 21502, Germany

5.1.2 ABSTRACT

The fast and contact free detection of biomagnetic vital signs could benefit clinical diagnostics in medical care, emergency services and scientific studies, hugely. A highly sensitive magnetoelectric sensor for detection of biomagnetic signals combined with the piezotronic effect is a promising path to increase the signal detection limit. Here, we present results of three ZnO microrods examined by nano X-ray diffraction and current voltage curves to investigate the crystalline structure influence on the Schottky contact properties. The measurements reveal different strain distributions for the three rods and that these are linked with the electrical properties, showing that the crystalline quality has a direct influence on the Schottky contact properties. An analytical model was created to determine the influence of the stress. Although rotation of the strain orientation changes the strain appearance in the measurement, it does not affect the Schottky contact properties.

5.1.3 INTRODUCTION

Semiconductor based magnetoelectric sensors could establish a new generation of sensor devices by combining magnetostrictive with piezoelectric materials.[160,161] These may be used to detect biomagnetic fields from the human physiology if sufficient sensitivity is met.[162–164] The magnetostrictive component reacts to an external magnetic field with a strain that is transferred into the piezoelectric component where it induces a piezoelectric potential.[160] This measurable potential change is directly correlated to the magnetic field strength. While direct detection of the piezoelectric potential only shows limited success for biomagnetic fields, a combination of this potential with a Schottky contact at a semiconductor metal interface[40,165] provides a promising alternative, called the piezotronic effect[13,112]. The Schottky barrier height is modified by the piezoelectric potential and is detectable as an altered current flow over the contact.[53] A wide range of piezotronic applications are under development, including

transistors, energy harvesting and sensors.[19,20,52,166,167] The piezotronic effect was described for a first time by Wang and Song.[14] Single ZnO nanowires were deflected by a conductive atomic force microscope tip. The rod bending lead to a piezoelectric effect induced potential which in turn changed the Schottky barrier height and thus generated a current. An *in situ* TEM study on ZnO nanowires visualized the crystal structure and simultaneously measured the current/voltage (*IV)* curves, showing a striking impact of bending on the conductivity.[16] This was attributed to a bending induced carrier trapping effect and reduction of the conduction channel size.

The Schottky contact and its barrier height are of great importance for the piezotronic effect,[45] for ZnO it was found that Al containing contacts lead to an ohmic behavior, while Au and Ag typically result in a Schottky contact with barrier heights of ~ 0.7 eV and ~ 0.8 eV, respectively.[45] Due to vacancies at the surface the contact formation and barrier height are hugely influenced by Fermi level pinning[168], which pin the ZnO Fermi level close to the oxygen defect level around 0.7 eV below the conduction band.[48] Additionally, the amount of vacancies near the interface strongly impact the Au/ZnO Schottky barrier height, ranging from an ohmic behavior for a high defect rate to a Schottky contact with a barrier height of 0.48 eV at a low defect concentration, with the reverse current being decreased by 2 orders of magnitude. [118]

Cathodoluminescence spectroscopy was used to investigate the density of point defects inside ZnO wires. It was shown that the defect density and, hence, the contact properties can be manipulated by the rod diameter and specific treatments such as ion milling and electron beam heating were used.[119]

Nano X-ray diffraction (nXRD) is an established technique to investigate the strain distribution with a high spatial resolution in microstructures.[169–171] In such a study, a 15 µm nanocrystalline CrN film was investigated utilizing a 100 nm sized X-ray beam. Inside the sample, regions of small crystallites rich in defects were found and attributed to nucleation zones. Improved mechanical properties of thin polycrystalline multilayer films were assigned to structural defects in the multiple nucleation zones.[172] A further study utilizing nano focused diffraction investigated defect rich GaN structures and showed that by tailoring the growth parameter an annihilation of threading dislocation is achieved.[153]

Previous nXRD studies by the authors investigated the strain behavior of micrometer sized ZnO rods coated with magnetostrictive FeCoSiB. A rod, up to 27 µm in diameter, exhibits an intrinsic compressive strain of 5.5×10^{-4} and an additional, magnetic field induced strain of 1×10^{-4} near the ZnO interface.[62] In a further publication, it was shown that the intrinsic strain

in ZnO rods can be tuned by modifying the rod dimension. The interface strain increases from 0.7×10^{-4} to 4×10^{-4} for a decreasing diameter from 50 µm to 5 µm.[152]

In this study, scanning nXRD and electrical examinations by *I-V* measurements are combined to investigate the crystalline structure and, by doing so, link the strain distribution inside ZnO rods with the Schottky barrier's electrical properties. Utilizing the nXRD technique, the strain was measured with a high reciprocal space resolution of 10^{-5} and a spatial resolution of 200-250 nm. Compared to other semiconductors with wurtzite-type structure, e.g. AlN and GaN, ZnO microstructures provide a large piezoelectric coefficient d_{33} (5.1 pm/V, 3.1 pm/V and 12.3 pm/V, respectively)[117,173] and are an ideal choice for the study of structure-property relations at the Schottky contact with X-ray sources. Three ZnO rods (R1 to R3) were investigated in this study, see the experimental section below for details regarding the samples and techniques. The recorded *I-V* curves for the three rods vary from near ideal, rectifying behavior to non-ideal behavior with huge reverse currents. The respective Bragg reflections, measured across the rod by scanning nano X-ray diffraction, vary from a single sharp Bragg peak for R1, to a broader peak distribution for R2 and a number of individual peaks close together for R3, as shown in Figure 5.2 g-i). The multiple peaks are evidence of different crystal domains and their boundaries will be associated with higher defect densities in the crystal. These crystal defects result in non-ideal Schottky barrier properties. Furthermore, an analytical model was created demonstrating that, depending on the measurement orientation, similar strain distributions may lead to different appearing measurements. Due to limited time available at modern synchrotron sources, required for this demanding experiment, a small selection of samples was measured. This study aims to show that the variety in the crystalline structure has considerable impact on the electrical properties and especially the Schottky contact.

5.1.4 Results and Discussion

A sketch of the experimental geometry in Figure 5.1 a) shows an Au coated ZnO microrod probed by an X-Ray beam. The momentum wave vectors k_{in} and k_{out} represent respectively the incoming and scattered X-Ray beam, given by the scattering vector q of the {0001} Bragg reflection. The scattering vector is pointing along the *c*-axis of the ZnO rod and the length is inverse proportional to ZnO's lattice parameter *c*. As it is difficult to identify an unstrained region within all three samples, we chose a reference value for a nominally unstrained sample of $c \approx 5.206$ Å, which is the average value of a selection of references for ZnO at room temperature and ambient pressure.[174–177] The relative (macro)strain defined as $\varepsilon = {}^{q_0}/_{q} - 1$, is determined from the measured Bragg reflections position q and the value q_0 calculated from

the reference lattice parameter c.[178] Macrostrain denotes an overall movement of the diffraction peak due to lattice parameter change.[179] Microstrain describes a local strain and its distribution in a coherent scattering region of the crystal leads to a broadening of the diffraction peak.[179] A positive strain is defined as tensile, describing increased lattice parameters in contrast to a negative, compressive strain referring to a shrinking of the lattice parameter.

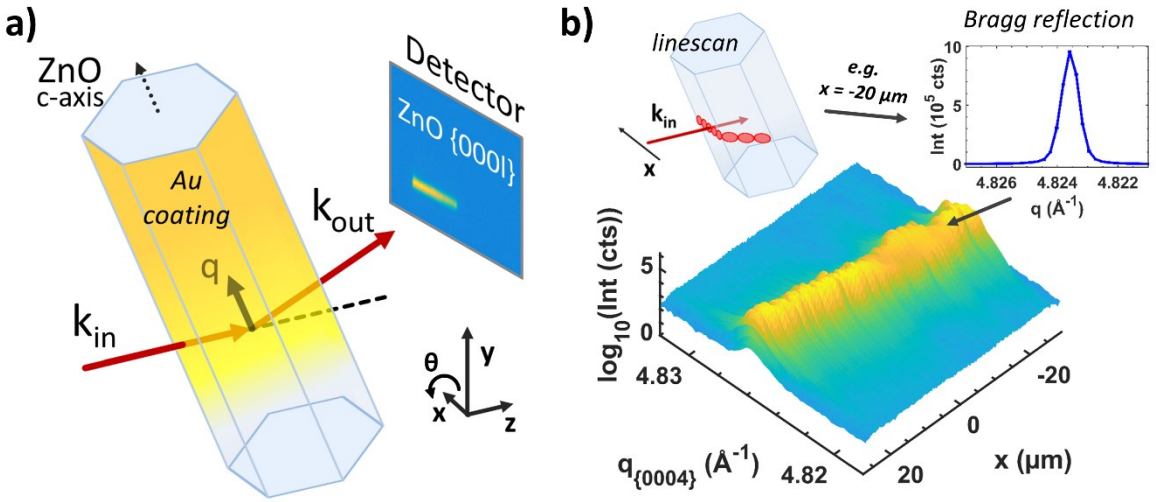

Figure 5.1: a) Sketch of the scattering geometry in this experiment. The incident k_{in} and scattered k_{out} wave vectors define the scattering vector q, which is oriented parallel to the ZnO rod's c axis and probes the {0001} Bragg reflections in the Au coated rod. The strain is sampled with a sub-µm step sized linescan along the x direction. b) Example of a Bragg reflection map visualizing the Bragg reflections (inset right) intensity and q values as a function of the spatial position x of the linescan across the sample (inset left). Compared to Figure 5.2 g-i) the strain map is tilted for an easier visualization of the concept.

To investigate a cross-section of the sample, a linescan was performed and the recorded Bragg reflection position holds access to the average, local strain with a spatial resolution of 250 nm, defined by the beam size and step size. For a line scan, the rod is moved in steps through the nano X-ray beam, as shown in the top left of Figure 5.1 b), and a Bragg reflection (Figure 5.1 b, top right) is recorded at each position. The Bragg reflection and its corresponding linescan spatial position x are combined in a Bragg reflection map, as exemplary shown for rod R1 in Figure 5.1 b) (further views of the map are included in the supplementary information, Figure 7.1).

5.1.4.1 Current-Voltage Investigations

IV curves were measured to characterize the electrical properties of the three ZnO rods, see Figure 5.2 a-c). The Schottky barrier height Φ_{bh} and ideality factor n were determined for all three samples by fitting the semi logarithmic *I-V* curves with a linear function.

An overview of the values is presented in Table 5.1 and are in agreement with previous results for ZnO Schottky contacts.[45] R1 and R2 (Figure 5.2 a,b)) show, qualitatively, the expected behavior of a rectifying Schottky contact with a distinct forward (positive voltage regime) and reverse direction.[39] But the ideality factor for R1, in contrast to R2, is bigger and a higher reverse current is measured. It appears that the Schottky contact of R2 is of higher quality. Figure 5.2 c) shows the measured *I-V* curve for R3 and, in contrast to the two previous rods, has a non-rectifying behavior with a huge reverse current and exhibits a high ideality factor. The overall behavior appears ohmic-like, even though the resistance of ~1 MΩ is too high for an ohmic contact. It appears that a Schottky contact is present, but with a huge reverse current. The increased ideality factor and huge reverse current in both R1 and R3 are possibly caused by a generation-recombination process in the Schottky depletion region of the ZnO.[39] This may be due to crystalline defects in the ZnO as previous studies on Schottky contacts shown that that the contact properties are immensely inflicted by defects near the interface[118,180] and that contact properties can be tailored by these.[119]

5.1.4.2 Scanning Nano XRD on ZnO Rods

Complementary scanning nano XRD was performed to investigate the crystalline structure in the three rods. The {0004} Bragg reflection was investigated for rod R1, R2 and the {0002} for R3. The respective rocking scans are shown in Figure 5.2 d-f) and were performed by varying the angle θ, see Figure 5.1 a), with the X-ray beam positioned at the center of the rods at $x = 0$. These Rocking scans were fitted with a Gaussian function and a full width at half maximum (FWHM) of 0.027 ± 0.003 °, 0.030 ± 0.003 ° and 0.042 ± 0.004 ° were found for R1, R2 and R3, respectively. From the Scherrer equation the respective size of coherent scattering crystal volume was calculated to be 264.5 ± 45.6 nm, 236.3 ± 27.1 nm and 317.5 ± 42.3 nm.[181] This is comparable to the volume probed by the X-ray nano beam (beam size (h × v) R1, R2: 250 nm × 350 nm; R3: 300 nm × 350 nm) and thus provides a lower limit for the size of coherent scattering regions in the crystal.

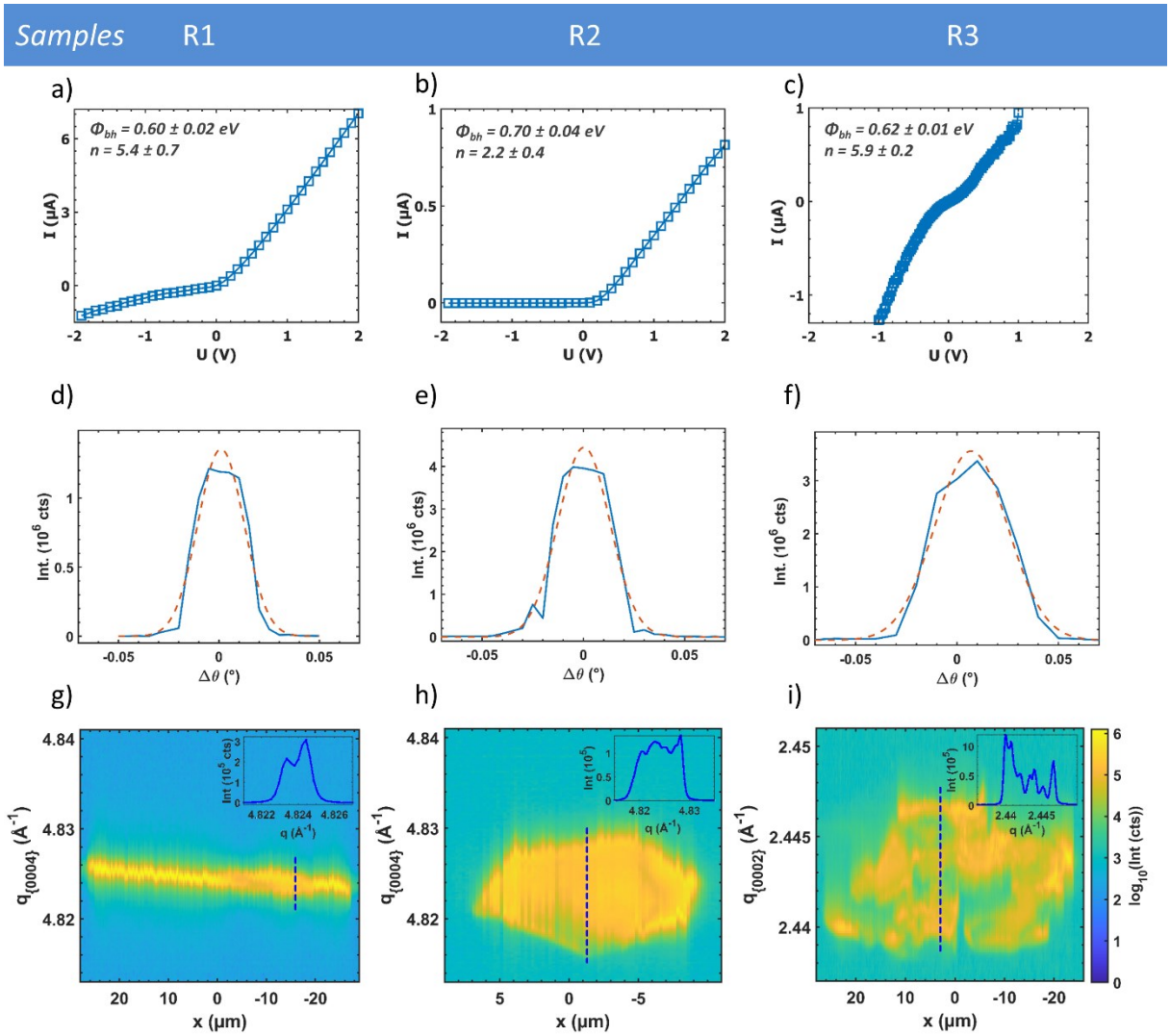

Figure 5.2: a-c) *I-V* curves for samples R1, R2 and R3, respectively. Including the Schottky barrier height Φ_{bh} and ideality factor n of the forward current. d-f) Rocking scans collected for the three rods and fitted with a Gaussian function. Note that R1 (d) and R2 (e) are collected at Bragg reflection {0004} and R3 (f) at {0002}. g-i) Respective Bragg reflection maps for R1, R2 and R3 visualizing change across the three rods. The insets show cuts through the Bragg reflection maps at x = -16 µm, -1.25 µm and 3 µm, respectively.

After the rocking scans were measured, Bragg reflection maps were collected to further investigate the behavior of the three rods by performing linescans along the x axis. Figure 5.2 g-i) show Bragg reflection maps with fundamentally different behavior for the rods R1 to R3. Insets show cuts through the respective Bragg reflection map. For comparison, all three presented linescans were measured in the Ag (R1 and R2) or Au (R3) covered parts of the ZnO rod and are representative for the overall behavior of the respective sample, further scans from five different positions on the samples are shown in Figure 7.2 to Figure 7.4 in the supplementary information. The values for the mean scattering vector q_{mean} and mean strain $\varepsilon_{\mathrm{mean}}$ in the rods and the minimum and maximum values q_{min} and q_{max} of the Bragg reflection maps are listed in Table 5.1.

Table 5.1: The Schottky contact metal, the barrier height Φ_{bh} and ideality factor n, both calculated from the *I-V* curves, for the Schottky contacts of the samples R1, R2 and R3. For all three samples the mean values of the scattering vector q_{mean} extracted from the Bragg reflection maps and strain ε_{mean}, calculated form q_{mean}, are presented. Furthermore, the minimum q_{min} and maximum q_{max} value from a 10% threshold to the maximum intensity of the Bragg reflection maps are listed. The bending radius for R1 and R2 is calculated from q_{min} and q_{max}.

sample	*contact metal*	Φ_{bh} [eV]	n	q_{mean} [Å^{-1}]	ε_{mean} [10^{-3}]	q_{min} [Å^{-1}]	q_{max} [Å^{-1}]	*bending radius* [mm]
R1	*Ag*	0.60 ± 0.02	5.4 ± 0.7	4.8246 ± 0.0008	0.63 ± 0.16	4.823 ± 0.0003	4.8266 ± 0.0003	74.5 ± 9.5
R2	*Ag*	0.70 ± 0.04	2.2 ± 0.4	4.8237± 0.0028	0.82 ± 0.55	4.8178 ± 0.0003	4.8293 ± 0.0003	6.4 ± 0.5
R3	*Au*	0.62 ± 0.01	5.9 ± 0.2	2.4436 ± 0.002	-12.19 ± 0.80	2.4392 ± 0.0002	2.4475 ± 0.0002	-

The q_{min} and q_{max} values are calculated as the minimum and maximum values of the scattering vector present in the Bragg reflection maps that show an intensity above a threshold of 10% of the maximum Bragg intensity. The Bragg reflection map of R1 in Figure 5.2 g) shows a well-defined distribution at each x position of the rod. Additionally, a uniform, almost linear change from left to right is observed. The positive, tensile strain ε_{mean} in Table 5.1 indicates that the lattice constant of the rod is extended along the c-axis and the linear change refers to a rod bending[182], the left edge of the rod is compressed relative to an extended crystal size at the right edge. Therefore, the rod is bent towards the left with a bending radius of 74.5 mm. (For further information on the bending radius calculation see the supplementary information). Furthermore, towards the right edge, between the positions x = -3 µm and -18 µm, the distribution is split with the maximum intensity decreasing by an order of magnitude, the overall q distribution width increases and two local maximums emerge as depicted in the inset of Figure 5.2 g), more detailed in Figure 7.5 in the supplementary information.

The Bragg reflection map of R2 shown in Figure 5.2 h), displays a hexagonal shape. In contrast to the behavior in sample R1 with its linear change, here, it shows a wide range of well distributed crystal lattice sizes for all positions x. The huge FWHM of the Bragg reflection of 7.9×10^{-3} Å^{-1} in R2 exemplary at x = 5 µm compared to 6.7×10^{-4} Å^{-1} for R1 at position x = 12 µm could be considered an indication for smaller size of coherent scattering crystal volumes, microstrain in these volumes or a combination of both. But this is unlikely because the Bragg reflection map of R2 shows an almost homogeneous Bragg intensity distribution and no distinct maximum in most of the Bragg reflection map, as shown in the inset of Figure 5.2 h) and for further Bragg reflections see Figure 7.6 in the supplementary information. It is more

likely that this broadening is caused by a (macro)strain change along the probed crystal volume in the beam path (see supplementary Figure 7.8) and is probably the result of a rod bending in z direction with a calculated radius of 6.4 mm. The bending, observed in R1 and R2, is likely the result of a mechanical stress induced while fixing the rod tips to two separate contacts of the sample holder to enable the electrical measurements.

The Bragg reflection map of R3 in Figure 5.2 i) displays a non-uniform behavior with a much higher absolute strain compared to the previous two rods. Moreover, peak splitting is observed multiple times across the rod with vastly varying q values and spatial sizes along the x direction. The peak splitting is shown in inset of Figure 5.2 i) and in Figure 7.7 in supplementary information. The peak splitting in the maps of R1 and prominently in R3 is strong evidence for the presence of different, coexisting coherent scattering regions that exhibit small differences in lattice spacing and/or orientation. These could be caused by a plastic deformation and/or fracture of the crystal due to high stress along the c axis, even though a study showed that ZnO rods can be elastically strained beyond 3%[183]. This is well above the here reported strain. Furthermore, the effect is present in both tensile (R1) as well as compressive strained samples (R3) and opposing strains causing the same kind of crystal deformation is unlikely. A better explanation is the growth of a non-single crystalline ZnO structure in parts of R1 and in the majority of rod R3.

Examinations of the crystalline quality using transmission electron microscopy (TEM) in combination with selected-area electron diffraction (ED) were performed on a similar ZnO rod, grown by the flame transport synthesis. The micrometer dimensions of the ZnO rod limited the examined area to its tapered tip as illustrated in Figure 7.9. ED pattern of a tilting series demonstrate that the ZnO rod exhibits a high crystal quality along the *c*-axis showing strong diffraction patterns usually observed for a single component. However, ED patterns slightly tilted away from edge-on zone-axis observation conditions revealed multiple weak reflections which could indicate the presence of minor crystalline components[184] or could result from dynamical diffraction events in a thick specimen. See Figure 7.9 in the supplementary information.

The growth of multiple crystals within the rod, could lead to at least two possible impacts, first, a divergence of the lattice orientation and, second, different lattice parameters for the multiple (possibly strained) crystalline structures. In R3 it is likely that a combination of both effects is present, resulting in multiple crystallites with different lattice parameter and orientation. At domain boundaries an increased density of crystal defects is expected, which is well known to influence the electrical properties of Schottky contacts.[118,119] This gives rise to the explanation

that the above reported *I-V* curves and the related electrical properties are the result of crystalline defects in the ZnO rods that got indirectly visualized by measuring multiple lattice parameter for different crystallites with nXRD. Furthermore, it appears that the number of different crystallites has an impact on the electrical properties, as well. In contrast to R1, microrod R3 with its apparent high amount of vastly differing crystallites exhibit a higher reverse current, possibly due to the higher number of domain boundaries and, hence, defects that contribute to the generation recombination process in the Schottky depletion region and decrease of the barrier height, e.g. due to inhomogeneities.[39,40,180]

5.1.4.3 Strain Model for Hexagonal Structure

For a more quantitative description of the measured strain distributions, an analytical model was developed to simulate the strain in a hexagonal rod, see Figure 5.3. The model in the *x*/*z* plane is extended along the *y* direction. The volume of the simulated rod with diameter $d = 1$ µm is divided into 10 nm voxels and to each of the voxels a strain value from an idealized strain distribution is attributed. This strain ε includes a constant strain ε_{const}, from a mechanical stress along the rod, and a linear component ε_{lin}, accounting for a rod bending. The equation for the model strain ε is:

$$\varepsilon(x_m, z_m) = \varepsilon_{const} + \varepsilon_{lin} \cdot \frac{x_m}{\frac{d}{2}} \tag{5.1}$$

Here, x_m and z_m are the model's spatial coordinates with the rod center at (0,0). These are comparable to the axes x and z in the measured data. A constant strain ε_{const} is present within the whole volume, with an additional linear change ε_{lin} along the x_m direction. The rod diameter d is included to ensure that the maximum strain ε_{lin} is reached at the edges of the rod along the *x*-axis. For the calculation of a model strainmap we recall that the X-ray beam probes at each *x* position a full cross section along *y* through the sample. Assuming that scattering contributions from spatially separated crystallites add up fully incoherent, the X-ray intensity distribution at a given strain value ε (or, more precisely, in an interval $\pm\Delta\varepsilon/2$ around this value) and position *x* is proportional to the sum of the intensities from all crystallites exhibiting this strain, along the beam path in *y*. The strain map visualizes the intensity for all strain values ε and all positions *x* across the sample. Replacing the X-ray intensity from crystallites in the real measurement with an amount of model voxels, exhibiting a strain in the specific range $\pm\Delta\varepsilon/2$, and the result is an artificial map $I(x_m,\varepsilon)$ of the simulated strain in the rod.

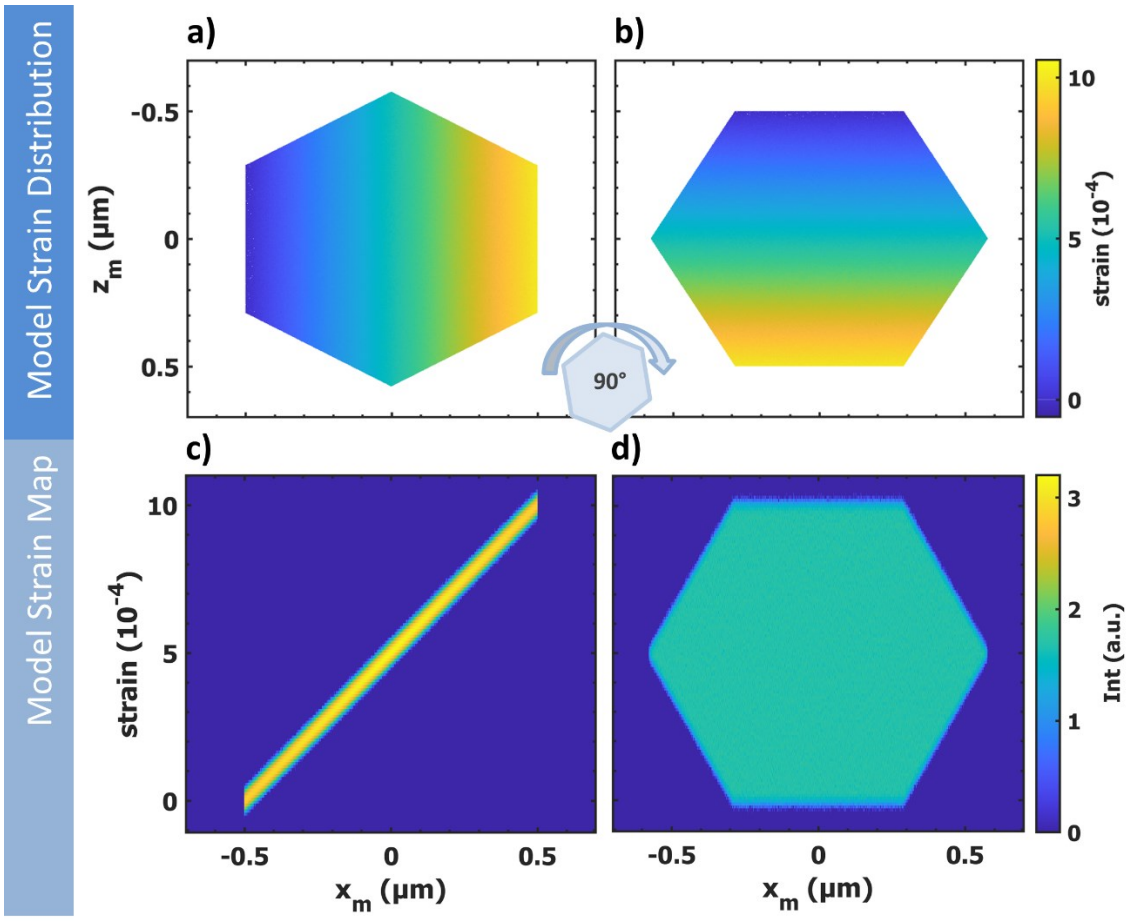

Figure 5.3: a) Strain distribution of a hexagonal shaped model structure with a linear strain increase from left to right. b) The model is rotated clockwise by 90°. c, d) The respective strain maps calculated from the model strain distributions in the upper row, the different orientation of the shape and strain directly influence the strain maps appearances.

Figure 5.3 a) shows the strain distribution inside a model rod with a constant offset $\varepsilon_{const} = 0.5 \times 10^{-3}$ and a linear contribution $\varepsilon_{lin} = 0.5 \times 10^{-3}$. In this way, the strain change from the left to the right edge of the rod is 0 to 1×10^{-3}. For Figure 5.3 b) the same model strain distribution is rotated clockwise around the y axis by 90°. From these simulated strain distributions, the respective strain maps were calculated, as described above. In Figure 5.3 c) the strain map of the first artificial strain distribution is displayed. It shows a linear strain change left to right from 0 to 1×10^{-3} and a mean strain of 0.5×10^{-3}, as expected. The second strain map in Figure 5.3 d), calculated from the rotated strain distribution, has a mean strain of 0.5×10^{-3}, as well. But it shows no linear increase of the strain in any direction, instead a well-distributed broadening of the strain ranging from 0 to 1×10^{-3} with a reduced strain intensity. These simulations imply that the Bragg reflection maps in Figure 5.2 d-f), displaying a striking similarity to the strain maps in Figure 5.3 c,d), are linked to the strain distribution and further, that the q range and shape of the maps are a direct result of the present strain distribution in the

rods. Furthermore, the Bragg reflection maps in Figure 5.2 d,e) for R1 and R2 are comparable, but are mainly different due to a rotated strain-to-probing orientation, likely due to bending in two perpendicular directions. This explains the qualitatively comparable *I-V* curves despite the difference in the respective strain maps.

In this study a Schottky barrier height change of around 14 % is reported, linked to the crystal quality. This change is by one order of magnitude stronger than a piezotronic induced height change of a Ag/ZnO Schottky barrier due to an applied mechanical stress of 70 MPa.[23] Another study reported a temperature dependent Schottky barrier height change of 35 % for a temperature drop from 300 K to 77 K and attributed this change to a lowering of the carrier density with decreasing temperature.[185] The carrier density can also be altered by doping the ZnO, e.g. with boron atoms.[186] For graphene/ZnO contacts, the Schottky barrier height was found to first increase with rising boron doping concentration but to decrease below the intrinsic height after reaching a doping level of 0.15 mol/l, with a relative Schottky barrier height change of 56 %.[186] In summary, the impact of the crystal quality is bigger than the strain induced change by the piezotronic effect, but is smaller than that of temperature or doping concentration induced changes. Furthermore, the reported impact of the crystalline quality is not solely limited to an altering Schottky barrier height but, as well, causes a change of the *I-V* characteristics ranging from rectifying Schottky diode to ohmic behavior, as it is known for different contact materials.[45] Therefore, the impact of ZnO crystalline quality is diverse and should be considered when designing devices and sensors.

5.1.5 Conclusion

In conclusion, following the electric characterization of Schottky contacts using *I-V* curves the crystal structure in three ZnO microrods was spatially resolved measured by nXRD. It was found that a well-defined strain distribution, with non-abrupt changes in the measured crystal lattice parameter, is strongly linked to the rectifying Schottky diode characteristics. In contrast, a highly strained crystal, exhibiting several coherent scattering domains rather than a single domain, causes non-ideal *I-V* characteristics, probably due to increased defect rates at the domain boundaries. It is shown that the crystallinity in semiconductor material has an immense impact on their electrical properties and strain revealing nXRD holds an opportunity to characterize the crystalline structure in semiconductor-based devices and enhance their performance. Further investigations of the crystallinity and a better understanding of its impact on the performance of piezotronic devices are a key for the optimization of such sensors. To this end, advanced techniques to investigate the crystalline structure are extremely helpful. A

combined approach using highly resolved transmission electron microscopy measurements,[187] multi Bragg diffraction,[188] and visualizations of the 3D strain distributions by coherent X-ray diffraction imaging[189,190] or ptychography[66,191] could provide deeper insights in future studies. For textured or polycrystalline samples, texture investigations,[192] or extending investigations to amorphous systems pair distribution function analysis from total scattering would be beneficial.[193,194] It is clear that X-ray techniques in particular, when combined with TEM, can deliver useful information for enhancing device design and performance.

5.1.6 Experimental Section

Sample Preparation: Flame transport synthesis was used for the production of the ZnO microstructures.[120] With this technique, it is possible to produce tailor made ZnO rods with diameters ranging from below 1 µm to a few hundred µm and lengths up to mm. Three ZnO rods were used, R1 to R3. The diameters of the samples are 55.5±0.6 µm, 15.2±0.6 µm and 51.3±0.6 µm, respectively. These were determined from optical images, see Figure 7.10 in the supplementary information. After both rod tips were fixed with epoxy to a sample holder, one end of the rod was coated with 100 nm Al to create an ohmic contact, the other end was covered in Ag glue, for sample R3 this end was first coated with 200 nm of gold by thermal evaporation and then partly covered with Ag glue. The Ag and Au on the ZnO establish an Schottky contact. Furthermore, the Ag glue was used at all contacts to fix and connect wires for the electrical measurements. An uncoated part in the middle of the ZnO rod was left free to prevent a short circuit between the Ag or Au contact and the Al.

Scanning Nano XRD: The experiment was performed at the MiNAXS endstation of the beamline P03 at the Petra III synchrotron at DESY .[149,195] The photon energy was 13 keV and the beam was focused with a Kirkpatrick-Baez mirror [196] down to 250 × 350 nm^2 (h × v) at the sample position. The first step was the initial search for the Bragg reflection by using a Pilatus 300k (R1 and R2) and Pilatus 1M (R3) with a sample detector distance of 24 cm to increase the observed q space. In a time-consuming procedure, it was necessary to search for, find and optimize the individual reflections of the {0004} (R1 R2), and {0002} (sample R3) Bragg reflections. To illustrate the high crystallinity of the rods rocking scans were collected and the summed-up detector images of these scans shown in supplementary information Figure 7.11) illustrating a narrow, high intense distribution of the selected Bragg peak. Further reflections found for R1 and prominently R3 are identified as Bragg reflections of the silver and gold coating, respectively. Further data was acquired using a Photonic Science CCD camera with 65 µm square sized pixels at a detector sample distance of 1.58 m for samples R1 and R2,

and 2.56 m for R3. First, a rocking scan was conducted to optimizing the scattered intensity by rotating the rods around the *x*-axis (Figure 5.1 a) and, second, a line scan in *x*-direction across the whole ZnO rod with 200 nm spatial step width. For the calculation of the coherent scattering crystal volume size w_{DS} the Scherrer equation was used, $w_{DS} = \frac{K\lambda}{\Delta(2\theta_0)\theta_0}$, with K = 0.89, X-ray wavelength λ, full width at half maximum (FWHM) of the Bragg reflection $\Delta(2\theta_0)$ in radians and the Bragg angle θ_0.[181] FWHM and peak width parameter sigma σ of a Gaussian function are related by, $FWHM = 2\sqrt{2\ ln2}\sigma$.

Current/Voltage (IV) Measurements: The combination of a Schottky and an ohmic contact allows one to measure the forward and reverse current of the Schottky contact. For the electrical measurements, a Keithley 2450 Sourcemeter was used to collect the *I-V* curves in a range of -2 to 2 V with a resolution of 0.1 V for the samples R1 and R2, and -1 to 1 V with 0.02 V steps for sample R3. The current accuracy is between $1x10^{-9}$ and $6x10^{-11}$ A and further $7x10^{-4}$ V for the sourced voltage. To distinguish the barrier height and ideality factor of the Schottky contact a linear function was fitted to the logarithm of the current in the range of 0.1 V to 0.3 V.[39] The intersection of the fitted line with the y-axis defines the current I_0 and further the barrier height $\phi_{bh} = \frac{kT}{q}\ln\left(\frac{A^*T^2}{J_0}\right)$, [39] with the Boltzmann constant k, temperature T= 294 K, elementary charge q, effective Richardson constant A^*= 32 A cm^{-2} K^{-2} [111,197] and the current density J_0 equals the current I_0 divided by the contact area size. From the fitted slope $\frac{d(\ln J)}{dV}$ of the fitted linear function, the ideality factor n is distinguished by employing $n = \frac{q}{kT}\frac{dV}{d(\ln J)}$.[39]

Transmission electron microscopy (TEM): TEM has been performed to study the crystallinity of the ZnO microstructures. The ZnO samples were transferred to TEM Cu-lacey grids with carbon support film after gentle crushing and dispersing them in butanol. A selected-area electron diffraction (SAED) tilting series on a ZnO microneedle was performed on a JEOL JEM2100 (LaB_6, 200 kV) microscope.

5.2 Modulation of Electrical Conductivity and Lattice Distortions in Bulk HVPE-Grown GaN

5.2.1 Publication 2 Overview

As seen in the previous section, the investigation of structural properties is an excellent tool to achieve a better understanding of the underlying mechanisms and enhance the further development of devices based on the obtained results. In this study the carrier concentrations as well as structural differences of as-deposited and etched GaN samples, see section 3.2, were investigated by means of photoluminescence, TEM and XRD techniques and the impact of etching on the electrical properties was determined. For the X-ray investigations the GaN (0004) Bragg reflection was recorded to determine the crystalline structure, complementary investigations of the structure were performed by TEM. Furthermore, rocking scans of the sample were obtained, to identify the difference between the geometry of the sample and the crystal growth direction.

This section is a manuscript published in ECS Journal of Solid Science and Technology.[198] (https://doi.org/10.1149/2.0041908jss)

Modulation of electrical conductivity and lattice distortions in bulk HVPE-grown GaN

Niklas Wolff,[1] Philipp Jordt,[2] Tudor Braniste,[3] Veaceslav Popa,[3] Eduard Monaico,[3] Veaceslav Ursaki,[3] Adrian Petraru,[4] Rainer Adelung,[5] Bridget M. Murphy,[2,6] Lorenz Kienle[1] and Ion Tiginyanu[3,7]

[1] Synthesis and Real Structure, Institute for Materials Science, Kiel University, Kiel 24143, Germany

[2] Institute for Experimental and Applied Physics, Kiel University, Kiel, 24118, Germany

[3] National Center for Materials Study and Testing, Technical University of Moldova, Stefan cel Mare av. 168, MD-2004 Chisinau, Republic of Moldova

[4] Nanoelectronics, Institute for Materials Science, Kiel University, Kiel 24143, Germany

[5] Functional Nanomaterials, Institute for Materials Science, Kiel University, Kiel 24143, Germany

[6] Ruprecht-Haensel Laboratory, Kiel University, Kiel 24118, Germany

[7] Academy of Sciences of Moldova, Stefan cel Mare av. 1, Chisinau 2001, Republic of Moldova

5.2.2 ABSTRACT

The nature of self-organized three-dimensional structured architectures with spatially modulated electrical conductivity emerging in the process of hydride vapor phase epitaxial growth of single crystalline n-GaN wafers is revealed by photoelectrochemical etching. The amplitude of the carrier concentration modulation throughout the sample is derived from photoluminescence analysis and localized heterogeneous piezoelectric response is demonstrated. The formation of such architectures is rationalized based on the generation of V-shaped pits and their subsequent overgrowth in variable direction. Detailed structure analysis with respect to X-ray diffraction and transmission electron microscopy gives striking evidence for inelastic strain to manifest in distortions of the $P6_3mc$ wurtzite-type structure. The deviation from hexagonal symmetry by angular distortions of the β angle between the basal plane and c-axis is found to be of around 1°. It is concluded that the lattice distortions are generated by the misfit strains originating during crystal growth, which are slightly relaxed upon photoelectrochemical etching.

5.2.3 INTRODUCTION

Over the last 20 years GaN has become one of the most important semiconductor materials and may replace Si in many electronic applications. Particularly, it is already replacing Si in LDMOS radio-frequency devices used in base stations for mobile communication as well as GaAs for radar applications.[199–205] The highly advantageous properties of GaN-based semiconductors such as high electron mobility and saturation velocity, high sheet carrier concentration at heterojunction interfaces, high breakdown field, and low thermal impedance make them extremely promising for high-power high-temperature microwave applications, as evidenced by their high Johnson`s figure of merit.[206–208] Exemplary, solid-state lighting optoelectronic devices assembled from white LEDs based on GaN are replacing conventional light sources such as incandescent bulbs and fluorescent lamps nowadays. This is due to their high efficiency, long operational lifetime, compact form factor, no emission of harmful ultraviolet (UV) or infrared radiation and low maintenance cost. A recent review also highlights the prospects of GaN LEDs for visible light communications (VLC) in both fiber and free-space embodiments.[209] The state-of-the-art technology enabling bandwidth of GaN LEDs in the range of >400 MHz has been explored and multi-gigabit- per-second VLC has been demonstrated.

Better performance characteristics than those of Si power devices make also GaN power devices promising for automotive applications.[210] These electronic applications are based on

using primarily silicon or silicon carbide substrates, since from a synthesis point of view thick GaN substrates are commercially unavailable. In spite of considerable progress in addressing the challenges related to significant mismatches between crystal lattices and thermal expansion coefficients, as well as silicon thermal stability when using Si substrates,[211] GaN-on-Si, GaN-on-SiC, and GaN-on-Sapphire remain costly solutions. In fact, GaN remains the most costly electronic material among the wide bandgap compounds (excluding single crystalline diamond).

For a long time, GaN has been grown by Metalorganic Chemical Vapor Deposition (MOCVD) on sapphire, Si, or SiC for research and device applications. However, challenges related to the growth of high-performance films remain, still hampering their utilization in devices.[212] Therefore, single crystalline GaN substrates are essential for future high-performance devices. Nowadays, there are three main technologies used for GaN crystal growth: hydride vapor phase epitaxy (HVPE), sodium flux and ammonothermal growth.[213] The last two approaches belong to the group of solution growth methods. High structural quality and high purity have been demonstrated by using the sodium flux growth method. However, it is supposed that this method is a perfect technology for fabricating seeds for further growth of gallium nitride but not for mass production of crystalline wafers, because this technological process is quite expensive and complicated.[213] On the other hand, the ammonothermal growth seems to be appropriate for mass production of GaN crystals, high structural quality substrates with 2-inch diameters and various electrical properties being successfully grown.[214] However, the main problem of this technology is the low growth rate of up to a few micrometers per hour. Apart from that, despite the high crystalline quality, the properties of ammonothermal GaN crystals and substrates are affected by the presence of impurities and other defects that hinder their use for device applications.[215] Therefore, the most appropriate approach for manufacturing GaN substrates is considered HVPE, due to the relatively high growth rate (>100 μm/h) and crystallization of high-purity material.[15] In spite of important advantages of this technology, however, achieving good crystalline quality is still challenging, because of the formation of V-shaped defects or pits, which lead to the formation of extended inhomogeneous structures upon subsequent overgrowth (see for example refs. [216,217]). Self-organized 3D nanostructured architectures including quasi-ordered concentric hexagonal structures generated during the growth of single crystalline *n*-GaN substrates by HVPE have been revealed by subjecting the samples to electrochemical or photoelectrochemical (PEC) etching.[216] It was supposed that these architectures are produced due to a fine modulation of doping related to the spatial

distribution of impurities in the volume of samples generated by some peculiarities of the HVPE growth.

In this paper, we demonstrate by means of transmission electron microscopy (TEM) that the self-organized nanostructured architectures disclosed by photoelectrochemical etching are not related to systematic variations of the crystal structure but by the modulation of electrical parameters, e.g. by zero and one dimensional defects. Furthermore, we disclose a monoclinic or triclinic lattice distortion of the wurtzite structure by the combination of electron diffraction (ED) and X-ray diffraction (XRD) techniques. We estimate the amplitude of modulation of the free carrier concentration by making use of photoluminescence spectroscopy. The prospects of employing the fine modulation of electrical conductivity for the purpose of nanostructuring by design of GaN and related materials are also discussed. We suggest that the lattice distortion is kinetically induced and measure residual misfit strains of the crystal which relax upon photoelectrochemical etching.

5.2.4 EXPERIMENTAL DETAILS

The experiments have been realized on 2-inch diameter HVPE-grown *n*-GaN single crystalline templates acquired from SAINT-GOBAIN Crystals. The 300 μm thick wurtzite-phase GaN substrates were of (0001)-orientation with virgin Ga-face and polished N-face. The density of threading dislocations in the substrates was in the range $(1–2)\times10^7$ cm^{-2}. PEC etching was carried out in a stirred 0.1 mol. aqueous solution of KOH for periods up to 30 min under in-situ ultraviolet (UV) illumination provided by focusing the radiation of a 350 W Hg lamp to a spot of about 3.5 mm in diameter on the sample surface. No bias field was applied to the sample during etching, the electrical circuit being closed with a platinum electrode in the electrolyte and an electrical contact made on the backside of the sample using a conductive silver paste. The morphology of as-grown and PEC-etched GaN samples was studied using Zeiss Ultra Plus and VEGA TESCAN TS 5130MM scanning electron microscopes equipped with INCA Energy 200 EDX System (Oxford Instruments) for chemical composition microanalysis, as well as using a NANOSTATION Atomic Force Microscope (AFM) from Surface Imaging Systems. The local piezoelectric response has been monitored by the piezoresponse force microscopy techniques (PFM) on a SmartSPM 1000 scanning probe microscope from AIST-NT. A sinusoidal modulation voltage of 10 V peak-to-peak at a resonance frequency of 247 kHz was applied between the conductive tip and the sample. The scan was performed in contact mode acquiring the topographic image simultaneously to the vertical piezoresponse amplitude and phase. The photoluminescence (PL) spectra were

measured in a temperature interval from 10 to 300 K under excitation by radiation from a He-Cd laser with the wavelength of 325 nm operating in a continuous-wave (CW) mode.

The transmission electron microscopy investigation was carried out on a FEI Tecnai F30 STwin instrument operating at 300 kV (spherical aberration constant C_S=1.2) to determine the structural features of as-grown HVPE single crystalline templates as well as PEC-etched GaN samples using electron diffraction and high-resolution (HRTEM) microscopy. Electron transparent cross-sectional specimens (~12x8 μm) were prepared via a dual beam scanning electron microscope FEI Helios Nanolab system performing a standard focused ion beam (FIB) technique. To account for the high surface roughness and to achieve a more homogenous covering of samples subjected to PEC etching we deposited a layer of carbon using the e-beam prior to the deposition of platinum protection layers to fill up the concentrically etched trenches.

For the high-resolution X-ray diffraction (HRXRD) investigations, we used a Rigaku Micromax rotating anode with the characteristic Cu-K_α X-ray energy, at a wavelength of 1.54 Å. The beam size was 1x1 mm^2 ($h \times v$) with a resolution of 2×10^{-4} $Å^{-1}$.

5.2.5 Results and Discussion

SEM images demonstrate some quasi-periodical modulation of the physical properties of as-grown HVPE samples both on the top surface (Figure 5.4 a), upper part) and in the bulk (a cross-sectional view is illustrated in the lower part of Figure 5.4 a). We suggest that these features are related to the modulation of the electrical conductivity across the sample volume, as SEM is sensitive to electrical parameters of the material. A model describing the occurrence of such modulations during the HVPE crystal growth has been proposed previously.[216,217]

The morphology of a GaN sample subjected to PEC etching as revealed by SEM and AFM is illustrated in Figure 5.4 b-d) which discloses concentric rings forming hexagonal patterned domains on the surface of the sample as shown in Figure 5.4 b). In PEC etched samples, the pattern in SEM images arise due to differences in the rates of electrochemical dissolution of regions exhibiting different values of electrical conductivity, while in as-grown samples the light-dark pattern is caused by the modulation of the electrical conductivity. So, PEC etching proves to be a versatile tool for disclosing patterns of electrical parameters in inhomogeneous semiconductors. One can see from Figure 5.4 b) that the formation of nanostructured domains starts at certain points at early stages of the crystal growth, and these domains develop further according to the previously proposed model.[216] The insert in Figure 5.4 b) suggests that these nucleation points are genetically related to sites with a high density of dislocations, which are evidenced by PEC etching, since it is well established that the dislocations in GaN are resistant

against PEC attack.[218–220] The morphology of regions where differently nanostructured domains intersect each other is illustrated in Figure 5.4 c,d). The 3D spatial architecture of these porous domains can be described as hollow cones which are concentrically stacked into each other as exemplified in Figure 7.12 (Supplementary Information) by a SEM image taken from an electrochemically etched sample.

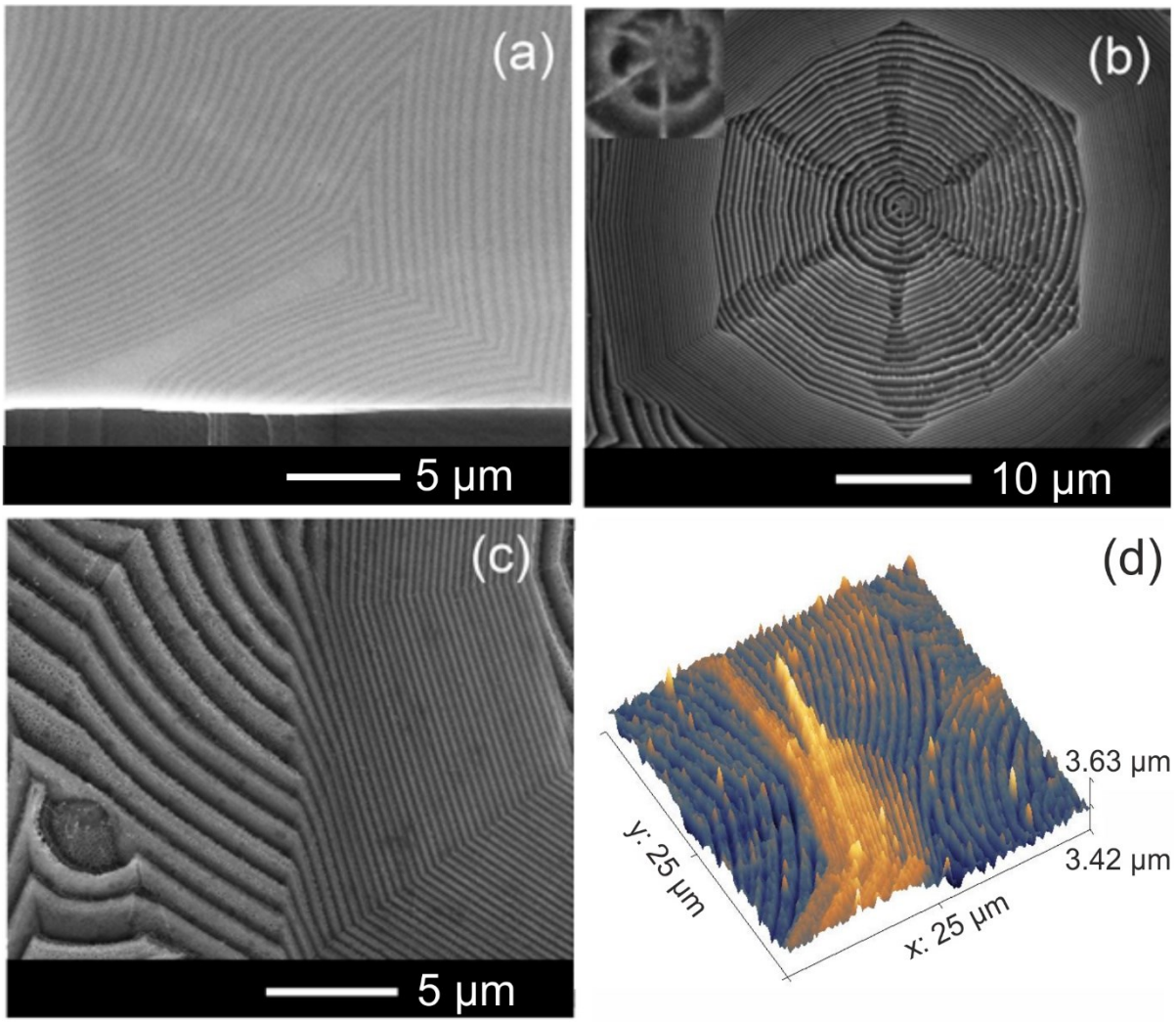

Figure 5.4: Oblique SEM view a) of a cleaved as-grown HVPE GaN sample revealing an alternating bright-dark pattern. SEM b,c) and AFM d) images of nanostructured regions showing the micrometer deep etched trenches produced in a HVPE GaN sample subjected to PEC etching.

Note that there is a difference in the mechanisms of electrochemical and PEC etching of GaN. In an electrochemical process, the regions possessing higher electrical conductivity usually are characterized by higher degree of porosity. In contrast to that, the etch rate during PEC etching decreases linearly with the logarithm of the carrier concentration, i.e. the regions with lower carrier concentration are etched faster than surrounding regions, which leads to the formation

of concentric rings along the surface subjected to etching.[220] Further images of the photoelectrochemically etched GaN surface can be found in Figure 7.13, illustrating the clear modulation of electrical conductivity.

An interesting issue is the estimation of the amplitude of modulation of electrical parameters across the material as a result of peculiarities of the HVPE growth. Qualitative PFM measurements revealed a modulation of the local piezoresponse within hexagonal patterned domains and boundary regions in between, further named "islands", a phenomenon which can be correlated with the presence of inversion domains.[221] The results are presented and discussed in Figure 7.14. Further, in a previous study by means of Kelvin Probe Force Microscopy,[216] it was suggested that the fine modulation of doping is related to the spatial distribution of impurities. It is difficult, however, to estimate the amplitude of modulation by means of this methodology. In this paper, we make use of PL spectroscopy for the purpose of evaluating the amplitude of spatial modulation of the free carrier concentration in the specimen. According to a semi-classical model regarding the broadening of impurity bands in heavily doped semiconductors developed by Morgan,[222] the carrier concentration can be estimated from the dependence of the photoluminescence full width at half maximum (FWHM) on carrier concentration. This model has been previously applied to explain the broadening of near-band-gap (NBG) photoluminescence in *n*-GaN films.[223] It was shown that the model can be reliably applied to GaN samples with electron concentration higher than 10^{18} cm^{-3}, and a calibration curve has been deduced for the relation between the FWHM of the NBG photoluminescence measured at 77 K and the electron concentration in the GaN material.

The PL spectra measured at 10 K for both the as-grown and the PEC etched samples (Figure 5.5 a)) are typical for GaN according to samples grown previously by using various technologies. Apart from the NBG PL band with the maximum at 3.471 eV, a series of PL bands with the intensity more than two orders of magnitude lower are observed in the spectral range from 3.0 to 3.4 eV. Note also the presence of a broad green PL band with nearly the same intensity in the visible spectral range (not shown in this figure). The band located at 3.37 eV could be attributed to a free-to-bound transition, while several bands in the spectral range of 3.2 – 3.3 eV followed by one- and two-phonon replicas are usually associated with donor-acceptor pair (DAP) transitions.[224,225] The origin of the 3.27 eV PL band as a DAP recombination has been well documented in the literature through its shift to higher photon energies with increasing the excitation power density and a transition from a DAP recombination to conduction band-acceptor recombination at elevated temperature. The PL band at 3.27 eV with two shoulders at 3.29 eV and 3.24 eV suggests the presence of different impurities in our

samples. However, additional investigations are needed to identify the chemical nature of the respective impurities.

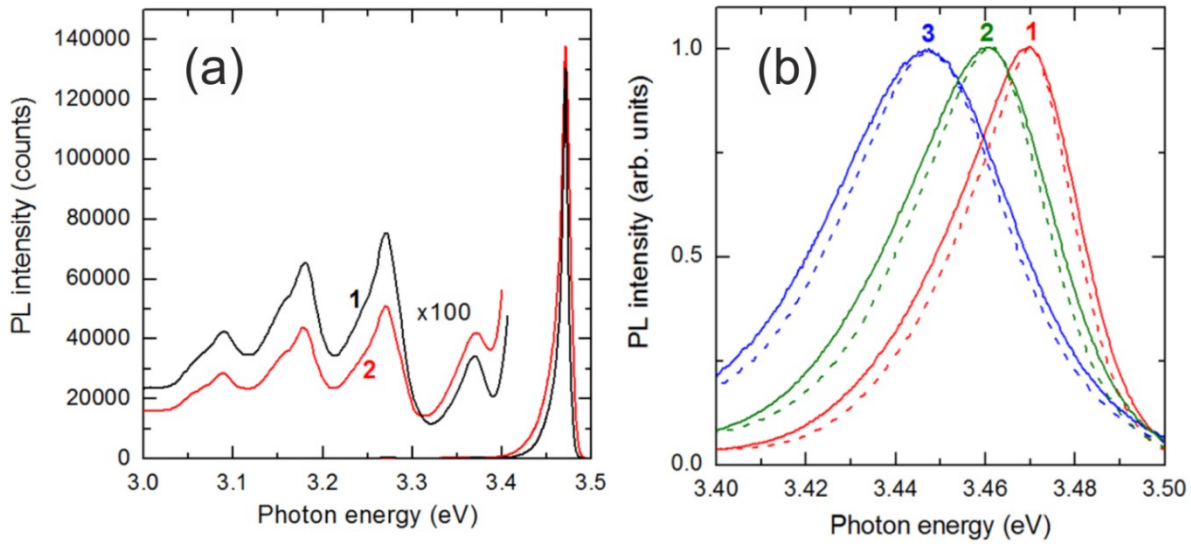

Figure 5.5: a) PL spectrum of as-grown (curve 1) and PEC etched (curve 2) GaN samples measured at 10 K. b) The NBG PL band measured at 75 K (curves 1), 100 K (curves 2) and 150 K (curves 3) in the as-grown (dashed line) and PEC etched (solid line) samples.

The analysis of the NBG PL band (Figure 5.5 b)) discloses its slight broadening in the PEC etched sample as compared to the as-grown one: the FWHM increases from 29 to 33 meV at 75 K, from 35 to 40 meV at 100 K, and from 42 to 47 meV at 150 K. By using the calibration curve from ref. [223], one can estimate that at 75 K the carrier concentration increases from 1.0×10^{18} cm^{-3} in the as-grown sample to 1.6×10^{18} cm^{-3} in the PEC etched sample, i.e. the carrier concentration increases by ca. 60 %. These data corroborate the previous findings that PEC etching removes basically the material with low conductivity and leaves areas with higher carrier concentration. On the other hand, the as-grown material contains nanorings with both low and high carrier concentration, i.e. the NBG PL band comes as a superposition of a narrow band from rings with low carrier concentration and a broader band from rings with higher carrier concentration. This means that the NBG PL band from areas with low carrier concentration should be even narrower, which would give a carrier concentration lower than the deduced value of 1.0×10^{18} cm^{-3}. In this context, it is clear that the amplitude of modulation of the electrical conductivity in the HVPE samples is even higher than 60%.

The results of TEM investigations show that the self-organized nanostructured electrical architectures produced during HVPE growth seem not to be related to regions of structural variation with respect to a single crystal material. Moreover, the comparison of the as-grown and PEC-etched samples demonstrates a high density of defects such as stacking faults and

dislocations close to the surface serving as possible attack sites for the PEC-etch. For the as-grown (0001) nanostructured GaN (see Figure 5.6 a,b)) dislocation networks originating at the (0001) GaN surface have been observed to extend 200-300 nm deep into the crystal. For the etched sample, a TEM lamella has been cut from the center of the circular formations. Dislocation networks were evidenced to be concentrated at the center of these hexagonal domains, developing along the polar direction throughout the prepared crystal lamella (Figure 5.6 d,e)). This observation is in congruence to previous investigations of pits at the center of the nanostructured architectures which are related to pile up of screw or mixed-type dislocations using AFM.[216] These defects were visualized by exploiting the diffraction contrast in the scanning TEM (STEM) high-angle annular dark-field mode after tilting away from the [2-1-10] diffraction condition of the crystal to enhance electron scattering processes at defects. Further, we report that after etching, neither dislocation networks nor stacking faults could be observed beneath the (0001) surface, indicating that defect rich regions of the crystal lattice have been preferentially under attack by the PEC-etch, which is especially active for regions with low carrier concentration. Indeed, several reports exist about the influence of crystal defects in GaN on the electric conductivity[225] especially related to threading dislocations and gallium vacancies by e.g. the existence of deep level trapping states[226] in the yellow luminescence band, the reduction of the minority carrier concentration at dislocations acting as non-radiative recombination centers[227] and low transverse mobility by scattering of electrons at charged dislocation lines.[228] However, the dislocation network observed at the center of nanostructured architectures has not been subjected to the PEC attack as evidenced by the STEM images and described in literature.[218] The mediation of stress due to crystal lattice mismatch and difference in thermal lattice expansion coefficients during growth introduces high defect densities of the family of screw, edge and mixed-type dislocations and have been shown to be concentrated at the substrate/film interface of ~6 mm thick HVPE grown GaN crystals, decreasing in density with growth direction.[229] Strategies to reduce the generation of high defect densities comprise the initiation of cracks in the sapphire substrate and homoepitaxial growth onto thin GaN seed layers.[230] However, with substantial thickness the large stresses generated lead to the self-separation of substrate and film and could manifest in lattice distortions.[231,232] The results of crystal structure investigations disclose a clear deviation from the $P6_3mc$ wurtzite-type structure in the as-grown and PEC etched samples.

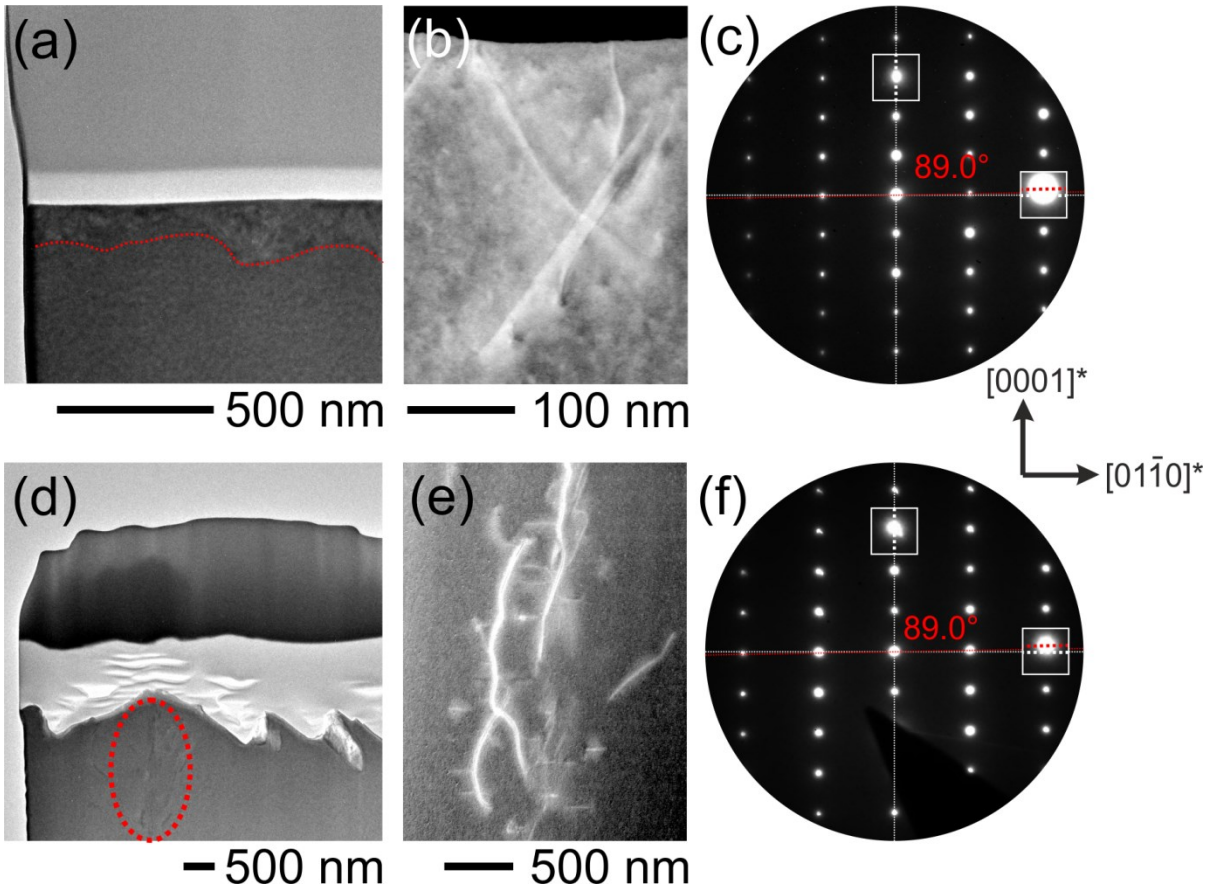

Figure 5.6: TEM cross-section investigation of the as-grown a-c) and PEC etched GaN bulk films d-f). a) As-grown GaN films show low surface roughness. The red line indicates a change in contrast between the upper and lower part of the crystal, which is related to a high density of near-surface defects such as stacking faults and threading dislocations as depicted in the STEM image in b). c) Selected area electron diffraction pattern in [2-1-10] zone axis showing the *c*-axis oriented film growth and a distortion of the reciprocal $\beta \approx 89°$ angle of the wurtzite-type crystal structure ($\alpha°=\beta°=90°$). d) Surface etched GaN crystal cut through the center of one hexagonal microdomain (marked with the red ellipse), where dislocation networks were observed in the STEM mode e). f) SAED pattern showing the deviation of the reciprocal β angle. The red dashed lines display the angular deviation of the intensities with respect to 90°, white dashed line.

A detailed electron diffraction (SAED) study from multiple selected areas revealed a slight deviation of the reciprocal unit-cell angle $\beta \approx 89°$ from rectangularity. The angle β is observed between the [0001]* and [01-10]* directions in the [2-1-10] zone axis pattern (we refer to the magnified insets, in which the red dashed lines display the angular deviation of the intensities with respect to 90°, white dashed line), as depicted in Figure 5.6 c,f). The lattice distortion was observed in several selected areas as evidenced from SAED experiments on the as-grown GaN sample (Figure 7.15). The reduction of symmetry was apparent irrespective of the slight bending of the lamella itself indicated by the increasing amount of out-of-zone axis orientation when moving from i) to iv) in Figure 7.15 a). Whereas SAED collects more averaged

information from a relatively large sample area of 0.785 µm² in this experiment, the β distortion was also locally observed at the nanoscale by high resolution imaging. HRTEM micrographs and their Fast Fourier Transforms (FFTs) (see Figure 5.7) taken from different areas of the patterned PEC etched sample show the defect-free nanostructures of the hillocks depicted in Figure 5.6 d). Whereas the analysis of this selected area by FFT (Figure 5.7 a,b) does not show any deviation from the 90° angle an even larger distortion of 88° could be observed in neighboring areas (see Figure 5.7 c,d). This finding indicates local lattice relaxation potentially due to the increase in free surface upon etching. The variation of the reciprocal angle according to the bulk wurtzite unit cell alters the angle β between the basal plane and the *c* axis. This angular distortion from 90° depending on the direction and the magnitude of strain results in a symmetry reduction in respect to the wurtzite aristotype. The symmetry of the deformed structure may be assigned to a maximum subgroup of $P6_3mc$, e.g. with monoclinic (C*m11* or C*1c1*) or triclinic symmetry. Due to missing superstructure reflections in the diffraction patterns, the symmetry reduction has to be assigned to as the t-type[233] (for *translationengleich*).

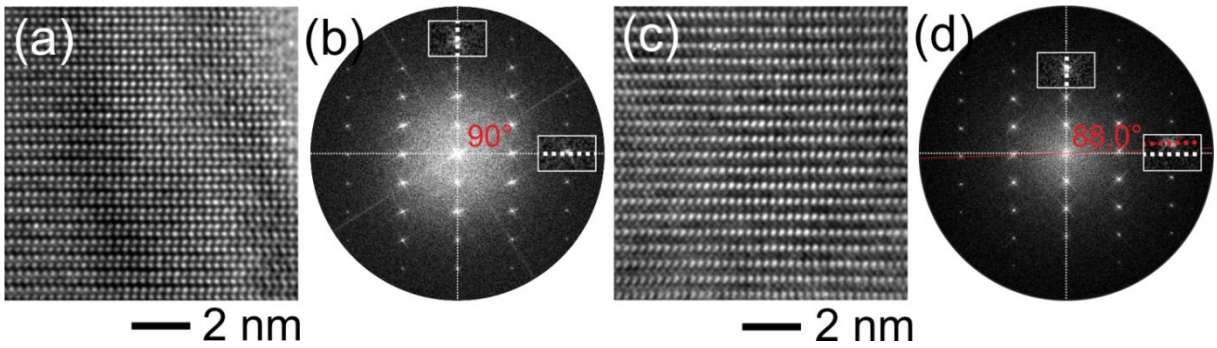

Figure 5.7: Local high resolution TEM study with corresponding FFT images on PEC etched samples showing areas with apparently no lattice distortion β = 90° a-b) and a stronger distortion of the crystal metrics β = 88° c-d) in GaN films.

Indeed, structural distortions of β ≈ 89.05° have been described by Rao *et al*. as triclinic lattice distortion in wurtzite-type gallium nitride films grown by metal organic vapor-phase epitaxy on sapphire substrates.[234] There, a triclinic distortion was investigated by electron diffraction studies using convergent beam electron diffraction (CBED) and SAED near the film/substrate interface. The large misfit strain during crystal growth was reasoned to be the origin for the lattice distortion and was observed to relax within 1 µm distance from the substrate interface.
In case of rapid growth conditions of a few hundred µm/h present in HVPE it seems apparent that the large film stresses due to the initial substrate/film misfit strain can introduce lattice distortions which are then unable to relax in the limited amount of time. Since the lamellae

observed in TEM only represent a small fraction of the entire sample volume, high-resolution X-ray diffraction has been applied as a complimentary technique to TEM to probe a larger volume of the sample. This offers quantitative information about the average bulk-like 3D lattice structure and residual strains in the sample with very high resolution.

The experimental setup of the high-resolution X-ray diffraction experiments is depicted schematically in Figure 5.8 a) displaying the 2*theta (2θ) measurement geometry. The β-distortion observed in the TEM was tracked down by measuring the angle omega ω, which is the equivalent deviation parameter between the *c*-axis and the surface normal, ω = 90° - β. Here, the two examples of a single crystal with $P6_3mc$ wurtzite-type structure with perfect ω = 0 geometry and a lattice distortion ω > 0 are presented. This offset angle ω is measured by performing rocking scans at several azimuthal positions achieved by a rotation (phi φ) horizontal to the surface normal and monitoring the $Q(\theta)$-shift in the maximum peak intensity of the GaN (004) Bragg reflection, Q being the reciprocal lattice vector.

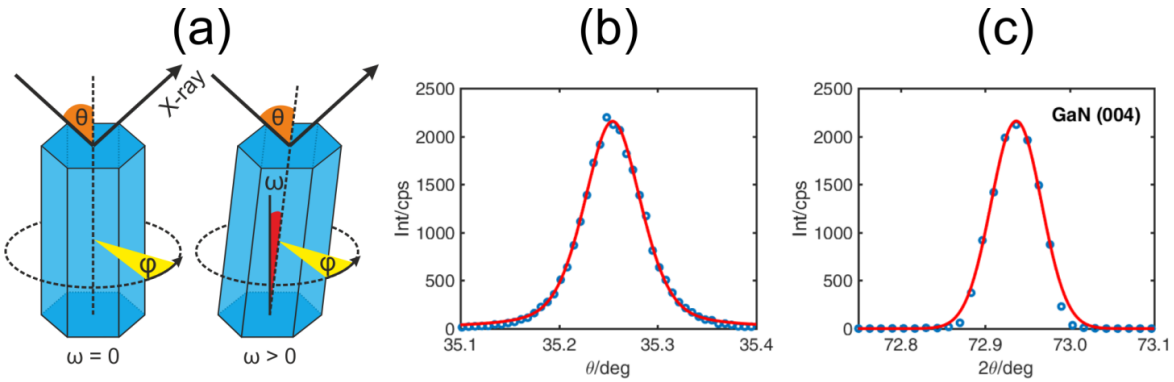

Figure 5.8: a) HRXRD measurement geometry for a hexagonal crystal first showing no triclinic lattice distortion ω = 90°-β = 0 and second with ω > 0 measured in dependence of the sample horizontal rotation angle phi φ in a 2*theta, 2θ, geometry. The single crystalline structure of the as-grown GaN crystal is demonstrated by representative rocking curves b) and Bragg scans c) of the (004) reflection, where lattice strains can be derived from peak fits (red curve).

The position of the GaN (004) Bragg reflection was determined to be 2θ = 72.935° and Q = 4.85 Å^{-1}, in agreement with the wurtzite-type structure[235] (a = 3.190Å, c = 5.189Å). The respective rocking curve, performed for optimizing the incident angle θ and the 2θ-scan of the GaN (004) reflection are shown in Figure 5.8 b) and Figure 5.8 c), respectively. The blue dotted data points were fitted by Voigt-profiles (red curve) with the contribution (Gauss 40%, Lorentzian 60%) to obtain the peak position and full-width at half maxima which are used to derive lattice strains along the crystal *c*-axis.

For the analysis of the deviation parameter ω representing the triclinic lattice distortion, rocking curves were performed at nine azimuthal rotation angles φ in steps of 30° for the as-grown and

etched samples and were evaluated for their intensity maxima peak position as presented in Figure 5.9 a). Both samples show coinciding angular dependence, which is apparent by the superposition of the measurement curves aligning the $\omega = 0$ data points. The deviation of ω with respect to the in-plane orientation is observed to oscillate between -1° and 1° over the measured range having their maxima separated by a 180° rotation in φ which indicates similar results to the lattice distortion $\beta = 89°$ observed with TEM. The respective values of the distortion measured for the as-grown and etched sample at $\varphi = 30°$ and $\varphi = 210°$ are $\omega_{as\text{-}grown} = 0.9585°$ and $\omega_{etched} = 0.9917°$, and $\omega_{as\text{-}grown} = -1.0356°$ and $\omega_{etched} = -1.0360°$, respectively. Therefore an average distortion of $\omega_{as\text{-}grown} = 0.9971°$ and $\omega_{etched} = 1.0139°$ can be derived for both samples, indeed indicating a structural phenomenon on the larger length scale, which can be described by a triclinic lattice distortion.

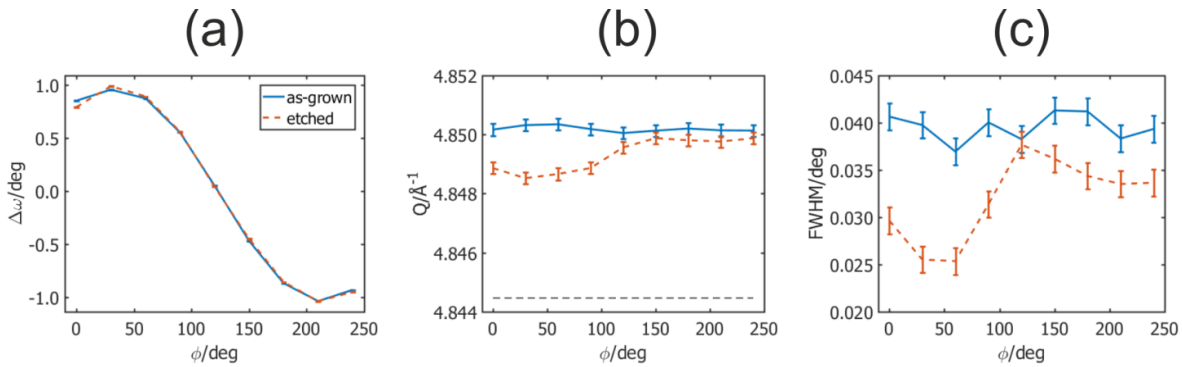

Figure 5.9: a) Variation of the deviation parameter omega $\Delta\omega$ in dependence of the rotation angle phi φ from HRXRD. The measurements are showing congruent behavior in the boundaries of -1° to 1° for the as-grown and etched samples. b) Compressive strain $\varepsilon_{as\text{-}grown} = -0.118\%$ and $\varepsilon_{etched} = -0.101\%$ with respect to the reference[235] (black dashed line). c) Full-width at half maximum values of fitted Bragg scans in dependence of the azimuthal rotation. The slightly smaller FHWM width of the etched sample indicates larger coherently diffracted domains which could be attributed to the reduction of defect density after etching.

Furthermore, lattice strain can be derived from the total reflection position $Q_{(004)}$ and can be resolved with very high precision of up to 10^{-5}, which provides a significant advantage over other methods of evaluating strain. The variation in the $Q_{(004)}$ value is plotted in Figure 5.9 b) for the as-grown and etched GaN samples in dependence of the rotation angle φ. The average Q values have been determined to $Q_{as\text{-}grown} = 4.8502 \pm 0.0001$ Å^{-1} and $Q_{etched} = 4.8493 \pm 0.0006$ Å^{-1} ($c_{as\text{-}grown} = 5.1818 \pm 0.0001$ Å and $c_{etched} = 5.1828 \pm 0.0006$ Å) which translates into a compressive strain of $\varepsilon_{as\text{-}grown} = -0.118\%$ and $\varepsilon_{etched} = -0.101\%$ with respect to the literature value of $Q_{(004)} = 4.8444$ Å^{-1} ($c_{(004)} = 5.189$ Å).[37] The presence of residual compressive stress in free standing HVPE grown bulk GaN substrates has been observed before by various techniques such as micro-reflectance spectroscopy,[236,237] HRXRD and

photoluminescence spectroscopy.[238] However, the amount of residual compressive strain on the *c*-axis reported in these studies is significantly smaller (by one order of magnitude) compared to this work. This discrepancy could possibly be explained by the triclinic lattice distortion observed in this work, reasoned by different crystal growth parameters, crystal thickness and the choice of substrate or intermediate layers to reduce interfacial stresses. Furthermore, electron diffraction experiments by Rao et. al. reporting about the triclinic distortion in 4.5 µm thick MOVPE GaN films on sapphire showed a tensile strained *c* lattice parameter by about 0.2%, which is at least in the same order of magnitude.[234] For the bulk-like GaN films investigated in this work, the determination of strain from ED pattern, however, seems not to be representative since the information gathered only pictures the first few micrometers and with lower strain precision of just 10^{-3}.

To conclude, next to a monoclinic or triclinic lattice distortion, the amount of residual strain in the HVPE grown crystal was determined by HRXRD to be compressive in *c*-axis direction by about 0.1% for both, the as-grown and etched sample, which slightly tends to relax for the latter. In Figure 5.9 c) the FWHM calculated from the Voigt fits of the Bragg scans is plotted over the azimuthal rotation φ. The mean value of the FWHM is 0.0395±0.0015° for the as-grown and 0.0319±0.0044° for the etched GaN. From the FWHM the size of the coherently diffracting domains can be derived which serves as an indicator for the defect density.[239,240] For the as-grown and etched GaN the mean domain sizes are determined to 111.7±4.3 nm and 140.7±20.8 nm, respectively. In conclusion, the etching process slightly increases the sizes of the coherently diffracting domains, which can be attributed to a reduction in the defect density after etching as evidenced from TEM experiments.

5.2.6 Conclusions

The results of this study demonstrate that the complex 3D nanoarchitectures disclosed by photoelectrochemical etching in HVPE-grown bulk GaN single crystals originate from the spatially modulated electrical conductivity and they prove not to be related to variations of the crystal structure. According to the analysis of the photoluminescence in as-grown and PEC etched samples, the amplitude of spatial modulation of the electrical conductivity in the HVPE-grown GaN is of at least 60%. On the other hand, combining TEM and HRXRD techniques provides a powerful methodological approach to gather structural information on the nanometer to millimeter length scale with high precision. These investigations reveal a distortion of the $P6_3mc$ wurtzite-type structure, indicated by the deviation from the hexagonal symmetry. This deviation varies from 0° to 2° at the nanoscale, while it is of around 1° when averaged over the

entire crystal. Furthermore, compressive lattice strain along the crystal *c*-axis derived from peak fits of rocking curves of the (004) reflection is found to be in the order of -0.1% and to be slightly relaxed in PEC-etched samples.

5.3 Visualizing Intrinsic 3D-Strain Distribution in Gold Coated ZnO Microstructures by Bragg Coherent X-ray Diffraction Imaging and Transmission Electron Microscopy with Respect to Piezotronic Applications

5.3.1 Publication 3 Overview

The goal of this study was to visualize and understand the strain distribution in gold coated ZnO rods, a model system for an Schottky contact as introduced in section 2.2. Studying ZnO can further contribute to an enhanced understanding of the piezotronic effect (section 2.3).
For this, Au coated ZnO rods, mounted in the SEFiR design, see section 4.1, were investigated by CXDI. The ZnO rods were similar to the ones used before in section 5.1, but the rod size had to be close to 1 µm to enable CXDI experiments, causing the sample mounting process to be even more challenging than before. Bragg CXDI, section 2.8, was employed to image the shape and strain distribution of the ZnO crystal in three dimensions. These measurements were performed at beamline ID-34-c at the Advanced Photon Source, located at the Argonne National Laboratory near Chicago. Complementary, the strain distribution at a ZnO/Au interface was visualized by geometric phase analysis from TEM micrographs.
This section is a manuscript published in Advanced Electronic Materials, analyzing the strain distribution in gold coated ZnO microstructures, visualized by CXDI and TEM and link these findings to previous conducted simulations of piezotronic devices.[241]
(https://doi.org/10.1002/aelm.202100546)

Visualizing Intrinsic 3D-Strain Distribution in Gold Coated ZnO Microstructures by Bragg Coherent X-ray Diffraction Imaging and Transmission Electron Microscopy with Respect to Piezotronic Applications

Philipp Jordt, Niklas Wolff, Stjepan B. Hrkac, Sindu Shree, Di Wang, Ross J. Harder, Christian Kübel, Rainer Adelung, Oleg G. Shpyrko, Olaf M. Magnussen, Lorenz Kienle, Bridget M. Murphy

P. Jordt, Prof. Dr. O. M. Magnussen, Dr. B. M. Murphy
Institute of Experimental and Applied Physics, Kiel University, Leibnizstr. 19, 24118 Kiel, Germany
Dr. B. M. Murphy, Prof. Dr. O. M. Magnussen

Ruprecht-Haensel Laboratory, Kiel University, 24118 Kiel, Germany
Dr. N. Wolff, Dr. S. Shree, Prof. Dr. R. Adelung, Prof. Dr. L. Kienle
Institute of Material Sciences, Kiel University, Kaiserstr. 2, 24143 Kiel, Germany
Dr. S. B. Hrkac, Prof. Dr. O. G. Shpyrko
Department of Physics, University of California San Diego, La Jolla, CA 92093, USA
Dr. R. J. Harder
X-ray Sciences Division, Argonne National Laboratory, Lemont, Illinois 60439, USA
Dr. D. Wang, Prof. Dr. C. Kübel
Karlsruhe Institute of Technology (KIT) & Karlsruhe Nano Micro Facility (KNMF), 76344 Eggenstein-Leopoldshafen, Germany
Prof. Dr. C. Kübel
Department of Materials & Earth Sciences, Technical University Darmstadt, 64287 Darmstadt, Germany

5.3.2 ABSTRACT

Novel devices ranging from bio magnetic field sensors to energy harvesting nano machines utilize the piezotronic effect. For optimal function, understanding the interaction of electrical and strain phenomena within the semiconductor crystal is necessary. Here, we present studies of a model piezotronic system, consisting of a ZnO microrod coated by a thin layer of gold, which forms a Schottky contact with the piezoelectric ZnO material. Coherent X-ray diffraction imaging (CXDI) and transmission electron microscopy (TEM) are used to visualize the structure and strain distribution, showing that the ZnO microrod exhibits strains of multiple origins in the bulk and at the interface. Strain values of -6×10^{-4} have been measured by CXDI at the ZnO/Au interface. The origin is shown to be a combination of an interface strain, possibly caused by the Schottky contact formation, and distinct, localized electrical fields inside the crystal which are assigned to electron depletion and screening in a bent ZnO/Au piezotronic rod. These findings will contribute to sensor development and to a better understanding of piezotronic applications.

5.3.3 INTRODUCTION

In the future, emerging technologies with semiconductor-based smart devices may include artificial skin,[242] synapsis,[20] energy harvesting [19,243] and magnetoelectric applications that rely on composites of piezoelectric and magnetostrictive materials.[160,162,244] A specific example for potential medical application is a small, highly sensitive magnetoelectric sensor capable to measure the low frequency magnetic fields originating in the human body.[163] As

these fields are really small in the pT to fT range, a promising approach to increase the sensitivity might be to exploit the piezotronic effect as a source of intrinsic signal amplification.[21,52,112,245] The piezotronic effect is found in piezoelectric semiconductors and combines the piezoelectric effect with the electric behavior of a Schottky contact at a semiconductor/metal interface.[29,39,246] External stress and crystal quality induce a strong electric response in piezoelectric semiconductors, changing the height of the Schottky barrier and the depletion width.[23,159] By the addition of a magnetostrictive material, the variation of external magnetoelastic stress imposed on the semiconductor material could further tune the conductivity across the Schottky barrier for potential sensor applications.

The majority of studies on the piezotronic effect concentrate on electrical characterization and employ predominantly ZnO, which is a well-known piezoelectric material with wurtzite-type crystal structure. These studies emphasized the direct influence of external mechanical stress on the Schottky barrier height in ZnO bulk [23] and microstructures [53,247] when stress is applied along the ZnO *c*-axis. Choosing the direction of applied stress can induce either tensile or compressive stresses which increase or decrease the Schottky barrier height accordingly.[49]

Additionally, it was shown that strain and an associated *E*-field can be induced by bending free-standing ZnO micro rods using an atomic force microscope (AFM).[14] The resulting change in conductivity was assigned to formation of a depletion region, thus shrinking the conduction channel size inside the rod. Combined analytical calculations and finite element method simulations, confirm that bending of ZnO wires lead to a negative potential at the compressed side and a positive potential on the relaxed side of the rod.[248] Further calculations considering n-type ZnO, indicate that the positive potential inside the ZnO rod is partly or fully screened, depending on the donor electron concentration.[55]

Previous studies by the authors already showed a complex strain behavior in ZnO micro rods.[62,152] FeCoSiB coated ZnO rods were investigated in detail by scanning nano X-ray diffraction (XRD). The strain was found to be non-uniform, with an asymmetric strain variation at the rod edges and a strong dependence of the strain profile on the aspect ratio. Two strain components were observed, an intrinsic strain due to the coating and an additional reactive strain that could be controlled by applying an external magnetic field to the magnetostrictive coating. Depending on the field direction, the total strain could be increased or reduced.

A powerful method for visualizing the shape and strain of nanostructures in three dimensions is CXDI.[28,90] With CXDI it is possible to visualize single grains, defects and strain with high precision inside functional materials [249,250] by reconstructing the complex amplitude and phase in small nanometer to micrometer sized single crystal objects.[89,251,252] Due to its high

crystallinity and simplicity of production, ZnO nanocrystals and rods have been a common subject.[89,253,254] CXDI was further employed to visualize the strain field inside other nanoparticles including lead,[88] polycrystalline particles in thin gold films [249] and batteries [250,255].

In this study, complementary techniques of reciprocal and real space analyses by means of Bragg CXDI and geometric phase analysis (GPA) performed on TEM micrographs were used to visualize the 3D and the estimated relative local strain distribution in piezotronic ZnO/Au microstructures in order to understand how it affects the Schottky barrier and related electrical properties.

CXDI provides a spatial resolution of 5-50 nm and a very high strain resolution of 10^{-5}. Complimentary, modern transmission electron microscopes offer a high spatial resolution better than 100 pm but its analytical spatial resolution to lattice strains is usually limited by the radius of a virtual aperture in GPA to 1-2 nm or the electron probe diameter, e.g. 2-6 nm in diffraction-based strain measurement techniques. Compared to CXDI, these techniques including GPA have a relatively poor strain resolution on the order of 2×10^{-3} in strain maps.[256] By the combination of Synchrotron- and TEM-based techniques, the inherent strain distribution can be visualized over a wide range of length scales. ZnO is ideal for such studies, because of its high crystallinity. Further information on the techniques and the sample preparation are given in the experimental section.

5.3.4 Reconstructed Strain Distribution from Coherent X-ray Diffraction Imaging

For the CXDI experiment one of the $\{10\bar{1}0\}$ ZnO Bragg reflections of a gold coated ZnO rod was investigated. The rod was illuminated with a coherent X-ray beam using the geometry shown in Figure 5.10 a). The recorded diffraction pattern around the $\{10\bar{1}0\}$ Bragg reflection in the q_x/q_z plane is shown in Figure 5.10 b), averaged over a 0.09 $Å^{-1}$ wide range in the q_y direction. The Bragg reflection has a full width at half maximum (FWHM) in q_x of $7.0 \times 10^{-4} \pm 0.1 \times 10^{-4}$ $Å^{-1}$, and a mean crystalline domain size of 927 ± 25 nm is determined. Furthermore, hexagonal symmetry and fringes from coherent scattering are clearly visible. From the fringe spacing a mean rod diameter of 940 ± 19 nm was calculated. This is in the same range as the calculated crystallite size, indicating an excellent crystal quality. From the information included in the coherent diffraction patterns of the ZnO rod, the complex amplitude of the rod's electron density was reconstructed by performing iterative phase retrieval.[99,257]

Data were collected at a number of positions along the rod in the *y* direction corresponding to the *c* axis as shown in Figure 5.10 a) and successfully reconstructed.

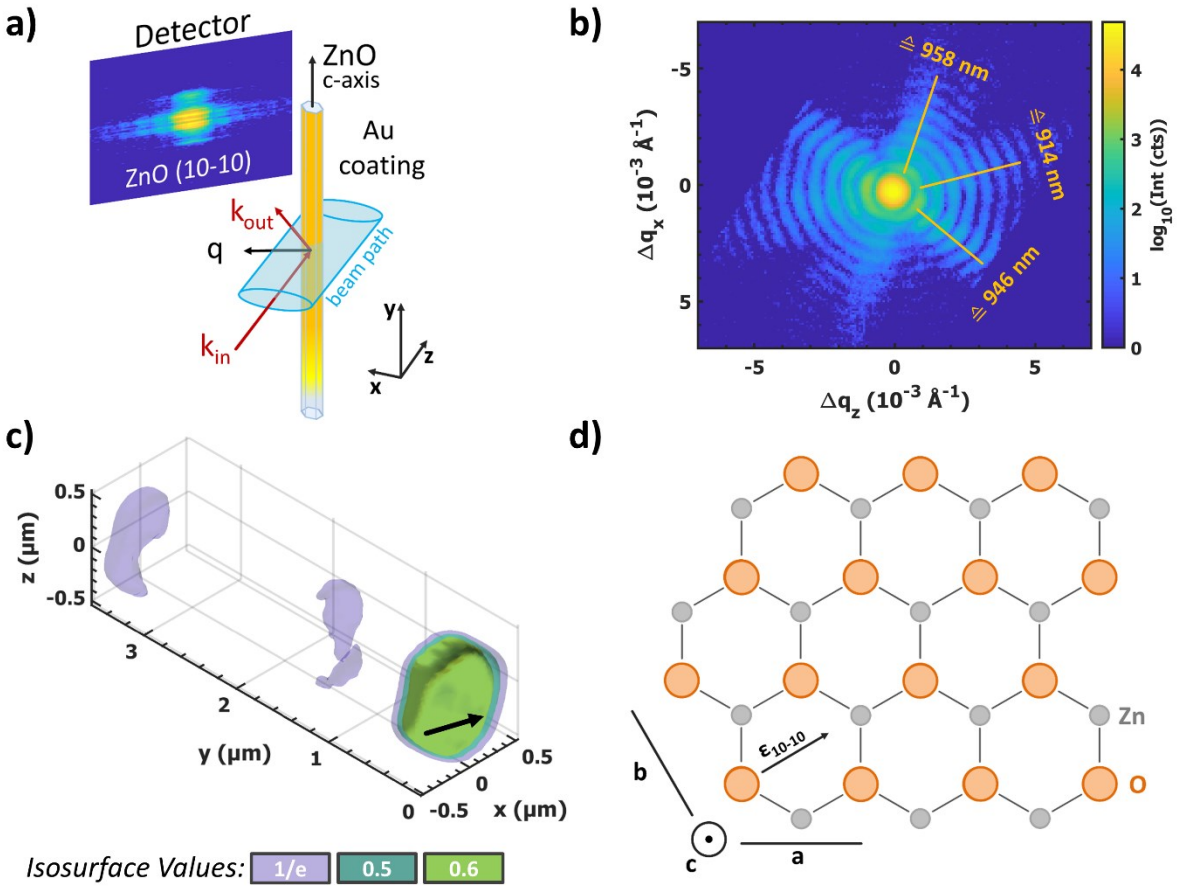

Figure 5.10: a) Sketch of the CXDI experiment for strain investigations of a gold coated ZnO rod. The scattering vector *q* of the $\{10\bar{1}0\}$ ZnO Bragg reflection, the *c*-axis of the ZnO and the path of the incident beam are indicated and a coordinate system for the further analysis is introduced. The detector image is uncorrected but is approximately aligned in the q_y and q_x directions. b) Diffraction pattern shown on log scale in the q_x/q_z plane. The rod diameter calculated from the fringe spacing is indicated for three directions within the ZnO (0001) plane. c) Displaying the reconstructed shape of the rod with multiple isosurfaces of 0.37 (1/e), 0.5 and 0.6. The direction of the scattering vector *q* is indicated by the black arrow. d) ZnO structure in the (0001) plane[35] and the measured strain component $\varepsilon_{10\bar{1}0}$.

These positions display a very similar behavior. Here, we focus on the data for one position to avoid repetition, as it is representative for all measured positions. The reconstructed electron density amplitude is displayed in Figure 5.10 c). Showing the corresponding reconstructed shape for three different isosurfaces with values 0.37 (1/e), 0.5 and 0.6.[190] Each isosurface connects data points of the same value inside a volume. For the further discussion only the front section between *y* 0 and 0.6 µm with isosurface 1/e will be considered.

In addition, CXDI measurements of the $\{10\bar{1}0\}$ Bragg reflection provide the strain component $\varepsilon_{10\text{-}10}$ along the corresponding scattering vector (indicated in Figure 5.10 c) by a black arrow).

This strain component describes g lattice deformation in the (0001) plane of the wurtzite-type structure (Figure 5.10 d). The strain distribution within the rod is calculated as the gradient of the displacement field, which is the reconstructed phase divided by the scattering vector (detailed description is given in the supplementary information).[82] This reconstructed phase contains information on the relative displacements of the atoms within the crystal, i.e., variations in strain. The Bragg reflection with maximum intensity on the detector was found at $q_{10\text{-}10} = 2.2319 \pm 0.0001$ Å^{-1}. A theoretical value for Zinc oxide is $q_{10\text{-}10} = 2.2324$ Å^{-1} corresponding to a lattice parameter of 2.8146 Å [35]. Comparing these values indicates a compressive global strain of 2.2×10^{-4} in the rod, relative to the theoretical value. To visualize the local strain, the reconstructed strain distribution in the sample is considered. A mean strain for the reconstructed volume is calculated by averaging the individual strain from each voxel in all three dimensions and found to be 5.8×10^{-5}. This is subtracted from the reconstructed strain at each point to give the relative strain distribution. The strain present in the sample is a combination of the average, global strain and the relative, reconstructed strain. For refraction corrected strain the phase shift due to the refractive index and the varying path lengths through the rod is considered [258,259] (procedure given in the SI). Furthermore, to align the scattering vector (black arrow) with the *x* axis in Figure 5.10 c), the reconstruction is rotated counterclockwise by 14.17 ° (Bragg angle). *X* and *Z* axis are the respective rotated positions.

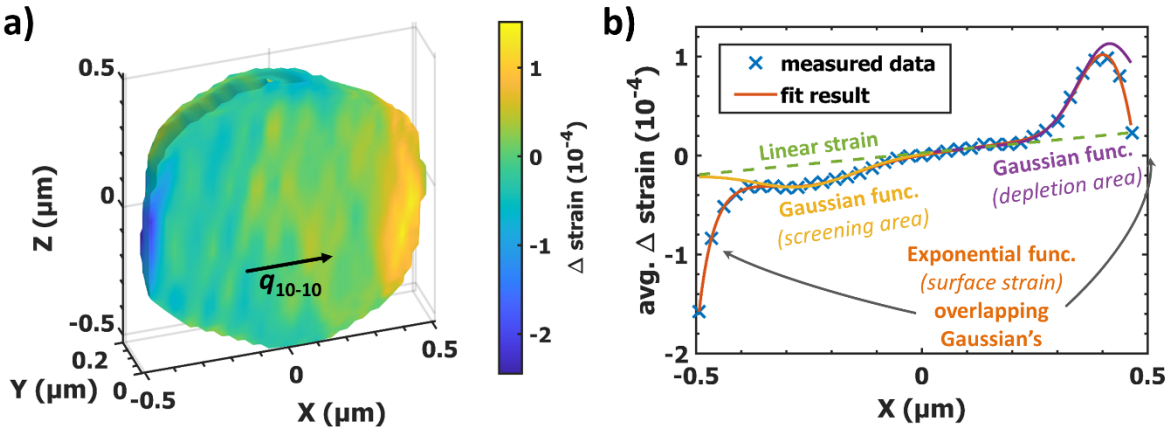

Figure 5.11: a) Reconstructed shape and refraction corrected strain of the ZnO rod (Isosurface 1/e) from CXDI. To illustrate the strain distribution in the *X*/*Z*-plane the reconstructed volume was cut in half in the *Y*-direction, with the front surface corresponding to a cross section through the center. The black arrow indicates the direction of the scattering vector $q_{10\text{-}10}$. b) Average strain along *Z* (blue crosses) as a function of *X*, from a), shown with the fit result of the model function (solid red line), the two Gaussian components of the model (purple and yellow solid line) and the fitted linear component (green dashed line).

The three-dimensional distribution of the reconstructed, refraction corrected, relative strain in a rod section of 0.4 µm × 1 µm × 1 µm is shown in Figure 5.11 a). For better accessibility of the strain distribution inside the rod, the reconstructed volume was cut in half along the *Y* axis. In agreement with literature, the interface exhibits a remarkable large strain compared to the bulk of the sample.[152] A strong compressive strain -2.2×10^{-4} is visible close to the left ZnO/Au interface, subsequently an increase of the strain is observed inside the rod. Towards the right interface a strong tensile strain 1.3×10^{-4} is observed. From this strain distribution the average of the strain in *Z* direction is calculated as a function of *X* and shown in Figure 5.11 b). The average strain (blue crosses) has a linear behavior near the sample center at *X* ~ 0 µm to 0.2 µm. Closer to the edges the strain changes drastically. Towards the right side (beginning at *X* ~ 0.25 µm) the strain increases over a range of 150 nm, before it settles and decreases closer towards the interface. On the left (*X* ~ -0.1 µm to -0.4 µm), the strain decreases slightly and settles over roughly 300 nm, then within the last ~ 100 nm towards the interface the strain decreases further.

5.3.4.1 Strain Modelling

To quantify the strain a model was developed, consisting of a minimal constant offset, a linear component due to rod bending. Further, two exponential functions at the edges account for interface strain as previously applied[152] and two Gaussian functions are assigned to bulk strain further inside the crystal to consider potential screening and depletion of electrons as motivated by previous simulations[55,248], where rod bending of a ZnO wire was shown to cause screening and depletion effects at opposing rod edges. The simulated electrical potential is linked to an electric field and causes a strain change due to the piezoelectric properties of ZnO. This model was fitted to the average strain data in Figure 5.11 c).

$$\varepsilon_{avg}(X) = \varepsilon_{B,CDI,l}\, exp\left(\frac{-\left(X-\mu_{B.CDI,l}\right)^2}{2\,{\sigma_{B,CDI,l}}^2}\right) + \varepsilon_{B,CDI,r}\, exp\left(\frac{-\left(X-\mu_{B,CDI,r}\right)^2}{2\,{\sigma_{B,CDI,r}}^2}\right)$$

$$+\varepsilon_{I,CDI,l}\, exp\left(\frac{-(X-x_1)}{\sigma_{I,CDI,l}}\right) + \varepsilon_{I,CDI,r} exp\left(\frac{X-x_n}{\sigma_{I,CDI,r}}\right) + \frac{\varepsilon_{bend}}{x_n-x_1}X + \varepsilon_{const} \qquad (5.2)$$

X is the position across the sample, with its first value x_1 and last value x_n inside the reconstructed volume. $\varepsilon_{B,CDI}$, $\sigma_{B,CDI}$ and $\mu_{B,CDI}$ are the fitted bulk strain, sigma and position of the Gaussian functions, respectively. The exponential functions are fixed to the opposing edges of the rod and have values for the interface strain $\varepsilon_{I,CDI}$ and sigma $\sigma_{I,CDI}$. The subscript *l* and *r* in the parameters of the exponential and Gaussian functions denote the position left and right relative to the rod center in Figure 5.11 a). Furthermore, there is a linear strain ε_{bend} and a

constant offset ε_{const}. The fitted $\sigma_{I,CDI}$ and $\sigma_{B,CDI}$ values can be interpreted as a measure for the spatial size of the effect, i.e., the penetration depth of the surface strain and the spatial size of the bulk strain. The red solid line in Figure 5.11 b) shows the fit result of the whole model function, for a more specific look the two Gaussian functions (purple and yellow lines) as along with the linear component (green dashed line) are shown. The exponential functions at the edges are implicitly included as the difference between the overall fit result and the Gaussian functions. See Table 5.2 for all values extracted from the fit model and the supplementary information for further details on the fitting procedure.

Table 5.2: it results of the model (equation (1)) for the strain ε, spatial position μ and size σ for bulk ($_{B,CDI}$) and interface ($_{I,CDI}$) strain components from CXDI reconstruction. The E field was calculated from the fitted $\varepsilon_{B,CDI}$ values. For comparison, the strain $\varepsilon_{I,TEM}$ distinguished by TEM and the measured surface strain ε_{ref} from a nano XRD experiment on FeCoSiB coated ZnO rods was included. Furthermore, strain from rod bending ε_{bend} and constant offset ε_{const} are shown.

pos.	$\sigma_{B,CDI}$ [nm]	$\mu_{B,CDI}$ [nm]	$\varepsilon_{B,CDI}$ [10^{-4}]	E [10^6 V/m]	$\sigma_{I,CDI}$ [nm]	$\varepsilon_{I,CDI}$ [10^{-4}]	ε_{ref}[a)] [10^{-4}]	$\varepsilon_{I,TEM}$ [10^{-3}]	ε_{bend} [10^{-4}]	ε_{const} [10^{-4}]
left	117.6 ±6.4	233.9 ±7.7	-0.22 ±0.02	4.37 ±0.22	34.9 ±1.3	-1.36 ±0.03	-4.0 ±0.5	-17.5 ±2.5	0.44 ±0.02	0.019 ±0.01
right	69.2 ±1.4	45.8 ±1.6	1.03 ±0.02	-20.27 ±0.28	43.0 ±2.3	-0.83 ±0.03				

[a)] S. B. Hrkac *et.al.*, *ACS Appl. Mater. Interfaces* 2017, *9*, 25571.

The linear strain from the model indicates a tensile strain along the ZnO *c*-axis on the left and a compressive strain at the right edge, possibly due to the rod being bent towards the right side (radius = 6.8 mm) and may be the result of an intrinsic bending from the growth or due to the coating process. The linear behavior is overlapped by two Gaussian functions modelling the bulk strain, which show a differing but consistent behavior. The Gaussian strain component on the right is of greater magnitude, smaller width and opposite sign compared to the one on the left. This non-symmetric distributions may be related to a potential screening and depletion of electrons in a bent rod as previously simulated[55,248]. As pointed out in these publications, bending of a ZnO wire leads to a change in the potential. Considering the local potential distribution, the negative potential on one edge of the wire causes a depletion of electrons, while the positive potential on the opposite side is screened at least partially by free electrons resulting in a non-symmetric potential distribution as present in n-type semiconductor. The related electric field leads to a measurable bulk strain in the piezoelectric rod. This bulk strain is overlapped by a symmetric strain towards the interface. This strain may be the result of the Schottky barrier formation at the ZnO/Au interface due to the inverse piezoelectric effect[30],

further details on the speculative mechanism are given in section four. For comparison, the typical donor concentration in n-type ZnO is $\sim 10^{16\text{-}18}\,\mathrm{cm}^{-3}$.[46,197] Together with the built-in potential $\Phi_i \sim 0.5\,\mathrm{V}$ [39,197] a Schottky barrier depletion width $W_d \approx 21.7\text{-}217.4$ nm is estimated.[39] This is in agreement with the mean width $\sigma_{I,CDI} = 39.0 \pm 6.4$ nm from Table 5.2, which corresponds to a calculated donor concentration of $3.1 \times 10^{17}\,\mathrm{cm}^{-3}$, details on the calculation are given in the supplementary information.

5.3.5 High-resolution TEM strain analysis of ZnO/Au interface

The (sub-)microscale CXDI strain analysis is complemented by a local strain analysis from a ZnO/Au interface with nanometer resolution using aberration-corrected high-resolution transmission electron microscopy (HRTEM) in combination with GPA on a comparable model system. Knowing the local strain distribution at the metal-semiconductor interface is essential for tuning the interfacial carrier transport properties across the Schottky contact as local strain can lower the barrier effectively.[260] The high spatial resolution of TEM enables to study interfacial layers or defects at or close to the interfaces, or electronically speaking the space-charge-region, as these defects provide additional electronic states in the bandgap and act as unwanted disturbance of the strain distribution.[261]

This model system consists of Au nanocrystals grown onto the $\{10\bar{1}0\}$ facets of a ZnO microstructure as depicted in the high-angle annular darkfield image recorded in scanning TEM mode of Figure 5.12 a) and the supporting sketch. The cross-section specimens were prepared such that the ZnO *c*-axis was aligned to the viewing direction. For some of the analyzed Au crystals, this alignment allowed a direct view onto the ZnO/Au interface without superposition artifacts. These experimental conditions allowed to observe potential systematic orientation relationships and enabled the analysis of local lattice strains. Note that a certain specimen thickness was preserved to minimize potential strain relaxation effects in a thin foil.[262] Selected area electron diffraction (SAED) experiments and fast Fourier transformation (FFT) of HRTEM micrographs display the [0001] zone axis pattern for the ZnO crystal and indicate certain in-plane correlations between the components, which can be described as ZnO$(11\bar{2}0)$/Au(111) in some regions and ZnO$(11\bar{2}0)$/Au(220) in other ones, based on the SAED pattern in Figure 5.12 b). The HRTEM micrograph (Figure 5.12 c) does not display a sharp interface but shows a slight misorientation between the incoherent lattices of ZnO and Au. The HRTEM micrograph and corresponding FFT display the hexagonal motif viewing on the [0001] ZnO zone axis. Lattice deformations of this hexagonal motif in real space will result in broader intensities in reciprocal space and can be mapped out with respect to a presumably undistorted reference

lattice within the micrograph (defect free area far away from the interface) by the geometric phase analysis method.[263] The highlighted in-plane and out-of-plane reflections in Figure 5.12 d) were selected by virtual apertures limiting the spatial resolution of the strain distribution to 1.5 nm.

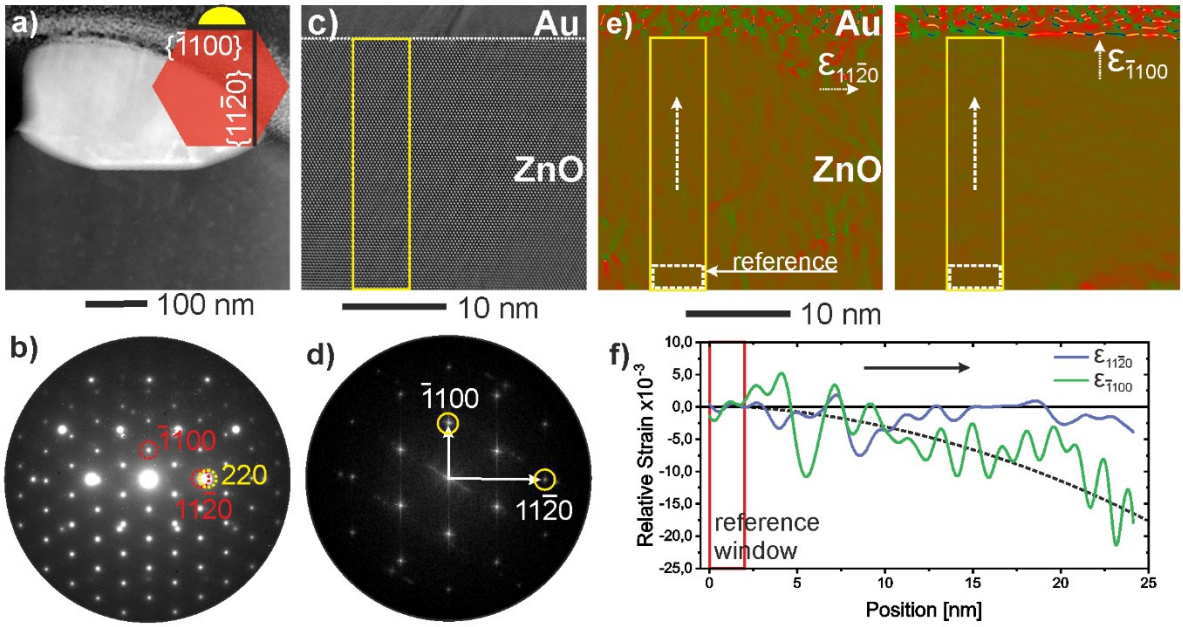

Figure 5.12: a) HAADF STEM image showing the cross-section of a ZnO/Au nanostructure simplified in the accompanying sketch. b) SAED pattern showing reflections of [0001] ZnO and [111] Au with ZnO(11$\bar{2}$0)/Au(220) in-plane orientation relationship. c) HRTEM micrograph showing the ZnO/Au interface (dashed line) d) FFT of the HRTEM micrograph in c) showing virtual apertures placed on in-plane and out-of-plane reflections of the ZnO component used for GPA. e) Strain distribution maps of the in-plane ($\varepsilon_{11\bar{2}0}$) and out-of-plane ($\varepsilon_{\bar{1}100}$) components of the symmetric strain tensor. The yellow boxes indicate the region for taking integrated strain profiles in relation to the selected reference lattice (white boxes). f) Estimated relative strain profiles showing increasing compressive strain in the out-of-plane component ($\varepsilon_{\bar{1}100}$) approaching the ZnO/Au interface. The dashed line serves as guide to the eye.

The relative local strain distribution in the ZnO lattice is presented in Figure 5.12 e) showing the in-plane ($\varepsilon_{11\bar{2}0}$) and out-of-plane ($\varepsilon_{\bar{1}100}$) components of the symmetric strain tensor within an experimental resolution of ~5 × 10^{-3}, which is estimated from the oscillation amplitudes being an artifact of defining the spatial resolution by placing the virtual apertures around the reflections in the FFT. Please note that the non-uniform strain distribution in the Au component can be considered as artifact of the method as well, since GPA only maps the deformation vectors in coherent lattices defined by the virtual apertures and the reference lattice. The larger changes in strain contrast resolved in the right part of the $\varepsilon_{11\bar{2}0}$ map within the ZnO component are possibly connected to lattice imperfections exhibiting larger lattice deformation strains.

To concentrate on the effect size of an interfacial strain on a defect-free lattice, the magnitude of relative strain inside ZnO is measured by integrating across regions (yellow frames) exhibiting a homogenous contrast, hence excluding the influence of larger strain distributions around lattice defects.

The examined profiles (Figure 5.12 f) exhibit an increasing relative compressive strain towards the interface for the out-of-plane component $\varepsilon_{\bar{1}100}$ reaching a value of -17.5 ± 2.5 × 10^{-3} and is distributed rather monotonously around zero strain for the in-plane component $\varepsilon_{11\bar{2}0}$.

In conclusion, despite interfacial layers, which are often chemically or structurally modified prior to Au-film deposition, an increasing compressive ZnO lattice structure is observed close to the ZnO/Au interface within the analytic capabilities of HRTEM and GPA.

This interfacial strain which was measured across 25 nm and with a lateral resolution of 1.5 nm increases towards the interface up to a value of $\varepsilon_{\bar{1}100,TEM}$ = -17.5 ± 2.5 × 10^{-3} and is compared to the CXDI results of an interface strain reaching up to $\varepsilon_{I,CDI}$ = -1.4 × 10^{-4} within a spatial resolution of 27.4 nm. The strain difference of two orders of magnitude is possibly due to the individual strengths in spatial and reciprocal resolution of both techniques. TEM detects a higher strain in a very localized spatial region. In contrast CXDI shows a lower strain but distributed over a larger spatial region. Extrapolating the CXDI strain towards the interface provides qualitative agreement. The discrepancy between the two results cannot be attributed completely to the differences in resolution of the two techniques. The different methodology of establishing ZnO/Au contacts for CXDI and TEM measurements might also have an impact on absolute strain values. For the CXDI experiment, an Au layer was deposited by thermal evaporation establishing a powder like structure, while the Au contact for TEM experiments has been prepared by sputtering a thin Au film and subsequent annealing to establish small Au crystalline droplets on the ZnO surface. The higher crystallinity of these droplets and better contact quality at the Au/ZnO interface might impose an increased magnitude of strain on the ZnO crystal. Concluding that, while both methods show a similar trend in this case, we are at the limit of their accuracy. Thus, a combination of TEM and CXDI highlights the fact that a strong, highly localized compressive strain is present at the ZnO/Au interface.

5.3.6 Electric Field E_Z calculated from Strain

Of major interest is the impact of the interface and bulk strain on the electrical properties. Therefore, we calculate the E field inside the crystal from the reconstructed strain (Figure 5.11 a) by employing the relation between the strain and the E field; $\varepsilon_{ij} = d_{ijk}E_k$.[264] A more specific explanation is given in the supplementary information. For the measured strain ε_x, the

corresponding E field E_z points along the c-axis of the ZnO rod and they are coupled by the piezoelectric strain coefficient d_{31} = -5.1 pC/N.[173] Since d_{31} has a negative value the calculated E field is inverted with respect to the strain.

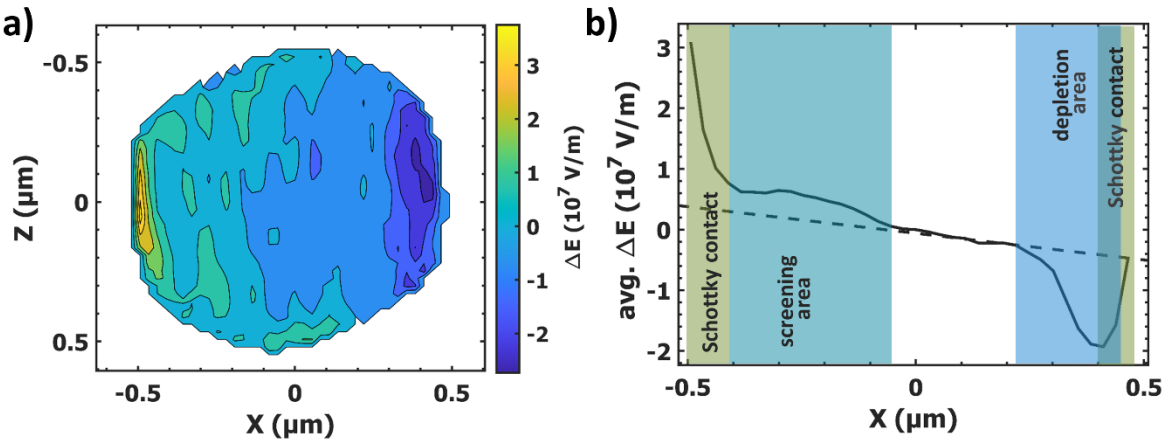

Figure 5.13: a) Contour plot of the E field distribution in the middle of the reconstructed volume, calculated from the strain distribution in Figure 5.11 a). b) Average E-field calculated along the Z direction in a), a linear increase is shown as a dashed line. Furthermore, the Schottky contact regions, screening and depleting areas are marked.

The relative E field is shown in Figure 5.13 a) for a cut through the middle of the reconstructed volume. Therein, a strong negative E field of -2.7 × 10^7 V/m is located near the right edge, towards the middle of the rod it is rising to a mean value of around 0 V/m and then rises further to positive field strength of up to 4.2 × 10^7 V/m near the left edge. A positive field of ~ 1 × 10^7 V/m is distributed around the center in a semicircle manner towards the left. For Figure 5.13 b) the average relative E field value is calculated and shows a similar but inverted behavior to the average strain in Figure 5.11 b). In the left region from X -0.1 µm to -0.3 µm the relative E field increases slowly to a maximum of 0.4 × 10^7 V/m, on the right in contrast we see a rapid decrease from X 0.25 µm to 0.4 µm reaching -2.0 × 10^7 V/m. All the quantitative values were fitted with the strain model and are presented in Table 5.2. There are four distinct areas of the E field and these may result from depletion and screening processes inside the rod, and further the coating and Schottky contact depletion region near the surface.

The compressive strain close to the interface, observed with both, TEM and XRD techniques, is likely the result from Au coating the ZnO surface. The Au coating may change the ZnO structure in at least two possible ways. Although the coating process is likely to induce a strain as proposed previously,[152] it was shown that for micro structures the thickness of a microrod coating does not exhibit a strong effect on the intrinsic strain of the piezoelectric component and that rather the rod diameter has the main effect on strain. This has also been observed for

thin ZnO films.[265] Additional strain may arise from the Schottky contact at the ZnO/Au interface. The proposed mechanism for the strain change at the interface is that the Schottky contact induces a potential and causes an electron depletion in the Schottky depletion region due to barrier formation. The related change of the electric field in vicinity of the Au interface leads to an impact on the crystalline structure, due to strain arising from the inverse piezoelectric effect[30]. A mechanical deformation of a piezoelectric component induces an electrical polarization, which can be measured as a piezoelectric voltage. In case of the inverse piezoelectric effect, polarization of charge centers in the material give rise to a mechanical strain. The electron depletion from the ZnO at the Schottky barrier gives rise to localized positive charge and thus polarized charge centers causing a local mechanical deformation. The measured width of the interface strain $\sigma_{\mathrm{I,CDI}}$ agrees with the calculated Schottky depletion width, as shown prior, and supports this mechanism as a source of interface strain. This explanation is a hypothesis, further experiments are required to achieve a better insight and understanding of the underlying effect. A possible path could be a measurement of the full strain tensor, by e.g. CXDI, and additional impedance spectroscopy to distinguish the Schottky barrier depletion width.

The macroscopic bending of the rod must be considered, as well. The non-symmetric strain distribution observed in Figure 5.11 can be explained by considering the *E* field distribution as shown in Figure 5.13, describing screening and depletion processes inside a bent, piezotronic rod.[55] However, to verify this unambiguously one would need to distinguish which of the two regions is depleted and which is screened. This is extremely challenging. Here, we consider that the *E* field is defined as force per charge, e.g., $E_z = F_z/q$, a weaker *E* field leads to a smaller force accelerating the electrons. Thus, the electron density is likely to be higher in the compressed region (left hand side Figure 5.11 b) and screens a positive potential more effectively. In comparison, the relaxed region on the right side of the rod results in a lower electron density due to the stronger force and thus electron depletion occurs. A similar effect has been proposed by Wang and Song to explain conduction behavior in a bent, piezotronic ZnO nanorod.[14] They also predict that introducing doping electrons to this system results in depletion of electrons and screening of the positive potential.[55] This is consistent with our results, as n-type ZnO was used in this experiment. CXDI provides a direct visualization and quantification of these effects.

5.3.7 CONCLUSION

TEM and CXDI techniques were combined to investigate and visualize the strain distribution of ZnO microstructures attached to Au. A strain was found at the ZnO/Au interface, likely to be a combination of strain induced by coating and strain due to the inverse piezoelectric effect at the Schottky contact. Furthermore, a non-symmetrical strain distribution inside the ZnO rod is attributed to depletion of electrons and screening of the positive potential due to rod bending. The high strain concentration at the coated microrod interface indicates a high potential for applications using piezotronic devices. The study of strain localization may advance the development of small electronic devices in the future, as already demonstrated for transistors based on the piezotronic effect[266]. Furthermore, highly sensitive and small sensors, based on piezotronics, may enable the design of portable sensors arrays, dedicated to measurement of biomagnetism from the human physiology, e.g., from the brain or heart, and this without the need for heavy and expensive equipment.

5.3.8 EXPERIMENTAL SECTION/METHODS

Bragg CXDI: The experiment was conducted at the beamline ID-34c of the Advanced Photon Source with a photon energy of 9 keV. The beam size was focused with a Kirkpatrick-Baez mirror and a slit was used to achieve the final beam size of $2000 \times 450\,\mathrm{nm}^2$ (h × v). The data were acquired by a timepix detector with 55 µm square sized pixels and at a detector sample distance of 2.8 m. A data series of the reciprocal space around the $\{10\bar{1}0\}$ Bragg peak was collected by rotating the sample around the ZnO's *c* axis in a range of 0.24 ° with a 0.002 ° step size. For the reconstruction of the complex electron density a combination of error reduction (ER) and Hybrid-Input-Output (HIO) algorithms were used.[98,99,257,267] Each 20 ER algorithm runs were followed by 180 HIO algorithm repetitions, with a total of 1020 runs. The shape was defined by a shrink wrap algorithm.[92] A low to high resolution reconstruction was performed by changing the sigma of the Gaussian mask in the shrink wrap routine from 3 to 1 and a partial coherence correction was employed.[106,268] For every measured scan 200 reconstructions with random starts were done to achieve a statistically reasonable result. An error metric calculated for every reconstruction was used to evaluate and pick the best results (see supplementary information). The chosen reconstructions were correlated and a final reconstruction calculated. The voxel size of the reconstructions is $27.4 \times 27.4 \times 27.4\,\mathrm{nm}^3$.

TEM: GPA is directly applied to the FFT of HRTEM image, which is modulated by the contrast transfer function (effect of spherical aberration and defocus mainly) to calculate lattice displacements with respect to a reference lattice with nanometer resolution and minimum

2×10^{-3} strain precision. The following microscopes were used during this study: A Tecnai F30 G² (300 kV, field emission gun (FEG)) and a Titan 80-300 operated at 300 kV equipped with an image corrector to correct spherical aberrations for HRTEM imaging. GPA was performed using a plug-in tool (FRWRtools plug-in, Christoph T. Koch, HU Berlin, Institute of Physics) for DigitalMicrograph™.

Sample Preparation: To produce the ZnO microstructures the flame transport synthesis was used.[120] With this technique, it is possible to produce tailor made ZnO rods with diameters ranging from below 1 µm to a few hundred µm and lengths up to mm. The diameter of the measured ZnO rod is 1.0 ± 0.2 µm. One end of the rod was fixed to a glass capillary by adhesive, the other end was free standing. The sample was coated with 50 nm gold in a thermal evaporation physical vapor deposition process from two opposing directions. The layer thickness was distinguished by measuring the deposition rate with a quartz crystal microbalance. For the TEM a model system exhibiting larger Au nanocrystals (diameter of 200 - 500 nm) on the ZnO surface was prepared by sputter deposition of a thin gold layer and subsequent annealing to 600 °C. A thin cross-section specimen containing these ZnO/Au interfaces were prepared by focused ion beam (FIB) technique cutting the ZnO microrod perpendicular to the (0001) plane.

5.4 Metallic Alloy FeCoSiB as novel Ohmic Contact on ZnO; Operando Electrical Investigation of a Piezotronic Magnet Field Microrod Sensor and complementary Coherent X-ray Diffraction Imaging of Strain Distribution

5.4.1 Manuscript 1 Overview

Building on the results and experience from the previous study in section 5.3, ZnO rods were investigated by CXDI, utilizing the advanced SEFiR design from section 4.1. Enabling simultaneous investigations of the electrical and structural properties. In this study, the ZnO rods were partly coated by magnetostrictive FeCoSiB, providing the opportunity to investigate the strain response induced by an external magnetic field.
This section is a manuscript prepared for submission, highlighting the impact of FeCoSiB on ZnO and its implementation as a magnetostrictive material for a piezotronic inspired magnetic field sensor, with a simultaneous visualization of the strain distribution.

Metallic Alloy FeCoSiB as novel Ohmic Contact on ZnO; Operando Electrical Investigation of a Piezotronic Magnet Field Microrod Sensor and complementary Coherent X-ray Diffraction Imaging of Strain Distribution

Philipp Jordt, Henning Vogt, Lukas Petersdorf, Sindu Shree, Wonsuk Cha, Ross Harder, Rainer Adelung, Olaf M. Magnussen, Bridget M. Murphy

P. Jordt, H. Vogt, L. Petersdorf, Prof. Dr. O. M. Magnussen, Dr. B. M. Murphy
Institute of Experimental and Applied Physics, Kiel University, Leibnizstr. 19, 24118 Kiel, Germany
Dr. B. M. Murphy
Ruprecht-Haensel Laboratory, Kiel University, 24118 Kiel, Germany
Dr. S. Shree, Prof. Dr. R. Adelung
Institute of Material Sciences, Kiel University, Kaiserstr. 2, 24143 Kiel, Germany
Dr. W. Cha, Dr. R. J. Harder
X-ray Sciences Division, Argonne National Laboratory, Lemont, Illinois 60439, USA

5.4.2 ABSTRACT

Ohmic contacts are of elementary importance to the design of semiconductor devices, enabling the integration of semiconductor structures in electronic devices for use in a wide variety of applications ranging from integrated circuits to sensors. In this study, it is shown that magnetron sputtered metallic alloy FeCoSiB on ZnO forms an ohmic contact. Additionally, FeCoSiB functionalizes the ZnO structure as a magnetic field sensor, due to its magnetostrictive properties. This was investigated for a ZnO micro rod, utilizing it as a piezotronic magnetic field sensor by employing a spatial separated FeCoSiB (ohmic) and silver (Schottky) contact. Current - Voltage curve measurements on the rod revealed an increase of the Schottky barrier height by 22 % and a simultaneous decrease of the ideality factor by 55 %, for an applied magnetic field of >2 mT. These remarkable changes are attributed to the piezotronic effect induced by the magnetostrictive strain from the FeCoSiB coating. Further, coherent X-ray diffraction studies on the same ZnO rod indicate a distinct magnetic field induced change of the strain distribution in the rod and, possibly, is the cause for the piezotronic change of the electrical properties.

5.4.3 INTRODUCTION

Piezotronic is denoting an effect of changing the electrical properties of a piezoelectric semiconductor by applying stress.[22,50,112] The effect was first described by Wang in 2006,[14] and is under research for a wide variety of applications since then, e.g. transistors, sensors and artificial synapses.[20,52,166,167] Piezotronic can be separated into two paths,[22] changes due to a longitudinal or transverse stress in respect to the crystallographic direction in which the piezoelectric effect is occurring in a semiconductor, e.g., for ZnO this direction is pointing along the *c* axis of the hexagonal wurtzite structure.[35] In the longitudinal chase, the resulting piezo potential leads to an accumulation of free electrons at the positive charged side of the structure and a screening of electrons at the opposite, negative side. The induced piezo potential, together with the electron accumulation and screening, causes a modification of the Schottky contact barrier height and width, and thus a measurable current change.[22,23,39] Schottky and ohmic contacts are the two possible contact types that can arise at a semiconductor metal interface.[40] In chase of a transversely stressed structure a changing conductivity was reported and explained by carrier trapping effects near the interface and shrinking of the conduction channel size, due to an electron screening.[16] This explanation of the conductivity change is supported by finite element simulations and analytical models for a transversely stressed ZnO rod, displaying a change of the piezo potential along and across a rod structure, resulting in a distinct potential

distribution and a shrinking of the conduction channel size.[55,248] For a highly sensitive piezotronic sensor it is beneficial to build a sensor with a combination of a Schottky and an ohmic contact, hence, the current is not hindered by diode behavior of two Schottky contacts for both polarizations of the applied voltages. Instead a clear forward current can be measured, leading to a higher measurable current change and thus an enhanced sensitivity.[21] In the chase of ZnO, prominent example for ohmic contacts are aluminum, nickel and titan.[45]

For the investigation of crystalline structure properties and related effects, e.g. strain in piezoelectric material, X-ray scattering is a well-known technique.[67,89,152] In a scanning nano X-ray diffraction (XRD) study,[62] the {10-10} Bragg reflection of a FeCoSiB coated ZnO rod with a diameter of 27 µm was investigated and the strain was spatially resolved measured across the rod. A magnetic field induced strain of 1×10^{-4} was found near the interface and attributed to the magnetostrictive induced strain from the FeCoSiB coating. An advanced XRD technique to visualize the three dimensional strain distribution of crystalline specimen is coherent X-Ray diffraction imaging (CXDI).[28,269] In a recent study, the full strain tensor of a tungsten crystal was mapped by Bragg CXDI (BCXDI), showing the potential of 3D investigation of small structures exhibiting crystal defects, derived from bigger specimen by focused ion-beam machining.[90] Furthermore, ZnO and GaN rods with sub µm diameters were investigated by CXDI and strain distributions from cuts through the rods were retrieved.[251,254]

5.4.4 FeCoSiB Ohmic Contact on ZnO

The zinc terminated side of a planer zinc oxide (ZnO) single crystal was coated with magnetostrictive metallic alloy $(Fe_{90}Co_{10})_{78}Si_{12}B_{10}$ by RF magnetron sputtering. The oxygen terminated side was spatially separated coated with aluminum (Al) by thermal evaporation and silver (Ag) glue. See inset of Figure 5.14 for a sketch of the sample design. These contacts were connected by Ag glue to wires to enable current/voltage (*I-V*) measurements utilizing a sourcemeter. For further information on the sample preparation and technical details see the experimental section at the end.

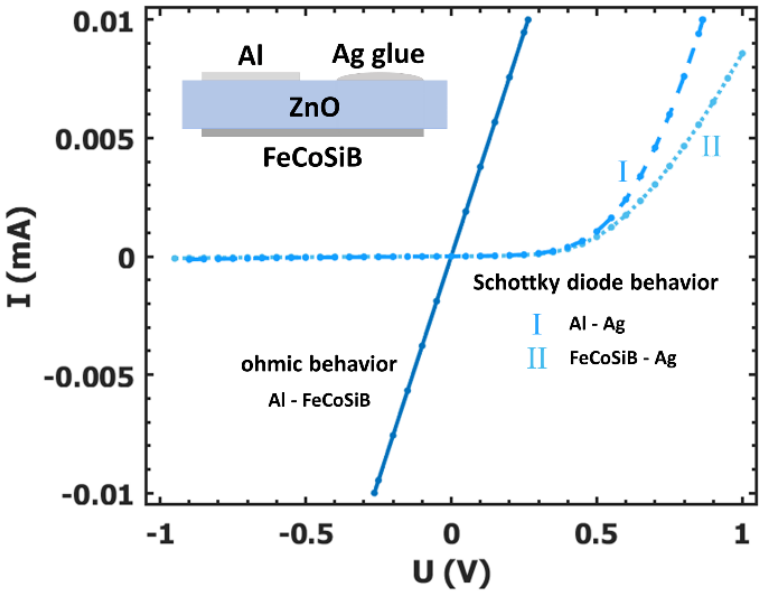

Figure 5.14: Inset (left top) shows a sketch of the experimental setup. A planar ZnO crystal was separately coated with metallic alloy FeCoSiB, Al and Ag glue. The solid *I-V* curve reveals an ohmic behavior for the measurement between the Al and FeCoSiB contact. Furthermore, the Al to Ag (I) as well as the FeCoSiB to Ag (II) *I-V* curves display Schottky diode behaviors with distinct forward and reverse current directions.

Figure 5.14 displays further the electrical behavior examined by *I-V* curves for three different connection schemes between the contacts (Al/ZnO/FeCoSiB, Al/ZnO/Ag and FeCoSiB/ZnO/Ag). The solid curve shows the measurement for the Al/ZnO/FeCoSiB scheme. Qualitatively an ohmic resistance is present resulting from two ohmic ZnO contacts. From the *I-V* curve an ohmic resistance of 26.39 ± 0.1 Ω was distinguished by fitting the slope with a linear function between -0.2 V and 0.2 V. Furthermore, a Schottky diode like behavior is observed in the *I-V* curve collected for the Al/ZnO/Ag configuration (dashed curve and marked with the roman number I). In the positive voltage regime, a forward current is observed and a weak, reverse current is present at negative voltages. From the respective semi-logarithmic *I-V* curve, a Schottky barrier height Φ_{bh} = 0.64 ± 0.1 eV and ideality factor n = 3.5 ± 0.3 were distinguished by fitting it with a linear function, see experimental section for further details on the procedure and supplementary information Figure 7.22. A similar Schottky diode behavior is observed in the FeCoSiB/ZnO/Ag configuration and is shown as the dotted curve in Figure 5.14, additionally marked with roman number II. Schottky barrier height Φ_{bh} = 0.66 ± 0.1 eV and ideality factor n = 3.1 ± 0.2 were found by fitting. The reported Schottky contact barrier heights and ideality factors are well in the range of previous studies.[45]

The three *I-V* curves prof that Al/ZnO as well as FeCoSiB/ZnO contacts are ohmic contacts and that Ag/ZnO forms a Schottky contact. Ohmic behavior of Al contacts and Schottky behavior

of Ag contacts corresponds to previous results for various ZnO contacts.[45] The ohmic behavior of FeCoSiB contacts is, to the authors best knowledge, the first report and adds another material to the known ohmic contact materials for ZnO. Ohmic properties of FeCoSiB contacts might be especially interesting for application, e.g. in piezotronic inspired magnetic field sensors, because the material is magnetostrictive and a functionalization of a sensor is realized without the need for an additional ohmic contact.

5.4.5 FeCoSiB Coated ZnO Microrod as Piezotronic Magnet Field Sensor

As mentioned in the previous section, FeCoSiB can be utilized to implement an ohmic contact at a ZnO structure and, simultaneously, add a functionally by its magnetostrictive properties. For the building of a functional magnetic field sensor, FeCoSiB was magnetron sputtered on a ZnO micro rod fabricated by flame transport synthesis.[120] Layout of this sensor is shown in Figure 5.15 a). First step in the building process of this sensor is fixing a ZnO needle to the 3D printed sample holder with a minimal amount adhesive to prevent the needle from moving. Second step is the application of Ag glue, limited to a fraction of the whole length of the needle. The Ag glue will serve as the Schottky contact. A partly insulated wire to enable the electrical investigations is fixed simultaneously by the Ag glue. Third step is the capsulation of the Ag glue and parts of the ZnO in an epoxy to prevent a short circuit occurring between the Ag and the FeCoSiB from the next step. Fourth step is magnetron sputtering of FeCoSiB on top of the sample. In the final step another wire is attached with Ag glue and enables electrical measurements. By realizing the sensor with, both, a Schottky and Ohmic contact this magnetic field sensor can be used in piezotronic manner.[21] For this, the FeCoSiB on top of the ZnO needle induces a strain in the needle, when exposed to an external magnet field. The strain in the ZnO causes a piezo potential that changes the Schottky barrier height and, thus, the current flow over the contact due to the piezotronic effect.[50,270] The in here presented sensor used a ZnO needle with a diameter of ~1.3 µm and a length of ~100 µm. For more information on the ZnO rod synthesis see the experimental section. NdFeB permanent magnets (10 mm × 10 mm × 4 mm) were used to investigate the magnet field impact on the sensor. The field strength at the sample position was changed by altering the distance between sample and magnet and, further, by combining up to two magnets. Field strengths for the different distances were calibrated with a Gaussmeter. Magnet field dependent electrical measurements on this sensor are presented in Figure 5.15 b), field strength varies form 0 mT to 13.2 mT. The measured *I-V* curves show no qualitatively visible effect of the magnet field on the electrical properties in a voltage regime between -2 V and 2 V. A small reverse current, between -0.01

nA and -3 nA, is present for negative bias voltages. In the forward direction of the Schottky contact, an exponential increase is visible at first, followed by a linear, ohmic increase at higher voltages. The inset in Figure 5.15 b) displays the same *I-V* curves, zoomed in on voltages between 0.1 V and 0.4 V. In there, a clear magnet field impact on the electrical properties is observed, the current varies up to 60 % at 0.4 V. This behavior could be explained by taking into account that the initial exponential increase in the *I-V* curves is probably related to and limiting by the Schottky barrier height and the generation recombination effect.[39] Thus ,the magnet field induced current change is likely the result of a barrier height change due to the piezotronic effect. After this initial exponential increase the high injection of minority carrier and serial resistance of the semiconductor become the limiting factors for the current.[39] It appears that this transition happens at around 1 V. Moreover, the linear slopes (1.5 V to 2 V) in the *I-V* curves were fitted with a linear function and the calculated ohmic resistance as a function of the applied magnet field is shown in Figure 5.15 c). The overall appearance of the resistivity appears to be constant, besides the resistivity $R_0 = 30.9 \pm 1.5$ kΩ at 0 mT is slightly below the mean value of all other resistivities with applied fields, $R_{mean} = 33.7 \pm 1.0$ kΩ, and may be an indication for further effects changing the electrical properties when a magnet field is present. This slight change of resistivity may be caused by piezoresistivity,[271] or induced by a conduction channel shrinking due to piezotronic in a bent rod.[16,55,248]

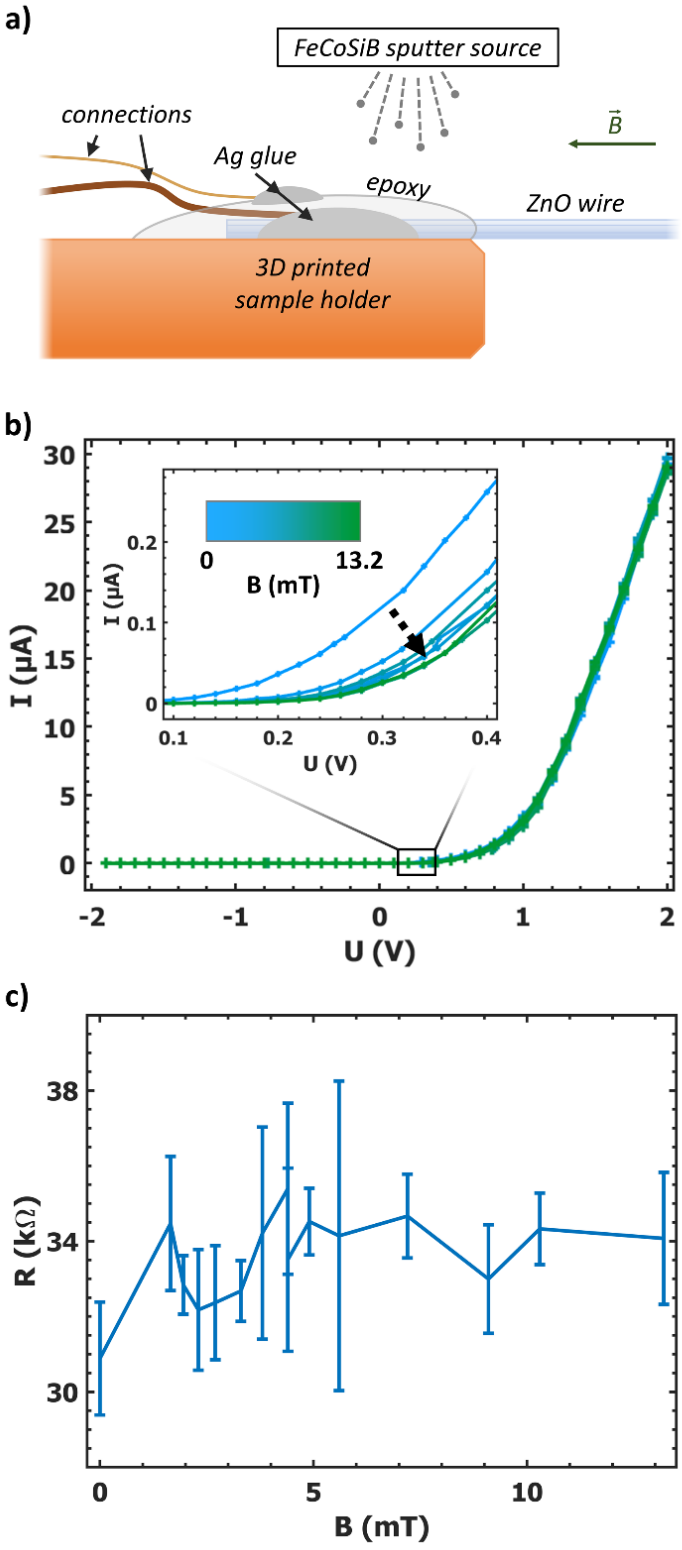

Figure 5.15: a) Sample holder sketch with an mounted ZnO rod and coated with FeCoSiB by magnetron sputtering. Two wires are included to enable electrical measurements. b) *I-V* curves collected for multiple magnet field strengths applied along the c-axis of the ZnO rod, ranging from 0 mT to 13.2 mT. The inset shows a magnified view of the *I-V* curves in the low voltage regime, displaying a clear, magnet field related change. c) Resistivity calculated from the slope of a linear fit to the *I-V* curves (Figure 5.14) between 1.5 V and 2 V.

For a more quantitative picture of the effects, Schottky barrier heights, as well as ideality factors were extracted from the *I-V* curves. In Figure 5.16 a) semi-logarithmic *I-V* curves for three magnet field strengths (0 mT, 3.8 mT and 13.2 mT) are presented. A clear decrease in the forward and reverse current up to four magnitudes is visible for an applied magnetic field, but for higher strengths of the applied magnetic field, it seems to have no prominent influence on the *I-V* characteristics. Deducing that the maximum effect strength generated by the FeCoSiB coating saturates between 0 mT and 3.8 mT. Furthermore, the measured current in the forward voltage regime above 1 V seems to be qualitatively similar. Inset of Figure 5.16 a) displays the semi logarithmic *I-V* curve in the low voltage regime of the measurement for a field strength of 3.8 mT. The Schottky contacts barrier height and ideality factor is extracted from a linear fit (red line) in the voltage range of 0.15 V to 0.25 V. Both, barrier heights and ideality factors were fitted in the variety of measured *I-V* curves for applied magnetic field strengths ranging from 0 mT to 13.2 mT. Figure 5.16 b) shows the magnetic field dependent change of the Schottky barrier height Φ_{bh} as well as the idealty factor *n*. The effective Barrier height of the Ag/ZnO contact has an initial value of 0.58 ± 0.01 eV for non-applied magnetic field and increases by roughly 22 % for applied fields to saturate at a mean barrier height with a standard deviation of 0.71 ± 0.02 eV. Magnetic field induced change seems to saturtae at around 2 mT, this value is in agreement with previous studies.[272] A decrease by 55 % is observed for the ideality factors, starting at an initial value of 2.59 ± 0.15 and saturating at a mean value of 1.44 ± 0.11. An increasing barrier height combined with a decreasing ideality factor was previously reported.[180]

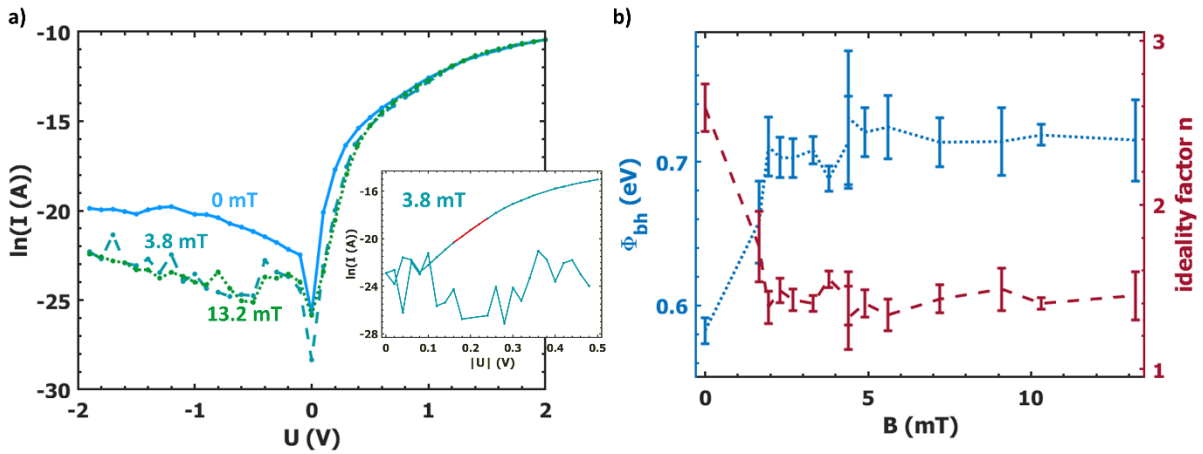

Figure 5.16: a) Semi-logarithmic *I-V* curves for magnet field strengths 0 mT, 3.8 mT and 13.2 mT. Inset shows the fitting range between 0.15 V and 0.25 V to extract the Schottky contacts barrier height and ideality factor. b) Magnet field strength dependent Schottky barrier heights Φ_{bh} (blue, dotted) and ideality factors n (red, dashed).

The Schottky contact barrier height undergoes a magnetic field induced change and leads to the measurable current decrease in the low forward voltage regime. Furthermore, the ideality factor is decreasing, implying that the contact becomes more ideal due to a lower generation recombination rate, altering interface states density or decreasing tunneling current.[40] This effect can as well be seen in the decreasing reverse current for applied magnetic fields in Figure 5.16 a). Both, increasing barrier height and decreasing ideality factor are probably linked to the piezotronic effect, arising from a strain induced by the magnetostrictive FeCoSiB coating, leading to a piezo potential and, further, to piezo charges that accumulate at the rod tip. These charges lead to an increase in barrier height and barrier thickness, possibly causing a shrinking of tunneling current through the barrier and thus a decreasing ideality factor due to the more ideal behavior of a thermionic emission driven current.[39] Could be as well explained by a decreasing rate of barrier height inhomogeneities, as proposed in previous studies.[40,180] The piezo charges may lead to a declining number of defect states near the interface and, hence, a decline in barrier height inhomogeneities.

5.4.5.1 Operando Coherent Diffraction Imaging

Complementary to the electrical examinations, the impact of the magnet field on the crystalline structure and strain in the same ZnO rod was visualized by BCXDI. Figure 5.17 a) displays the BCXDI geometry to measure the {0002} Bragg reflection of the ZnO rod. Scattering vector $\vec{q}$ is defined by the wavevectors of the incoming $\vec{k}_{in}$ X-ray beam from the source and outgoing $\vec{k}_{out}$ diffracted beam and is oriented parallel to the c-axis of the ZnO rod. Furthermore, a right-handed cartesian coordinate system is introduced with *x* pointing in direction of the scattering vector along the rod axis, *y* and *z* are perpendicular to the rod's c axis. A fine rocking measurement was collected by rotating the rod around the *y* axis, mapping the reciprocal space around the Bragg reflection. Cross section in the $\Delta q_z/\Delta q_y$ plane through the center of the {0002} reflection from the interpolated rocking measurement is shown in Figure 5.17 b), here, measurement without an applied magnetic field. There in, the expected hexagonal structure for ZnO micro rods is visible, including fringes. The spacing between the maxima of the fringes calculate to a mean rod diameter of 1472 ± 243 nm, combining all three main directions. Full width at half maximum of the reflection in the three directions is related to a mean size of the coherent scattering crystal volume of 967 ± 297 nm, calculated with the Scherrer equation.[181] Indicating a single crystalline ZnO rod.

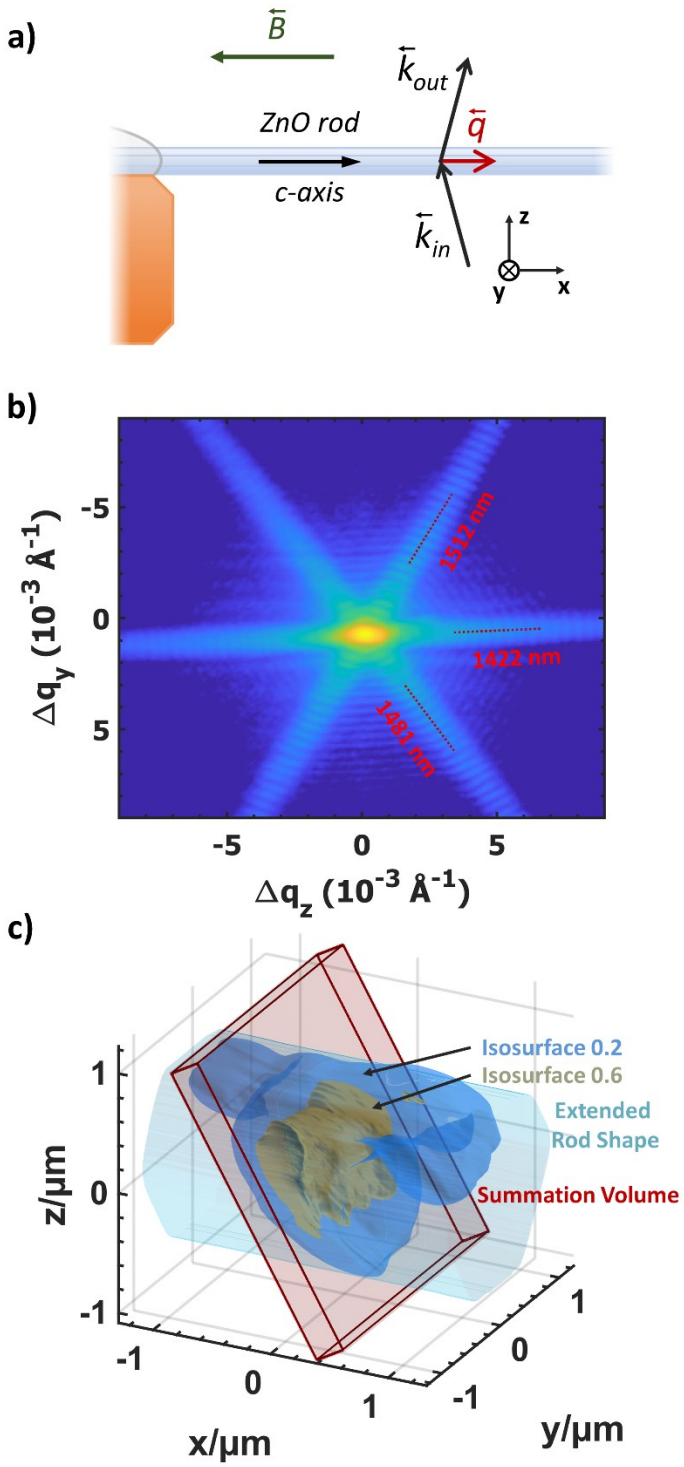

Figure 5.17: a) Sketch of the BCXDI geometry utilized to measure the {0002} ZnO rods Bragg reflection. Scattering vector $\vec{q}$ is defined by the incoming $\vec{k}_{in}$ and outgoing $\vec{k}_{out}$ wave vectors and is pointing along the c axis of the ZnO crystalline structure. Additionally, a magnetic field could be applied by varying a permanent magnet to sample distance. b) Cut through the $\Delta q_z/\Delta q_y$ plane of the measured {0002} Bragg reflection with estimated rod sizes from fringe oscillations. c) Isosurfaces 0.2 (dark blue) and 0.6 (yellow) of the reconstructed electron density amplitude. Rod shape defined by the 0.2 isosurface was extended to better visualize the rod dimensions (light blue). Summation volume for further analysis of the reconstructed strain is shown in red shades.

Along the streak roughly parallel to q_z the fringes are much less pronounced, and the high intense center of the Bragg reflection is non-symmetrical and stretched along this direction. These changes may be indicating a present strain distribution.[251] A magnified cut around the center is shown in Figure 7.23 in the supplementary information. The authors are aware that the presented data and reconstructions are obtained from data collected at the edge of spatial limitations for CXDI, limited by the coherence lengths accessible at modern synchrotron sources, but are confident that a qualitative approach of presenting the data may still have an impact on the overall picture of the sample.

Due to the huge rod diameter of around 1.3 µm, the in comparison small beam size in x direction of around 500 nm and a Bragg angle of $\theta_0 = 15.5°$, the reconstruction of the electron density is tilted, as shown in Figure 5.17 c). The electron density is visualized by isosurfaces with values of 0.2 and 0.6 and exhibits additional features on the upper edge ($z \approx 0.8$ µm) along x, probably due to the non-ideal data quality obtained at the spatial limit for CXDI. Furthermore, a summation volume is introduced, shown in red shades. This is used to extract a tilted cut from the reconstruction and calculate mean values along the x direction of the relative strain distribution present inside this volume. A positive, tensile and negative, compressive strain are defined as an increase and decrease of the lattice parameter, respectively. The maximum rod shape of the isosurface 0.2 inside the summation volume is extended along the c axis of the rod and shown in Figure 5.17 d) as a light blue shade, to enable an easier accessibility and visualization of the rod shape.

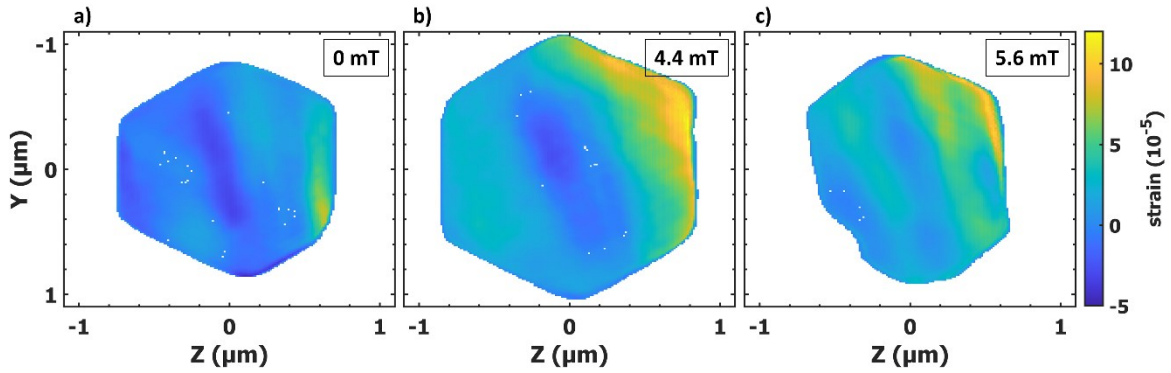

Figure 5.18: a) Reconstructed strain distribution in a FeCoSiB coated ZnO rod obtained from Bragg CXDI of the {0002} Bragg reflection. b) Same rod section measured for an applied magnetic field of 4.4 mT and c) 5.6 mT.

Rod cross sections of the strain distributions for 0 mT, 4.4 mT and 5.5 mT are shown in Figure 5.18 a-c), respectively. Exhibiting a strong increase of the strain at the right upper edge of the

rod section (y = -0.6 µm, z = 0.7 µm) and, thus, the rod probably is bend by the non-symmetrical strain. Furthermore, in Figure 5.18 b) it may be that the strain on the opposite edge (y = 0.5 µm, z = -0.6 µm) is slightly elevated in comparison to the rod center, but the observable overall strain change of roughly 1.7×10^{-4} is close to the strain resolution limit of around 1×10^{-4}. These qualitative visible deviations in the strain distribution may be the cause for the piezotronic effect. Due to a strain in a piezo electric material the arising piezo potential leads to an accumulation of electrons in the Schottky contact region and further to an increase of the barrier height, as it was observed in the current voltage measurements. Furthermore, the relative strain change in the rod for an applied magnetic field can be utilized to investigate the influence of the piezoresistive effect.[271] In a previous study,[271] a resistivity change of ~ 2 kΩ at 32 kΩ was reported for a 4 % strained ZnO rod. The here reported resistivity change of 2.8 kΩ at around 32 kΩ was measured for a more than two magnitude smaller strain of below 0.02 %. A more promising explanation for the resistivity change is the piezotronic effect in a bent nano wire. The induced piezo potential distribution in a bent wire leads not solely to the measured barrier height change, but as well to a shrinking of the conduction channel and trapping of carriers and, thus, to an altered conductivity.[16] This indicates that the piezoresistive effect is of minor importance for the reported conduction change compared to the piezotronic effect and this fits previous findings.[273]

Please note that the ZnO rod was coated with FeCoSiB by magnetron sputtering prior to the experiment by a source in positive *z* direction, hence, coating the right-hand side of the rod. Implying that the highest strain is present on the site of the coated rod surface. But due to the imperfect CXDI data, further investigation to confirm these findings are necessary. A combined approach of transmission electron microscopy and an examination of the full strain tensor in a smaller specimen by BCXDI might be especially helpful towards a better understanding.

5.4.6 Conclusion

Current voltage curves were utilized to investigate a planar ZnO structure, partly coated with magnetron sputtered magnetostrictive metallic alloy FeCoSiB. It was reported, possibly for the first time, that the resulting contact is of ohmic nature. In further experiments the electrical properties and strain distribution in a ZnO rod were determined by *I-V* curves and CXDI examinations. An external magnetic field applied to the micro rod induced a piezotronic related increase of the Schottky barrier height and decrease of the ideality factor at an additional silver contact. This change is attributed to the magnetostrictive strain induced piezo potential change in the ZnO rod. Furthermore, a slight increase of the resistance is measured for applied magnetic

fields and attributed to a piezotronic induced shrinking of the conduction channel size inside a bent ZnO rod. Evidence of a magnetostrictive strain induced bending of the rod was found in reconstructed strain distributions obtained by CXDI. These results show the coexistence of two piezotronic effects changing the electrical properties of ZnO microstructures and display the need to include both effects in the design process for future (microstructure) piezotronic devices. Further studies investigating samples with smaller dimensions are necessary to obtain a better CXDI data quality and achieve a further understanding of the mechanism occurring inside the rods during magnetic field induced strain. Possibly combined in a complimentary approach with transmission electron microscopy measurements to visualize the mechanism on multiple length scales.

5.4.7 Experimental Section/Methods

Sample Preparation: The planar ZnO sample was purchased from CrysTec GmbH with orientation [0001] and had dimensions of 10 mm × 10 mm × 0.5 mm (width × length × thickness). ZnO micro rods were produced by the flame transport synthesis.[120] This technique enables the production of tailor made ZnO rods with diameters ranging from below 1 µm to a few hundred µm and lengths up to mm. Diameter of the measured ZnO rod was distinguished by CXDI to be 1.3 ± 0.5 µm. For the sample design and building process please see section 3 (FeCoSiB Coated ZnO Microrod as Piezotronic Magnet Field Sensor). One-inch $(Fe_{90}Co_{10})_{78}Si_{12}B_{10}$ magnetron sputter target was commercially acquired from EVOCHEM GmbH. For the FeCoSiB sputtering process a vacuum chamber was evacuated to ~10^{-8}, argon was inserted and the plasma ignited at a pressure of ~10^{-2}. The samples were RF magnetron sputtered at 110 W for 60 minutes resulting in a calculated FeCoSiB layer thickness of ~15 nm. The aluminum on the planar sample was deposited by thermal evaporation in an evacuated vacuum chamber at pressure ~10^{-3}. Final layer thickness of 100 nm was measured by a quartz crystal microbalance.

Current/Voltage (I-V) Curves: For the electrical measurements, a Keithley 2450 Sourcemeter was used to collect the *I-V* curves in a range of -1 to 1 V with a resolution of 0.05 V for the planar ZnO sample and -2 to 2 V with a resolution down to 0.02 V in the -0.5 to 0.5 voltage regime for the ZnO rod sample. The current accuracy is between 1×10^{-9} A and 6×10^{-11} A (depending on the measurement range) and 7×10^{-4} V for the sourced voltage. Combination of a Schottky and an Ohmic contact allows one to measure the forward and reverse current of the Schottky contact. To distinguish the barrier height and ideality factor of the Schottky contact a linear function was fitted to the logarithm of the current in the range of 0.1 V to 0.25 V for the

planar sample and between 0.15 V and 0.25 V for the rod.[39] The intersection of the fitted line with the *y*-axis of the *I-V* graph defines the current I_0 and further the barrier height $\phi_B = \frac{kT}{q}\ln\left(\frac{A^*T^2}{J_0}\right)$, [39] with the Boltzmann constant k, temperature T= 294 K, elementary charge q, effective Richardson constant A^*= 32 A cm^{-2} K^{-2} [111,197] and the current density J_0 equals the current I_0 divided by the contact area size. From the fitted slope $\frac{d(\ln J)}{dV}$ of the fitted linear function, the ideality factor n is distinguished by employing $n = \frac{q}{kT}\frac{dV}{d(\ln J)}$.[39]

Magnet Field Measurement: Magnet field measurements to calibrate the permanent magnet was performed with a MAGSYS HGM09s gaussmeter. Gauss meter was placed at the sample position in the empty sample holder, magnetic field strengths were measured for multiple distances and these were noted on the holder as calibration marks for following measurements. Measurement resolution in the range up to 100 mT is 10 µT.

Bragg Coherent X-ray Diffraction Imaging (CXDI): The experiment was conducted at the beamline ID-34c of the Advanced Photon Source at a photon energy of 9.1 keV. The beam size was focused with a Kirkpatrick-Baez mirror and a slit was used to define the final beam size of 480 × 2200 nm^2 (h × v). The data were acquired by a timepix detector with 55 µm square sized pixels and at a detector sample distance of 2.0 m. A data series of the reciprocal space around the {0002} Bragg peak was collected by rocking the sample around the *y* axis in a range of 0.6 ° with a 0.003 ° step size. For the reconstruction of the complex electron density a combination of error reduction (ER) and Hybrid-Input-Output (HIO) algorithms were used.[98,99,257,267] Each 20 ER algorithm runs were followed by 180 HIO algorithm repetitions, with a total of 1020 runs. The shape was defined by a shrink wrap algorithm.[92] A low to high resolution reconstruction was performed by changing the sigma of the Gaussian mask in the shrink wrap routine from 3 to 1 and a partial coherence correction was employed.[106,268] For every measured scan 200 reconstructions with random starts were performed to achieve a statistically reasonable result. By utilizing an error metric of the reconstructions, the middle 100 out of 200 reconstructions were chosen. These reconstructions were correlated and a final reconstruction calculated. Voxel size of 12.9 × 12.9 × 12.9 nm^3 was achieved in the reconstructions and is a measure for the spatial resolution.

5.5 Nanostabilization of Tetragonal Distorted FeCo Variants in Ultra-Thin FeCo/TiN Multilayer Film

5.5.1 Publication 4 Overview

As seen in the previous section 5.4, the magnetostrictive component is of elementary importance for the design of a functional magnetic field sensors. In this section the focus is on the structural investigation of the magnetostrictive component. Multilayer structures based on magnetostrictive FeCo and TiN thin layers, see section 3.4, were investigated by TEM and X-ray to reveal the impact of annealing processes on the crystalline structure of the materials and the overall structure of the multilayer system. XRR, as well as, XRD methods were used, see sections 2.6 and 2.5, respectively, giving access to the average layer structure of the multilayers and the crystalline properties of the TiN layers. This section is a manuscript published in Materials Characterization.[274] (https://doi.org/10.1016/j.matchar.2021.110871)

Nanostabilization of Tetragonal Distorted FeCo Variants in Ultra-Thin FeCo/TiN Multilayer Films

Niklas Wolff[a], Philipp Jordt[b], Justin Jetter[c], Henning Vogt[b], Andriy Lotnyk[d], Klaus Seemann[e], Sven Ulrich[e], Eckhard Quandt[c], Bridget M. Murphy[b], Lorenz Kienle[a]

a Synthesis and Real Structure, Institute for Materials Science, Kiel University, 24143 Kiel, Germany
b Institute for Experimental and Applied Physics, Kiel University, 24118 Kiel, Germany
c Inorganic Functional Materials, Institute for Materials Science, Kiel University, 24143 Kiel, Germany
d Leibniz Institute of Surface Engineering (IOM), 04318 Leipzig, Germany
e Institute for Applied Materials (IAM-AWP), Karlsruhe Institute of Technology (KIT), 76344 Eggenstein-Leopoldshafen, Germany

5.5.2 Abstract

Composites of ultra-thin nanolayers of FeCo/TiN with individual layer thickness of a few unit cells offer stability at elevated temperatures and exhibit defined magnetic properties which can be tuned by variying the layers thickness making them interesting candiates as components for

magnetoelectric (ME) sensors. Initial studies describing the nanostructure of such thin films, however, left uncertainty about their exact crystal structure. With aberration-corrected microscopes the characterization of the local structure down to the atomic scale is possible to address the real structure with high precision. Here, by means of atomic resolution TEM imaging together with X-ray diffraction analysis, we were able to describe the nanostructure to be composed of individual layers of FeCo and TiN forming a superlattice with a defined cube-on-cube orientation relationship. The simulation of electron diffraction pattern featuring superlattice reflections on basis of structural modeling together with geometric phase analysis verified a defined orientation relationship resolving in the nanostabilization of a tetragonal distorted FeCo unit cell with $c/a < 1$.

5.5.3 INTRODUCTION

Multilayer architectures of FeCo and TiN have been designed and examined in the past by Klever *et al.*[134]. For the purpose of smart wear protection coatings with self monitoring functions. The combination of high hardness and temperature resistivity of TiN and the tunable magnetic characteristics of the ferromagnetic alloy FeCo suggests multilayers of FeCo/TiN for the magnetic phase in magnetoelectric (ME) composite sensors, e.g., for biomagnetic imaging.[275,276] In this respect, the magnetic properties of the composite can be effectively tuned by the layer thickness of FeCo and TiN layers, demonstrating a low coercive field of $\mu_0 H_c = 0.30$ mT and a saturation magnetization of $\mu_0 H_s = 0.4$ T usingFeCo layers of about 1 nm in thickness.[134] In general, the reduction of the FeCo layer thickness down to the nanoscale is known to gradually “soften” the magnetic characteristics yielding a low coercive field at high saturation magnetization.[277–279] In ME composites, the available biomagnetic signal is in principal read out by a voltage change which is induced via the transfer of magnetostrictive strain arising in a soft magnetic material such as FeCoSiB onto a piezoelectric material such as AlN.[130,280,281] In the ME magnetic field sensor these FeCoSiB/AlN composites are deposited onto silicon substrates and shaped into cantilever geometry. One promising approach is to detect magnetic fields by using the magnetoelastic properties of the magnetostrictive part via the ΔE-effect, which is the effective softening of the Youngs modulus E of a magnetostrictive material in the small strain regime[282,283]. Herein, the easy measurable frequency shift of the resonance frequency upon application of an alternating external magnetic bias field results in the elastic softening of the magnetic phase and proved high sensitivity in the order of 100 pT/Hz^{-1} at the biomagnetic relevant low frequency regime between 10 to 100 Hz.[284] The limit of detection of these sensors was theoretically calculated and demonstrated to show improvement by an

increase in the quality factor Q, e.g. by device geometry or by operation in vacuum. The ΔE-based ME sensors benefit significantly more on an improvement of Q than conventional ME sensors when magnetic noise can be suppressed efficiently.[285] However, the MEMS process flow for vacuum encapsulation includes elevated temperatures which exceed the temperature stability of the magnetic properties of the amorphous FeCoSiB[129]. In this respect, nanolayers of crystalline FeCo/TiN potentially offer defined magnetic properties together with temperature stability up to 600 °C.

The thin film architecture and the nanostructure of the individual components are important parameters for the magnetostriction behavior in those systems. Fukzawa et al.[286] demonstrated that the saturation magnetostriction can be largely influenced by the interface quality and resulting internal stress in FeCo. The structure analysis is therefore decisive to control the micro- and nanostructure of the layered architecture with respect to deposition parameters to achieve a potentially high quality magnetic phase with large magnetostriction as component for ME sensors. Reports on the multilayer architecture including nanostructure analysis have been initially published by Klever *et al*.[287] using Auger electron spectroscopy, X-ray diffraction (XRD) and electron diffraction (ED) techniques as well as high-resolution transmission electron microscopy (HRTEM) imaging. The studied FeCo/TiN architectures demonstrated temperature stability up to 600 °C and a strongly textured and columnar growth was observed. Refering to Klever *et al*., the nanostructural details were subject of two major hypothesis: (i) The multilayer thin film architecture as well as the growth conditions result in the incorporation of a high volume fraction of Fe and Co atoms into an fcc TiN lattice by sequential magnetron sputter deposition, (ii) a (Ti,Fe,Co)N solid solution in a pseudo-fcc crystal structure is formed as a consequence of collision induced atomic mixing and subsequent nanostabilization.

For this work, we used atomic resolution microscopy and report about nanostructure investigation and structural modeling on a similar FeCo/TiN multilayer in order to address the hypothesis. The results imply the formation of a textured superlattice composed of individual layers of FeCo (CsCl-structure) and TiN (NaCl-structure) showing a defined cube-on-cube orientation relation. As a result of the in-plane lattice mismatch, tensile in-plane strain was observed for the FeCo unit cell resulting in the nanostabilization of tetragonal distorted variants.

5.5.4 Materials and Methods

The investigated multilayer film of [FeCo(0.7 nm)/TiN(1.6 nm)]$_{153}$ with a nominal thickness of 400 nm was deposited during former work reported by Klever *et al.* [134] by non-reactive magnetron sputter deposition on a modified Leybold Z550 sputter setup using targets of FeCo

and TiN with 99.9% chemical purity and 150 mm in diameter. For sputtering of multilayers, SiO_2/Si substrates were placed onto a rotatable substrate table at a distance of 50 mm to the target surfaces. The target surfaces were sputter cleaned for 15 min. in a pure Ar atmosphere (6.0 purity) at 0.5 Pa total pressure prior to deposition at a base pressure of $<1 \times 10^{-6}$ mbar in the vacuum chamber. Preconditioning of the substrate surfaces took place under the same conditions for 20 min at a substrate bias voltage of -320 V sustained by an RF plasma. The Ar total pressure during the film deposition process was 0.2 Pa in order to sustain a DC plasma in front of the TiN target by supplying 700 W DC power while maintaining a RF plasma (250 W power) in front of the FeCo target. After determining the depositon rate, the multilayer was deposited by rotating the substrate in between the center positions of both targets. An annealing step was performed after deposition for 60 min. in vacuum (p < 1x10-8 mbar) at 600 °C in a static magnetic field of $\mu_0 H = 50$ mT.

The structure analysis on one individual as-deposited multilayer and one individual heated multilayer is performed using methods of transmission electron microscopy (TEM) and X-ray diffraction (XRD). The multilayers are deposited in the same process run, so it is assumed that they were structurally similar in the as-deposited state. In this respect, HRTEM enables the study of the atomic structure whereas the selected area electron diffraction (SAED) and energy-dispersive X-ray spectroscopy (EDS) in scanning mode give microstructural and spatially resolved chemical information of the multilayers, respectively. Large scale average information about the microstructure is obtained by Bragg X-ray diffraction, providing details about the crystallinity and strain on a macroscopic scale.

In addition, X-ray reflectivity (XRR) can assess the atomic and molecular scale interface structure even in the absence of a long-range order by providing access to the electron density across the entire multilayer. Thus we obtained average and localized data on the multilayer structure, the layer sequence and surface composition.

HRTEM and SAED data are collected on a Titan 80-300 microscope with an image-side spherical aberration (C_S)-corrector and sub-nanometer resolution. HRTEM micrographs are recorded under negative C_S imaging (NCSI)[288] conditions exploiting the benefits of having a favorable contrast transfer function to allow for a direct interpretation of the projected crystal structure without the need to correlate the HRTEM micrographs with image simulations[289]. Such imaging conditions reduce the delocalization of object information to below the information limit of the microscope and generate an image displaying atomic columns as bright dots on a dark background. Scanning (S)TEM measurements including EDS are performed on a FEI Titan³ G² 60-300 kV microscope operating at 300 keV. The TEM specimen preparation

is performed by a focused ion beam (FIB) routine on a FEI Helios 600 dual beam FIB-SEM machine equipped with an Omniprobe micromanipulator following a standard lift-out procedure and subsequent ion-beam milling at 30 kV, 0.46 nA and 5 kV, 81 pA in the final stages to reduce possible ion-beam damage to the sample surface. Kinematic simulation of electron diffraction patterns and high-resolution phase contrast images are computed to verify the experimental data and NCSI imaging conditions using the JEMS program[290]. Processing of HRTEM micrographs included noise filtering[291] and is carried out via the *Gatan* Digital Micrograph 2.3 software package (DM).

The XRD experiments are performed on a Rigaku Micromax rotating anode radiating at the characteristic Cu-Kα energy with a wavelength of 1.54 Å. The beam size was 1x1 mm^2 (horizontal and vertical) with a resolution of $2x10^{-4}$ $Å^{-1}$. The measurements are performed on a standard four circle diffractometer setup using the SPEC diffractometer software. Compution of experimental data sets is carried out using *MATLAB* and *xrayutilities (build 1.5)* program packages.

Pole-figure measurements are performed on a Rigaku SmartLab 9kW XRD utilizing a rotation anode radiating at the characteristic Cu-Kα energy with a wavelength of 1.54 Å. The beam is scattered using a parabolic mirror to create a parallel X-ray beam at a tube voltage of 45 kV and a tube current of 200 mA. Construction and evaluation of the pole-figures is performed with the program Rigaku 3D Explore Version 3.1.1.0.

5.5.5 Results and Discussion

5.5.5.1 Microstructure of FeCo/TiN thin films

The average microstructure of one as-deposited and one annealed FeCo/TiN multilayer is characterized by the combination of XRR measurements, Bragg XRD scans and SAED. The details of the nanostructure inherent to the FeCo/TiN mulitlayer are analyzed by structure models derived from electron and X-ray diffraction data along with HRTEM as discussed in the following. The temperature induced changes to the microstructure caused during the annealing procedure are discussed.

The XRR data collected on both, the as-deposited and the annealed multilayer are presented in Figure 5.19 a). The XRR is plotted up to wave vector of 0.7 $Å^{-1}$ to concentrate on the layer thickness. The electron density (Figure 5.19 b) is calculated from a model consisting of a sum of error functions modeling the layer structure. The fit was realized with the Parrat algorithm[75] as model function and was refined using the Levenberg-Marquardt algorithm. The Fourier

transform of the electron density was compared with the measured intensity and the electron density model recursively to obtain a good fit.

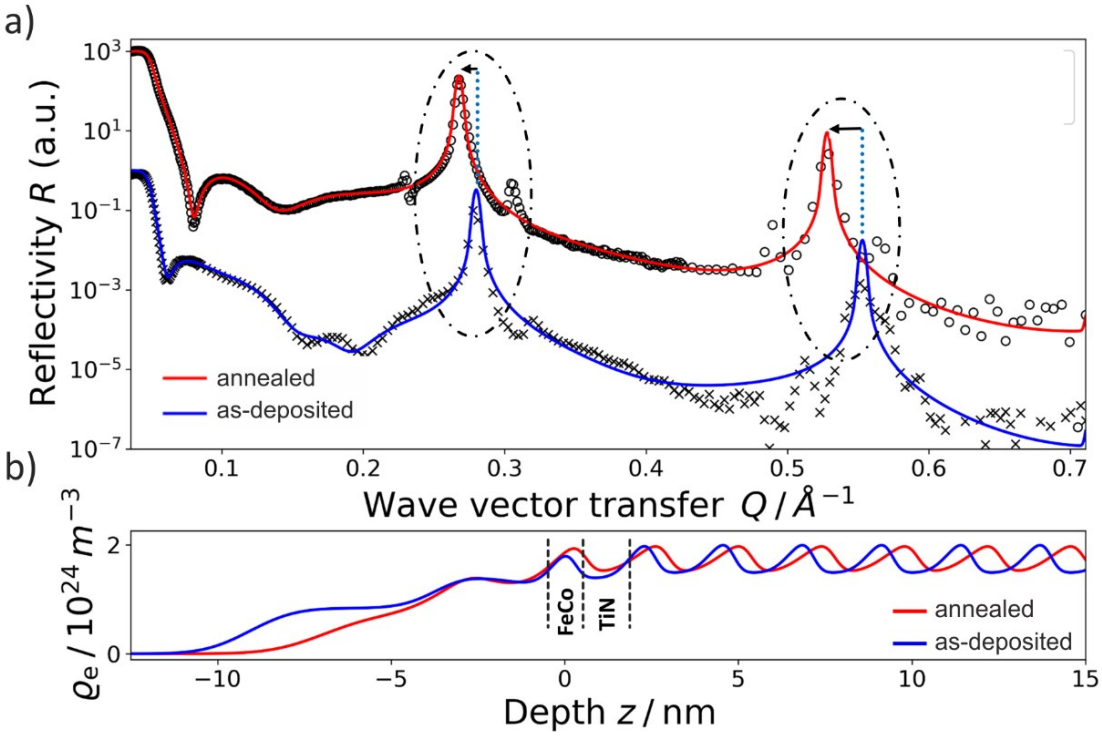

Figure 5.19: a) X-ray reflectivity curves of the as-deposited and annealed FeCo/TiN multilayers. The data indicates superlattice reflections at ~0.27 Å^{-1} and ~0.52 Å^{-1} moving towards smaller values as a consequence of annealing. b) Calculated electron density variation denoted to the TiN capping layer and oscillations of the periodic superlattice. The depth value of 0 indicates the second FeCo layer counted from the surface.

The reflectivity curves feature characteristic superlattice reflections, which represent the first and second order reflections of constructive interference of a multilayer on a solid substrate. The positions of these reflections are characteristic for Λ, the thickness of a single FeCo/TiN bilayer from the superlattice. After heating, the superlattice reflections show a position shift to smaller wave vectors, indicating a non-reversible lattice expansion relative to the as-deposited multilayer. From fitting the reflectivity data,the calculations showed an increase of the superlattice periodicity s from Λ = 22.826±0.003 Å (d_{FeCo} = 6.8±0.7 Å and d_{TiN} = 16.0±0.7 Å) for the as-deposited multilayer up to Λ = 23.915±0.003 Å (d_{FeCo} = 8.3±0.4 Å and d_{TiN} = 15.6±0.4 Å) for the annealed multilayer. According to the fit results the vertical thickness d_{FeCo} of the FeCo layers in the superlattice increases by a remarkable value of 22 %. The larger total Λ implies an expansion of ~4.8 % in film growth direction and may be explained by temperature induced lattice deformations such as the release of tensile lattice strains or unforeseen structural rearrangements. However, the measured periodicity length is in good agreement with the numbers reported by Klever (Λ = 2.6 nm). This impact of annealing is

further supported by SAED analysis, given in Figure 7.25, showing a position shift of the superlattice reflections in agreement with an increase in Λ. The calculated thickness of the individual components matches on average to six monolayers of FeCo (d_{FeCo} = 6.8±0.7 Å) and seven monolayers of TiN (d_{TiN} = 16.0±0.7 Å). The additional oscillations besides the superlattice reflections visible e.g. at 0.31 $Å^{-1}$ in the annealed multilayer, correspond to a typical length of 74 ± 5 Å and 79 ± 5 Å for the as-deposited and annealed multilayer, respectively. This modulation can be attributed to the combined thickness of the TiN capping layer and the first FeCo and TiN layers at the surface, which show signs of detoriation after annealing, as incidated by a lower electron density calculated and presented in Figure 5.19 b).

In more detail, the electron density which is derived from XRR (Figure 5.19 b) shows a continuous increase in the first 10 nm from the film surface before transforming into oscillations of the same amplitude. With respect to the as-deposited multilayer, the oscillation period of the electron density is observed to increase for the annealed multilayer in consequence of the observed superlattice expansion. The electron density distribution at the surface accounts for a thick TiN capping layer deposited onto the last bilayer unit. The slow increasing electron density profile indicates high surface roughness of the capping layer, characterized by an amplitude of 10.3 ± 0.7 Å and 12.2 ± 0.4 Å for the as-deposited and annealed multilayer, respectively. The overall TiN capping layer thickness was measured giving 57.0±1.7 Å and 36.0±1.0 Å for the annealed multilayer sample. The smaller observed thickness, accompanied by lower atomic density and the increased surface roughness is attributed to deterioration of the protective capping layer by annealing.

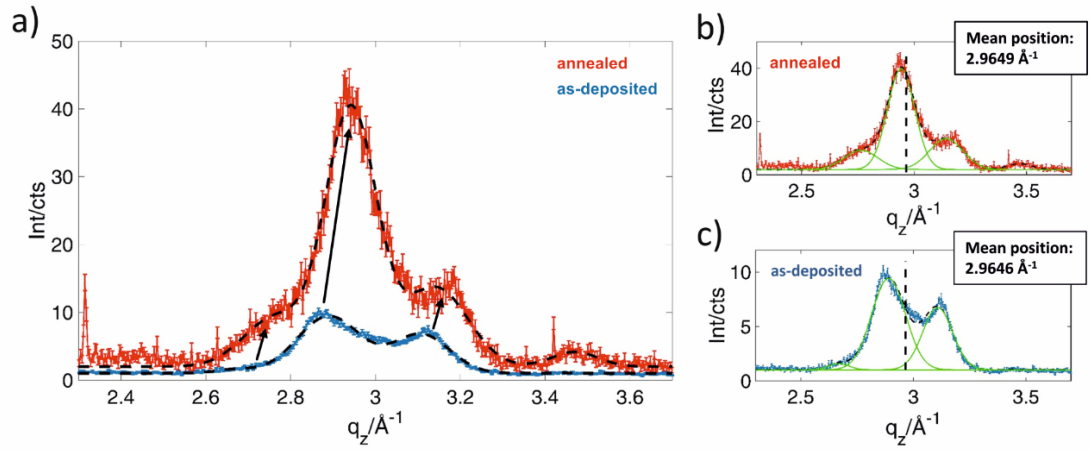

Figure 5.20: a) Diffracted intensity around the TiN (002) Bragg reflection. Laue oscillations are observed due to the periodic superlattice. The superlattice reflection intensity distribution is shown as a function of the scattering vector *q*. (blue) as-deposited and (red) heated multilayer. b-c) Fit of the peak intensity modulation by three Gaussian functions and linear background offset (green lines). The *q*-position of the TiN (002) reflection is indicated with the vertical dashed lines.

Using X-ray Bragg diffraction, the crystal structure of the TiN layers was investigated by measuring the reciprocal space at the position of the TiN (002) reflection for the as-deposited and heated multilayer. In the following discussion we will always refer to the (002) TiN reflection as the majority component of the multilayer when addressing the out-of-plane reflections of the superlattice, if not otherwise identified. This diffraction data and the according fits are provided in Figure 5.20. The displayed modulation of the intensity distribution around the measured Bragg position are described as Laue oscillations of 0.45 $Å^{-1}$ corresponding to a measure of 13 Å, which is in the same order of the TiN layer thickness in the superlatticeas discussed in the XRR section above. [287,292] The fits are calculated by a least-square refinement of sum of three Gaussian functions to the data. To determine the original (002) Bragg reflection wave vector position, the mean position of the three reflections was determined to be 2.9646±0.0013 $Å^{-1}$ for the as-deposited and 2.9649±0.0013 $Å^{-1}$ for the annealed multilayer. This correlates to a lattice constant of $d_{(002)}$ = 2.12 Å, which is in excellent agreement with the calculated position of the TiN (002) reflection and indicates TiN in its NaCl-type crystal structure. Further, the positions of the associated superlattice reflections around the TiN (002) reflection position are subjected to shifts in wave vector and intensity. That might hint to temperature related changes of the superlattice structure reflecting in the modulation of *c*-axis intensities. However, there was no definite observation of chemical intermixing on annealed specimens retaining the multilayer heterostructure (see Figure 5.21 g).

The shape and the spacing of the intensity modulation reflects the observed increase of Λ. A single FeCo Bragg reflection (or its Laue oscillation) could not be evidenced by XRD at its theoretical position observed for thick films or bulk samples. It is reasonable to suppose that the lack of intensity is due to poor long-range crystallinity of the FeCo component or due to changes of the CsCl-type crystal structure within the superlattice.

Low magnification scanning TEM images are shown in Figure 5.21 a) and Figure 5.21 b) to provide a direct impression of the thin film morphology. The iterative sputter deposition of TiN and FeCo material directly onto the native Si/SiO_2 substrate is promoting a discrete multilayer film with columnar microstructure perpendicular to the substrate surface.

The diffuse intensities distributed on concentric rings of Fast Fourier Transform (FFT) pattern calculated from HRTEM micrographs evidence the absence polycrystalline texture within the first 10 bilayers of film growth as shown in Figure 5.21 c). In comparison, the FFTs from any region above these initial layers describe the evolution from randomly oriented nanocrystalline grains into a highly *c*-textured crystalline structure (see Figure 5.21 d). The well-separated intensities in the FFT pattern display the formation of columnar grains (or regions) describing

a *c*-axis texture, similar to thin films of AlN[281]. The individual columns favor defined azimuthal rotations around the *c*-direction described below and in Ref.[287]. The individual columns can be visualized by mapping out the origin of intensity of the in-plane (020) and (-220) reflections, corresponding to columns with cubic TiN [100] and [110] orientations (Figure 5.21 e and Figure 5.21 f).

The morphology of the layers across *c* is characterized by distinct roughness. From the overview STEM images recorded at the bottom and top surface of the film, a higher roughness is observed within the first 30 nm of film growth and is flattening out with increasing film thickness. At the top side of the 400 nm thick film, quasi-parallel layers without noticeable roughness are established.

The elemental maps presented in Figure 5.21 g) show the distribution of Fe, Co and Ti for the heated multilayer. According to the EDS maps, the periodicity of FeCo and TiN layers is preserved after annealing showing no direct evidence of temperature effects such as interdiffusion or recrystallization accompanied with a breakdown of the layered structure.

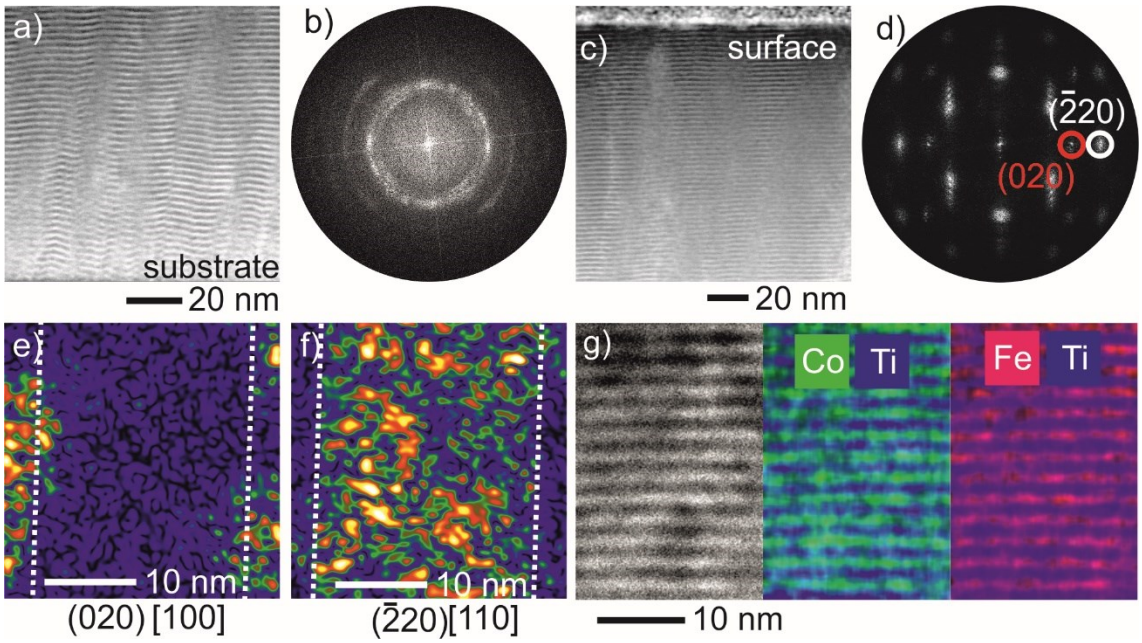

Figure 5.21: Structure evolution of the FeCo/TiN multilayer . a,c) Overview STEM images recorded close to the substrate interface (a) and at top surface (c). b,d) FFT analysis of regions close to the substrate and film surface on the as-deposited multilayer. b) FFT obtained close to the substrate shows almost no specific texture. d) FFT obtained close to the film surface shows a strong *c*-texture. e,f) Intensity maps of the phase component of the respective (2-20) and (020) reflections visualize high intensity (bright regions) in columnar domains with [110] and [100] crystallographic orientation. The white dashed lines guide the eye to show the columnar domains g) EDS mapping showing the chemical distribution of Fe, Co and Ti in a multilayer architecture (annealed multilayer).

5.5.5.2 Description of Orientation Relationships

SAED experiments yield information about the average local structure of the annealed multilayer composed of layers of TiN and FeCo. The SAED pattern is presented in Figure 5.22 a) and reflects the columnar microstructure showing the superposition of multiple zone axis (ZA) patterns specified by the [100], [110], [210] and [310] notations with respect to the principal component as already described in Ref.[287] and presented in Figure 7.26. A columnar microstructure with small grain size is supported by the growth zone model by Thornton or Anders for small argon pressure and no substrate heating.[293,294] In extension of a simple superposition of individual ZA patterns the experimental SAED pattern features periodic intensity distributions along *c* (see Figure 5.21 d) and Figure 5.22 a). This intensity modulation is indicative for a defined structural connection between the lattices of FeCo and TiN establishing a superlattice with a well defined periodicity length of $\Lambda \sim 2.26$°nm, which is in excellent agreement with XRR experiments.

In addition, the tipped, elongated and diffuse shape of the reflections is rationalized by a small angle preceding rotational misalignment of the *c*-axis of the columnar grain structure[295,296] or by layer roughness. Overall, the SAED experiment demonstrated highly *c*-textured layers of FeCo and TiN consisting of at least three domains showing a dominant fibre texture[297]. The dominant *c*-axis fibre texture of the superlattice is further supported by pole-figure (PF) measurements of the as-deposited and annealed multilayer shown in Figure 7.27.

The bilayer thickness Λ and the different columnar domains of the as-deposited multilayer are imaged by aberration corrected high-resolution microscopy. Representative HRTEM micrographs are presented in Figure 5.22 b) and Figure 7.28 showing the impact of aberration correction on the phase contrast micrographs, which allows a clear identification of individual layers. The HRTEM micrograph of Figure 5.22 b) displays individual layers of TiN and FeCo with nearly monoatomic flat interfaces of the as-deposited multilayer. From the inset, two discernable oriented lattices with different out-of-plane lattice constants and a lattice orientation corresponding to the [100] and [110] orientations for the FeCo and TiN layers are identified, respectively. Further analysis of the periodic variations of the phase contrast in HRTEM micrographs presented in Figure 7.29 hint that, at least locally, FeCo crystallizes in its low temperature ordered B2 phase forming a monoatomic interface with opposing Co and N atoms. These results suggest, that the in-plane lattice mismatch of 5.2% between these two structures is compensated by coherent in-plane lattice strains at the interface in one or both components which is resulting in a strained superlattice[298]. A cube-on-cube relationship is expected in a wide range of materials[299].

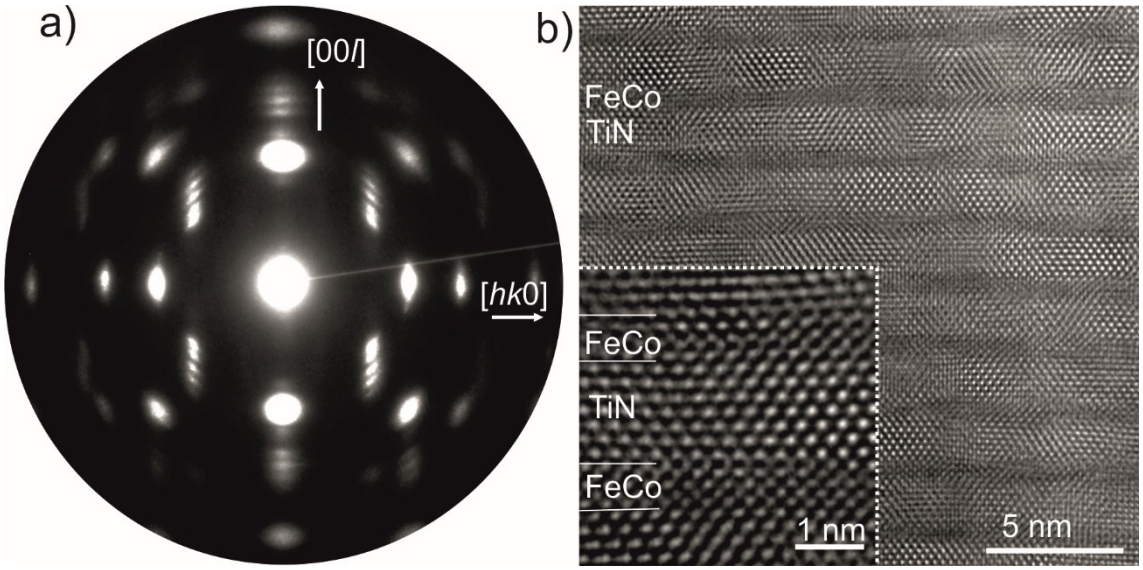

Figure 5.22: a) SAED pattern recorded at the center of the as-deposited multilayer film. The SAED pattern is composed of the superposition of multiple zone axes [*uv*0]. The domains particularly display crystallographic orientations with respect to the TiN lattice of [100], [110] and [310] and show superlattice reflections along the [00*l*] direction arising from the nanoscale repetitive layering scheme with their corresponding FeCo counterpairs in [110], [100] and [210] orientation, respectively. b) HRTEM micrograph showing individual layers of FeCo and TiN. On average, the individual FeCo layers extend over two unit cells (~7 Å) and the TiN layers over three unit cells (~16 Å).

5.5.5.3 Structural Modeling

The cube-on-cube relationship is described by a 45° rotational alignment between the experimentally observed TiN[100] and FeCo[110] oriented lattices and serves as starting point for structural modeling using the crystallographic relationships demonstrated in Figure 5.23 a) and b). However, for an in-plane lattice misfit of 5.2 % between the cubic structures large strains are expected at the interfaces. In some cases, the major amount of stress is compensated by only one component until a layer thickness of several angstroms is reached without formation of misfit dislocations. This phenomenon called *pseudomorphism*.[300] In this special case of epitaxy, the constrained in-plane lattice promotes the nanostabilization of metastable phases, e.g. tetragonal distorted variants[301–303]. From the experimental data, an in-plane lattice expansion from 2.85 Å to about 2.96 Å is determined for FeCo, which is matching with the TiN in-plane lattice constants. Based on these results, the pseudomorphic growth characteristic of the superlattice is introduced into a model describing the average structure of the as-despoited superlattice structure (Figure 5.23 c).

To relate the nanostructure data to the electron diffraction and X-ray scattering observations, a structural model for the as-deposited superlattice is designed and used for subsequent simulation. The design of this supercell model is described in the following steps: (1) A

modification of the cubic [110]-oriented TiN unit cell is constructed to provide a common description of the components in [100] orientation. The new tetragonal TiN unit cell is described by lattice parameters of a^t and b^t = 3.00 Å and by keeping c_{TiN} = 4.25 Å constant. (2) The [100]-oriented TiN unit cell is tripled in *c*-direction and connected to two unit cells of [100] FeCo at the (001) face. (3) In agreement with experimental evidence a coherently in-plane strained FeCo lattice is assumed, in approximation to a pseudomorphically grown heterostructure. Hence the a^t and b^t in-plane lattice constants are set to 3.00 Å. (4) In a simple physical consideration, the expansion of the in-plane lattice of the FeCo unit cell is accompanied by compressive strain on the out-of-plane parameter to preserve a constant volume. Indeed, atomic distances of 2.65 Å - 2.75 Å were measured in *c*-direction on the HRTEM data between. Further spacings at the interface could be obtained as well and are implemented in the model using a compressed lattice parameter c_{FeCo} = 2.65 Å, which was the lowest observed lattice parameter to create a strongly tetragonal distorted FeCo variant. Overall, a structural model is set up by three tetragonal unit cell variants of the undistorted cubic TiN lattice connected to two tetragonal distorted unit cells of FeCo with total unit cell dimensions of a_{SL} = 3.00 Å, b_{SL} = 3.00 Å, c_{SL} = 22.00 Å. Implementing an unstrained c_{FeCo} = 2.85 Å into the supercell model results in minimal changes of the reflection positions and intensity due to the larger c_{SL} = 22.60 Å. Considering a constant unit cell volume and a resulting lattice parameter of 2.74 Å, it has to be assumed that the superlattice is not strained equally but is varying in between 2.85 Å and 2.65 Å giving rise to the diffuse superlattice reflections. The described incremental steps are assisted by knowledge obtained from kinematic simulation of electron diffraction pattern to check the models' validity. Note, one possibility to transfer this model to the annealed samples would require the introduction of further tensile lattice strains in the out-of-plane direction of the superlattice. However experimental evidence by direct imaging methods is missing for the specific multilayer sample.

The superposition of single kinematic simulations of zone axis patterns corresponding to the three major domains using the described supercell model is given in Figure 5.23 d) and shows acceptable agreement with the experimental pattern (Figure 5.22 a). The individual presentation of the rotated supercell model and the simulated ED patterns are shared in Figure 7.30 for completeness. However, the supercell model is refined comparing highly localized measured HRTEM data with average SAED data and is regarded only as an approximation to the average structure. Further, the simulation is only exact to display the position of superlattice reflections but fails to quantify the experimental reflection intensity, because the simulation based on the supercell as single crystals and not as domains of strongly confined width.

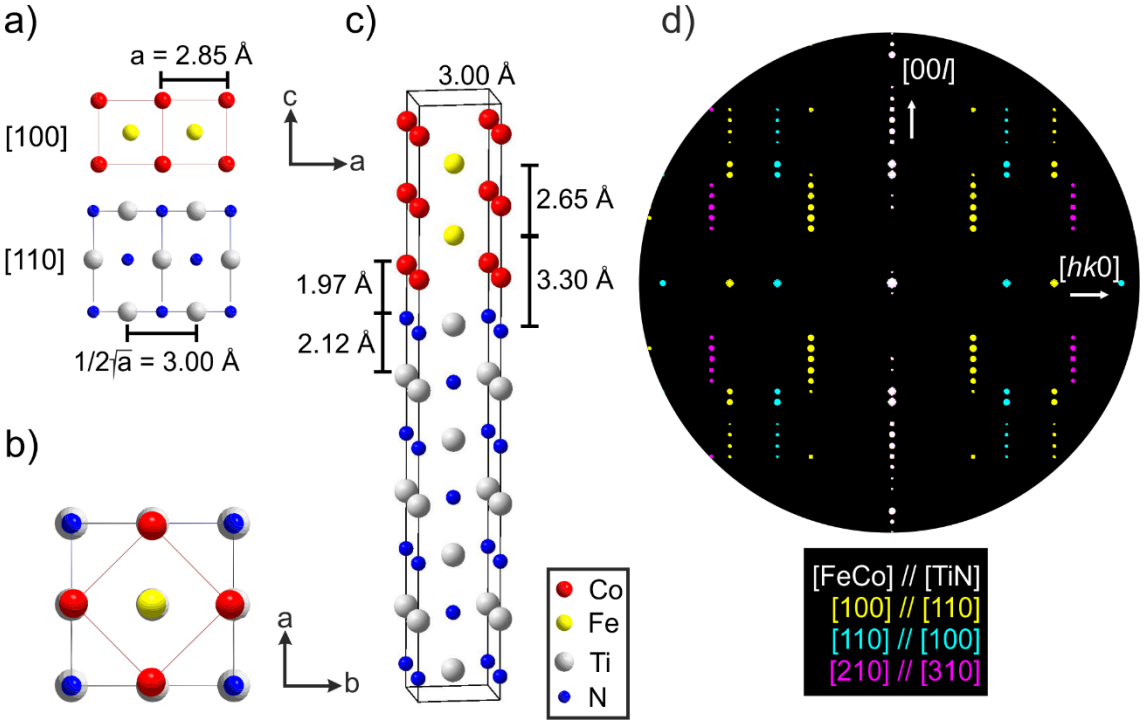

Figure 5.23: a) Cubic unit cells of the FeCo and TiN lattice in [100] and [110] orientation. b) 45°-rotated cube-on-cube relationship in top-view showing a lattice mismatch of 3.00 Å // 2.85 Å. c) Supercell model based on pseudomorphic growth by in-plane lattice expansion of FeCo and compression of the *c*-parameter. d) Kinematic simulations of electron diffraction intensity for each zone axis based on the epitaxial relationship of the supercell model are superimposed in the presented pattern.

5.5.5.4 Verification of compensated in-plane strain by geometric phase analysis

Besides the agreement between the position of periodic reflections arising in supercell based simulations and the experimental SAED pattern pointing to the formation of a superlattice with similar in-plane lattice constants, the variation of the in-plane lattice parameter *a* was calculated by geometric phase analysis (GPA)[263,304] mapping the in-plane strain distribution in the superlattice with respect to the TiN lattice The GPA map was calculated using the (002) and (-220) reflections of the FFT to display the variation of the in-plane component with respect to the strain tensor as depicted in Figure 5.24. The mapped in-plane strain distribution shows alternating tensile and compressive strain along the thin FeCo layers on a scale of ±1% with respect to the reference TiN lattice (Figure 7.31), which is a deviation of only about 0.03 Å. This finding reflects the in-plane lattice expansion of the tetragonal distorted FeCo unit cell determined by SAED, HRTEM and subsequent modeling under the premise of the pseudomorphic growth scheme. Further, indicators of in-plane strain are visualized in the TiN itself presumably indicating small angle tilts between individual grains.

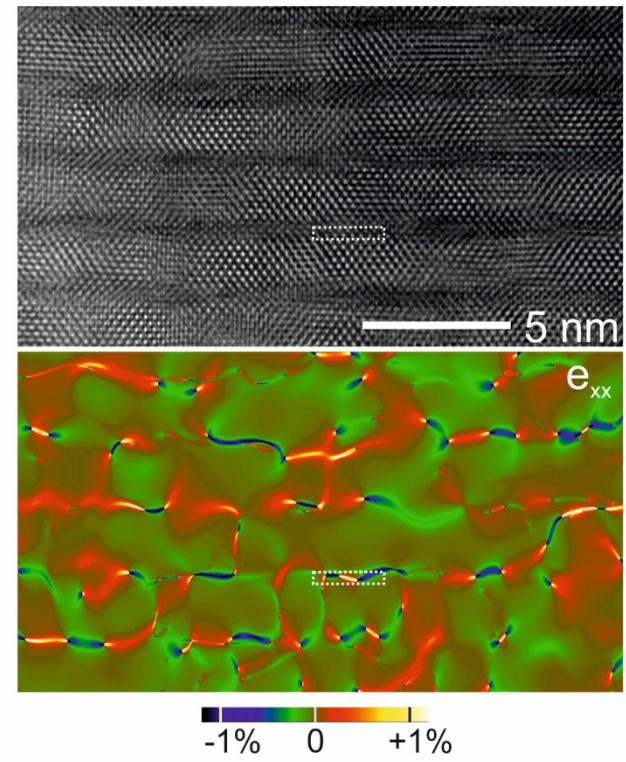

Figure 5.24: HRTEM micrograph and corresponding map of in-plane lattice variations with respect to the TiN lattice demonstrated by geometric phase analysis. Almost negligible tensile and compressive strains alternate at the location of FeCo layers demonstrating pseudomorphism. Strain within the TiN layers is related to small mistilts within the cubic lattice. The dashed box marks the position of strain profiles depicted in Figure 7.31.

The nanostabilization of body centered tetragonal (bct) variants of FeCo with c/a >1 is intended to induce large perpendicular uniaxial magnetic anisotropies in ultra-thin nanoscale films leading to a huge magnetic hardening of FeCo films.[301,305–308] The required lattice deformation can be achieved by the right choice of underlayer, which should promote an in-plane compressive strain to the FeCo unit cell.[309–311] However, with increasing film thickness, the applied lattice strains quickly relax after some few nanometers (e.g. 3.4 nm) and the large perpendicular uniaxial magnetic anisotropy is lost.[311,312] Such film relaxation effects can be impeded by the incorporation with impurity atoms such as V, N or C to stabilize bct FeCo structures in films with a thickness of over 100 nm.[313,314]

Contrary, there are also several approaches of strain engineering in order to soften the magnetic properties by thermal annealing, adequate underlayers or a multilayer architecture in combination with a non-magnetic or ferromagnetic material. In case of underlayers or multilayers, the magnetic softening can be reasoned by the simple decrease of grain size according to Hoffmann's ripple theory.[277,315,316] In this respect, multilayers of Co/FeCo starting on a layer of Co introduces smaller grain growth within the FeCo layer resulting in a very low in-plane coercivitiy along the hard axis in comparision to FeCo underlayer.[277] The

same was observed for FeCo layers separated by Ag interlayers.[279] In a different approach, the in-plane magnetic anisotropy was reported to be reduced by the application of an external tensile strain in films of FePt.[317] In the former study on the magnetic properties on identical $[FeCo/TiN]_{384}$ films (Λ = 2.6 nm) deposited up to a film thickness of 1000 nm using the identical process, a coercive field of 0.30 mT with an in-plane anisotropy was reported.[134] The effect of layer thickness was also demonstrated in comparison to slightly thicker layers (Λ = 4.3 nm) of FeCo of showing a coercive field of 1.33 mT. It is expected, that the reduction of the coercive field is related to the smaller layer thickness. But the new insights on the atomic structure of FeCo in these nanolayers at least opens speculation about the contribution of the tetragonal distortion ($c/a < 1$) to the in-plane anisotropy. However, since atomic scale investigations on the FeCo structure are missing on these reported films, we can only speculate about the exact layer thickness and the critical layer thickness of FeCo on TiN, where relaxation of the tetragonal variant occurs. Also, there are no reports to our knowledge about the influence of an in-plane tetragonal lattice distortion with $c/a < 1$ on the magneto-crystalline anisotropy energy or its impact in comparison to the grain size. To differentiate between both contributions, the deposition of epitaxial lattice matched films, e.g. FeCo[100]/Mo[110] with identical layer thickness but cubic FeCo unit cells might be essential.

5.5.6 Conclusion

The microstructural evolution and the nanostructure growth epitaxy in sputter deposited FeCo/TiN ultra-thin films with bilayer periodicity of 2.26 Å have been investigated using the combination of aberration corrected TEM imaging, X-ray scattering and electron diffraction methods supported by modeling and structure simulations. These studies shed new light on the nanostructure of sputter-deposited growth of nanolayers of FeCo/TiN superlattices and result in the following observations:

- FeCo/TiN multilayers exhibit a columnar microstructure which is described by a strong fibre texture which is evolving after some nanometers.
- The FeCo/TiN nanolayers form a defined superlattice which was characterized by XRD and TEMA 45°-rotated cube-on-cube orientation relationship between FeCo and TiN was verified, enabled by pseudomorphic growth resulting in tensile in-plane strain acting on the FeCo lattice to match with the TiN (001) plane. In this scheme, tetragonal distorted variants of FeCo are stabilized.
- Temperature induced lattice changes in FeCo/TiN multilayers have been observed and discussed by both electron diffraction and X-ray scattering methods.

6. CONCLUSION

CRC 1261 - Magnetoelectric Sensors: From Composite Materials to Biomagnetic Diagnostics aims to develop a functional sensor for medical applications. The main goal of this thesis was to investigate promising materials and effects for biomagnetic field sensors and link the findings to sample behavior. To achieve this goal a variety of X-ray techniques were employed to visualize structure and strain. The results obtained strengthen our understanding of, both, the materials and effects investigated and will help to improve the design of biomagnetic field sensors within the CRC. Of great interest was the piezotronic effect, as it is a possible path to enhance the sensitivity of biomagnetic field sensors and specifically the investigation of ZnO, as a model system for piezotronic devices. Further topics were structural investigations of etched GaN samples and the impact of thermal treatment on FeCo/TiN multilayer structures.

In these experiments, multiple X-ray techniques were utilized. The bulk crystalline structure was investigated by XRD while XRR gave access to the near surface sample structure. To achieve spatially resolved crystal structure measurements, scanning nanofocus XRD was used. This technique, a more sophisticated version of XRD, utilizes a small intense X-ray beam, accessible at modern synchrotrons, and combines it with a scanning approach to cover a wide sample area, achieving a spatially resolution of around 100 nm or below while enabling a strain resolution of $\sim 10^{-5}$. For an even higher spatial resolution close to 10 nm, the coherent scattering technique CXDI was used and gave the possibility to visualize the strain in three dimensions.

During the thesis, the sample holder design, as discussed in Chapter 4.1, was continually developed. The original design of the 3D printed sample holders, the mounting procedure and materials, were improved over the years and adopted to changing experimental needs. This evolution resulted in the development of the SEFiR sample holder design, with only one fixed end compared to both ends fixed as for the preliminary sample holders, relieving the mechanical stress from the mounting procedure and enabling CXDI experiments on thin samples.

The multiple beamtimes and experiments, resulted in four publications in peer-review journals and one manuscript, included in chapter Results5. The experiments were carried out at third generation synchrotron sources, Petra III at the DESY in Hamburg and the Advanced Photon Source near Chicago. Additional X-ray measurements took place at the FRED laboratory X-ray source based at Magnussen group laboratory in the institute of experimental and applied physics in Kiel University.

In an initial study, nXRD and electrical characterization were combined to investigate the relation between crystalline structure and electrical behavior of ZnO based Schottky contacts.

The strain distribution was spatially resolved visualized by nXRD while the electrical properties, in particular, the barrier height and ideality factors of the Schottky contact, were quantified by *I-V* characterization. The findings highlighted the impact of the crystalline quality on the electrical properties of the Schottky contact. The data show that a ZnO rod with a well-defined strain distribution and solely non-abrupt deviations in the lattice parameter exhibits ideal Schottky barrier behavior with excellent rectifying diode characteristic. In contract, a rod where high strain and multiple coherent scattering domains are observed displays unwanted ohmic like behavior. This is attributed to an increased defect rate. An analytical model could describe the strain distribution in the rod.

The second study considered the modulation of electrical conductivity and lattice distortions in GaN samples grown by HVPE. A combined TEM and XRD approach revealed differences in as deposited and PEC etched samples. Photoluminescence measurements showed an 60 % increase of the carrier concentration in PEC etched GaN compared to as deposited material. XRD and TEM structure analysis highlight an inelastic strain in distortions of the wurtzite structure. Further, the XRD measurements reveal a deviation of around 1° from the ideal hexagonal structure for the average GaN crystals, while this deviation may rise to up to 2° on a nanoscale, observed by TEM. It is concluded that the lattice deviations result from misfit strains, due to the high growth rate and that they can be slightly released by PEC etching.

In a third, complementary TEM and CXDI study, the strain distributions in ZnO microstructures coated with gold were visualized to investigate the impact of the Schottky contact and piezotronic effect on the crystal structure. Both, a bulk and an interface component are present in the reconstructed strain distribution of the CXDI measurements. A qualitatively comparable interface strain is seen in GPA results from TEM micrographs. It is likely that the interface strain results from the Schottky contact formation, as the measured width close to 39 nm, is in accordance with the calculated depletion width for a ZnO Schottky contact. The observed asymmetric bulk strain is attributed to a screening of electric potential and depletion of electrons, as predicted by a previous simulation for a bent piezoelectric rod.

A subsequent CXDI study investigated the strain distribution in a ZnO rod, partly coated with magnetostrictive FeCoSiB and exposed to an external magnetic field. The advanced SEFiR sample holder was used to build a model piezotronic inspired magnetoelectric sensor. The design allowed investigation of both the strain and electrical properties of the sensor. Electrical investigation showed that FeCoSiB coating provides an ohmic contact on ZnO and additionally that an applied external magnetic field causes an increase of the measured Schottky barrier height and a decrease of the ideality factor, proving that this design is suitable for use as a model

piezotronic magnetic field sensor. CXDI on the same ZnO rod indicates a distinct magnetic field induced change of the strain distribution in the rod, possibly, the cause for the piezotronic change of the electrical properties.

In a fifth study, thin FeCo/TiN multilayers were investigated by means of TEM and X-ray techniques to distinguish the crystalline and multilayer structure and examine the effect of annealing. In these experiments multiple X-ray techniques were utilized. The bulk crystalline structure was investigated by XRD, while XRR gave access to the near surface sample structure. The FeCo and TiN layers were found to form a superlattice with a columnar microstructure with a fibre texture and a cube-on-cube orientation is observed. Electron diffraction simulation predict that the FeCo layers are deformed by a tensile in-plane strain to match their lattice parameter with the TiN. The XRR results show a ~4.8 % expansion of the superlattice thickness due to the annealing, this staggering change may be caused by release of strain in the FeCo layers.

In summary, XRR, XRD, nXRD and CXDI were successfully utilized in the presented studies to investigate and visualize the crystal structure of ZnO and link these results to the Schottky contact, magnetostrictive and piezotronic behavior. Further, crystal structure changes were observed in etched GaN and for annealed FeCo/TiN multilayer structures. The extraordinary high strain resolution of those X-ray techniques has proven to be highly beneficial for the measurement of small crystal structure changes, while the three-dimensional visualization of strain achieved by CXDI measurements exhibit an extraordinary tool for investigations of complex strain distributions. The findings from these studies of model sensor systems will support the knowledge-based design of biomagnetic field sensors in the CRC 1261.

A perspective for further experiments succeeding this work is to extend the current studies to more complex sensor designs. Planned X-ray scattering pair distribution function analysis will expand investigations to amorphous components of magnetoelectric sensors. Phytography is another promising X-ray scattering technique. It is a sophisticated extension of CXDI and enables the investigation of much larger specimen. An interesting subsequent experiment may be to combine spatially resolved strain distribution from phytography, with impedance spectroscopy on Schottky barrier width. Combining both techniques may give access to a better understanding of the microscopic changes near the Schottky contact. Furthermore, a transition from ZnO as the model system to other sensor materials, used more prominently within the CRC, such as GaN and AlN, may have a big impact on the overall success of the CRC 1261.

With advances in machine learning and artificial neural networks, these may be a key to faster and better analysis of the obtained measurements. Foremost, the computationally intensive and slow solution of the inverse problem for the reconstruction of the strain distribution from the measured Bragg reflection in CXDI experiments may benefit immensely from such a development.

7. Supporting Information

Local Strain Distribution in ZnO Microstructures Visualized with Scanning Nano X-ray Diffraction and Impact on Electrical Properties

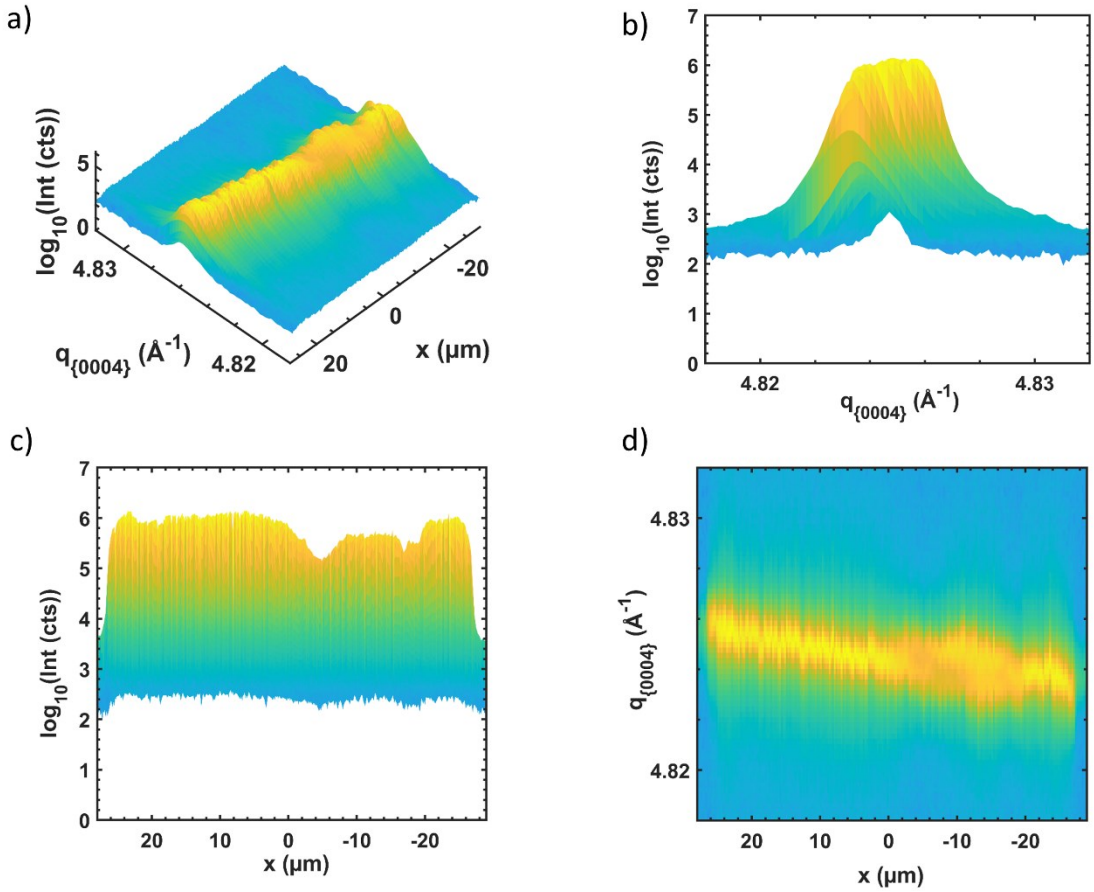

Figure 7.1: Multiple views of the strainmap in Figure 5.1 b). a) Shows the above presented strainmap view, b) and c) display the intensity of the Bragg reflection as a function of the strain and spatial linescan position x, respectively. d) Displays the strain as a function of the position x including a color-coded intensity.

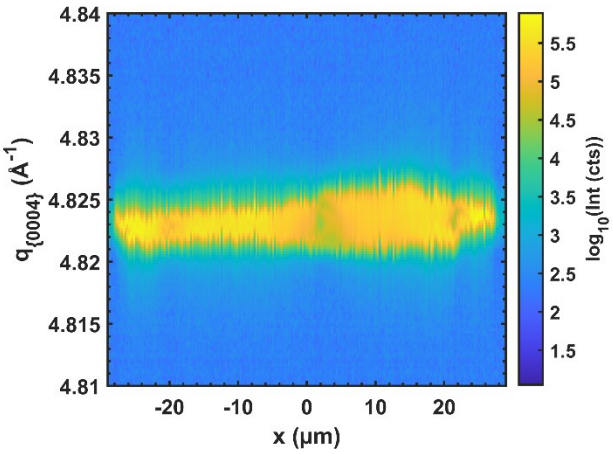

Figure 7.2: Strainmap from an uncoated part of rod R1. The position on the rod is further separated from the connection point to the sample holder, compared to the strainmap in Figure 5.2 g) and may be an explanation for the less pronounced linear change of the strain distribution. This gives rise to the idea that the rod bending is induced by the mounting.

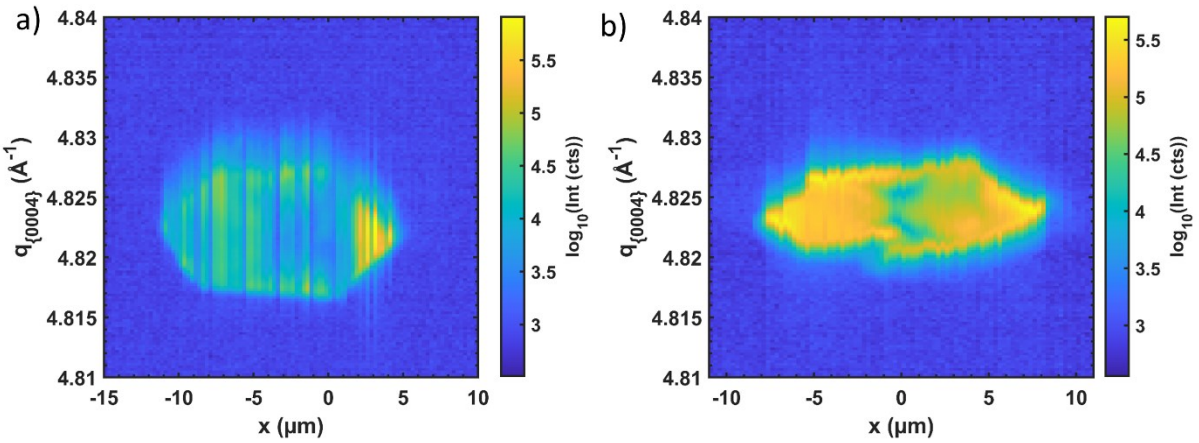

Figure 7.3: Strainmaps collected on rod R2, a) uncoated part and b) Ag coated part. A hexagonal strainmap appearance is found again, compare to Figure 5.2 h).

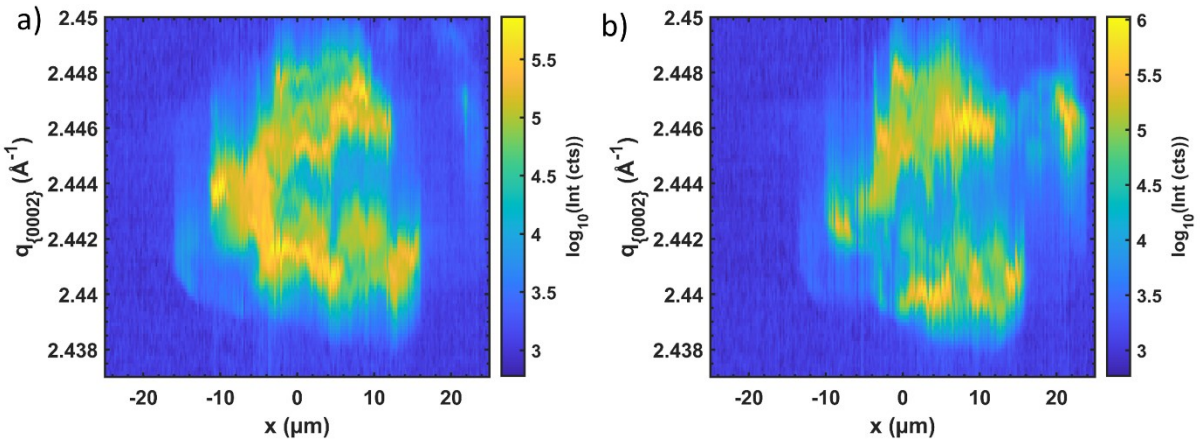

Figure 7.4: a) Strainmap of an uncoated part on R3 and b) from an Al coated part. An immensely variation of the Bragg peak is observed in all measured parts of rod R3.

Calculation of the bending radius in strained rods

For the calculation of the radius the crystal size on the compressed side is compared with the one at the extended side of the rod. Given that the compressed side has a crystal size $c_1 = {2\pi}/{q_{\max}}$ and the extended side a size of $c_2 = {2\pi}/{q_{\min}}$, from Table 5.1 in the main part. Geometrical considerations for two similar shaped triangles of different size show for the bending radius r and the rod diameter d:

$$\frac{r+d}{c_2} = \frac{r}{c_1} \tag{7.1}$$

And the resulting equation for *r* is.

$$r = d\frac{c_1}{c_2 - c_1} \tag{7.2}$$

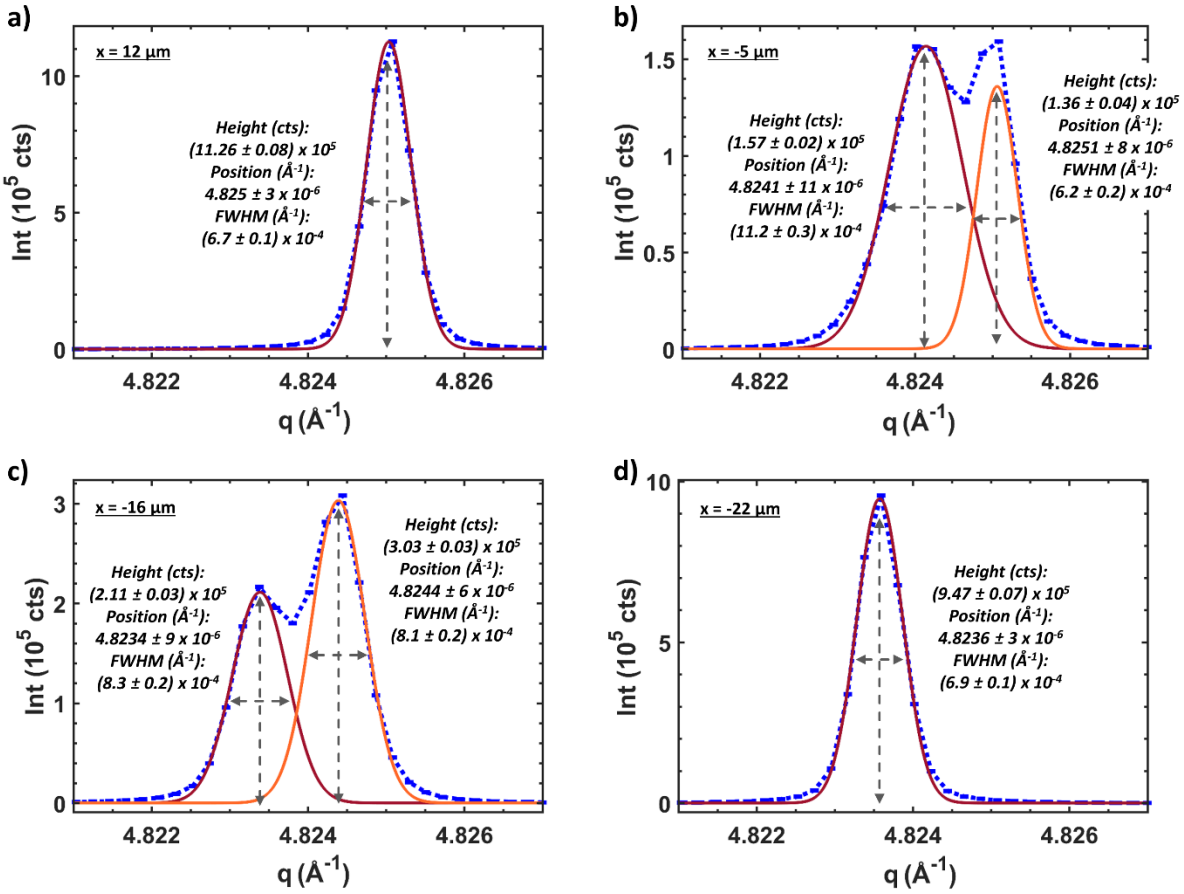

Figure 7.5: a-d) The respective Bragg reflection recorded at the line scans x coordinates 12 µm, -5 µm, -16 µm and -22 µm, from the Bragg reflection map of R1 shown in Figure 5.2 d). During the linescan a splitted structure arises, showing two distinct peaks and leads to the conclusion that separate coherent scattering crystal volumes of the rod with differing lattice parameters were probed. Furthermore, the FWHM of the reflection increases during the splitting and is probably caused by a shrinking of the coherent scattering crystal volumes.

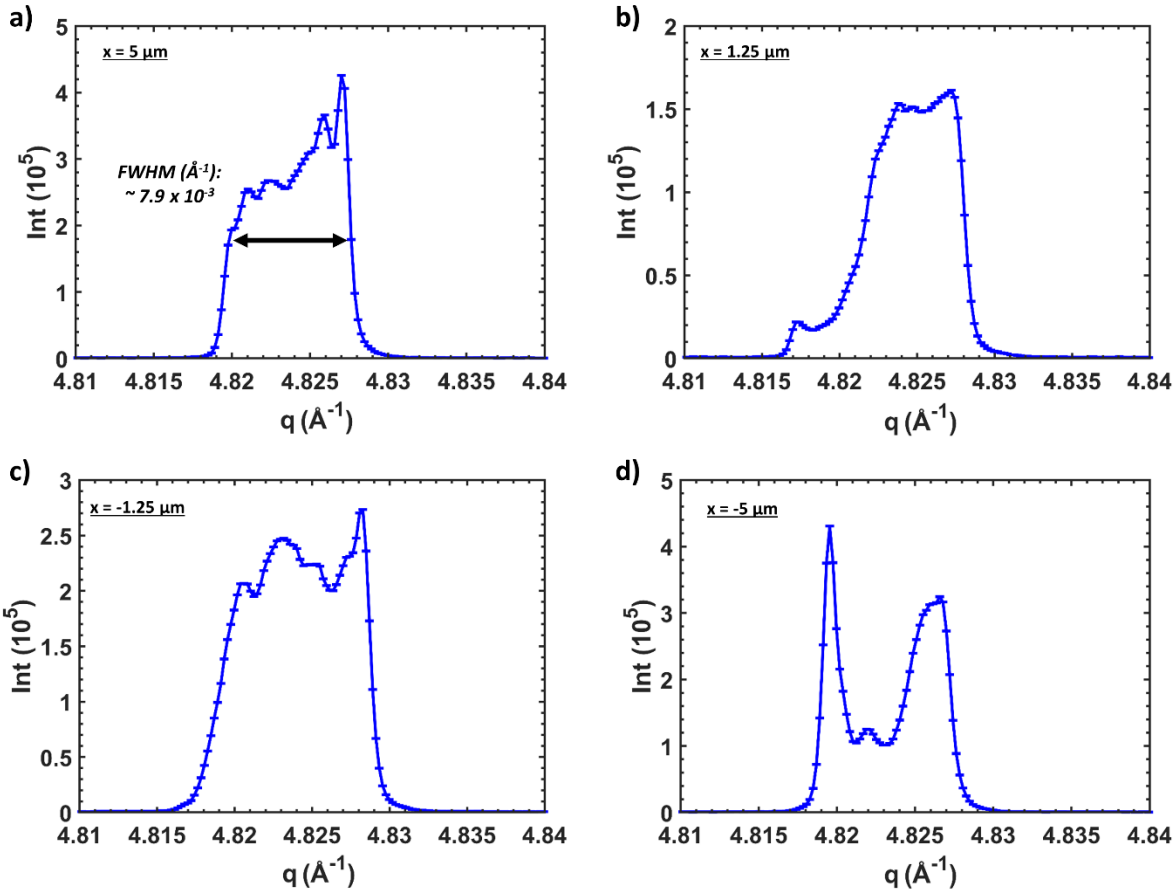

Figure 7.6: a-d) Four Bragg reflections measured for R2 at *x* positions 5 µm, 1.25 µm, -1.25 µm, -5 µm of the linescan across the rod.

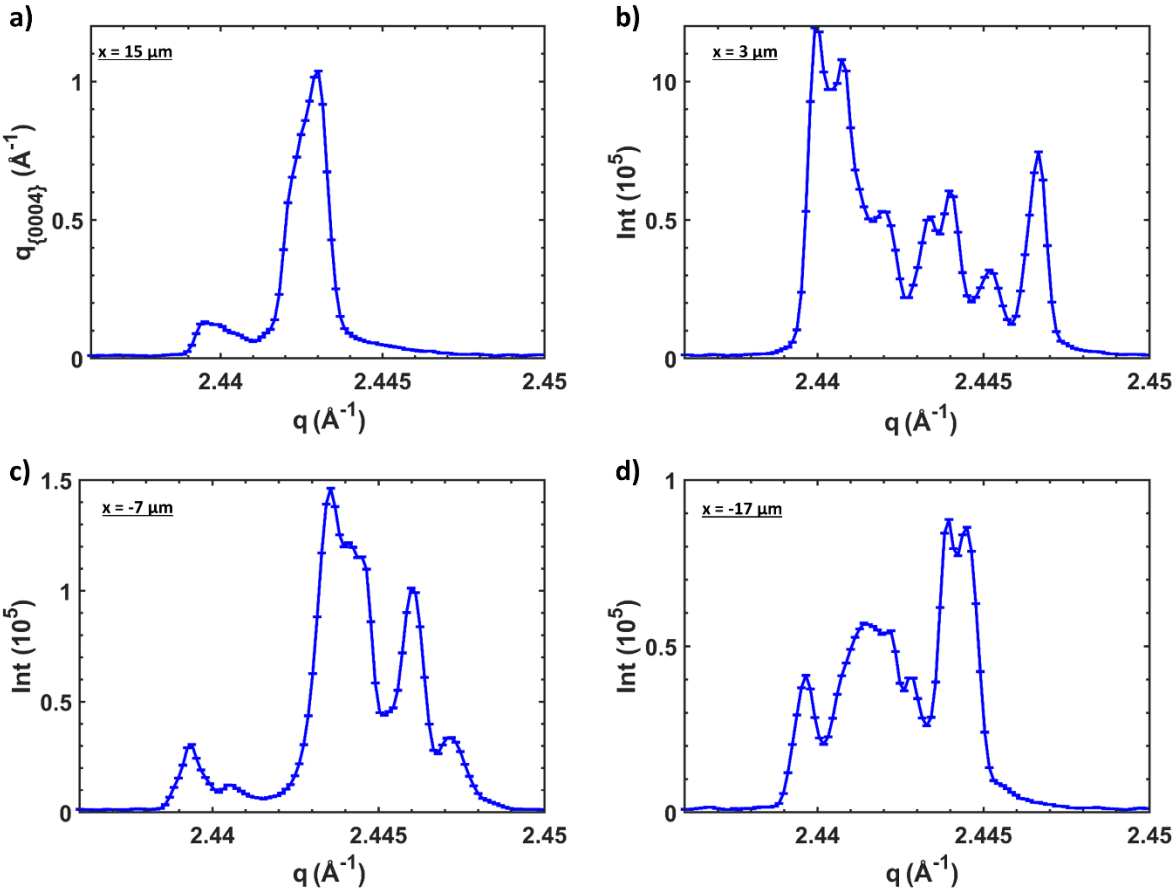

Figure 7.7: a-d) Four Bragg reflections measured for R3 at *x* positions 15 µm, 3 µm, -7 µm, -17 µm of the linescan across the rod.

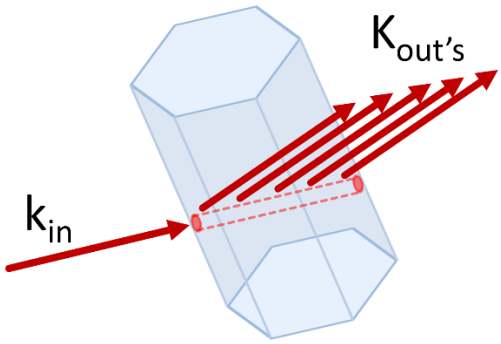

Figure 7.8: X-Ray beam path through the rod along the direction of the incident wave vector k_{in}, and being scattered by multiple crystallites in the rod, indicated by the multiple exiting wave vectors $k_{out's}$.

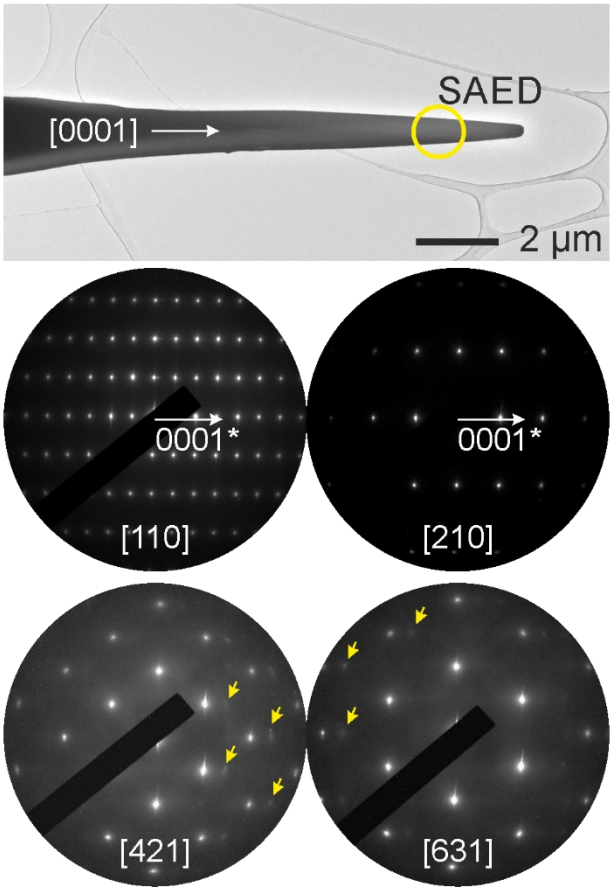

Figure 7.9: TEM image of a tapered ZnO microstructure and corresponding tilting series using selected-area electron diffraction on the thin parts of the nanowire. SAED zone axis patterns of this tilting series prove the growth direction of the nanowire to be along its c-axis. All patterns display strong diffraction intensities indicating a single crystal material. The curvature of the ZnO needle is reflected in streaking of the strong reflections perpendicular to the growth direction. For the zone axis orientations [421] and [631] multiple weak reflections (see yellow arrows) are observed which could belong to a second intergrown minority component or could result from multiple dynamical diffraction events, which have to be considered at the present sample thickness.

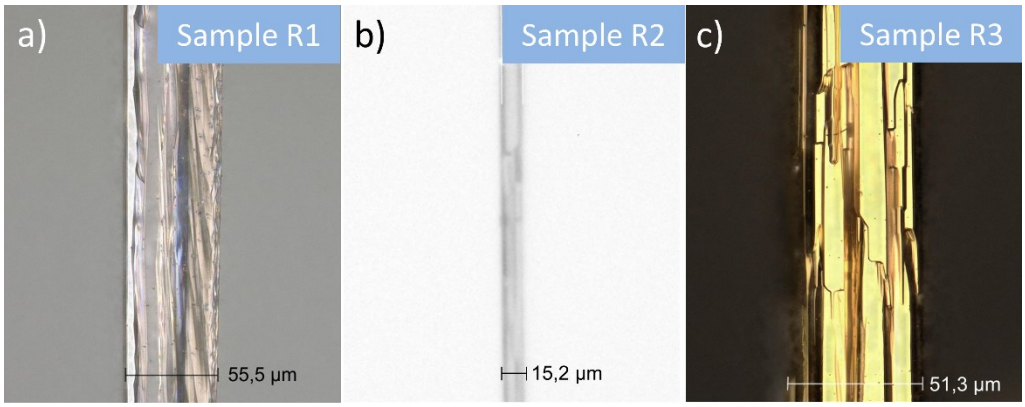

Figure 7.10: Optical images of the three samples R1, R2 and R3. Length measures are included in all three images. a,b) Pictures of uncoated ZnO rod parts on R1 and R2. c) Image of an Au coated part of sample R3. Acquired using a Keyence VHX 7000 digital microscope for samples R1 and R3 and a Zeiss Primostar microscope for sample R2.

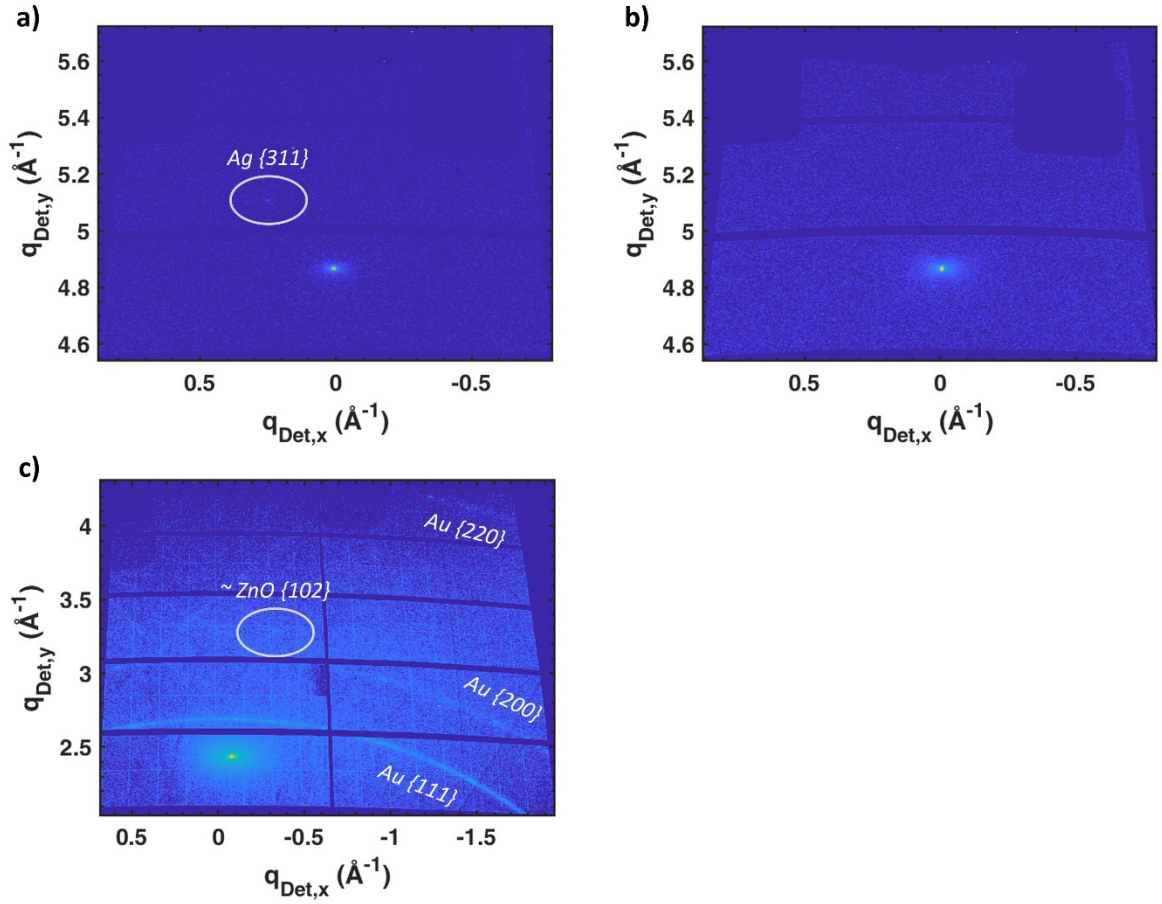

Figure 7.11: Summed up detector images from rocking scans performed for sample R1 ZnO {0004} (a), R2 ZnO {0004} (b) and R3 ZnO {0002} (c) collected with Pilatus detector at a close sample detector distance of 24 cm to cover a huge range of q space. Rods R1 and R2 display an overall high crystallinity with an absence of further ZnO Bragg reflections, in a) an additional, weak reflection (circle, q = 5.11 Å^{-1}) is present, probably {311} from the Ag glue. R3 shows a high intense, narrow reflection, as well. But an additional, weak reflection is observed (circle, q = 3.31 Å^{-1}) and may be the ZnO {102} reflection. Indicating that a second, minority crystalline component may be present in the ZnO rod. Furthermore, three powder like

diffraction rings at q 2.69 $Å^{-1}$, 3.12 $Å^{-1}$ and 4.38 $Å^{-1}$ are visible and are most probably caused by the {111}, {200} and {220} Bragg reflections of the Gold coating, respectively

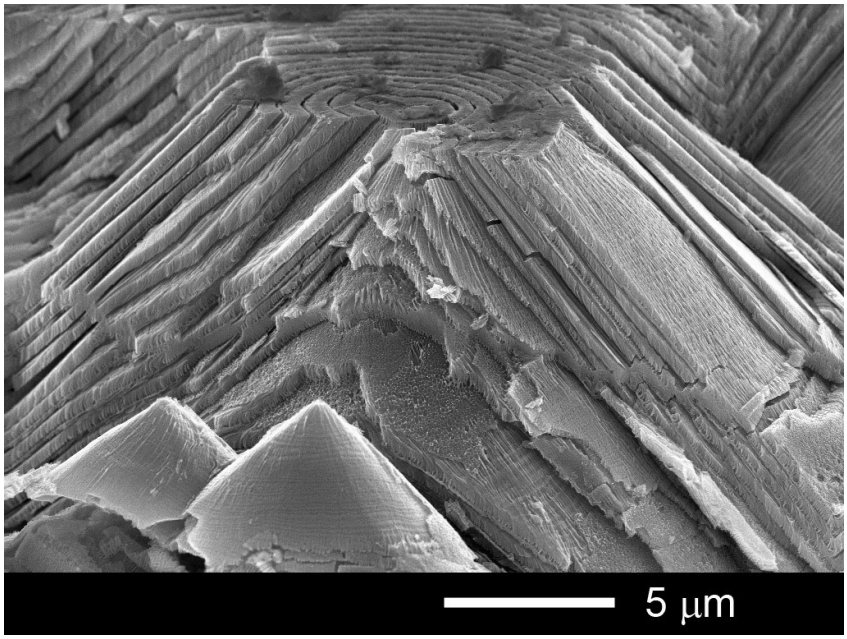

Figure 7.12: Multilayer conical porous structures formed in bulk HVPE-grown GaN subjected from the top surface (N-face) to electrochemical etching in 0.3 mol. HNO_3 electrolyte under 22 V anodic bias for 20 min. Unlike the PEC etching, in the case of electrochemical etching the anodisation potential was applied between two electrodes. The sample has served as working electrode while a mesh of Pt wire served as counter electrode.

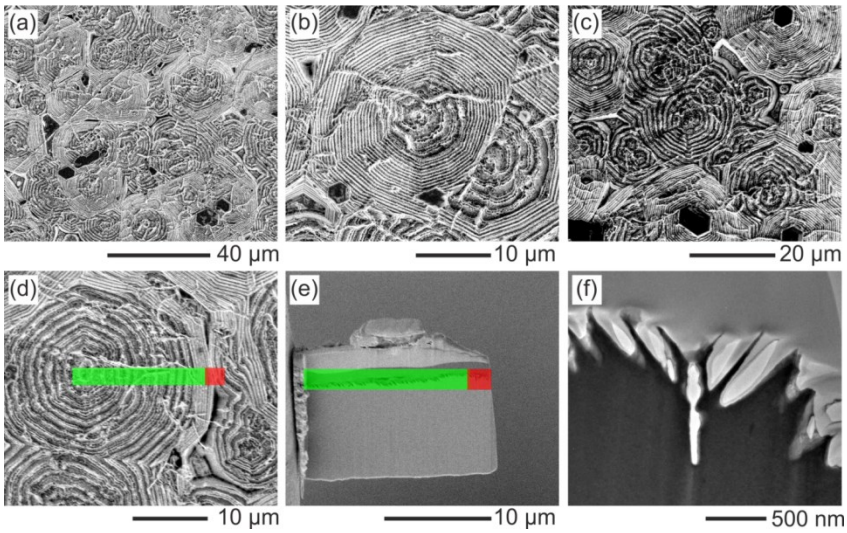

Figure 7.13: a-d) SEM images of the bulk GaN surface after photoelectrochemical etching. The colored bar in d) and e) highlights the region of a TEM sample prepared by FIB, whereas the red bar indicates the boundary region between two adjacent concentric structures with modulated electrical parameters. f) TEM image of this boundary region containing one "island" with different polarity as shown in Figure 7.14. The photoelectrochemical etching

produced a straight and deep trench at the “island” in contrast to the inclined etch pits produced at the concentric structures, which is consistent to the peculiarities of the proposed growth scheme in ref. 4[216].

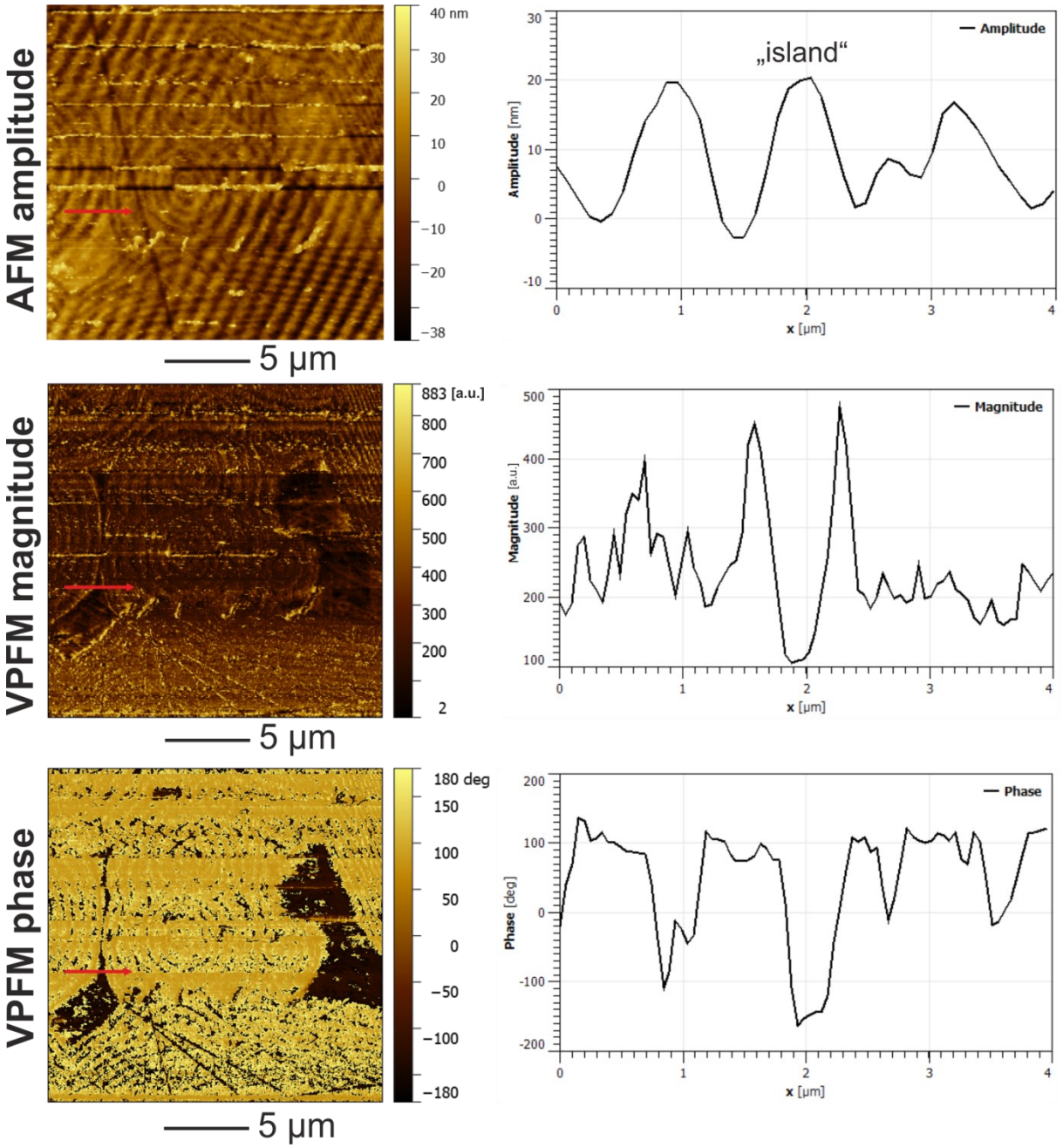

Figure 7.14: Piezoresponse force microscopy (PFM) measurements of the as grown GaN surface at 247 kHz resonance frequency. AFM topology and the corresponding vertical PFM magnitude and phase signals are displayed. The positions of profiles are indicated by the red arrows. See text for details.

The contact mode AFM image depicts the topology of the surface which is described by circular formations exhibiting alternating rings of different elevation which are occasionally separated by islands. Random oriented scratches, fringe pattern (see the lower right corner) and horizontal measuring artefacts superimpose the image. The topology of the surface is

shown in the respective AFM amplitude profile which is taken over the circular structures and bridging the island (see red arrow). The height difference between the “hill” and “valley” rings and islands is 20 nm peak-to-peak, with hills and islands having roughly the same elevation.

The vertical PFM magnitude image further resembles the topography map but with inverted contrast, therefore an amplification of piezoresponse by the topography can be neglected. The island and hill structures basically show a smaller piezoresponse than the valley structures. A closer inspection of the piezoresponse profile reveals a minimum in magnitude for the island which is bracketed by valley-type rings showing very high piezoresponse at their edges. Additionally, such modulation is also observed in the phase image. Valley-type rings showing larger magnitude in piezoresponse with respect to the hill-type rings exhibit pronounced kinks in the phase (dark contrast in the image and profile). The inversion of the phase signal is also true for the islands, although in contrast to valley-type rings, here the piezoresponse magnitude was observed to be small.

According to theory the piezoelectric response of Ga- and N-face domains will vibrate in-phase and out-of-phase with the modulation voltage, respectively. The pronounced phase difference (more than ~200°) and phase shift can be explained by the experimental setup and capacitive effects between sample and tip, hence only qualitative statements are feasible. However, the small piezoresponse of the island, together with the inversion of the phase signal is a clear indication of a domain with inversed polarity featuring inversion domain boundaries as displayed by the high magnitude regions surrounding the island[221,318].

On the contrary, the modulation of phase and magnitude of the hill- and valley-type rings is believed to have different origin than the inversion of polarity. Moreover, the magnitude and phase could be influenced by several factors which include artefacts of topography, variation of surface charge or piezoactivity, rather than polarization inversion[319]. Please, note that scratches also show the same phase to magnitude correlation like the valley-type rings. In correlation to the real structure, these valley-type rings having smaller lateral dimension coincide with material removed during the PEC etch which can be rationalized from Figure 7.12. These conical stacked structures are supposed to feature an alternating spatial modulation of dopants[216]. Further, no indication of inversion domain boundaries have been found in the TEM investigation of cross-section through these single crystalline conical structures.

Therefore we conclude from PFM measurements that inversion domains with opposite polarization than the conical structures are formed during the fast growth process, therefore showing a microscale modulation of piezoelectric parameters.

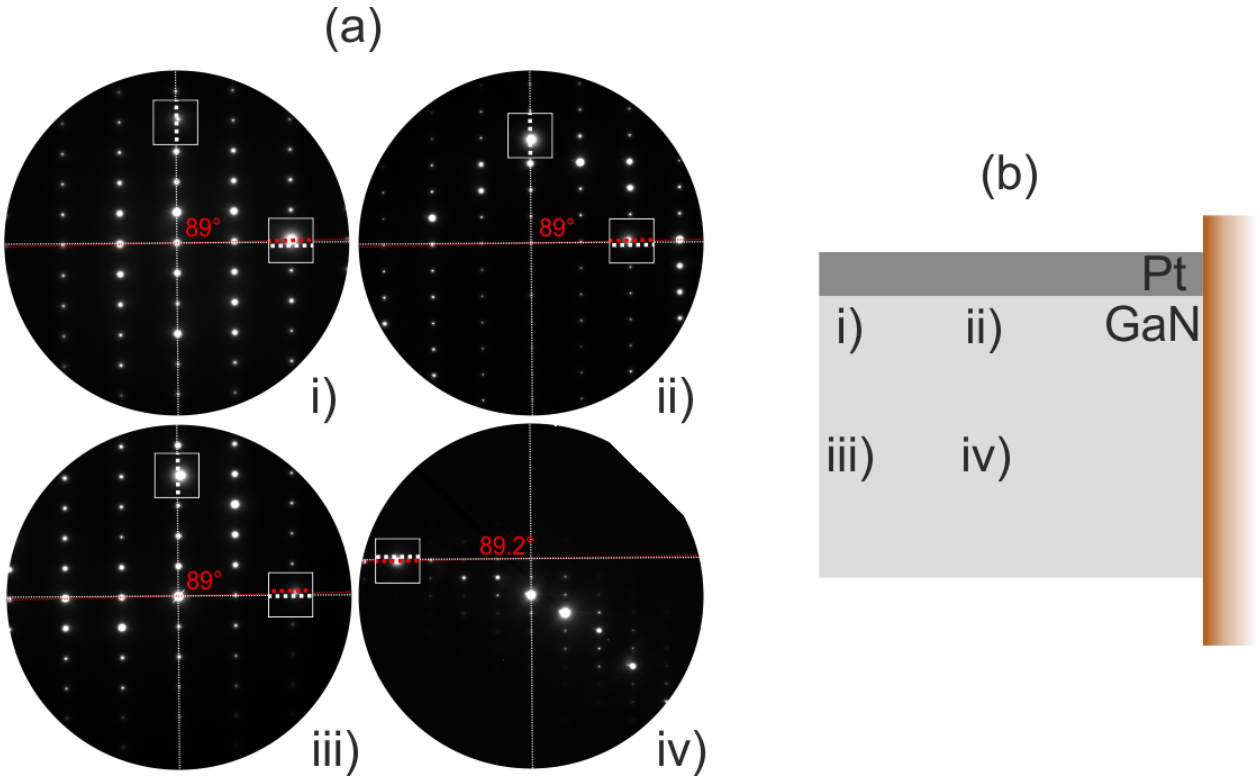

Figure 7.15: a) Selected area (diameter of aperture 500 nm) electron diffraction studies screening four positions on the TEM lamella. The specimen was tilted into [2-1-10] orientation for position i) and no further sample tilt was performed during the experiment. The triclinic distortion showing $\beta \approx 89°$ of the wurtzite structure of GaN is observed to be present at all four positions, irrespective the crystalline distortions of the lamella which are apparent from the increasing deviation from the zone axis condition set in i). b) Sketch of the specimen lamella showing the positions of electron diffraction experiments.

Justification of the chosen reconstruction volume for analysis

The reconstruction from y 0 to 0.7 µm (Figure 5.10 c) will be used for the further analysis for it appears that this is the real ZnO structure that was investigated. This is justifiable from first: the hexagonal shape of the reconstruction in this segment, which is expected from the ZnO wurtzite structure, second: the high amplitude of the reconstruction with the isosurfaces close together and third: this part has a size along y of 449±56 nm, this matches with the beam size of 471±1 nm, which is the FWHM of a Gauss function fitted to the beam shape. Furthermore, the partly reconstructed structures (y > 1 µm) are oriented along the macroscopic *c* axis of the rod. The reason for these reconstructions could be an additional partly coherent beam hitting the sample along the y direction, that may result from diffraction of the slits defining the incident beam.

Refraction correction of the phase

A refraction correction of the reconstructed phase may be necessary,[258,259] in order to account for an individual phase shift due to different beam path lengths through the rod material with its refractive index $n = 1 - \delta - i\beta$ (for 9 keV photon energy, δ = 1.275 × 10^{-5} and β = 2.149 × 10^{-7}). To calculate the path length through the rod, the reconstructed shape was utilized to count the voxels that are passed by the beam to reach a specific position in the rod volume, when entering and exiting in the direction of k_{in} and k_{out}. This was done individually for every voxel of the reconstructed volume and by multiplying with the voxel size, a path length d is determined. The final phase shift $\phi = k\delta d$ including the wave vector $k = 2\pi/\lambda$ is calculated and the reconstructed phase is corrected by subtracting the phase shift. Here, a maximum phase shift of around 0.6 was found and a refraction correction of the data is necessary. For β the effect is almost two orders of magnitude less and is neglected.

The Au layer deposited on the ZnO rod cause a phase shift, as well. At 9 keV photon energy the index of refraction parameters for Au are δ = 3.739 × 10^{-5} and β = 3.235 × 10^{-6}. For a path length of 100 nm through the Au a phase shift of 0.17 is calculated. This is around a quarter of the calculated phase shift for the ZnO rod. Furthermore, the non-symmetrical deposition from

two directions and, additional, high roughness typical for thermal evaporation deposition processes, would lead to a complex model of the Au layer with high uncertainty. Considering the comparable low phase shift and the complex layer modelling, the Au layer is neglected in this paper.

Reconstructed phase to strain calculation

The strain is calculated from the phase of the reconstructed complex electron density. [82,259] First step is the calculation of the displacement field $u = \phi/q$, including the phase ϕ and scattering vector $q = 4\pi/\lambda \times \sin(Bragg\ angle)$. From this is seen, a phase of 2π is equal to a displacement of $2\pi/q$, which is the distance between two parallel lattice planes d_{hkl}. Finally, the strain is the gradient of the displacement field. In the case of a scattering vector pointing in x direction it simplifies to $\epsilon_x = du/dx$.

Calculation of carrier concentration from depletion width

The equation for the calculation of the depletion width W_d as a function of the carrier concentration N_D and temperature T at zero voltage is rearranged as follows.[39]

$$W_d = \sqrt{\frac{2\epsilon_s}{eN_D}\left(\Phi_i - \frac{k_bT}{e}\right)} \rightarrow N_D = \frac{2\epsilon_s}{eW_d^2}\left(\Phi_i - \frac{k_bT}{e}\right) \tag{7.3}$$

Including built-in potential $\Phi_i \sim 0.5\,\mathrm{V}$ [39,197], elementary charge e, Boltzmann constant k_b and permittivity ϵ_s of around nine times the vacuum permittivity[320,321]. For a given depletion width of 39.0 nm the calculated donor concentration is $3.1 \times 10^{17}\,\mathrm{cm^{-3}}$.

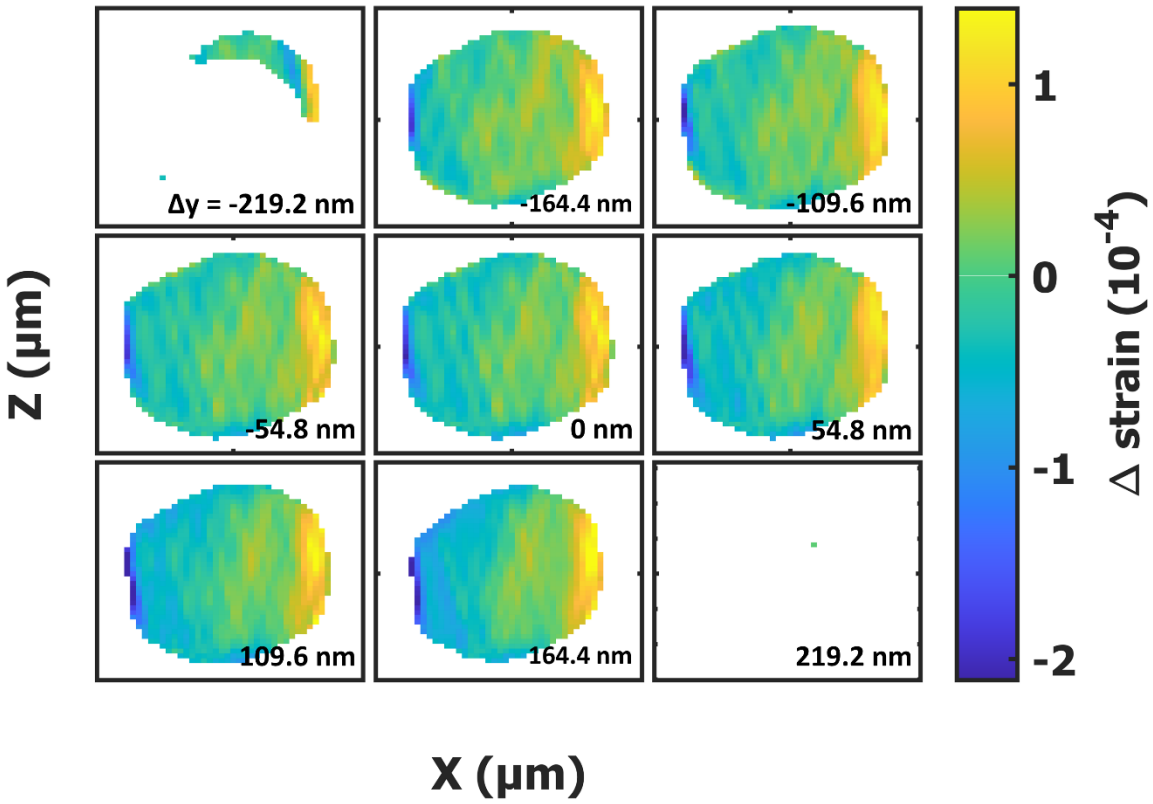

Figure 7.16: Multiple cuts through the reconstructed volume with a y spacing of 54.8 nm, each. In total a length of 438.4 nm along the y-axis.

Fitting: Model justification, procedure and table of results

The fit model to describe the strain consist of constant, linear, exponential and Gauss functions. The physical reasoning behind the different functions is: first, the constant function models a uniform strain that is well distributed over the whole sample. Second, the linear part is due to bending of the rod that may be introduced by a stress perpendicular to the c-axis. Third, the exponential part is introduced to describe the strain change near the surface of the rod. A strain often decays by a power law, here an exponential function is used for simplicity. Fourth, the Gaussian function was chosen to model the additional strain near the surface because the strain seems to peak near but not exactly at the interface and it was shown in theoretical calculation that the potential in a bend ZnO rod saturates near the surface.[55] A saturation process can be described by a sigmoid function e.g. the error function. Because the strain in a piezoelectric material is connected to the E field, i.e., the gradient of the potential, a Gaussian function, which is the derivative of the error function, is a justifiable choice.

For the fitting, a nonlinear least square method was used with a trust region algorithm. The error values were calculated from a 95% confidence interval of the fitted values. The following model *F(x)* was implemented to fit the data sets of the average strain:

$$F(x) = \varepsilon_{Gauss,1}\, exp\left(\frac{-(x-\mu_1)^2}{2\,{\sigma_{Gauss,1}}^2}\right) + \varepsilon_{Gauss,2}\, exp\left(\frac{-(x-\mu_2)^2}{2\,{\sigma_{Gauss,2}}^2}\right)$$

$$+\varepsilon_{exp,1}\, exp\left(\frac{-(x-x_1)}{\sigma_{exp,1}}\right) + \varepsilon_{exp,2} exp\left(\frac{x-x_n}{\sigma_{exp,2}}\right) + \frac{\varepsilon_{lin}}{x_n - x_1} + c \qquad (7.4)$$

The function depend on the variable x, which is the position across the sample, with its first value x_1 = 110, 111 (for the two measured datasets, one presented in this paper and the other at the end of the supplementary, respectively) and last value x_n = 145, 148 inside the reconstructed volume for the rod position presented in the main text and a second position on the rod, respectively. ε_{Gauss}, σ_{Gauss} and μ are the height (strain), sigma and position of the Gauss functions. The positions of the exponential functions 1 and 2 are fixed to the edges of the rod at x_1 and x_n, respectively. There are further the strain ε_{exp} and sigma σ_{exp} of the exponential functions. ε_{lin} is the linear change of the strain from one edge x_1 of the rod to the other x_n and c is a constant offset in the strain. The spatial sizes of the effects are calculated by multiplying the fitted values with the voxel size (27.4 nm).

Table 7.1: First row are the fit results for the rod position presented in the main part and second row for the additional position. The strain results are dimensionless, all other are in numbers of voxels.

$\varepsilon_{Gauss,1}$ [10^{-5}]	$\sigma_{Gauss,1}$	μ_1	$\varepsilon_{Gauss,2}$ [10^{-5}]	$\sigma_{Gauss,2}$	μ_2	$\varepsilon_{exp,1}$ [10^{-5}]	$\sigma_{exp,1}$	$\varepsilon_{exp,2}$ [10^{-5}]	$\sigma_{exp,2}$	ε_{lin} [10^{-5}]	c [10^{-5}]
-2.23 ±0.11	4.29 ±0.24	121.54 ±0.28	10.34 ±0.14	2.52 ±0.06	146.33 ±0.06	-13.56 ±0.25	1.27 ±0.05	-8.29 ±0.24	1.57 ±0.09	4.42 ±0.16	0.19 ±0.05
-3.18 ±0.29	4.00 ±0.48	115.57 ±0.54	12.71 ±0.43	2.32 ±0.12	146.26 ±0.14	-5.53 ±0.77	0.26 ±0.44	-5.49 ±0.76	0.38 ±0.28	5.38 ±0.43	-0.17 ±0.13

E-Field calculation from strain

To calculate the E field (component) from the measured strain component ϵ_x the following relation is used.[264]

$$\epsilon_{ij} = d_{ijk} E_k \qquad (7.5)$$

Including the strain tensor ϵ_{ij}, tensor of the piezoelectric strain coefficient d_{ijk} and the electric field vector E_k. Due to symmetry considerations for the hexagonal wurtzite structure the tensor d_{ijk} reduces to:[264]

$$\begin{pmatrix} 0 & 0 & 0 & 0 & d_{15} & 0 \\ 0 & 0 & 0 & d_{15} & 0 & 0 \\ d_{31} & d_{31} & d_{33} & 0 & 0 & 0 \end{pmatrix} \quad (7.6)$$

Strain along the three, independent crystal orientations are related to the electric field component E_3.

$$\epsilon_{11} = d_{31}E_3 \quad (7.7)$$

$$\epsilon_{22} = d_{31}E_3 \quad (7.8)$$

$$\epsilon_{33} = d_{33}E_3 \quad (7.9)$$

ϵ_{11} is equivalent to the measured strain ϵ_x from the paper. The measured strain belongs to one of the symmetrical $\{10\bar{1}0\}$ Bragg reflections and the equations (7.7) and (7.8) are valid for all of them. These are scalar relations, so it is possible to solve for the electric field component as a function of the measured strain and the piezoelectric strain coefficient.

Furthermore, shearing contributions of the strain are induced by the E field components E_1 and E_2. Therefore, the electric field in the Schottky contacts depletion region, laying in the basal plane of the ZnO, causes a shearing and no lattice parameter changes.

$$\epsilon_{23} = d_{15}E_1 \quad (7.10)$$

$$\epsilon_{12} = d_{15}E_2 \quad (7.11)$$

$$\epsilon_{31} = 0 \quad (7.12)$$

Choosing reconstructions by utilizing the chi parameter

The chi value calculated by the reconstruction algorithm, is a measure for the difference between the reconstructed amplitude and measured Bragg peak intensity and was utilized to sort the reconstructed results by quality and pick the best ones for a final reconstruction. Two hundred reconstructions with random starts were performed for both positions. For the position presented in the paper 76 out of 200 and for the second position, presented in the supporting information, 151 out of 200 performed reconstructions were chosen for further analysis (see Figure 7.17). The final reconstructions are made by correlating all chosen reconstructions with each other. In Figure 7.17 a), the chi values related to the first position are distributed around two broad maximums. The reconstructions of the first maximum were chosen for further analysis and the correlated reconstruction is shown in Figure 5.10 c). It is of the expected hexagonal shape and size and has high amplitude values of 0.7 and above. In contrast, the

correlated reconstruction of the second maximum at around chi = 0.056 (histogram in Figure 7.18 a) shown in Figure 7.18 b) has a maximum amplitude of below 0.2. The histogram for the second position in Figure 7.17 b) is a narrow distribution of chi values with a sharp maximum at around 0.049. The reconstructed shape is shown in Figure 7.19 b).

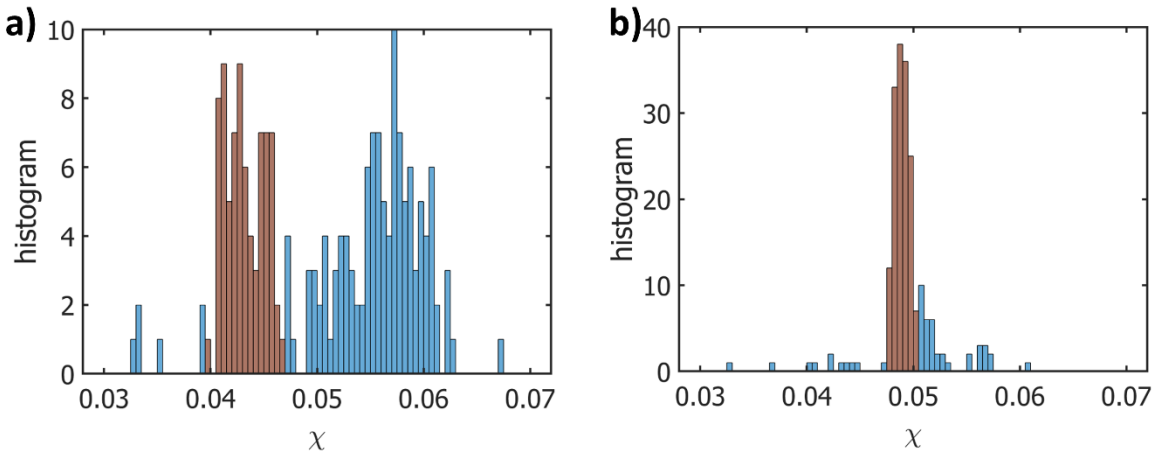

Figure 7.17: Histogram of the Chi distribution in positions P1 a) and P2 b). In total 200 reconstructions were conducted for each position. Chi is a measure of the correlation between the reconstructed amplitude and the measured intensity of the Bragg peak. The areas in red are the Chi values that were used for the final reconstructions.

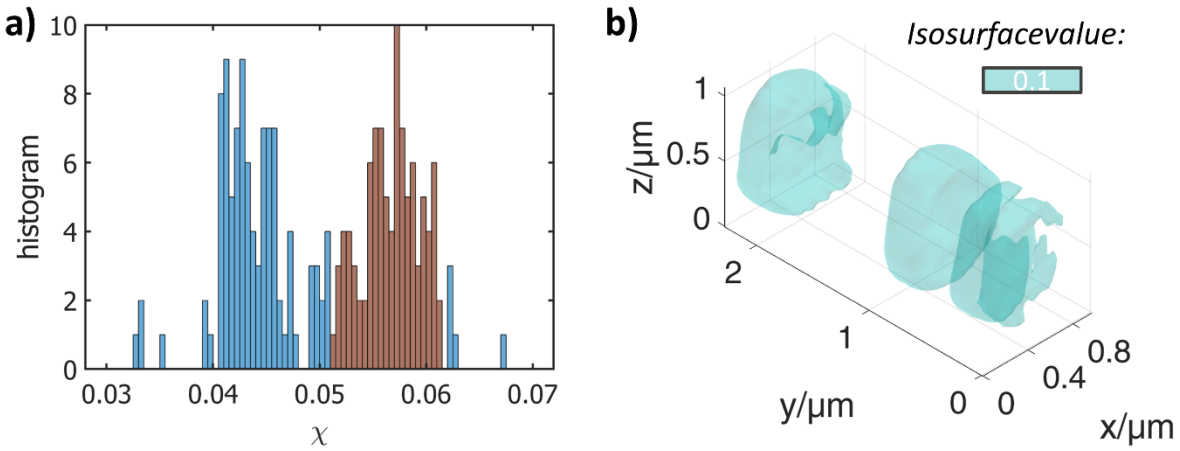

Figure 7.18: a) Chi histogram in position P2. b) Reconstructed amplitude from the red shaded area in a). The maximum value of the reconstructed amplitude is below 0.2.

Reconstruction and results of second position on the rod

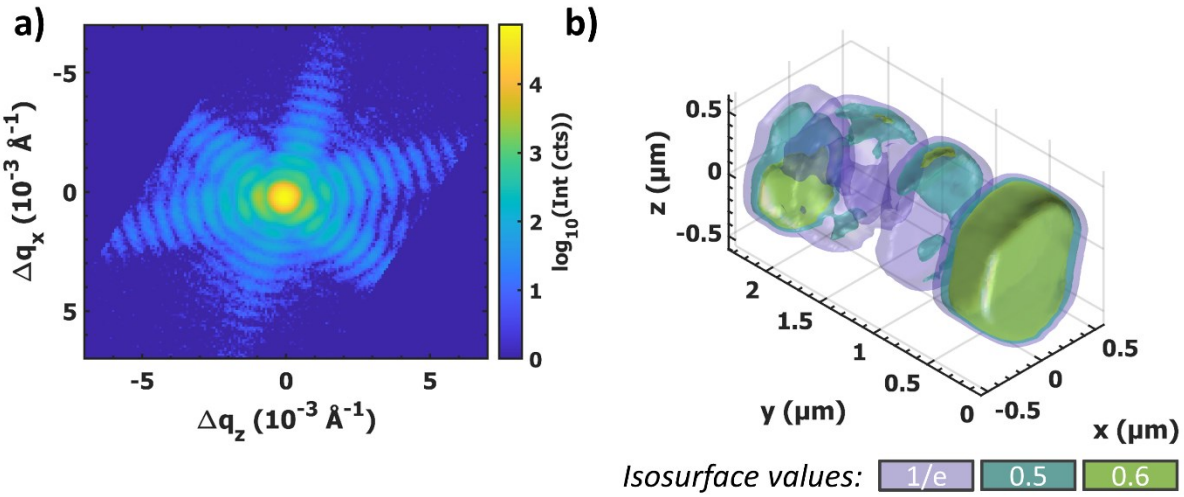

Figure 7.19: a) Diffraction pattern of the scan in the second spatial position along the rod. b) The corresponding reconstructed structure with three isosurface values (1/e, 0.5 and 0.6).

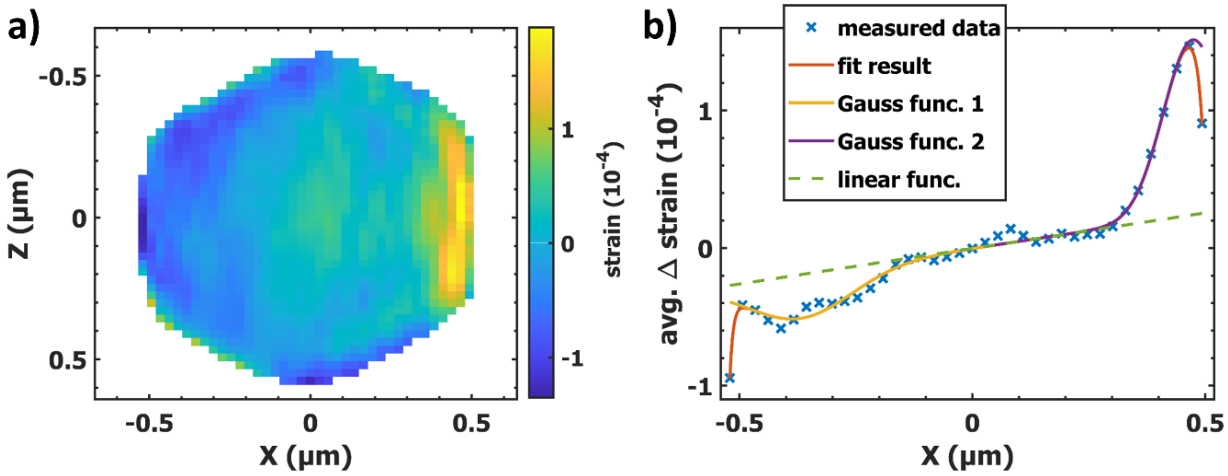

Figure 7.20: Reconstructed shape and strain in the second position. a) Cross section view of the refraction corrected strain through the middle in y of the reconstructed volume. b) The average strain (blue crosses) was calculated along axis z in a) and is shown as a function of axis x. Further, fit result of the model function to the average data (solid red line), the two Gauss functions from the fit model (purple and yellow solid line) and the fitted linear component (green dashed line) are shown.

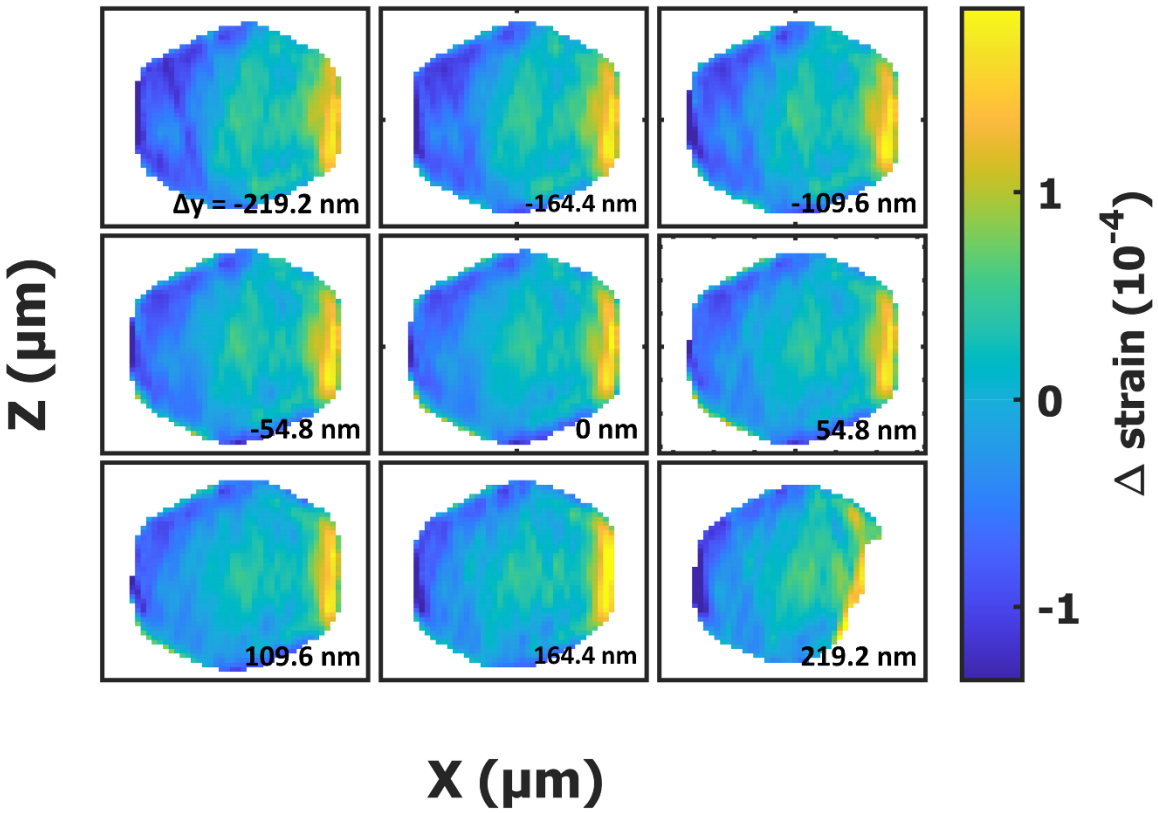

Figure 7.21: Multiple cuts through the reconstructed volume in the second position. The spacing between each cut is 54.8 nm in y direction. In total a length of 493.2 nm along.

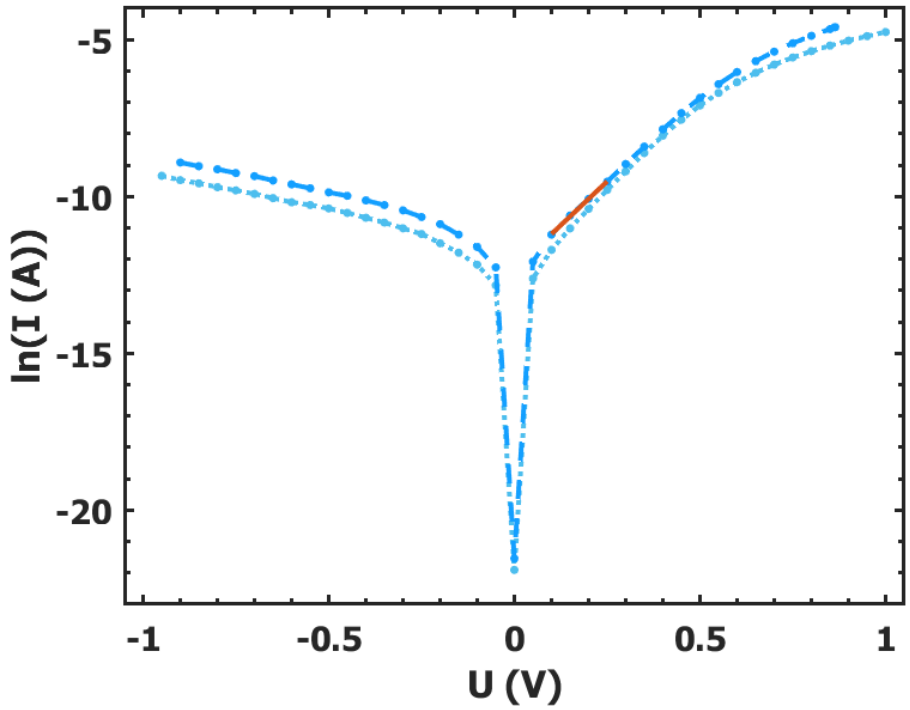

Figure 7.22: Semi-logarithmic *I-V* curves for the Al/ZnO/Ag (dashed line) as well as the FeCoSiB/ZnO/Ag (dotted line) measurements, compare with Figure 5.14. Small red solid line indicates a linear fit in the range 0.1 V to 0.25 V to extract the Schottky contacts barrier height and ideality factor.

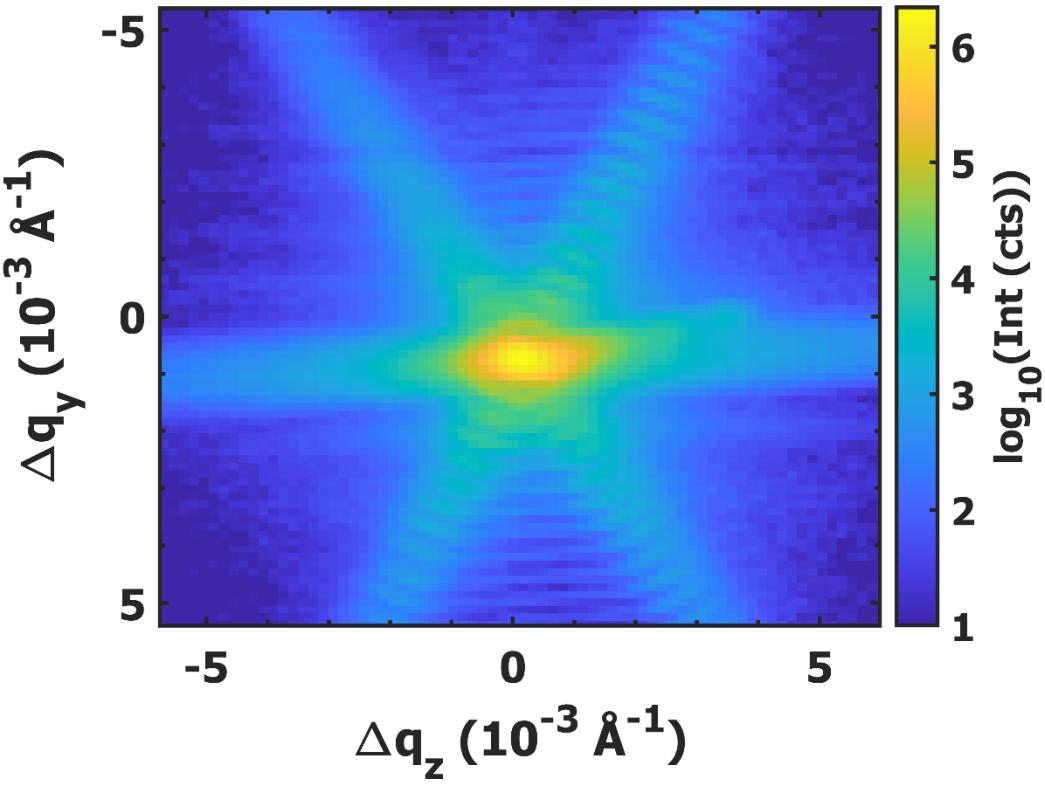

Figure 7.23: Cut of the Bragg reflection shown in Figure 5.17 b) magnifying the fringes around the center. Asymmetric appearance of the reflection in q_z is visible and possibly caused by an strain change in the z direction.

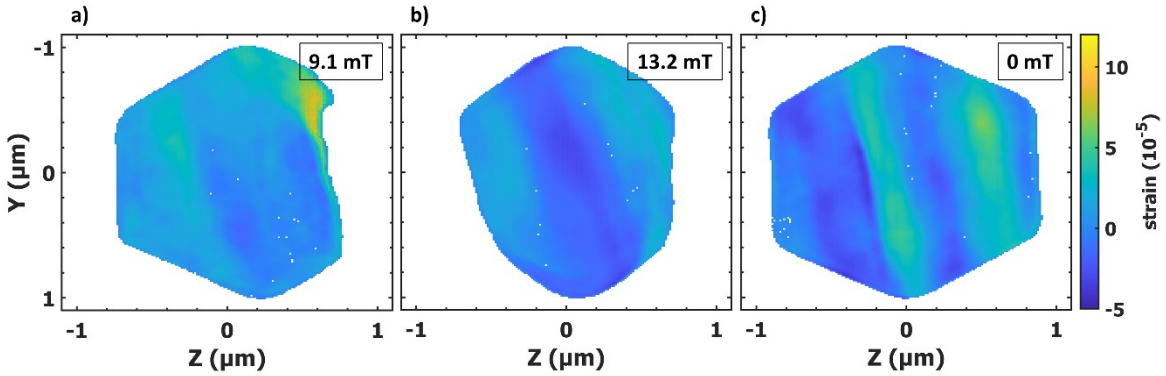

Figure 7.24: Reconstructed strain distribution measured by CXDI for applied B fields of 9.1 mT (a), 13.2 mT (b) and a post magnetic field measurement with no applied magnetic field (c). Color-coded strain is shown on the same range as in Figure 5.18. Reconstructions are of no high quality due to the huge diameter, which is of similar size as the coherence length of the probing X-ray beam.

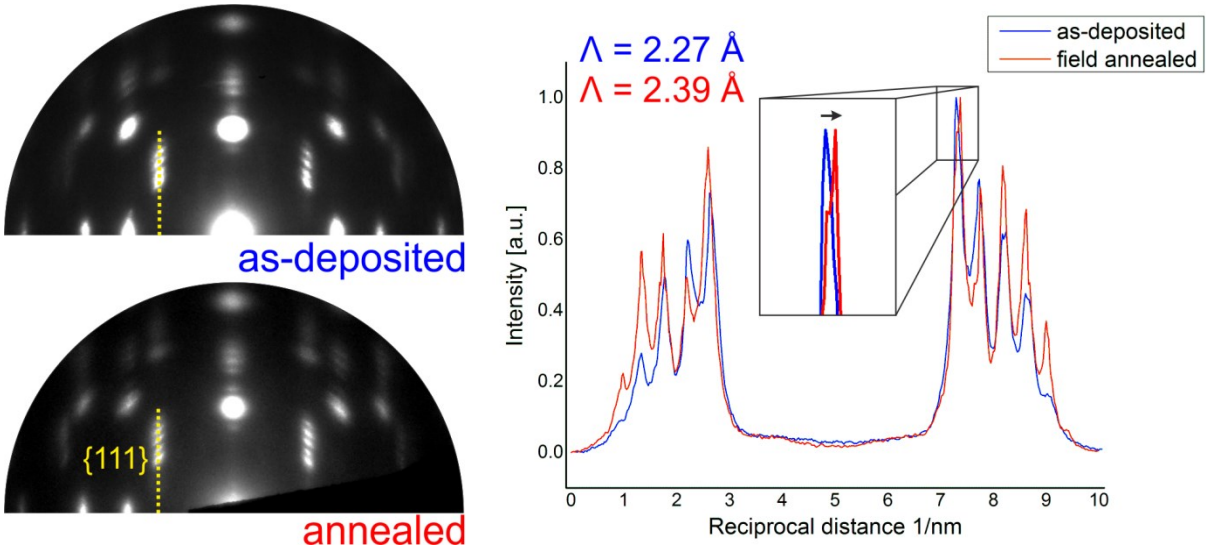

Figure 7.25: Temperature induced lattice deformations upon annealing at 600 °C for 1 h in vacuum. The electron diffraction pattern of the as-deposited and annealed sample shows no distinct differences concluding that the multilayer structure integrity is resistant against this temperature treatment. The intensity profiles over the periodic superlattice reflections prolonging from TiN {111} intensity reveal small lattice deformations. The distance between the superlattice reflections is decreased resulting in a measurable increase in the periodicity length from 2.27 Å to 2.39 Å.

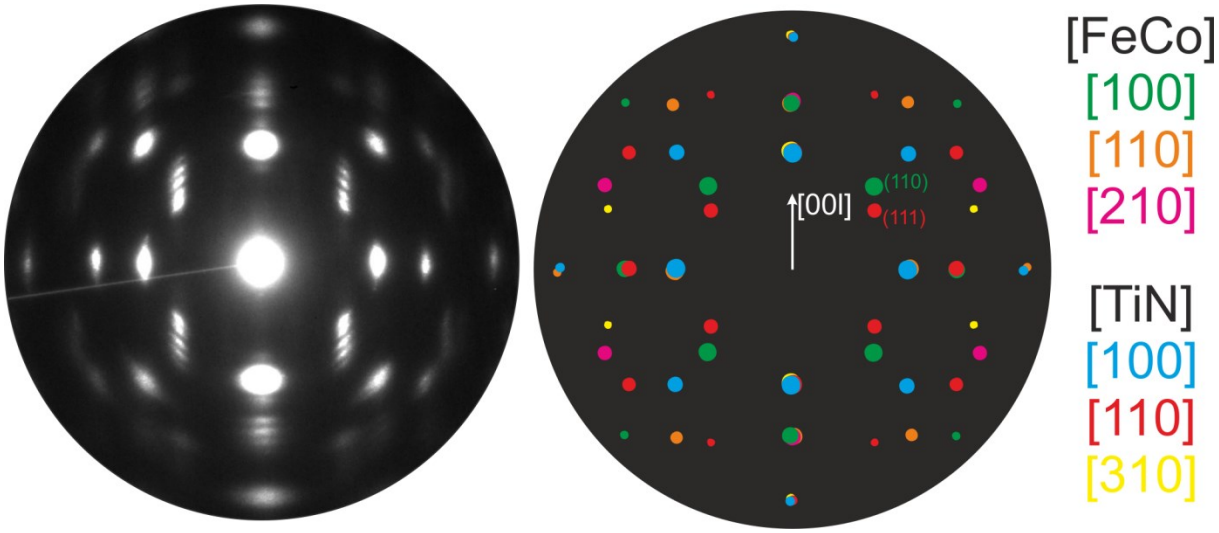

Figure 7.26: Experimental SAED pattern and the superimposed single component spot patterns of the respective zone axis.

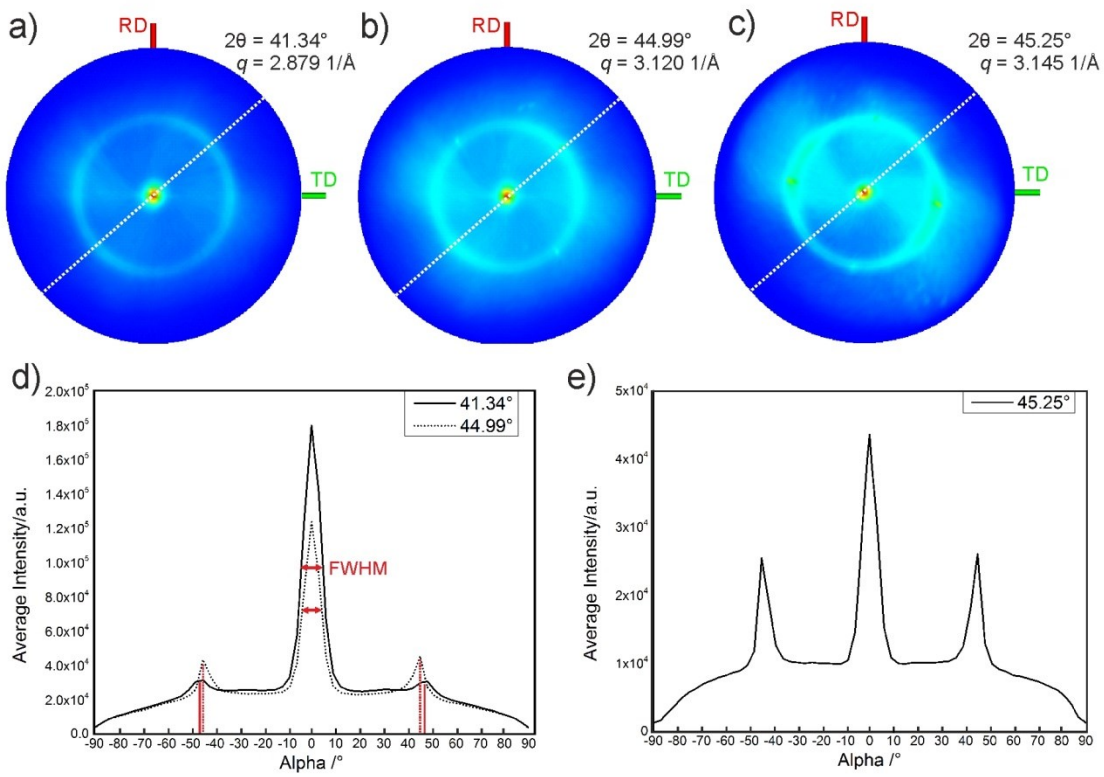

Figure 7.27: Pole-fig. (PF) measurements of the out-of-plane superlattice reflections prove high fibre texture in film growth direction. a,b) PFs of the as-deposited multilayer recorded on the pronounced superlattice reflections at 41.34° and 44.99° discussed in Figure 5.20 of the main manuscript. c) PF of the heated multilayer recorded on the second superlattice reflection at 45.25° d,e) Intensity profiles drawn across the PF hemisphere as indicated by the white dashed lines in the PFs. The angle alpha describes the opening between the in-plane and out-of-plane direction of the hemisphere.

For the as-deposited multilayer two PFs (Figure 7.27 a, b) were recorded selecting the *q*-vectors of the superlattice reflections located at $q = 2.879$ 1/Å (2θ:41.34°) and $q = 3.120$ 1/Å (2θ:44.99°). The PFs show the accumulation of diffraction intensity around α = 0° with the peak of intensity having a full-width at half maximum (FWHM) of 8.6° and 8.1° describing the small precession of the superlattice *c*-axis. A further feature of the PF which has to be explained is the ring-shape diffuse intensity distribution having an α-tilt angle of ~45° with respect to the film out-of-plane direction. The intensity ratio between the out-of-plane component and the ring-intensity (Figure 7.27 d) is decreasing and becoming more defined in FWHM (8.8° to 5.8°) accompanied with a small shift in the angle α (47° to 45°) by selecting the maximum of the second superlattice reflection at 2θ ≈ 45°. From the SAED pattern shown in Figure 5.22 and Figure 7.26 it becomes clear that the ring-shaped intensity is a contribution of the row of superlattice reflections starting from the indicated TiN (111) reflection to the FeCo (110). These diffuse superlattice reflections get into Bragg diffraction condition for the selected *q*-vectors when tilting the specimen by α ≈ 45°. The azimuthal rotation of domains around the out-of-

plane component is creating the ring-shaped diffuse intensity having a defined majority component as indicated by the accumulation of intensity within the ring. Consequently, the out-of-plane intensity maximum in the heated multilayer (PF at q = 3.145 1/Å) shows a slightly smaller FHWM of 7.6° which could indicate an improvement of fibre texture. Interestingly, also the intensity of the diffraction ring becomes even more pronounced for the heated multilayer, a feature which was also evidenced for the same row of superlattice reflections in Figure 7.25.

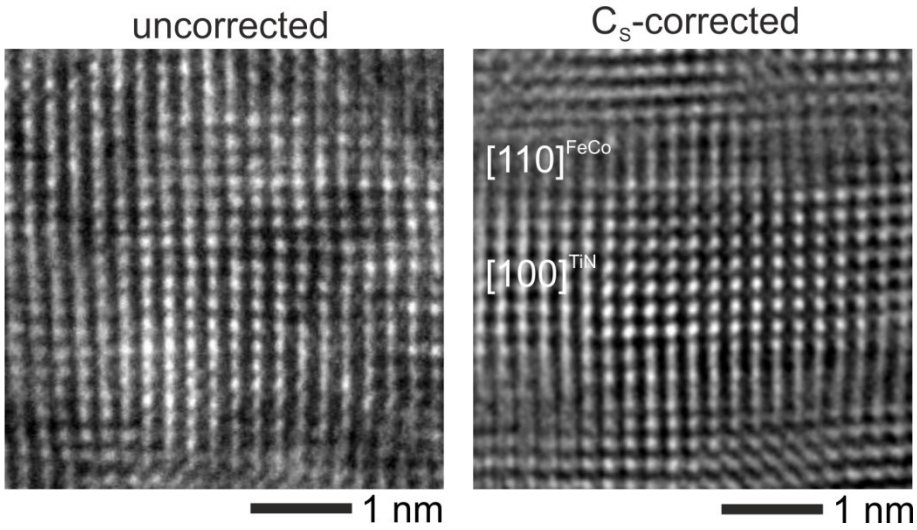

Figure 7.28: Comparison of uncorrected and C_S-corrected HRTEM micrographs. Without image correction no significant difference of the phase contrast intensities is apparent to distinct between [110] orientation of FeCo and [100] orientation TiN according to the 45° rotation cube-on-cube epitaxy. However, imaging with a small negative C_S value clearly resembles differences in the phase contrast micrographs.

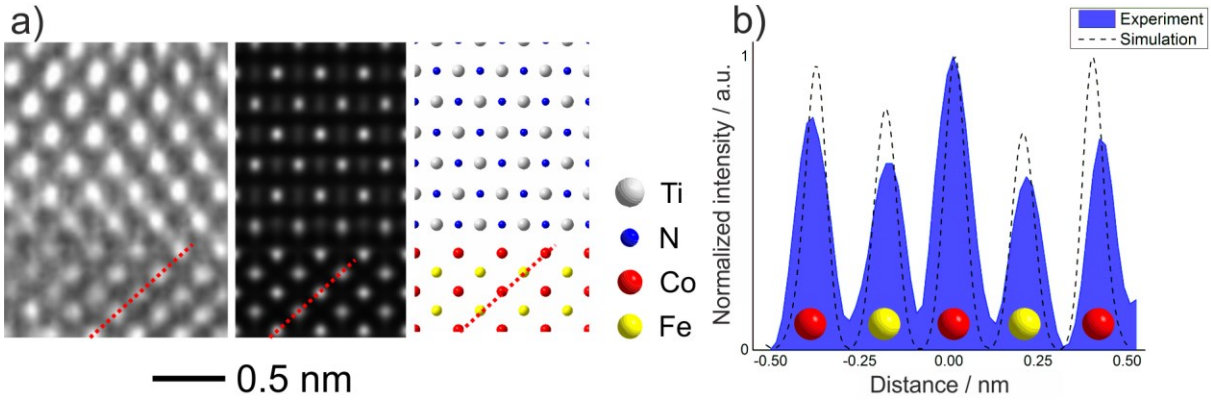

Figure 7.29: a) Experimental HRTEM micrograph, simulated phase contrast image and supercell model in [100] orientation. The presented HRTEM simulation was performed with a multislice algorithm within the JEMS program using the following setting: A slight negative spherical aberration coefficient to account for the imaging conditions used during the

experiment C_S= −0.12 mm, a defocus of −18.2 nm and a thickness of 2.1 nm. b) Comparison of intensity profiles across the (110) plane of the FeCo layer extracted from the experimental and simulated images. The experimental variation of the phase contrast generated for a Co and Fe atom correlates well with the simulation based on the ordered B2 structure of FeCo.

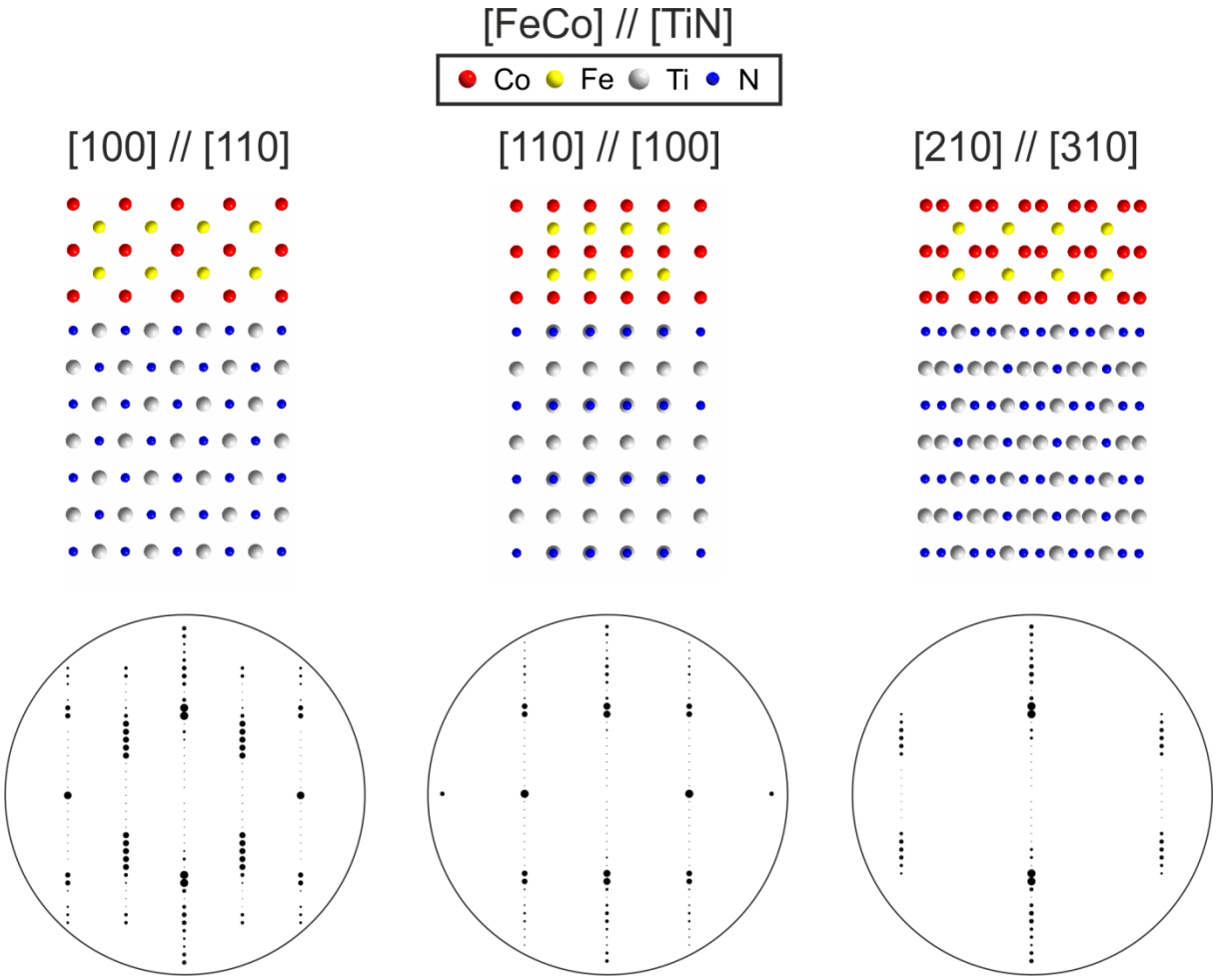

Figure 7.30: Representation of the supercell model and the single ED pattern in the experimentally observed orientation of the three major domains.

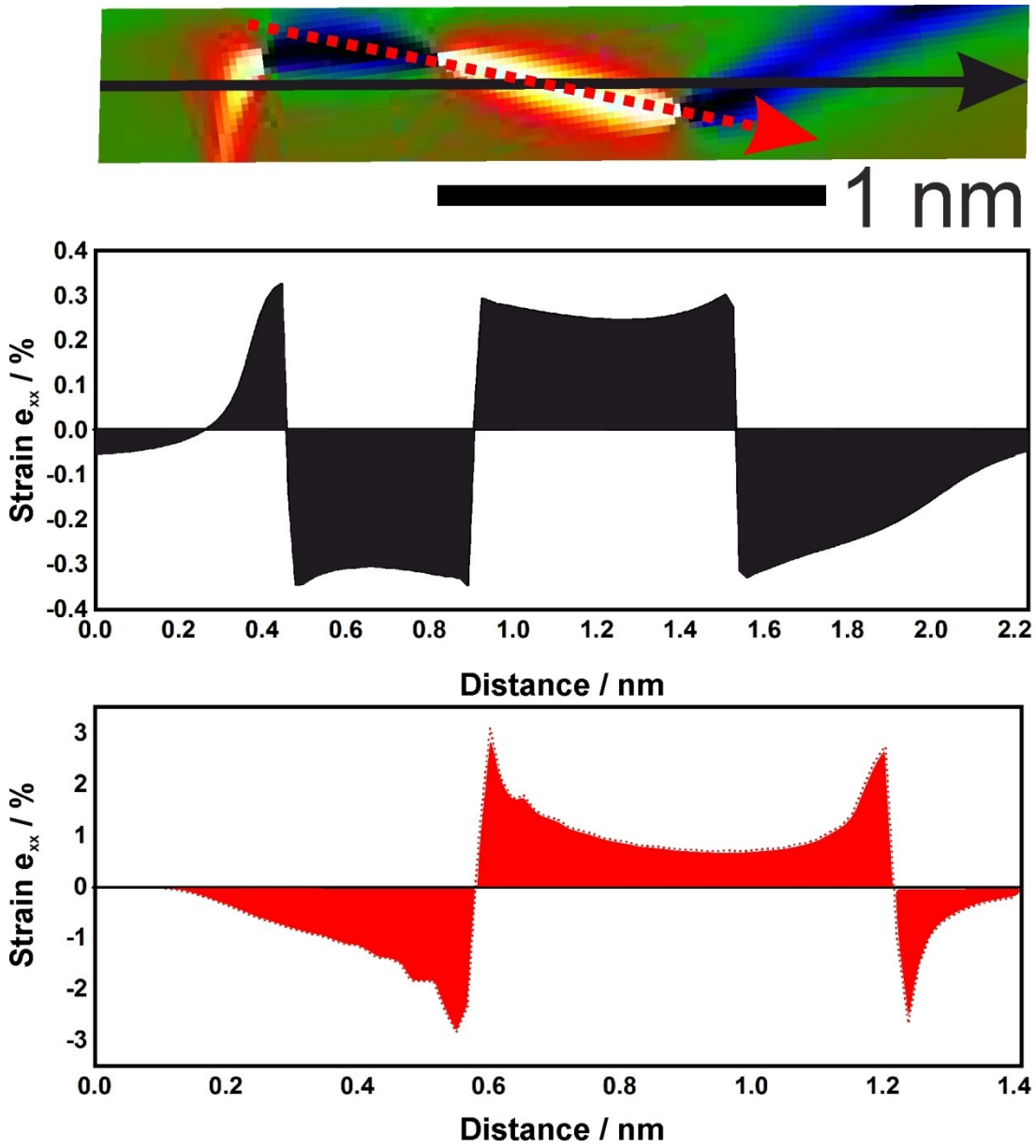

Figure 7.31: Strain profiles across hot spots located in the FeCo layer. The average in-plane strain (full area along black arrow) is alternating between tensile and compressive being in magnitude smaller than 0.4% on average. A profile drawn across the hot spot centers (along the red arrow) indicates the strain being locally larger than 1% of the reference (2.96 Å).

REFERENCES

[1] Williamson & Kaufman. "Biomagnetism". *J. Magn. Magn. Mater.* **22**, 129–201 (1981).

[2] Little, Pogosyan, Neal, Zavala, *et al.* "Adaptive deep brain stimulation in advanced Parkinson disease". *Ann. Neurol.* **74**, 449–457 (2013).

[3] Sternickel & Braginski. "Biomagnetism using SQUIDs: Status and perspectives". in *Superconductor Science and Technology* vol. 19 160–161 (2006).

[4] Langel & Estes. "The near-earth magnetic field at 1980 determined from Magsat data.". *J. Geophys. Res.* **90**, 2495–2509 (1985).

[5] Jaklevic, Lambe, Silver & Mercereau. "Quantum interference effects in Josephson tunneling". *Phys. Rev. Lett.* **12**, 159–160 (1964).

[6] Körber, Storm, Seton, Makela, *et al.* "SQUIDs in biomagnetism: A roadmap towards improved healthcare". *Superconductor Science and Technology* vol. 29 113001 (2016).

[7] Cohen, Edelsack & Zimmerman. "Magnetocardiograms taken inside a shielded room with a superconducting point-contact magnetometer". *Appl. Phys. Lett.* **16**, 278–280 (1970).

[8] Cohen. "Magnetoencephalography: Detection of the brain's electrical activity with a superconducting magnetometer". *Science (80-.).* **175**, 664–666 (1972).

[9] Budker & Romalis. "Optical magnetometry". *Nature Physics* vol. 3 227–234 (2007).

[10] Taue, Sugihara, Kobayashi, Ichihara, *et al.* "Development of a highly sensitive optically pumped atomic magnetometer for biomagnetic field measurements: A phantom study". *IEEE Trans. Magn.* **46**, 3635–3638 (2010).

[11] Marauska, Jahns, Greve, Quandt, *et al.* "MEMS magnetic field sensor based on magnetoelectric composites". *J. Micromechanics Microengineering* **22**, (2012).

[12] Wainer. "High Titania Dielectrics". *Trans. Electrochem. Soc.* **89**, 331 (1946).

[13] Wang. "Nanopiezotronics". *Adv. Mater.* **19**, 889–892 (2007).

[14] Wang & Song. "Piezoelectric nanogenerators based on zinc oxide nanowire arrays". *Science (80-.).* **312**, 242–246 (2006).

[15] Pepper. "Metals and semiconductors". *Phys. Bull.* **25**, 287–287 (1974).

[16] Yang, Wang, Tian, Xu, *et al.* "The piezotronic effect of zinc oxide nanowires studied by in situ TEM". *Adv. Mater.* **24**, 4676–4682 (2012).

[17] Jenkins, Nguyen, Zhu & Yang. "Piezotronic effect: An emerging mechanism for sensing applications". *Sensors (Switzerland)* **15**, 22914–22940 (2015).

[18] Takei, Takahashi, Ho, Ko, *et al.* "Nanowire active-matrix circuitry for low-voltage macroscale artificial skin". *Nat. Mater.* **9**, 821–826 (2010).

[19] Zhou, Wang, Han, Rai, *et al.* "Vertically aligned cdse nanowire arrays for energy harvesting and piezotronic devices". *ACS Nano* **6**, 6478–6482 (2012).

[20] Chen, Gao, Zhao, Zhang, *et al.* "Piezotronic Graphene Artificial Sensory Synapse". *Adv. Funct. Mater.* **29**, 1900959 (2019).

[21] Gröttrup, Kaps, Carstensen, Smazna, *et al.* "Piezotronic-based magnetoelectric sensor: Fabrication and response". *Phys. status solidi* **213**, 2208–2215 (2016).

[22] Wang. "Piezotronic and piezophototronic effects". *J. Phys. Chem. Lett.* **1**, 1388–1393 (2010).

[23] Keil, Frömling, Klein, Rödel, *et al.* "Piezotronic effect at Schottky barrier of a metal-ZnO single crystal interface". *J. Appl. Phys.* **121**, (2017).

[24] Friedrich, Knipping & von Laue. "*Interferenz-Erscheinungen bei Röntgenstrahlen*". (Sitzungsberichte der Mathematisch-Physikalischen Classe der Königlich-Bayerischen Akademie der Wissenschaften zu München, 1912).

[25] Chason & Mayer. "Thin film and surface characterization by specular X-ray reflectivity". *Crit. Rev. Solid State Mater. Sci.* **22**, 1–67 (1997).

[26] Hanke, Dubslaff, Schmidbauer, Boeck, *et al.* "Scanning x-ray diffraction with 200 nm spatial resolution". *Appl. Phys. Lett.* **92**, 193109 (2008).

[27] Thibault, Dierolf, Menzel, Bunk, *et al.* "High-resolution scanning X-ray diffraction microscopy". *Science (80-.).* **321**, 379–382 (2008).

[28] Robinson & Harder. "Coherent X-ray diffraction imaging of strain at the nanoscale". *Nat. Mater.* **8**, 291–298 (2009).

[29] Martin. "Piezoelectricity". *Phys. Rev. B* **5**, 1607–1613 (1972).

[30] Levine. "Inverse piezoelectric effect in polymers". *J. Appl. Polym. Sci.* **9**, 3351–3357 (1965).

[31] Manbachi & Cobbold. "Review Development and application of piezoelectric materials for ultrasound generation and detection". *Ultrasound* **19**, 187–196 (2011).

[32] Curry, Ke, Chorsi, Wrobel, *et al.* "Biodegradable piezoelectric force sensor". *Proc. Natl. Acad. Sci. U. S. A.* **115**, 909–914 (2018).

[33] Liu, Liu, Zhao, Xu, *et al.* "Design and Experiments of a Single-Foot Linear Piezoelectric Actuator Operated in a Stepping Mode". *IEEE Trans. Ind. Electron.* **65**, 8063–8071 (2018).

[34] Özgür, Alivov, Liu, Teke, *et al.* "A comprehensive review of ZnO materials and

devices". *Appl. Phys. Rev.* **041301**, (2005).

[35] Ellmer, Klein & Rech. "*Transparent Conductive Zinc Oxide*". (Springer-Verlag Berlin Heidelberg, 2008).

[36] Morkoç & Özgür. "General Properties of ZnO". in *Zinc Oxide* 1–76 (Wiley, 2009). doi:10.1002/9783527623945.ch1.

[37] Waseem, Jeong, Johar, Kang, *et al.* "Enhanced piezoelectric output of NiO/nanoporous GaN by suppression of internal carrier screening". *Semicond. Sci. Technol.* **33**, 065007 (2018).

[38] Crowell & Sze. "Current transport in metal-semiconductor barriers". *Solid. State. Electron.* **9**, 1035–1048 (1966).

[39] Sze & Ng. "*Physics of Semiconductor Devices*". *Physics of Semiconductor Devices* (Wiley-Interscience, 2006). doi:10.1002/0470068329.

[40] Tung. "The physics and chemistry of the Schottky barrier height". *Appl. Phys. Rev.* **1**, 11304 (2014).

[41] Look & Claflin. "P-type doping and devices based on ZnO". in *Physica Status Solidi (B) Basic Research* vol. 241 624–630 (John Wiley & Sons, Ltd, 2004).

[42] Ellmer & Bikowski. "Intrinsic and extrinsic doping of ZnO and ZnO alloys". *J. Phys. D. Appl. Phys.* **49**, 413002 (2016).

[43] Zhang, Wei & Zunger. "Intrinsic n-type versus p-type doping asymmetry and the defect physics of ZnO". *Phys. Rev. B - Condens. Matter Mater. Phys.* **63**, 075205 (2001).

[44] Murphy & Good. "Thermionic Emission, Field Emission, and the Transition Region". *Phys. Rev.* **102**, 1464–1473 (1956).

[45] Brillson & Lu. "ZnO Schottky barriers and Ohmic contacts". *Journal of Applied Physics* vol. 109 121301 (2011).

[46] Hagemark & Chacka. "Electrical transport properties of Zn doped ZnO". *J. Solid State Chem.* **15**, 261–270 (1975).

[47] Kim, Kim, Park, Seong, *et al.* "Formation of low resistance nonalloyed Al/Pt ohmic contacts on n-type ZnO epitaxial layer". *J. Appl. Phys.* **94**, 4225–4227 (2003).

[48] Allen & Durbin. "Influence of oxygen vacancies on Schottky contacts to ZnO". *Appl. Phys. Lett.* **92**, 122110 (2008).

[49] Gao, Zhou, Gu, Fei, *et al.* "Effects of piezoelectric potential on the transport characteristics of metal-ZnO nanowire-metal field effect transistor". *J. Appl. Phys.* **105**, 113707 (2009).

[50] Zhang, Liu & Wang. "Fundamental theory of piezotronics". *Adv. Mater.* **23**, 3004–3013

(2011).

[51] Duan, Cong, Jiang, Zhang, *et al.* "ZnO Thin Film Flexible UV Photodetectors: Regulation on the ZnO/Au Interface by Piezo-Phototronic Effect and Performance Outcomes". *Adv. Mater. Interfaces* **6**, 1900470 (2019).

[52] Mintken, Schweichel, Schröder, Kaps, *et al.* "Nanogenerator and piezotronic inspired concepts for energy efficient magnetic field sensors". *Nano Energy* **56**, 420–425 (2019).

[53] Zhou, Gu, Fei, Mai, *et al.* "Flexible piezotronic strain sensor". *Nano Lett.* **8**, 3035–3040 (2008).

[54] Wu. "Barrier height reduction of the Schottky barrier diode using a thin highly doped surface layer". *J. Appl. Phys.* **51**, 4919–4922 (1980).

[55] Gao & Wang. "Equilibrium potential of free charge carriers in a bent piezoelectric semiconductive nanowire". *Nano Lett.* **9**, 1103–1110 (2009).

[56] Lee. "Magnetostriction and magnetomechanical effects". *Reports on Progress in Physics* vol. 18 184–229 (1955).

[57] Koon, Williams & Das. "Giant magnetostriction materials". *J. Magn. Magn. Mater.* **100**, 173–185 (1991).

[58] Chopra & Wuttig. "Non-Joulian magnetostriction". *Nature* **521**, 340–343 (2015).

[59] Abes, Koops, Hrkac, McCord, *et al.* "Domain structure and reorientation in CoF e2 O4". *Phys. Rev. B* **93**, 1–7 (2016).

[60] Thomas & Gibbs. "Anisotropy and magnetostriction in metallic glasses". *J. Magn. Magn. Mater.* **103**, 97–110 (1992).

[61] Smyth & Martin. "x Ray crystallography". *Journal of Clinical Pathology - Molecular Pathology* vol. 53 8–14 (2000).

[62] Hrkac, Abes, Koops, Krywka, *et al.* "Local magnetization and strain in single magnetoelectric microrod composites". *Appl. Phys. Lett.* **103**, 1–6 (2013).

[63] Li, Senesi & Lee. "Small Angle X-ray Scattering for Nanoparticle Research". *Chemical Reviews* vol. 116 11128–11180 (2016).

[64] Neder & Korsunskiy. "Structure of nanoparticles from powder diffraction data using the pair distribution function". *J. Phys. Condens. Matter* **17**, (2005).

[65] Tegze & Faigel. "X-ray holography with atomic resolution". *Nature* **380**, 49–51 (1996).

[66] Pfeiffer. "X-ray ptychography". *Nat. Photonics* **12**, 9–17 (2018).

[67] Als-Nielsen & McMorrow. "*Elements of Modern X-ray Physics*". *Elements of Modern X-ray Physics: Second Edition* (2011). doi:10.1002/9781119998365.

[68] Wanzenberg, Agapov, Brefeld, Brinkmann, *et al.* "Design status of the ultra-low

emittance synchrotron facility PETRA IV". in *AIP Conference Proceedings* vol. 2054 (American Institute of Physics Inc., 2019).

[69] Khubbutdinov, Menushenkov & Vartanyants. "Coherence properties of the high-energy fourth-generation X-ray synchrotron sources". *J. Synchrotron Rad* **26**, 1851–1862 (2019).

[70] Geloni, Saldin, Samoylova, Schneidmiller, *et al.* "Coherence properties of the European XFEL". *New J. Phys.* **12**, 35021 (2010).

[71] Emma, Akre, Arthur, Bionta, *et al.* "First lasing and operation of an ångstrom-wavelength free-electron laser". *Nat. Photonics* **4**, 641–647 (2010).

[72] Bragg, Bragg Apr, H Bragg & Professor of Physics. "The reflection of X-rays by crystals". *Proc. R. Soc. London. Ser. A, Contain. Pap. a Math. Phys. Character* **88**, 428–438 (1913).

[73] Kiessig. "Untersuchungen zur Totalreflexion von Röntgenstrahlen". *Ann. Phys.* **402**, 715–768 (1931).

[74] Kiessig. "Interferenz von Röntgenstrahlen an dünnen Schichten". *Ann. Phys.* **402**, 769–788 (1931).

[75] Parratt. "Surface studies of solids by total reflection of x-rays". *Phys. Rev.* **95**, 359–369 (1954).

[76] Ocko, Wang, Davenport & Isaacs. "In situ x-ray reflectivity and diffraction studies of the Au(001) reconstruction in an electrochemical cell". *Phys. Rev. Lett.* **65**, 1466–1469 (1990).

[77] Braslau, Deutsch, Pershan, Weiss, *et al.* "Surface roughness of water measured by x-ray reflectivity". *Phys. Rev. Lett.* **54**, 114–117 (1985).

[78] Magnussen, Ocko, Regan, Penanen, *et al.* "X-Ray Reflectivity Measurements of Surface Layering in Liquid Mercury". *Phys. Rev. Lett.* **74**, 4444–4447 (1995).

[79] Gibaud & Hazra. "X-ray reflectivity and diffuse scattering". *Curr. Sci.* **78**, 1467–1477 (2000).

[80] Lovell & Richardson. "Analysis methods in neutron and X-ray reflectometry". *Curr. Opin. Colloid Interface Sci.* **4**, 197–204 (1999).

[81] Lengeler. "Coherence in X-ray physics". *Naturwissenschaften* vol. 88 249–260 (2001).

[82] Xiong, Moutanabbir, Reiche, Harder, *et al.* "Coherent X-ray diffraction imaging and characterization of strain in silicon-on-insulator nanostructures". *Adv. Mater.* **26**, 7747–7763 (2014).

[83] Miao, Charalambous, Kirz & Sayre. "Extending the methodology of X-ray

crystallography to allow imaging of micrometre-sized non-crystalline specimens". *Nature* **400**, 342–344 (1999).

[84] Robinson & Vartanyants. "Use of coherent X-ray diffraction to map strain fields in nanocrystals". *Appl. Surf. Sci.* **182**, 186–191 (2001).

[85] Miao, Ishikawa, Johnson, Anderson, *et al.* "High resolution 3D X-ray diffraction microscopy". *Phys. Rev. Lett.* **89**, 088303/1-088303/4 (2002).

[86] Chapman & Nugent. "Coherent lensless X-ray imaging". *Nat. Photonics* **4**, 833–839 (2010).

[87] Vartanyants & Singer. "Coherence properties of hard x-ray synchrotron sources and x-ray free-electron lasers". *New J. Phys.* **12**, 35004 (2010).

[88] Pfeifer, Williams, Vartanyants, Harder, *et al.* "Three-dimensional mapping of a deformation field inside a nanocrystal". *Nature* **442**, 63–66 (2006).

[89] Newton, Leake, Harder & Robinson. "Three-dimensional imaging of strain in a single ZnO nanorod". *Nat. Mater.* **9**, 17–19 (2010).

[90] Hofmann, Phillips, Das, Karamched, *et al.* "Nanoscale imaging of the full strain tensor of specific dislocations extracted from a bulk sample". *Phys. Rev. Mater.* **4**, 013801 (2020).

[91] Karpov & Fohtung. "Bragg coherent diffractive imaging of strain at the nanoscale". *J. Appl. Phys.* **125**, 121101 (2019).

[92] Marchesini, He, Chapman, Hau-Riege, *et al.* "X-ray image reconstruction from a diffraction pattern alone". *Phys. Rev. B* **68**, (2003).

[93] Faulkner & Rodenburg. "Movable aperture lensless transmission microscopy: A novel phase retrieval algorithm". *Phys. Rev. Lett.* **93**, 023903–1 (2004).

[94] Miao, Kirz & Sayre. "The oversampling phasing method". *Acta Crystallogr. Sect. D Biol. Crystallogr.* **56**, 1312–1315 (2000).

[95] Bates. "Fourier phase problems are uniquely solvable in mute than one dimension. I: underlying theory". *Optik (Stuttg).* **5**, (1982).

[96] Miao, Sayre & Chapman. "Phase retrieval from the magnitude of the Fourier transforms of nonperiodic objects". *J. Opt. Soc. Am. A* **15**, 1662 (1998).

[97] Biermanns, Davydok, Paetzelt, Diaz, *et al.* "Individual GaAs nanorods imaged by coherent X-ray diffraction". in *Journal of Synchrotron Radiation* vol. 16 796–802 (International Union of Crystallography, 2009).

[98] Marchesini. "A unified evaluation of iterative projection algorithms for phase retrieval". *Rev. Sci. Instrum.* **78**, (2007).

[99] Fienup. "Phase retrieval algorithms: a comparison". *Appl. Opt.* **21**, 2758 (1982).

[100] Luke. "Relaxed averaged alternating reflections for diffraction imaging". **21**, 37–50 (2005).

[101] Bauschke, Combettes & Luke. "Hybrid projection–reflection method for phase retrieval". *J. Opt. Soc. Am. A* **20**, 1025 (2003).

[102] Elser. "Phase retrieval by iterated projections". *J. Opt. Soc. Am. A* **20**, 40 (2003).

[103] Robinson, Vartanyants, Williams, Pfeifer, *et al.* "Reconstruction of the shapes of gold nanocrystals using coherent x-ray diffraction". *Phys. Rev. Lett.* **87**, 1–4 (2001).

[104] Schroer, Boye, Feldkamp, Patommel, *et al.* "Coherent X-Ray Diffraction Imaging with Nanofocused Illumination". **090801**, 1–4 (2008).

[105] Diaz, Mocuta, Stangl, Mandl, *et al.* "Coherent diffraction imaging of a single epitaxial InAs nanowire using a focused x-ray beam". *Phys. Rev. B - Condens. Matter Mater. Phys.* **79**, 125324 (2009).

[106] Clark, Huang, Harder & Robinson. "High-resolution three-dimensional partially coherent diffraction imaging". *Nat. Commun.* **3**, 993–996 (2012).

[107] Di Mauro, Fragalà, Privitera & Impellizzeri. "ZnO for application in photocatalysis: From thin films to nanostructures". *Mater. Sci. Semicond. Process.* **69**, 44–51 (2017).

[108] Mishra & Adelung. "ZnO tetrapod materials for functional applications". *Mater. Today* **21**, 631–651 (2018).

[109] Theerthagiri, Salla, Senthil, Nithyadharseni, *et al.* "A review on ZnO nanostructured materials: energy, environmental and biological applications". *Nanotechnology* **30**, 392001 (2019).

[110] Lallo da Silva, Caetano, Chiari-Andréo, Pietro, *et al.* "Increased antibacterial activity of ZnO nanoparticles: Influence of size and surface modification". *Colloids Surfaces B Biointerfaces* **177**, 440–447 (2019).

[111] Schmidt-Mende & MacManus-Driscoll. "ZnO - nanostructures, defects, and devices". *Mater. Today* **10**, 40–48 (2007).

[112] Wang & Wang. "Advances in piezotronic transistors and piezotronics". *Nano Today* vol. 37 101108 (2021).

[113] Gao, Han, Cui, Tey, *et al.* "ZnO nanoparticles as an antimicrobial tissue adhesive for skin wound closure". *J. Mater. Chem. B* **5**, 4535–4541 (2017).

[114] Kucheyev, Bradby, Williams, Jagadish, *et al.* "Mechanical deformation of single-crystal ZnO". *Appl. Phys. Lett.* **80**, 956–958 (2002).

[115] Kim, Jung, Kim, Yoon, *et al.* "Young's modulus of ZnO microwires determined by

various mechanical measurement methods". *Curr. Appl. Phys.* **14**, 166–170 (2014).

[116] Desai & Haque. "Mechanical properties of ZnO nanowires". *Sensors Actuators, A Phys.* **134**, 169–176 (2007).

[117] Lueng, Chan, Surya & Choy. "Piezoelectric coefficient of aluminum nitride and gallium nitride". *J. Appl. Phys.* **88**, 5360–5363 (2000).

[118] Brillson, Mosbacker, Hetzer, Strzhemechny, *et al.* "Dominant effect of near-interface native point defects on ZnO Schottky barriers". *Appl. Phys. Lett.* **90**, 102116 (2007).

[119] Cox, Foster, Jarjour, Wenckstern, *et al.* "Defect Manipulation To Control ZnO Micro-/Nanowire-Metal Contacts". (2018) doi:10.1021/acs.nanolett.8b02892.

[120] Mishra, Kaps, Schuchardt, Paulowicz, *et al.* "Fabrication of macroscopically flexible and highly porous 3D semiconductor networks from interpenetrating nanostructures by a simple flame transport approach". *Part. Part. Syst. Charact.* **30**, 775–783 (2013).

[121] Pankove. "GaN: From fundamentals to applications". *Mater. Sci. Eng. B* **61**–**62**, 305–309 (1999).

[122] Leszczynski, Teisseyre, Suski, Grzegory, *et al.* "Lattice parameters of gallium nitride". *Appl. Phys. Lett.* **69**, 73–75 (1996).

[123] Xia, Xia & Ruoff. "High-pressure structure of gallium nitride: Wurtzite-to-rocksalt phase transition". *Phys. Rev. B* **47**, 12925–12928 (1993).

[124] Ashfaque, Khan & Rao. "Gallium Nitride (GaN) Nanostructures and Their Gas Sensing Properties: A Review". *Sensors 2020, Vol. 20, Page 3889* **20**, 3889 (2012).

[125] Pearton, Abernathy, Thaler, Frazier, *et al.* "Wide bandgap GaN-based semiconductors for spintronics". *Journal of Physics Condensed Matter* vol. 16 R209 (2004).

[126] Zhao, Pu, Han, Du, *et al.* "Piezotronic Effect in Polarity-Controlled GaN Nanowires". *ACS Nano* **9**, 8578–8583 (2015).

[127] Beach & Berkowitz. "Giant magnetic field dependent impedance of amorphous FeCoSiB wire". *Appl. Phys. Lett* **64**, 3652 (1994).

[128] Kailath, Kumar & Mitra. "Effect of metalloids on crystallization and magnetic behaviour of FeCoSiB based metallic glass". *Bull. Mater. Sci.* **29**, 127–131 (2006).

[129] Hrkac, Lage, Köppel, Strobel, *et al.* "Amorphous FeCoSiB for exchange bias coupled and decoupled magnetoelectric multilayer systems: Real-structure and magnetic properties". *J. Appl. Phys.* **116**, 134302 (2014).

[130] Hayes, Schell, Salzer, Burdin, *et al.* "Electrically modulated magnetoelectric AlN/FeCoSiB film composites for DC magnetic field sensing". *J. Phys. D. Appl. Phys.* **51**, 354002 (2018).

[131] Nishizawa & Ishida. "The Co-Fe (Cobalt-Iron) System". *Bull. Alloy Phase Diagrams* **5**, 250 (1984).

[132] Couderchon & Tiers. "Some aspects of magnetic properties of Ni-Fe and Co-Fe alloys". *J. Magn. Magn. Mater.* **26**, 196–214 (1982).

[133] Cooke, Wang, Watts, Zuberek, *et al.* "The Effect of thermal treatment, composition and substrate on the texture and magnetic properties of FeCo thin films". *J. Phys. D. Appl. Phys.* **33**, 1450–1459 (2000).

[134] Klever, Stüber, Leiste, Nold, *et al.* "Multifunctional FeCo/TiN multilayer thin films with combined magnetic and protective properties". *Adv. Eng. Mater.* **11**, 969–975 (2009).

[135] Yang, Li, Yang, Yan, *et al.* "Reduction-Nitridation Synthesis of Titanium Nitride Nanocrystals". *J. Am. Ceram. Soc.* **86**, (2003).

[136] Lunney. "Pulsed laser deposition of metal and metal multilayer films". *Appl. Surf. Sci.* **86**, 79–85 (1995).

[137] Lafford, Gibbs & Shearwood. "Magnetic, magnetostrictive and structural properties of iron-cobalt/silver multilayers". *J. Magn. Magn. Mater.* **132**, 89–94 (1994).

[138] Wolff. "TEM Image of sample FeCo/Tin #125 (200keV JEOL ARM 200F) obtained by N. Wolff". *Kiel Univ. Tech. Fac. AG Prof. Kienle* (2020).

[139] Dai, Pan & Wang. "Novel nanostructures of functional oxides synthesized by thermal evaporation". *Advanced Functional Materials* vol. 13 9–24 (2003).

[140] Kelly & Arnell. "Magnetron sputtering: A review of recent developments and applications". *Vacuum* vol. 56 159–172 (2000).

[141] Cantalini, Sun, Faccio, Pelino, *et al.* "NO2 sensitivity of WO3 thin film obtained by high vacuum thermal evaporation". *Sensors Actuators, B Chem.* **31**, 81–87 (1996).

[142] Liu, Chen, Luo, Leng, *et al.* "Thermal evaporation and characterization of Sb2Se3 thin film for substrate Sb2Se3/CdS solar cells". *ACS Appl. Mater. Interfaces* **6**, 10687–10695 (2014).

[143] Swann. "Magnetron sputtering". *Phys. Technol.* **19**, 67–75 (1988).

[144] Hegedus. "*Current±Voltage Analysis of a-Si and a-SiGe Solar Cells Including Voltage-dependent Photocurrent Collection*". *Ltd. Prog. Photovolt. Res. Appl* vol. 5 (1997).

[145] Pursiainen, Linder, Jaeger, Oberschmid, *et al.* "Identification of aging mechanisms in the optical and electrical characteristics of light-emitting diodes". *Appl. Phys. Lett.* **79**, 2895–2897 (2001).

[146] Kim, Muster, Krstic, Park, *et al.* "Field-effect transistor made of individual V2O5 nanofibers". *Appl. Phys. Lett.* **76**, 1875–1877 (2000).

[147] Lee, Fung, Beling & Au. "A systematic approach to the measurement of ideality factor, series resistance, and barrier height for Schottky diodes". *J. Appl. Phys.* **72**, 4739–4742 (1992).

[148] Stettner. "*FRED Manual*". (2014).

[149] Buffet, Rothkirch, Döhrmann, Körstgens, *et al.* "P03, the microfocus and nanofocus X-ray scattering (MiNaXS) beamline of the PETRA III storage ring: The microfocus endstation". *J. Synchrotron Radiat.* **19**, 647–653 (2012).

[150] Krywka, Keckes, Storm, Buffet, *et al.* "Nanodiffraction at MINAXS (P03) beamline of PETRA III". in *Journal of Physics: Conference Series* vol. 425 072021 (Institute of Physics Publishing, 2013).

[151] P. & Baez. "Formation of optical images by X-rays". *J. Opt. Soc. Am.* **38**, 766–774 (1948).

[152] Hrkac, Koops, Abes, Krywka, *et al.* "Tunable Strain in Magnetoelectric ZnO Microrod Composite Interfaces". *ACS Appl. Mater. Interfaces* **9**, 25571–25577 (2017).

[153] Barchuk, Motylenko, Schneider, Förste, *et al.* "Defect-rich GaN interlayer facilitating the annihilation of threading dislocations in polar GaN crystals grown on (0001)-oriented sapphire substrates". *J. Appl. Phys.* **126**, 085301 (2019).

[154] Wieland, Krywka, Mick, Willumeit-Römer, *et al.* "Investigation of the inverse piezoelectric effect of trabecular bone on a micrometer length scale using synchrotron radiation". *Acta Biomater.* **25**, 339–346 (2015).

[155] Li, Xie, Maxey & Harder. "Methods for operando coherent X-ray diffraction of battery materials at the Advanced Photon Source". *J. Synchrotron Radiat.* **26**, 220–229 (2019).

[156] Kim, Chung, Kim, Yun, *et al.* "Defect Dynamics at a Single Pt Nanoparticle during Catalytic Oxidation". *Nano Lett.* **19**, 5044–5052 (2019).

[157] Passos, Rochet, Manente, Suzana, *et al.* "Three-dimensional strain dynamics govern the hysteresis in heterogeneous catalysis". *Nat. Commun.* **11**, 1–8 (2020).

[158] Hrauda, Zhang, Wintersberger, Etzelstorfer, *et al.* "X-ray nanodiffraction on a single SiGe quantum dot inside a functioning field-effect transistor". *Nano Lett.* **11**, 2875–2880 (2011).

[159] Jordt, Wolff, Hrkac, Shree, *et al.* "Local Strain Distribution in ZnO Microstructures Visualized with Scanning Nano X-ray Diffraction and Impact on Electrical Properties". *Adv. Eng. Mater.* (2021) doi:10.1002/adem.202100201.

[160] Ma, Hu, Li & Nan. "Recent Progress in Multiferroic Magnetoelectric Composites: from Bulk to Thin Films". *Adv. Mater.* **23**, 1062–1087 (2011).

[161] Spaldin & Ramesh. "Advances in magnetoelectric multiferroics". *Nature Materials* vol. 18 203–212 (2019).

[162] Lage, Kirchhof, Hrkac, Kienle, *et al.* "Exchange biasing of magnetoelectric composites". *Nat. Mater.* **11**, 523–529 (2012).

[163] Hayes, Salzer, Reermann, Yarar, *et al.* "Electrically modulated magnetoelectric sensors". *Appl. Phys. Lett.* **108**, (2016).

[164] Greve, Woltermann, Quenzer, Wagner, *et al.* "Giant magnetoelectric coefficients in (Fe90 Co 10)78 Si12 B10 -AlN thin film composites". *Appl. Phys. Lett.* **96**, 7–10 (2010).

[165] Tung. "Schottky-Barrier formation at single-crystal metal-semiconductor interfaces". *Phys. Rev. Lett.* **52**, 461–464 (1984).

[166] Hu, Zhang, Li & Wang. "Piezotronic Transistor Based on Topological Insulators". *ACS Nano* **12**, 779–785 (2018).

[167] Zhu, Zhou, Jing, Hua, *et al.* "Piezotronic Effect Modulated Flexible AlGaN/GaN High-Electron-Mobility Transistors". *ACS Nano* **13**, 13161–13168 (2019).

[168] Walukiewicz. "Mechanism of Fermi-level stabilization in semiconductors". *Phys. Rev. B* **37**, 4760–4763 (1988).

[169] Rogan, Tamura, Swift & Üstündag. "Direct measurement of triaxial strain fields around ferroelectric domains using x-ray microdiffraction". *Nature Materials* vol. 2 379–381 (2003).

[170] Schölli, Leake, Schulli & Leake. "X-ray nanobeam diffraction imaging of materials". *Curr. Opin. Solid State Mater. Sci.* **22**, 188–201 (2018).

[171] Todt, Krywka, Zhang, Mayrhofer, *et al.* "Indentation response of a superlattice thin film revealed by in-situ scanning X-ray nanodiffraction". *Acta Mater.* **195**, 425–432 (2020).

[172] Keckes, Bartosik, Daniel, Mitterer, *et al.* "X-ray nanodiffraction reveals strain and microstructure evolution in nanocrystalline thin films". *Scr. Mater.* **67**, 748–751 (2012).

[173] Catti, Noel & Dovesi. "Full piezoelectric tensors of wurtzite and zinc blende ZnO and ZnS by first-principles calculations". *J. Phys. Chem. Solids* **64**, 2183–2190 (2003).

[174] Desgreniers. "High-density phases of ZnO: Structural and compressive parameters". *Phys. Rev. B - Condens. Matter Mater. Phys.* **58**, 14102–14105 (1998).

[175] Kisi & Elcombe. "*u Parameters for the Wurtzite Structure of ZnS and ZnO using Powder Neutron Diffraction*". *Acta Crystallographica* vol. 45 (1989).

[176] Gerward & Olsen. "*The High-Pressure Phase of Zincite*". *Jorunal of Synchrotron Radiation* vol. 2 (1995).

[177] Reeber. "Lattice parameters of zno from 4.2°to 296°k". *J. Appl. Phys.* **41**, 5063–5066

(1970).

[178] Abes, Koops, Hrkac, Quandt, *et al.* "Direct measurements of field-induced strain in magnetoelectric composites by X-ray diffraction studies of forbidden reflections". *J. Appl. Phys.* **113**, 124303 (2013).

[179] Zhao & Zhang. "Microstrain and grain-size analysis from diffraction peak width and graphical derivation of high-pressure thermomechanics". *J. Appl. Crystallogr.* **41**, 1095–1108 (2008).

[180] Li, Li & Zhang. "Analysis of the carrier transport mechanism and barrier height formation of graphene/Zr–ZnO Schottky contact by I-V-T". *Mater. Sci. Semicond. Process.* **106**, 104793 (2020).

[181] Langford & Wilson. "Scherrer after sixty years: A survey and some new results in the determination of crystallite size". *J. Appl. Crystallogr.* **11**, 102–113 (1978).

[182] Adeagbo, Thomas, Nayak, Ernst, *et al.* "First-principles study of uniaxial strained and bent ZnO wires". *Phys. Rev. B - Condens. Matter Mater. Phys.* **89**, 195135 (2014).

[183] Agrawal, Peng, Gdoutos & Espinosa. "Elasticity Size Effects in ZnO Nanowires-A Combined Experimental-Computational Approach". (2008) doi:10.1021/nl801724b.

[184] Wolff, Hrkac, Ditto, Duppel, *et al.* "Crystallography at the nanoscale: Planar defects in ZnO nanospikes". *J. Appl. Crystallogr.* **52**, 1009–1015 (2019).

[185] Hu, Klein, Su, Niu, *et al.* "Temperature dependence of the piezotronic effect in ZnO nanowires". *Nano Lett.* **13**, 5026–5032 (2013).

[186] Li, Li, Zhang, Tong, *et al.* "Influence of B doping on the carrier transport mechanism and barrier height of graphene/ZnO Schottky contact". *J. Phys. D. Appl. Phys.* **51**, 095104 (2018).

[187] Zhang, Firestein, Fernando, Siriwardena, *et al.* "Recent Progress of In Situ Transmission Electron Microscopy for Energy Materials". *Adv. Mater.* **32**, 1904094 (2020).

[188] Johannes, Rensberg, Grünewald, Schöppe, *et al.* "Determination of the full deformation tensor by multi-Bragg fast scanning nano X-ray diffraction Determination of the full deformation tensor". *J. Appl. Crystallogr.* **53**, 99–106 (2020).

[189] Shi, Burdet, Chen, Xiong, *et al.* "X-ray ptychography on low-dimensional hard-condensed matter materials". *Applied Physics Reviews* vol. 6 11306 (2019).

[190] Carnis, Gao, Labat, Kim, *et al.* "Towards a quantitative determination of strain in Bragg Coherent X-ray Diffraction Imaging: artefacts and sign convention in reconstructions". *Sci. Rep.* **9**, 1–13 (2019).

[191] Holler, Guizar-Sicairos, Tsai, Dinapoli, *et al.* "High-resolution non-destructive three-

dimensional imaging of integrated circuits". *Nature* **543**, 402–406 (2017).

[192] Howell, Bashir, De Pastina, Matloub, *et al.* "Effect of ALN seed layer on crystallographic characterization of piezoelectric ALN". *arXiv* vol. 37 021504 (2018).

[193] Zhang, Zhao, Jin, Xue, *et al.* "Local Structure and Short-Range Order in a NiCoCr Solid Solution Alloy". *Phys. Rev. Lett.* **118**, 205501 (2017).

[194] Roelsgaard, Dippel, Borup, Nielsen, *et al.* "research papers". 299–304 (2019) doi:10.1107/S2052252519001192.

[195] Krywka, Neubauer, Priebe, Salditt, *et al.* "A two-dimensional waveguide beam for X-ray nanodiffraction". *J. Appl. Crystallogr.* **45**, 85–92 (2012).

[196] Krywka & Müller. "Micro- and nanodiffraction". in *X-Ray Diffraction: Modern Experimental Techniques* 55–88 (Pan Stanford Publishing Pte. Ltd., 2015). doi:10.1201/b15674-4.

[197] Wu & Wong. "Fabrication and Impedance Analysis of n-ZnO Nanorod/p-Si Heterojunctions to Investigate Carrier Concentrations in Zn/O Source- Ratio-Tuned ZnO Nanorod Arrays". *Adv. Mater.* **19**, 2015–2019 (2007).

[198] Wolff, Jordt, Braniste, Popa, *et al.* "Modulation of Electrical Conductivity and Lattice Distortions in Bulk HVPE-Grown GaN". *ECS J. Solid State Sci. Technol.* **8**, Q141–Q146 (2019).

[199] Waltereit, Bronner, Quay, Dammann, *et al.* "GaN-based high-frequency devices and circuits: A Fraunhofer perspective". *Physica Status Solidi (A) Applications and Materials Science* vol. 209 491–496 (2012).

[200] Maroldt, Quay, Dennler, Schwantuschke, *et al.* "(In)AlGaN heterojunction field effect transistors and circuits for high-power applications at microwave and millimeter-wave frequencies". *Jpn. J. Appl. Phys.* **52**, 08JN13 (2013).

[201] Waltereit, Bronner, Brückner, Dammann, *et al.* "Recent developments in GaN HEMTs and MMICs for high power electronics". in (Japan Society of Applied Physics, 2013). doi:10.7567/ssdm.2013.j-6-1.

[202] Koyama, Barsegyan & Walker. "Implications of using kW-level GaN transistors in radar and avionic systems". in *2015 IEEE International Conference on Microwaves, Communications, Antennas and Electronic Systems, COMCAS 2015* (Institute of Electrical and Electronics Engineers Inc., 2015). doi:10.1109/COMCAS.2015.7360465.

[203] Lerner, Eisenbrandt, Bower, Bonafede, *et al.* "Integration of GaN HEMTs onto Silicon CMOS by micro Transfer Printing". in *Proceedings of the International Symposium on Power Semiconductor Devices and ICs* vols 2016-July 451–454 (Institute of Electrical

and Electronics Engineers Inc., 2016).

[204] Waltereit, Bronner, Quay, Dammann, *et al.* "GaN HEMTs and MMICs for space applications". *Semicond. Sci. Technol.* **28**, 74010 (2013).

[205] Mishra & Guidry. "Lateral GaN Devices for Power Applications (from kHz to GHz)". in 69–99 (Springer, Cham, 2017). doi:10.1007/978-3-319-43199-4_4.

[206] Shur & Davis. "*GaN-Based Materials and Devices*". vol. 33 (WORLD SCIENTIFIC, 2004).

[207] Walker. "*Handbook of RF and Microwave Power Amplifiers*". *Handbook of RF and Microwave Power Amplifiers* (Cambridge University Press, 2011). doi:10.1017/cbo9781139015349.

[208] Pengelly, Wood, Milligan, Sheppard, *et al.* "A review of GaN on SiC high electron-mobility power transistors and MMICs". *IEEE Transactions on Microwave Theory and Techniques* vol. 60 1764–1783 (2012).

[209] Rajbhandari, McKendry, Herrnsdorf, Chun, *et al.* "A review of gallium nitride LEDs for multi-gigabit-per-second visible light data communications". *Semiconductor Science and Technology* vol. 32 023001 (2017).

[210] Kachi. "Recent progress of GaN power devices for automotive applications". *Jpn. J. Appl. Phys.* **53**, 100210 (2014).

[211] Piner. "(Invited) Gallium Nitride on Silicon". *ECS Trans.* **77**, 95–98 (2017).

[212] Keller, Li, Laurent, Hu, *et al.* "Recent progress in metal-organic chemical vapor deposition of (0001¯) N-polar group-III nitrides". *Semiconductor Science and Technology* vol. 29 113001 (2014).

[213] Bockowski, Iwinska, Amilusik, Fijalkowski, *et al.* "Challenges and future perspectives in HVPE-GaN growth on ammonothermal GaN seeds". *Semiconductor Science and Technology* vol. 31 093002 (2016).

[214] "*Technology of Gallium Nitride Crystal Growth*". vol. 133 (Springer Berlin Heidelberg, 2010).

[215] Suihkonen, Pimputkar, Sintonen & Tuomisto. "Defects in Single Crystalline Ammonothermal Gallium Nitride". *Adv. Electron. Mater.* **3**, 1600496 (2017).

[216] Tiginyanu, Stevens-Kalceff, Sarua, Braniste, *et al.* "Self-Organized Three-Dimensional Nanostructured Architectures in Bulk GaN Generated by Spatial Modulation of Doping". *ECS J. Solid State Sci. Technol.* **5**, P218–P227 (2016).

[217] Lee, Lee, Park, Watanabe, *et al.* "Cross sectional CL study of the growth and annihilation of pit type defects in HVPE grown (0001) thick GaN". *J. Cryst. Growth* **351**, 83–87

(2012).

[218] Díaz-Guerra, Piqueras, Popa, Cojocaru, *et al.* "Spatially resolved cathodoluminescence of GaN nanostructures fabricated by photoelectrochemical etching". *Appl. Phys. Lett.* **86**, 1–3 (2005).

[219] Popa, Tiginyanu, Ursaki, Volcius, *et al.* "A GaN-based two-sensor array for methane detection in an ethanol environment". *Semicond. Sci. Technol.* **21**, 1518–1521 (2006).

[220] Lewandowska, Weyher, Kelly, Konczewicz, *et al.* "The influence of free-carrier concentration on the PEC etching of GaN: A calibration with Raman spectroscopy". *J. Cryst. Growth* **307**, 298–301 (2007).

[221] Rodriguez, Gruverman, Kingon & Nemanich. "Piezoresponse force microscopy for piezoelectric measurements of III-nitride materials". *J. Cryst. Growth* **246**, 252–258 (2002).

[222] Morgan. "Broadening of Impurity Bands in Heavily Doped Semiconductors". *Phys. Rev.* **139**, A343 (1965).

[223] Iliopoulos, Doppalapudi, Ng & Moustakas. "Broadening of near-band-gap photoluminescence in n-GaN films". *Appl. Phys. Lett.* **73**, 375 (1998).

[224] Dingle & Ilegems. "Donor-acceptor pair recombination in GaN". *Solid State Commun.* **9**, 175–180 (1971).

[225] Paskova, Arnaudov, Paskov, Goldys, *et al.* "Donor-acceptor pair emission enhancement in mass-transport-grown GaN". *J. Appl. Phys.* **98**, 033508 (2005).

[226] Kozodoy, Ibbetson, Marchand, Fini, *et al.* "Electrical characterization of GaN p-n junctions with and without threading dislocations". *Appl. Phys. Lett.* **73**, 975 (1998).

[227] Elsner, Jones, Heggie, Sitch, *et al.* "Deep acceptors trapped at threading-edge dislocations in GaN". *Phys. Rev. B* **58**, 12571 (1998).

[228] Rosner, Carr, Ludowise, Girolami, *et al.* "Correlation of cathodoluminescence inhomogeneity with microstructural defects in epitaxial GaN grown by metalorganic chemical-vapor deposition". *Appl. Phys. Lett.* **70**, 420 (1998).

[229] Fujito, Kubo, Nagaoka, Mochizuki, *et al.* "Bulk GaN crystals grown by HVPE". *J. Cryst. Growth* **311**, 3011–3014 (2009).

[230] Kim, Lee, Moon, Hong, *et al.* "Preparation and properties of free-standing HVPE grown GaN substrates". *J. Cryst. Growth* **194**, 37–42 (1998).

[231] Bairamov, Gürdal, Botchkarev, Morkoç, *et al.* "Direct evidence of tensile strain in wurtzite structure n−GaN layers grown on n−Si(111) using AlN buffer layers". *Phys. Rev. B* **60**, 16741 (1999).

[232] Vailionis, Boschker, Siemons, Houwman, *et al.* "Misfit strain accommodation in epitaxial ABO3 perovskites: Lattice rotations and lattice modulations". *Phys. Rev. B* **83**, 064101 (2011).

[233] Hahn, Shmueli & Arthur. "*International tables for crystallography*". (Dordrecht: Reidel, 1983).

[234] Sridhara Rao, McLaughlin, Kappers & Humphreys. "Lattice distortions in GaN on sapphire using the CBED–HOLZ technique". *Ultramicroscopy* **109**, 1250–1255 (2009).

[235] Schulz & Thiemann. "Crystal structure refinement of AlN and GaN". *Solid State Commun.* **23**, 815–819 (1977).

[236] Geng, Sunakawa, Sumi, Yamamoto, *et al.* "Growth and strain characterization of high quality GaN crystal by HVPE". *J. Cryst. Growth* **350**, 44–49 (2012).

[237] Geng, Yamaguchi, Sunakawa, Sumi, *et al.* "Residual Strain Evaluation by Cross-Sectional Micro-Reflectance Spectroscopy of Freestanding GaN Grown by Hydride Vapor Phase Epitaxy". *Jpn. J. Appl. Phys.* **50**, 01AC01 (2011).

[238] Darakchieva, Paskova, Paskov, Monemar, *et al.* "Residual strain in HVPE GaN free-standing and re-grown homoepitaxial layers". *Phys. status solidi* **195**, 516–522 (2003).

[239] Heying, Wu, Keller, Li, *et al.* "Role of threading dislocation structure on the x-ray diffraction peak widths in epitaxial GaN films". *Appl. Phys. Lett.* **68**, 643 (1998).

[240] Heinke, Kirchner, Einfeldt & Hommel. "X-ray diffraction analysis of the defect structure in epitaxial GaN". *Appl. Phys. Lett.* **77**, 2145 (2000).

[241] Jordt, Wolff, Hrkac, Shree, *et al.* "Visualizing Intrinsic 3D-Strain Distribution in Gold Coated ZnO Microstructures by Bragg Coherent X-Ray Diffraction Imaging and Transmission Electron Microscopy with Respect to Piezotronic Applications". *Adv. Electron. Mater.* (2021) doi:10.1002/aelm.202100546.

[242] Wu, Wen & Wang. "Taxel-Addressable Matrix of Vertical-Nanowire Piezotronic Transistors for Active and Adaptive Tactile Imaging". *Science (80-.).* **340**, 952–958 (2013).

[243] Zhou, Yang, Zhu, Li, *et al.* "Piezoelectric nanogenerators with high performance against harsh conditions based on tunable N doped 4H-SiC nanowire arrays". *Nano Energy* **83**, 105826 (2021).

[244] Zhou, Maurya, Yan, Srinivasan, *et al.* "Self-Biased Magnetoelectric Composites: An Overview and Future Perspectives". *Energy Harvest. Syst.* **3**, 1–42 (2015).

[245] Liu, Zhang, Zhang & Lin Wang. "First principle simulations of piezotronic transistors". *Nano Energy* **14**, 355–363 (2015).

[246] Louie, Chelikowsky & Cohen. "Ionicity and the theory of Schottky barriers". *Phys. Rev. B* **15**, 2154–2162 (1977).

[247] Wu, Wei & Wang. "Strain-gated piezotronic logic nanodevices". *Adv. Mater.* **22**, 4711–4715 (2010).

[248] Gao & Wang. "Electrostatic potential in a bent piezoelectric nanowire. The fundamental theory of nanogenerator and nanopiezotronics". *Nano Lett.* **7**, 2499–2505 (2007).

[249] Yau, Cha, Kanan, Stephenson, *et al.* "Bragg coherent diffractive imaging of single-grain defect dynamics in polycrystalline films". **742**, 739–742 (2017).

[250] Ulvestad, Singer, Cho, Clark, *et al.* "Single particle nanomechanics in operando batteries via lensless strain mapping". *Nano Lett.* **14**, 5123–5127 (2014).

[251] Lazarev, Dzhigaev, Bi, Nowzari, *et al.* "Structural Changes in a Single GaN Nanowire under Applied Voltage Bias". *Nano Lett.* **18**, 5446–5452 (2018).

[252] Gao, Harder, Southworth, Guest, *et al.* "Three-dimensional optical trapping and orientation of microparticles for coherent X-ray diffraction imaging". **116**, (2019).

[253] Huang, Harder, Leake, Clark, *et al.* "Three-dimensional Bragg coherent diffraction imaging of an extended ZnO crystal". *J. Appl. Crystallogr.* **45**, 778–784 (2012).

[254] Xiong, Huang, Leake, Newton, *et al.* "Coherent x-ray diffraction imaging of ZnO nanostructures under confined illumination". *New J. Phys.* **13**, (2011).

[255] Lin, Liu, Yu, Cheng, *et al.* "Synchrotron X-ray Analytical Techniques for Studying Materials Electrochemistry in Rechargeable Batteries". *Chemical Reviews* vol. 117 13123–13186 (2017).

[256] Cooper, Denneulin, Bernier, Béché, *et al.* "Strain mapping of semiconductor specimens with nm-scale resolution in a transmission electron microscope". *Micron* **80**, 145–165 (2016).

[257] Fienup & Wackerman. "Phase-retrieval stagnation problems and solutions". *J. Opt. Soc. Am. A* **3**, 1897 (1986).

[258] Harder, Pfeifer, Williams, Vartaniants, *et al.* "Orientation variation of surface strain". *Phys. Rev. B* **76**, 1–4 (2007).

[259] Favre-Nicolin, Mastropietro, Eymery, Camacho, *et al.* "Analysis of strain and stacking faults in single nanowires using Bragg coherent diffraction imaging". *New J. Phys.* **12**, 35013 (2010).

[260] Ma, Dai, Yu & Huang. "Interface Schottky barrier engineering via strain in metal-semiconductor composites". *Nanoscale* **8**, 1352–1359 (2016).

[261] Lee, Ju, Kim, Yoo, *et al.* "Change in equilibrium position of misfit dislocations at the

GaN/sapphire interface by Si-ion implantation into sapphire - I. Microstructural characterization". *AIP Adv.* **5**, 077180 (2015).

[262] Hull. "Finite element analysis of stress relaxation in thin foil plan-view transmission electron microscopy specimens". *Appl. Phys. Lett.* **63**, 2291–2293 (1993).

[263] Hÿtch & Potez. "Geometric phase analysis of high-resolution electron microscopy images of antiphase domains: Example Cu3Au". *Philos. Mag. A* **76**, 1119–1138 (1997).

[264] Morkoç & Özgür. "*Zinc oxide : fundamentals, materials and device technology*". *Wiley* (2008). doi:10.1002/9783527623945.ch1.

[265] Kumar, Singh, Sharma, Kumar, *et al.* "Investigation of structural and optical properties of ZnO thin films of different thickness grown by pulsed laser deposition method". *Phys. B Condens. Matter* **552**, 221–226 (2019).

[266] Wang, Liu, Gao, Pang, *et al.* "Ultrathin Piezotronic Transistors with 2 nm Channel Lengths". *ACS Nano* **12**, 4903–4908 (2018).

[267] Bauschke, Combettes & Luke. "On the structure of some Phase Retrieval algorithms". *J. Opt. Soc. Am. A* **19**, 1334 (2002).

[268] Vartanyants & Robinson. "Partial coherence effects on the imaging of small crystals using coherent x-ray diffraction". *J. Phys. Condens. Matter* **13**, 10593–10611 (2001).

[269] Kim, Choi, Yun, Kang, *et al.* "Nanoscale Strain Imaging using Coherent X-ray Light Sources". **73**, 793–804 (2018).

[270] Wang & Wu. "Piezotronics and piezo-phototronics—Fundamentals and applications". (2014) doi:10.1093/nsr/nwt002.

[271] Kaps, Bhowmick, Gröttrup, Hrkac, *et al.* "Piezoresistive Response of Quasi-One-Dimensional ZnO Nanowires Using an in Situ Electromechanical Device". *ACS Omega* **2**, 2985–2993 (2017).

[272] Abes, Koops, Hrkac, Greve, *et al.* "Direct measurements of field-induced strain at magnetoelectric interfaces by grazing incidence x-ray diffraction". *Appl. Phys. Lett.* **102**, 1–5 (2013).

[273] Zhu & Yang. "Separation of the piezotronic and piezoresistive effects in a zinc oxide nanowire". *Nanotechnology* **25**, (2014).

[274] Wolff, Jordt, Jetter, Vogt, *et al.* "Nanostabilization of tetragonal distorted FeCo variants in ultra-thin FeCo/TiN multilayer films". *Mater. Charact.* **172**, 110871 (2021).

[275] Röbisch, Salzer, Urs, Reermann, *et al.* "Pushing the detection limit of thin film magnetoelectric heterostructures". *J. Mater. Res.* **32**, 1009–1019 (2017).

[276] Reermann, Durdaut, Salzer, Demming, *et al.* "Evaluation of magnetoelectric sensor

systems for cardiological applications". *Meas. J. Int. Meas. Confed.* **116**, 230–238 (2018).

[277] Liu & Morisako. "Soft magnetic properties of FeCo films with high saturation magnetization". *J. Appl. Phys.* **103**, 7–726 (2008).

[278] Pan & Du. "(FeCo/Co-M)n soft magnetic multilayers with uniaxial anisotropy and very high saturation magnetization". *J. Appl. Phys.* **93**, 5498–5502 (2003).

[279] Staruch, Gopman, Iunin, Shull, *et al.* "Reversible strain control of magnetic anisotropy in magnetoelectric heterostructures at room temperature". *Sci. Rep.* **6**, 1–9 (2016).

[280] Marauska, Dankwort, Quenzer & Wagner. "Sputtered thin film piezoelectric aluminium nitride as a functional MEMS material and CMOS compatible process integration". in *Procedia Engineering* vol. 25 1341–1344 (Elsevier, 2011).

[281] Hrkac, Kobler, Marauska, Petraru, *et al.* "Structural study of growth, orientation and defects characteristics in the functional microelectromechanical system material aluminium nitride". *J. Appl. Phys.* **117**, 14301 (2015).

[282] Gojdka, Jahns, Meurisch, Greve, *et al.* "Fully integrable magnetic field sensor based on delta-E effect". *Appl. Phys. Lett.* **99**, 223502 (2011).

[283] Jahns, Zabel, Marauska, Gojdka, *et al.* "Microelectromechanical magnetic field sensor based on Δ e effect". *Appl. Phys. Lett.* **105**, 52414 (2014).

[284] Zabel, Reermann, Fichtner, Kirchhof, *et al.* "Multimode delta-E effect magnetic field sensors with adapted electrodes". *Appl. Phys. Lett.* **108**, 222401 (2016).

[285] Spetzler, Kirchhof, Reermann, Durdaut, *et al.* "Influence of the quality factor on the signal to noise ratio of magnetoelectric sensors based on the delta-E effect". *Appl. Phys. Lett.* **114**, 183504 (2019).

[286] Fukuzawa, Kamiguchi, Koi, Iwasaki, *et al.* "Saturation magnetostriction of an ultrathin CoFe free-layer on double-layered underlayers". *J. Appl. Phys.* **91**, 3120–3124 (2002).

[287] Klever, Seemann, Stüber, Ulrich, *et al.* "Epitaxially stabilized TiN/(Ti,Fe,Co)N multilayer thin films in (pseudo-)fcc crystal structure by sequential magnetron sputter deposition". *J. Phys. D. Appl. Phys.* **43**, 6 (2010).

[288] Jia, Houben, Thust & Barthel. "On the benefit of the negative-spherical-aberration imaging technique for quantitative HRTEM". *Ultramicroscopy* **110**, 500–505 (2010).

[289] Garbrecht, Spiecker, Tillmann & Jäger. "Quantitative atom column position analysis at the incommensurate interfaces of a (PbS)1.14NbS2 misfit layered compound with aberration-corrected HRTEM". *Ultramicroscopy* **111**, 245–250 (2011).

[290] Stadelmann. "EMS - a software package for electron diffraction analysis and HREM

image simulation in materials science". *Ultramicroscopy* **21**, 131–145 (1987).

[291] Kilaas. "Optimal and near-optimal filters in high-resolution electron microscopy". *Journal of Microscopy* vol. 190 45–51 (1998).

[292] Schuller. "New class of layered Materials". *Phys. Rev. Lett.* **44**, 1597–1600 (1980).

[293] Thornton. "*High Rate Thick Film Growth*". *Ann. Rev. Mater. Sci* vol. 7 (1977).

[294] Anders. "A structure zone diagram including plasma-based deposition and ion etching". *Thin Solid Films* **518**, 4087–4090 (2010).

[295] Stavroyiannis, Christides, Niarchos, Kehagias, *et al.* "Low-field giant magnetoresistance in (111)-textured Co/Au multilayers prepared with magnetron sputtering". *J. Appl. Phys.* **84**, 6221–6228 (1998).

[296] Yarar, Hrkac, Zamponi, Piorra, *et al.* "Low temperature aluminum nitride thin films for sensory applications". *AIP Adv.* **6**, 75115 (2016).

[297] Detavernier, Özcan, Jordan-Sweet, Stach, *et al.* "An off-normal fibre-like texture in thin films on single-crystal substrates". *Nature* **426**, 641–645 (2003).

[298] Vandenberg, Gershoni, Hamm, Panish, *et al.* "Structural perfection of InGaAs/InP strained-layer superlattices grown by gas source molecular-beam epitaxy: A high-resolution x-ray diffraction study". *J. Appl. Phys.* **66**, 3635–3638 (1989).

[299] Palmstrøm. "Epitaxy of dissimilar materials". *Annu. Rev. Mater. Sci.* **25**, 389–415 (1995).

[300] Chopra. "Metastable Thin Film Epitaxial Structures". *physica status solidi (b)* vol. 32 489–507 (1969).

[301] Andersson, Burkert, Warnicke, Björck, *et al.* "Perpendicular magnetocrystalline anisotropy in tetragonally distorted Fe-Co alloys". *Phys. Rev. Lett.* **96**, 037205 (2006).

[302] Andersson, Björck, Lidbaum, Sanyal, *et al.* "Structure of Fe-Co/Pt(001) superlattices: A realization of tetragonal Fe-Co alloys". *J. Phys. Condens. Matter* **19**, 016008 (2007).

[303] Fu, Li, Misra, Hoagland, *et al.* "Mechanical properties of sputtered Cu/V and Al/Nb multilayer films". *Mater. Sci. Eng. A* **493**, 283–287 (2008).

[304] Hÿtch, Snoeck & Kilaas. "Quantitative measurement of displacement and strain fields from HREM micrographs". *Ultramicroscopy* **74**, 131–146 (1998).

[305] Matsuura, Tezuka & Sugimoto. "Increased uniaxial perpendicular anisotropy in tetragonally distorted FeCo-Ti-N films". *J. Appl. Phys.* **117**, 17–738 (2015).

[306] Andersson & Bjorck. "Anisotropy tuning in tetragonal FeCo alloys". in *Journal of Nanoscience and Nanotechnology* vol. 10 6186–6189 (2010).

[307] Burkert, Nordström, Eriksson & Heinonen. "Giant magnetic anisotropy in tetragonal

FeCo alloys". *Phys. Rev. Lett.* **93**, 027203 (2004).

[308] Şaşioğlu, Friedrich & Blügel. "Strong magnon softening in tetragonal FeCo compounds". *Phys. Rev. B - Condens. Matter Mater. Phys.* **87**, 020410 (2013).

[309] Liu, Kanda & Morisako. "The effect of underlayers on FeCo thin films". in *Journal of Physics: Conference Series* vol. 266 012037 (Institute of Physics Publishing, 2011).

[310] Warnicke, Andersson, Björck, Ferré, *et al.* "Magnetic anisotropy of tetragonal FeCo/Pt(001) superlattices". in *Journal of Physics Condensed Matter* vol. 19 226218–226228 (IOP Publishing, 2007).

[311] Winkelmann, Przybylski, Luo, Shi, *et al.* "Perpendicular magnetic anisotropy induced by tetragonal distortion of FeCo alloy films grown on Pd(001)". *Phys. Rev. Lett.* **96**, 257205 (2006).

[312] Lao, Jung & Sahashi. "Strong perpendicular uniaxial magnetic anisotropy in tetragonal Fe0.5Co0.5 films of artificially ordered B2 state". *IEEE Trans. Magn.* **50**, (2014).

[313] Hasegawa, Niibori, Takemasa & Oikawa. "Stabilisation of tetragonal FeCo structure with high magnetic anisotropy by the addition of V and N elements". *Sci. Rep.* **9**, 1–9 (2019).

[314] Reichel, Giannopoulos, Kauffmann-Weiss, Hoffmann, *et al.* "Increased magnetocrystalline anisotropy in epitaxial Fe-Co-C thin films with spontaneous strain". *J. Appl. Phys.* **116**, 213901 (2014).

[315] Jung, Doyle, Wittig, Al-Sharab, *et al.* "Soft anisotropic high magnetization Cu/FeCo films". *Appl. Phys. Lett.* **81**, 2415–2417 (2002).

[316] Jung, Doyle & Matsunuma. "Influence of underlayers on the soft properties of high magnetization FeCo films". in *Journal of Applied Physics* vol. 93 6462–6464 (American Institute of PhysicsAIP, 2003).

[317] Lukashev, Horrell & Sabirianov. "Tailoring magnetocrystalline anisotropy of FePt by external strain". in *Journal of Applied Physics* vol. 111 7–318 (American Institute of PhysicsAIP, 2012).

[318] Balke, Maksymovych, Jesse, Herklotz, *et al.* "Differentiating Ferroelectric and Nonferroelectric Electromechanical Effects with Scanning Probe Microscopy". *ACS Nano* **9**, 6484–6492 (2015).

[319] Jesse, Mirman & Kalinin. "Resonance enhancement in piezoresponse force microscopy: Mapping electromechanical activity, contact stiffness, and Q factor". *Appl. Phys. Lett.* **89**, 22906 (2006).

[320] Mahmood, Gould, Hassan & Salih. "D.c. properties of ZnO thin films prepared by r.f.

magnetron sputtering". *Thin Solid Films* **270**, 376–379 (1995).

[321] Ondo-Ndong, Essone-Obame, Moussambi & Koumba. "Capacitive properties of zinc oxide thin films by radiofrequency magnetron sputtering". *J. Theor. Appl. Phys.* **12**, 309–317 (2018).

ABBREVIATIONS

AFM	Atomic Force Microscope
APS	Advanced Photon Source
BCXDI	Bragg Coherent X-ray Diffraction Imaging
CDI	Coherent Diffraction Imaging
CRC	Collaborative Research Centre
CXDI	Coherent X-ray Diffraction Imaging
DESY	Deutsches Elektronen Synchrotron
DFG	Deutsche Forschungsgemeinschaft
ED	Electron Diffraction
EDS	Energy-Dispersive X-ray Spectroscopy
ER	Error reduction algorithm
FFT	Fast Fourier Transform
FIB	Focused Ion Beam
FT	Fourier Transform
FTS	Flame Transport Synthesis
FWHM	Full Width at Half Maximum
GPA	Geometric Phase Analysis
HIO	Hybrid-Input-Output algorithm
HRTEM	High Resolution Transmission Electron Microscopy
HVPE	Hydride Vapor Phase Epitaxy
iFT	Inverse Fourier Transform
imref	Quasi Fermi Level
I-V	Current/Voltage
ME	Magnetoelectric
NBG	Near Band Gap
nXRD	Nano X-ray Diffraction
OPM	Optical pumped atomic magnetometer
PEC	Photoelectrochemical
PL	Photoluminescence
PVD	Physical Vapor Deposition
RF	Radio Frequency
SEFiR	Single-End Fixed Rod sample holder

SEM	Scanning Electron Microscope
SQUID	Superconducting quantum interference devices
STEM	Scanning Transmission Electron Microscopy
TEM	Transmission Electron Microscopy
XRD	X-ray Diffraction
XRR	X-ray Reflectometry/Reflectivity

EIDESSTATTLICHE ERKLÄRUNG

Ich erkläre, dass diese Arbeit nach Inhalt und Form die eigene Arbeit ist, abgesehen von der Beratung durch meine Betreuerin Dr. B. M. Murphy, und ich keine weiteren Quellen bzw. Hilfestellungen erhalten habe, abgesehen von den angegebenen.
Die Arbeit ist unter Einhaltung der Regeln guter wissenschaftlicher Praxis der Deutschen Forschungsgemeinschaft entstanden. Es wurde mir kein akademischer Grad entzogen.
Die eingereichte Arbeit hat weder ganz noch zum Teil schon bei einer anderen Stelle im Rahmen eines Prüfungsverfahrens vorgelegen, Teile der Arbeit wurden jedoch in wissenschaftlichen Journalen veröffentlicht.
Eine Übersicht aller im Rahmen dieser Arbeit entstandenen Veröffentlichungen, inklusive einer Einschätzung des erbrachten Eigenanteils, ist dem folgendem Kapitel Wissenschaftliche Beiträge/Eigenanteil zu entnehmen.

Kiel, den

_____

Philipp Jordt

WISSENSCHAFTLICHE BEITRÄGE/EIGENANTEIL

Im Rahmen dieser Arbeit wurden folgende wissenschaftliche Beiträge als Veröffentlichungen in Fachzeitschriften oder mündliche Vorträge bzw. Posterpräsentationen auf Konferenzen erbracht.

Zur Einschätzung des erbrachten Eigenanteils in den Veröffentlichungen wird eine Einteilung in die folgenden sechs Aufgabenbereiche vorgenommen:

1) Experimentelles Konzept
2) Planung/Vorbereitung
3) Messung
4) Auswertung
5) Texterstellung
6) Korrektur und Finalisierung

Für jeden der Teilaspekte wird ein Wert zwischen 0 (kein Arbeitsanteil) und 10 (vollständig) angegeben.
Dies stellt eine subjektive Einschätzung des erbrachten Arbeitsanteils dar und spiegelt nicht zwangsläufig die Einschätzung der beteiligten Koautoren wider, wurde jedoch nach bestem Wissen und Gewissen vorgenommen.

Veröffentlichungen in Fachzeitschriften/Manuskripte:

Jordt, P., Hrkac, S. B., Gröttrup, J., Davydok, A., Krywka, C., Wolff, N., Kienle, L., Adelung, R., Magnussen, O. M., & Murphy, B. M. (2021). Local Strain Distribution in ZnO Microstructures Visualized with Scanning Nano X-Ray Diffraction and Impact on Electrical Properties. *Advanced Engineering Materials*, 2100201. (https://doi.org/10.1002/adem.202100201)

Konzept	*Planung*	*Messung*	*Auswertung*	*Text*	*Korrektur*
5/10	7/10	6/10	9/10	8/10	5/10

Jordt, P., Wolff, N., Hrkac, S. B., Shree, S., Wang, D., Harder, R. J., Kübel, C., Adelung, R., Sphyrko, O. G., Magnussen, O. M., Kienle, L., & Murphy, B. M. (2021). Visualizing Intrinsic 3D-Strain Distribution in Gold Coated ZnO Microstructures by Bragg Coherent X-ray Diffraction Imaging and Transmission Electron Microscopy with Respect to Piezotronic Applications. *Advanced Electronic Materials*, 2100546. (https://doi.org/10.1002/aelm.202100546)

Konzept	*Planung*	*Messung*	*Auswertung*	*Text*	*Korrektur*
7/10	7/10	5/10	7/10	7/10	4/10

Jordt, P., Vogt, H., Petersdorf, L., Shree, S., Cha. W., Harder, R. J., Adelung, R., Magnussen, O. M., & Murphy, B. M. (2021). Metallic Alloy FeCoSiB as Ohmic Contact on ZnO and Operando Electrical Investigation of a Piezotronic Magnet Field Microrod Sensor, combined with Coherent X-ray Diffraction Imaging of the Strain Distribution. (*manuscript*)

Konzept	*Planung*	*Messung*	*Auswertung*	*Text*	*Korrektur*
8/10	9/10	6/10	9/10	8/10	-/10

Wolff, N., Jordt, P., Jetter, J., Vogt, H., Lotnyk, A., Seemann, K., Ulrich, S., Quandt, E., Murphy, B. M., & Kienle, L. (2021). Nanostabilization of tetragonal distorted FeCo variants in ultra-thin FeCo/TiN multilayer films. *Materials Characterization*, 172, 110871. (https://doi.org/10.1016/j.matchar.2021.110871)

Konzept	*Planung*	*Messung*	*Auswertung*	*Text*	*Korrektur*
0/10	3/10	3/10	3/10	2/10	1/10

Wolff, N., Jordt, P., Braniste, T., Popa, V., Monaico, E., Ursaki, V., Petraru, A., Adelung, R., Murphy, B. M., Kienle, L., & Tiginyanu, I. (2019). Modulation of electrical conductivity and lattice distortions in bulk HVPE-grown GaN. *ECS Journal of Solid State Science and Technology*, *8*(8), Q141. (https://doi.org/10.1149/2.0041908jss)

Konzept	*Planung*	*Messung*	*Auswertung*	*Text*	*Korrektur*
0/10	1/10	3/10	2/10	2/10	1/10

Koops, C. T., Hrkac, S. B., Abes, M., Jordt, P., Stettner, J., Petraru, A., Kohlstedt, H., Hrkac, H., Wolff, N., Kienle, L., Seeck, O. H., Nisbet, G., Magnussen, O. M., & Murphy, B. M. (2019). Elastic Coupling at Epitaxial Multiferroic Interfaces: in situ X-ray Studies of Electric Field Induced Strain. In *International Conference on Nanotechnologies and Biomedical Engineering* (pp. 187-191). Springer, Cham. (https://doi.org/10.1007/978-3-030-31866-6_38)

Konzept	*Planung*	*Messung*	*Auswertung*	*Text*	*Korrektur*
0/10	0/10	0/10	0/10	1/10	1/10

Mündliche Vorträge auf wissenschaftlichen Konferenzen:

Understanding enhanced strain in piezotronic ZnO micro structures using operando nanofocus diffraction, *Euro Intelligent Materials*, Kiel, 2017

_____

Stress induced deformation in piezotronic micro structures studied by X-ray nano diffraction, *German Conference for Research with Synchrotron Radiation, Neutrons and Ion Beams at Large Facilities (SNI)*, München, 2018

_____

Strain study of piezotronic ZnO microstructures utilising X-ray nanodiffraction techniques, *DPG-Frühjahrstagung*, Regensburg, 2019

_____

Strain distribution in piezotronic ZnO microstructures visualised by X-ray nanodiffraction techniques, *Euro Intelligent Materials*, Kiel, 2019

Posterpräsentationen auf wissenschaftlichen Konferenzen:

Stress induced deformation and piezotronic behavior in ZnO micro structures, *DESY User Meeting*, Hamburg, 2016

_____

Microstructure and Structural Change of Magnetoelectric and Piezotronic Sensors, *Projektantrag SFB 1261 Vorstellung Teilprojekt A6*, Kiel, 2016

_____

Investigating strain and piezotronic behavior in ZnO micro structures using operando Nanofocus diffraction, *DESY User Meeting*, Hamburg, 2017

_____

Uncovering Planar Defects: Combined X-Ray Diffraction and Electron Microscopy, *Euro Intelligent Materials*, Kiel, 2017

_____

Piezotronic related strain effects in ZnO microstructures, *DESY User Meeting*, Hamburg, 2018

_____

Studies of stress induced deformation in ZnO micro structures by X-ray diffraction, *Material Science and Engineering (MSE)*, Darmstadt, 2018

_____

Combined insitu X-ray nanodiffraction and electrical examination of piezotronic ZnO microstructures, *DESY User Meeting*, Hamburg, 2019

_____

ZnO and the influence of strain on the piezotronic effect visualized with *insitu* X-Ray (coherent) nano diffraction, *DESY User Meeting*, Hamburg, 2020

_____

Strain impact on the piezotronic effect in ZnO rods visualized with X-Ray diffraction in sub-µm resolution, *DESY User Meeting*, Hamburg, 2021

BETREUTE ARBEITEN

Im Rahmen dieser Arbeit wurden die folgenden wissenschaftlichen Arbeiten bearbeitet und betreut:

Henning Vogt, *Simultane piezotronische Messungen und Streuuntersuchungen an ZnO Kristallsäulen*, *Bachelorarbeit*, 2016

_____

Finn Christiansen, *Aufbau und Charakterisierung eines Hochfluss-Röntgendiffraktometers mit Fokussierung*, *Masterarbeit*, 2017/18

_____

Hannes Caesar, *Strom-Spannungs-Messungen an piezotronischen Zinkoxid Mikrostrukturen*, *Bachelorarbeit*, 2018

_____

Jan-Philipp Kress, *Röntgenbeugung und Reflektivitätsmessung an Magnetostrukturen FeCo/TiN*, *Bachelorarbeit*, 2018

_____

Henning Vogt, *Untersuchungen von magnetostriktiven und piezotronischen Mikrostrukturen mittels Röntgenstreumethoden*, *Masterarbeit*, 2018/19

_____

Lukas Petersdorf, *Untersuchung der elektrischen Eigenschaften von piezotronischen Nanostrukturen*, *Bachelorarbeit*, 2019

_____

Nikolas Hayen, *Untersuchungen magnetostriktiver Multischichten mittels Röntgenbeugung*, *Bachelorarbeit*, 2019

DANKSAGUNG

Diese Arbeit ist erst ermöglicht geworden durch den Beitrag von vielen verschiedenen Personen, die alle ihren ganz persönlichen Einfluss und Abdruck in dieser Arbeit hinterlassen haben. Sei es durch Unterstützung beim Aufbau, der Durchführung, der Analyse der Experimente gewesen oder durch eine großartige und freundschaftliche Arbeitsumgebung.
Ganz besonders möchte ich meiner Betreuerin Dr. Bridget Murphy danken, durch ihre Unterstützung und Zusprache diese Arbeit erst möglich wurde. Insbesondere da sie mir das Vertrauen und die Möglichkeit gegeben hat, diese Arbeit im Rahmen des SFB 1261 zu erstellen.
Des Weiteren möchte ich Prof. Lorenz Kienle für seine Unterstützung meiner Forschung danken. Seine Einblicke von Seiten der Elektronenmikroskopie waren stets eine Bereicherung und große Hilfe bei unseren gemeinsamen Projekten.
Prof. Olaf Magnussen möchte ich danken für die herzliche Aufnahme in der Arbeitsgruppe und das Fachwissen und die Ideen, mit denen er meine Experimente unterstütze.
Meinem Projektpartner/Mitstreiter Dr. Niklas Wolff gilt mein besonderer Dank für eine großartige Zusammenarbeit und viele konstruktive Diskussionen, um unser Projekt voranzubringen.
Dr. Stjepan Hrkac möchte ich außerordentlich dafür danken, dass er mir am Anfang meiner Promotion stets hilfreich zur Seite stand und mir viele Tipps und Kniffe bei der Probenherstellung und deren Messungen gegeben hat.
Prof. Oleg Shpyrko danke ich für die Möglichkeit meines Aufenthalts an der University of San Diego und eine freundliche Aufnahme in seine Arbeitsgruppe. Besonders hervorheben möchte ich die Hilfe durch Devin Cela und Dr. Anatoly Shabalin und ihren Versuchen mir CXDI verständlich zu machen.
Dr. Jochim Stettner gilt mein Dank für seinen unermüdlichen Einsatz um FRED und WILMA bestmöglich zu warten und dafür, dass er mir bei den Messungen mit Rat und Tat zur Seite stand.
Prof. Rainer Adelung, Dr. Jorit Gröttrup, Dr. Sindu Shree und Mona Stoelting möchte ich für die Herstellung der ZnO Nadeln und die Unterstützung bei elektrischen Messungen danken.
Monika Seeger, Linda Sommer und Claudia Läufer danke ich für ihre stets freundliche Hilfe, die mich nie allein mit allerlei Formalitäten gelassen haben.
Karsten Tarhouni, Arndt Seeger und Joost Jakobs möchte ich danken für ihren technischen Sachverstand, ohne den es so manches Experiment nicht gegeben hätte.

Dipl.-Ing. Matthias Greve danke ich für seine Unterstützung bei der Entwicklung und Optimierung der verschiedenen Experimente.
Der zentralen Werkstatt des Physikzentrums gilt mein besonderer Dank, da ohne die von ihnen hergestellten Experimente diese gesamte Arbeit nicht möglich gewesen wäre.
Den Master und Bachelor Studierenden, Henning Vogt, Finn Christiansen, Hannes Caesar, Jan-Philipp Kress, Lukas Petersdorf und Nikolas Hayen, gilt mein Dank für die von ihnen erzielten Ergebnisse, die zum Erfolg des Projektes beigetragen haben.
Bei Jonas Warias, Tim Wiegman, Malte Jacobsen, Björn Haushahn, Svenja Hövelmann, Andrea Sartori, Lasse Kattwinkel, Timo Fuchs, Reihaneh Amirbeigiarab, Rajendra Prasad Giri, Talina Rush, Sven Festersen, Martin Runge, Nicolai Krekiehn, Christian Koops und allen weiteren aktuellen oder ehemaligen Mitgliedern der Arbeitsgruppe, die ich im Laufe der Jahre kennen lernen durfte, möchte ich mich für eine tolle Arbeitsumgebung und viele konstruktive wie auch oftmals erheiternde Gespräche bedanken.

Ganz besonders möchte ich mich bei Wiebke, Petra, Johannes, Tobias, meiner gesamten Familie und allen Freunden für die großartige Unterstützung und Freundschaft bedanken.

APPENDIX

A. PERMISSIONS FOR REPRINT

Wiley-CH:

Reuse My Published Work

As a Wiley author, you retain certain reuse rights when you sign your Copyright Transfer Agreement (CTA). Refer back to this agreement if you are seeking permission to:

- Republish an extract of your own published work.
- Include your article in your thesis.
- Use copies for your internal teaching purposes.

If you still require a formal permission license, please make the request through RightsLink and select "author of this Wiley work" and your appropriate reuse rights to download your license.

Elsevier:

Can I use material from my Elsevier journal article within my thesis/dissertation? –

As an Elsevier journal author, you have the right to Include the article in a thesis or dissertation (provided that this is not to be published commercially) whether in full or in part, subject to proper acknowledgment; see the Copyright page for more information. No written permission from Elsevier is necessary.

This right extends to the posting of your thesis to your university's repository provided that if you include the published journal article, it is embedded in your thesis and not separately downloadable.

IOP:

Can I use my article as part of my thesis/dissertation after it has been published with IOP?

When you transfer the copyright in your article to IOP, we grant back to you certain rights, including the **right to include all or part of the Final Published Version of the article within any thesis or dissertation.** Please note you may need to obtain separate permission for any **third party content** you include within your article. Please include citation details, "© IOP Publishing. Reproduced with permission. All rights reserved". The only restriction is that if, at a later date, you want to share your thesis/dissertation online, permission to include the Final Published Version of the article within the online version of your thesis/dissertation will need to be sought from IOP. Alternatively, you may choose to replace the article in the online version of your thesis/dissertation with either a Preprint or the Accepted Manuscript version (if the embargo period has passed), provided you comply with our Preprint or Author Rights: Accepted Manuscript policy, as relevant.